

WL-TR-97-2086



**THERMAL PERFORMANCE OF A SCRAMJET
COMBUSTOR OPERATING AT MACH 5.6 FLIGHT CONDITIONS**

**Scott D. Stouffer
Richard D. Neumann
Deems S. Emmer**

**University of Dayton Research Institute
300 College Park
Dayton, OH 45469**

October 1997

Final Report for Period May 1996 - March 1997

Approved for public release: distribution unlimited

**AERO PROPULSION AND POWER DIRECTORATE
WRIGHT LABORATORY
AIR FORCE MATERIEL COMMAND
WRIGHT-PATTERSON AFB, OHIO 45433-7251**

19980831 019

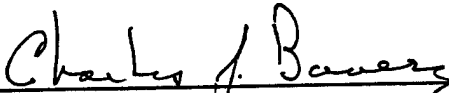
DTIC QUALITY INSPECTED 1

NOTICE

USING GOVERNMENT DRAWINGS, SPECIFICATIONS, OR OTHER DATA INCLUDED IN THIS DOCUMENT FOR ANY PURPOSE OTHER THAN GOVERNMENT PROCUREMENT DOES NOT IN ANY WAY OBLIGATE THE US GOVERNMENT. THE FACT THAT THE GOVERNMENT FORMULATED OR SUPPLIED THE DRAWINGS, SPECIFICATIONS, OR OTHER DATA DOES NOT LICENSE THE HOLDER OR ANY OTHER PERSON OR CORPORATION; OR CONVEY ANY RIGHTS OR PERMISSION TO MANUFACTURE, USE, OR SELL ANY PATENTED INVENTION THAT MAY RELATE TO THEM.

THIS REPORT IS RELEASABLE TO THE NATIONAL TECHNICAL INFORMATION SERVICE (NTIS). AT NTIS, IT WILL BE AVAILABLE TO THE GENERAL PUBLIC, INCLUDING FOREIGN NATIONS.

THIS TECHNICAL REPORT HAS BEEN REVIEWED AND IS APPROVED FOR PUBLICATION.



GOVERNMENT MONITOR

CHARLES J. BAUER

High Speed Systems Development Branch
Propulsion Sciences & Advanced Concepts Division
Propulsion Directorate



SUPERVISOR

KENNETH PHILIPPART, Major, USAF

Chief, High Speed Systems Development Branch
Propulsion Sciences & Advanced Concepts Division
Propulsion Directorate



DIVISION CHIEF

PARKER L. BUCKLEY, Deputy Chief

Propulsion Sciences & Advanced Concepts Division
Propulsion Directorate

Do not return copies of this report unless contractual obligations or notice on a specific document requires its return.

REPORT DOCUMENTATION PAGE			Form Approved OMB No. 0704-0188	
Public reporting burden for this collection of information is estimated to average 1 hour per response, including the time for reviewing instructions, searching existing data sources, gathering and maintaining the data needed, and completing and reviewing the collection of information. Send comments regarding this burden estimate or any other aspect of this collection of information, including suggestions for reducing this burden, to Washington Headquarters Services, Directorate for Information Operations and Reports, 1215 Jefferson Davis Highway, Suite 1204, Arlington, VA 22202-4302, and to the Office of Management and Budget, Paperwork Reduction Project (0704-0188), Washington, DC 20503.				
1. AGENCY USE ONLY (Leave blank)		2. REPORT DATE October 1997	3. REPORT TYPE AND DATES COVERED FINAL; May 1996 - March 1997	
4. TITLE AND SUBTITLE Thermal Performance of a Scramjet Combustor Operating at Mach 5.6 Flight Conditions			5. FUNDING NUMBERS C: F33615-92-C-2218 PE: 62203F PR: 3048 TA: 05 WU: AL	
6. AUTHOR(S) Scott D. Stouffer Richard D. Neumann Deems S. Emmer				
7. PERFORMING ORGANIZATION NAME(S) AND ADDRESS(ES) University of Dayton Research Institute 300 College Park Dayton OH 45469			8. PERFORMING ORGANIZATION REPORT NUMBER UDR-TR-97-90	
9. SPONSORING/MONITORING AGENCY NAME(S) AND ADDRESS(ES) Aero Propulsion and Power Directorate Wright Laboratory Air Force Materiel Command Wright-Patterson AFB OH 45433-7251 POC: Ellen Strobel, AFRL/PRSF, 937-255-4027			10. SPONSORING/MONITORING AGENCY REPORT NUMBER WL-TR-97-2086	
11. SUPPLEMENTARY NOTES				
12a. DISTRIBUTION AVAILABILITY STATEMENT Approved for public release: distribution unlimited			12b. DISTRIBUTION CODE	
13. ABSTRACT (Maximum 200 words) This report describes the experimental data and the procedures used in acquiring and reducing the thermal loads data during tests of a hydrocarbon-fueled scramjet combustor at United Technologies Research Center (UTRC). This research effort is part of the UTRC effort to develop dual-mode scramjet combustor technology to support the development of Mach 8 missile technology. The objective of the thermal loads testing was to map the thermal and mechanical loads, including heat transfer, dynamic and static pressures, and skin friction in a scramjet combustor during direct-connect scramjet tests. The tests were conducted at the UTRC Ramjet/Scramjet direct-connect combustor test facility in East Hartford, CT.				
14. SUBJECT TERMS Scramjet Combustor, Thermal Loads Tests, Heat Flux			15. NUMBER OF PAGES 144	
			16. PRICE CODE	
17. SECURITY CLASSIFICATION OF REPORT UNCLASSIFIED	18. SECURITY CLASSIFICATION OF THIS PAGE UNCLASSIFIED	19. SECURITY CLASSIFICATION OF ABSTRACT UNCLASSIFIED	20. LIMITATION OF ABSTRACT SAR	

Table of Contents

List of Figures	iv
List of Tables	vii
Foreword	viii
Nomenclature	ix
1.0 Introduction	1
2.0 Experimental Apparatus	3
2.1 Test Facility	3
2.2 Combustor Model	3
3.0 Instrumentation and Data Analysis Procedures	4
3.1 Heat Flux Measurement	4
3.2 Skin Friction Measurements	4
3.3 Instrument Locations	5
3.4 Data System	8
3.5 Data Analysis Procedures	9
3.6 Test Matrix	9
4.0 Heat Transfer Correlation Procedure	10
5.0 Results	13
5.1 Bottom Wall Heat Flux Measurements	13
5.2 Injector Wall Heat Transfer	16
5.3 Skin Friction Measurements	18
5.4 Loss of the Silicon Oil in the Skin Friction Gage Cavity	23
6.0 Data Files from the Mach 5.6 Tests	24
6.1 Heat Transfer and Temperature Data Files	24
6.2 Skin Friction Data Files	24
7.0 Status of the Instrumentation and Data System	26
8.0 Summary and Conclusions	27
9.0 Recommendations	30
10.0 References	31
11.0 Appendix A: Conversion of Temperature to Heat Flux	32
References for Appendix A	40
12.0 Appendix B: Figures	41

List of Figures

Figure 1.	Layout of Heat Flux and Skin Friction Instrumentation for the Mach 5.6 Test.....	42
Figure 2.	Sketch of Coaxial Thermocouple	43
Figure 3.	Sketch of the Skin Friction Gage.....	44
Figure 4.	Coaxial Thermocouple Locations on the Pilot Mounting Frame	45
Figure 5.	A Flow Chart of the Data Acquisition Process	46
Figure 6.	Raw and Smoothed Temperature Traces for a Typical Thermocouple	47
Figure 7.	Effect of the Recovery Temperature on the Stanton Number (Test 886, $x = 11.5"$, $y = 1"$)	48
Figure 8.	Correlation of the Peak Heating in Front of a Cylinder-Wall Junction.....	49
Figure 9.	Wall Temperatures at Selected Locations During Run 884	50
Figure 10.	Initial and Peak Temperatures Along the Centerline of the Bottom Wall.....	51
Figure 11.	Initial and Peak Temperatures on the Bottom Wall During Run 884	52
Figure 12.	Initial and Peak Temperatures on the Bottom Wall During Run 886.....	53
Figure 13.	Wall Temperatures Upstream of the Shock Interaction in Run 884.....	54
Figure 14.	Heat Fluxes at Selected Locations During Run 884.....	55
Figure 15.	Detail of Unstart During Run 884 for the Gage at $x = 12"$	56
Figure 16.	Film Coefficient for the Gage at $x = 12"$	57
Figure 17.	Comparison of Reference Heating to the Reference Heating in the Experiment at WPAFB	58
Figure 18.	Comparison of Peak Heating in the Shock Interaction Region to the Peak Heating in the Experiment at WPAFB (No Fuel)	59
Figure 19.	Film Coefficient Along the Bottom Wall in Test 884	60
Figure 20.	Film Coefficient Along the Bottom Wall in Test 886	61
Figure 21.	Film Coefficient Along the Bottom Wall in Test 887	62
Figure 22.	Pressure and Film Coefficient Ratios Along the Centerline in Test 884	63
Figure 23.	Pressure and Film Coefficient Ratios Along the Centerline in Test 886	64
Figure 24.	Pressure and Film Coefficient Ratios Along the Centerline in Test 887	65
Figure 25.	Ratio of $h_{fuel-on}/h_{fuel-off}$ Along the Wall Opposite the Injector.....	66
Figure 26.	Film Coefficients for Gage 101 ($x = 4.05"$, $y = 0"$)	67
Figure 27.	Film Coefficients for Gage 102 ($x = 6.09"$, $y = 0"$)	68
Figure 28.	Film Coefficients for Gage 103 ($x = 7.25"$, $y = 0"$)	69
Figure 29.	Film Coefficients for Gage 104 ($x = 7.5"$, $y = 0.48"$)	70
Figure 30.	Film Coefficients for Gage 105 ($x = 7.5"$, $y = 1.0"$)	71
Figure 31.	Film Coefficients for Gage 106 ($x = 7.5"$, $y = 1.83"$)	72
Figure 32.	Film Coefficients for Gage 108 ($x = 8.65"$, $y = 0.43"$)	73
Figure 33.	Film Coefficients for Gage 109 ($x = 8.65"$, $y = 0.69"$)	74
Figure 34.	Lateral Distribution of the Heat Flux Augmentation Ratio $h_{fuel-on}/h_{fuel-off}$ Downstream of the Injectors.....	75
Figure 35.	Voltage from the Vitiated Heater Total Pressure Transducer.....	76
Figure 36.	Skin Friction at $x = 11.5"$, $y = 1"$ During the Cold Flow Test	77
Figure 37.	Skin Friction at $x = 11.5"$, $y = -1"$ During the Cold Flow Test	78

Figure 38.	Skin Friction at $x = 13"$, $y = 1"$ During the Cold Flow Test	79
Figure 39.	Skin Friction at $x = 15"$, $y = -1"$ During the Cold Flow Test	80
Figure 40.	Skin Friction at $x = 17"$, $y = -1"$ During the Cold Flow Test	81
Figure 41.	Skin Friction at $x = 20.5"$, $y = 1"$ During the Cold Flow Test	82
Figure 42.	Skin Friction at $x = 23"$, $y = -1"$ During the Cold Flow Test	83
Figure 43.	Skin Friction at $x = 23.5"$, $y = 0"$ During the Cold Flow Test	84
Figure 44.	Skin Friction at $x = 24.6"$, $y = 0"$ During the Cold Flow Test	85
Figure 45.	Skin Friction at $x = 25.5"$, $y = -1"$ During the Cold Flow Test	86
Figure 46.	Skin Friction at $x = 28.5"$, $y = 0"$ During the Cold Flow Test	87
Figure 47.	Skin Friction at $x = 11.5"$, $y = 1"$ During Test 884	88
Figure 48.	Skin Friction at $x = 11.5"$, $y = -1"$ During Test 884	89
Figure 49.	Skin Friction at $x = 13"$, $y = 1"$ During Test 884	90
Figure 50.	Skin Friction at $x = 15"$, $y = -1"$ During Test 884	91
Figure 51.	Skin Friction at $x = 17"$, $y = -1"$ During Test 884	92
Figure 52.	Skin Friction at $x = 20.5"$, $y = 1"$ During Test 884	93
Figure 53.	Skin Friction at $x = 23"$, $y = -1"$ During Test 884	94
Figure 54.	Skin Friction at $x = 23.5"$, $y = 0"$ During Test 884	95
Figure 55.	Skin Friction at $x = 24.6"$, $y = 0"$ During Test 884	96
Figure 56.	Skin Friction at $x = 25.5"$, $y = -1"$ During Test 884	97
Figure 57.	Skin Friction at $x = 28.5"$, $y = 0"$ During Test 884	98
Figure 58.	Skin Friction at $x = 11.5"$, $y = 1"$ During Test 886	99
Figure 59.	Skin Friction at $x = 11.5"$, $y = -1"$ During Test 886	100
Figure 60.	Skin Friction at $x = 13"$, $y = 1"$ During Test 886	101
Figure 61.	Skin Friction at $x = 15"$, $y = -1"$ During Test 886	102
Figure 62.	Skin Friction at $x = 17"$, $y = -1"$ During Test 886	103
Figure 63.	Skin Friction at $x = 20.5"$, $y = 1"$ During Test 886	104
Figure 64.	Skin Friction at $x = 23"$, $y = -1"$ During Test 886	105
Figure 65.	Skin Friction at $x = 23.5"$, $y = 0"$ During Test 886	106
Figure 66.	Skin Friction at $x = 24.6"$, $y = 0"$ During Test 886	107
Figure 67.	Skin Friction at $x = 25.5"$, $y = -1"$ During Test 886	108
Figure 68.	Skin Friction at $x = 28.5"$, $y = 0"$ During Test 886	109
Figure 69.	Skin Friction at $x = 11.5"$, $y = 1"$ During Test 887	110
Figure 70.	Skin Friction at $x = 11.5"$, $y = -1"$ During Test 887	111
Figure 71.	Skin Friction at $x = 13"$, $y = 1"$ During Test 887	112
Figure 72.	Skin Friction at $x = 15"$, $y = -1"$ During Test 887	113
Figure 73.	Skin Friction at $x = 17"$, $y = -1"$ During Test 887	114
Figure 74.	Skin Friction at $x = 20.5"$, $y = 1"$ During Test 887	115
Figure 75.	Skin Friction at $x = 23"$, $y = -1"$ During Test 887	116
Figure 76.	Skin Friction at $x = 23.5"$, $y = 0"$ During Test 887	117
Figure 77.	Skin Friction at $x = 24.6"$, $y = 0"$ During Test 887	118
Figure 78.	Skin Friction at $x = 25.5"$, $y = -1"$ During Test 887	119
Figure 79.	Skin Friction at $x = 28.5"$, $y = 0"$ During Test 887	120
Figure 80.	The Skin Friction at $x = 11.5"$, $y = 1"$	121
Figure 81.	The Skin Friction at $x = 15"$	122

Figure 82.	Comparison of Skin Friction and Heat Transfer at $x = 11.5"$, $y = 1"$ During Run 886.....	123
Figure 83.	Comparison of Skin Friction and Heat Transfer at $x = 11.5"$, $y = -1"$ During Run 886.....	124
Figure 84.	Comparison of Skin Friction and Heat Transfer at $x = 13"$, $y = 1"$ During Run 886.....	125
Figure 85.	Comparison of Skin Friction and Heat Transfer at $x = 15"$, $y = -1"$ During Run 886.....	126
Figure 86.	Comparison of Skin Friction and Heat Transfer at $x = 17"$, $y = -1"$ During Run 886.....	127
Figure 87.	Comparison of Skin Friction and Heat Transfer at $x = 20.5"$, $y = 1"$ During Run 886.....	128
Figure 88.	Comparison of Skin Friction and Heat Transfer at $x = 23"$, $y = -1"$ During Run 886.....	129
Figure 89.	Comparison of Skin Friction and Heat Transfer at $x = 24.6"$, $y = 0"$ During Run 886.....	130
Figure 90.	Comparison of Skin Friction and Heat Transfer at $x = 25.5"$, $y = -1"$ During Run 886.....	131
Figure 91.	Comparison of Skin Friction and Heat Transfer at $x = 28.5"$, $y = 0"$ During Run 886.....	132
Figure 92.	Semi-infinite Response of Dow-Corning Silicon Oil to a Constant Heat Flux of $10 \text{ BTU/ft}^2\text{-s}$	133
Figure 93.	Temperature Distribution Through the Wall at $x = 23"$, $y = -1"$ During Run 886.....	134
Figure 94.	A Section of File bt884fa.txt.....	135

List of Tables

Table 1.	Positions of the Coax Thermocouples Installed in the Wall Opposite the Injectors (UTRC Coordinates)	6
Table 2.	Positions of Combined Skin Friction/Wall Temperature Gages on the Wall Opposite the Injectors.....	7
Table 3.	Positions of Coax Thermocouples Installed in the Injector Block	8
Table 4.	Recovery Temperatures Used in the Calculation of the Film Coefficient in Figures 19 -21	15
Table 5.	Film Coefficient Augmentation Ratios $h_{fuel-on}/h_{fuel-off}$ for the Gages on the Injector Side of the Combustor	18
Table 6.	The Average Shear Force During the Cold Flow Test (Primary Axis).....	19
Table 7.	The Average Shear Force During the Cold Flow Test (Secondary Axis)	20

Foreword

This report describes the test procedures and the thermal loads data acquired during the Mach 5.6 Aerothermal Loads Tests. The work was performed for the Propulsion Development Branch (WL/POPR) of the Aero Propulsion and Power Directorate at Wright-Patterson AFB. This work was carried out during the period from May 1996 through March 1997 under contract F33615-92-C-2218-TASK 24. Ellen M. Strobel served as the Air Force contract manager and Ted Norbut served as the project engineer. Mr. Arthur Lewis served as the program manager for UDRI.

The authors wish to thank Ira Kay, Ron Lehrach, Jim McNamara, and Todd McCleod of United Technologies Research Center for their assistance in carrying out the experimental tests.

Nomenclature

C_f	skin friction coefficient
c_p	specific heat (BTU/lbm-°R)
h	film coefficient (BTU/ft ² -s-°R)
H	heat function, $H \equiv \frac{h}{\left(\frac{T_\infty}{T_*}\right)^{0.6} \mu_\infty}$ (BTU/lbf-s-°R)
P	pressure (lbf/in ²)
Pr	Prandtl number, $Pr \equiv \frac{\mu c_p}{k}$
q	heat flux (BTU/ft ² -s)
Re_x	Reynolds number
St	Stanton number, $St \equiv \left(\frac{h}{\rho_\infty c_p U_\infty} \right)$
T	temperature (°R)
U	velocity (m/s)
ρ	density (lbm/ft ³)
τ	wall shear (lbf/ft ²)
μ	viscosity (lbf-s/ft ²)

Subscripts

0	total
pk	peak
r	recovery
ref	reference or flat plate values
w	wall
∞	freestream conditions
*	reference condition for compressible flow

1.0 Introduction

This report describes the experimental data and the procedures used in acquiring and reducing the thermal loads data during tests of a hydrocarbon-fueled scramjet combustor at United Technologies Research Center (UTRC). This research effort is part of the UTRC effort to develop dual-mode scramjet combustor technology to support the development of Mach 8 missile technology. The objective of the thermal load tests was to map the thermal and mechanical loads, including heat transfer, dynamic and static pressures, and skin friction in a UTRC/Pratt & Whitney (UTRC/PW) scramjet combustor during direct-connect scramjet tests. The tests were conducted at the UTRC Ramjet/Scramjet direct-connect combustor test facility in East Hartford CT, and included personnel from UTRC/PW, UDRI, and SAIC. UDRI was responsible for the heat flux and skin friction measurements.

The original test plan included tests at combustor entrance conditions corresponding to flight Mach numbers of 5.6, 7.0 and 8.0. However, tests were conducted only at the $M = 5.6$ entrance conditions because of the unavailability of the UTRC Mach 3.7 facility nozzle that is required for the Mach 7 and 8 tests. It is anticipated that the higher Mach number tests will be performed after the nozzle fabrication is completed by UTRC.

This experimental effort is the second phase of a UDRI effort to map the thermal environment in the UTRC/PW SCRAMjet combustor. The first phase, which was conducted in Cell 19 at WPAFB, was an experimental study of the heat flux due to shock interference heating in the combustor with no fuel injection. The details of the shock interference study are reported in Reference 1. In the present study, the heat transfer was measured for a direct-connect hydrocarbon-fueled scramjet combustor. The tests were conducted with both unheated gaseous ethylene and the heated products from the endothermic reaction of Jet A, which was passed through a catalytic reactor to simulate regenerative cooling of the structure.

This report first describes the test facility combustor that was developed by UTRC. The thermal instrumentation is described next. A total of 82 coaxial thermocouples and 11 skin friction gages were used in this study. Most of the heat flux measurements and all of the skin friction measurements were on the wall that was opposite the main fuel injectors. A limited number of gages (8) were placed on the injector wall in the nearfield of the pilots.

A mobile 120-channel data system, which was developed for this research, is then discussed along with the data reduction procedures. The data system was based on the HP 3852A using a 16-bit high speed A/D. Software control for the system was written in the Labview visual programming language.

Thermal loads data were acquired for one test using gaseous ethylene and two tests using reformed Jet A fuel. The wall temperature and heat transfer data were saved in

spreadsheet format and have been transmitted to Pratt and Whitney. Significant results of the study are:

1. The use of coaxial thermocouple gages for the measurement of detailed heat transfer measurement of the heat transfer in scramjet combustors was demonstrated in a combusting environment for 50 second run times.
2. The coaxial gages were shown to provide a rapid, localized indication of wall heating. As a result, they were effective in determining where combustion occurred.
3. As a side effect of the ability to detect rapid thermal transients, it was shown that the coaxial thermocouple could be an effective indicator of unstart phenomena.
4. The measurements on the combustor wall opposite the main injectors showed that, for the tests with the reformed Jet A fuel, P/P_{ref} along the wall was roughly proportional to h/h_{ref} . On this basis, it appears that the heat transfer increase after fuel was turned on was solely due to the local pressure increase, which was, in turn, caused by shocks and combustion on the other side of the combustor. It does not appear that the increased heat flux was caused by reaction of the fuel injected from the secondary injectors on this wall. It is possible that there was an ignition delay that caused the fuel from the secondary injectors to react downstream of the last measurement location, which was 7 inches downstream of the secondary injectors.
5. During the test with gaseous ethylene, the heat transfer increased dramatically several inches downstream of the secondary injectors, which were located on the wall opposite the main injectors, implying that there was significant reaction of the secondary fuel upstream of these gages.
6. A limited number of gages on the pilot side of the combustor showed higher heating rates than that on the wall opposite the main injectors at the same axial location. The heating rates varied with the highest heating observed during the test with gaseous ethylene.
7. The results with the skin friction gages were somewhat ambiguous. Five of the gages did not appear to track the operational events (vitiator heater on, fuel on, fuel off) of the test. The skin friction coefficient for the six gages that appeared to roughly track the operational events ranged from $C_f = 0.0015$ to 0.0075 . However, there was considerable drift in the skin friction measurements relative to the changes in the film coefficient during the test. We attribute this drift to thermal effects on the strain gages of the displacement sensor.

2.0 Experimental Apparatus

2.1 Test Facility

Tests were conducted in the UTRC ramjet/scramjet test facility, which is a direct-connect combustor test facility located in Test Cell 5 of the jet burner test stand at UTRC. The purpose of the direct-connect combustor test facility was to simulate the flow into the combustor of the scramjet engine at a required flight Mach number. The air for the tests was heated in a vitiated-air heater. In the vitiated heater, hydrogen was burned in a lean mixture of oxygen to increase the enthalpy, and air was added to the products to increase the oxygen content to 21%. Before entering the combustor, the flow from the vitiated heater was accelerated through a two-dimensional converging-diverging facility nozzle, which was physically connected to the combustor. The facility nozzle, previously calibrated by UTRC, was shown to have a Mach number of approximately 2.9 for the tests with total temperatures over 2200°R.

2.2 Combustor Model

The combustor was designed by UTRC/PW. Figure 1 is a side view of the combustor, which also shows the instrumentation layout. The combustor had a 2" high x 6" wide entrance cross-section and was 49" long. The combustor walls were uncooled, 1.125" thick, 4130 Steel. As shown in Figure 1, two cowl pilots were mounted on 6 degree compression ramps. The cowl pilots served two purposes. First, fuel that was added to the subsonic flow through the cowl autoignites to provide flameholding. Secondly, the outside of the cowling serves as the primary fuel injection location. A total of 12 0.062"-diameter normal fuel injectors were used as secondary fuel injectors. The secondary fuel injection locations are also shown in Figure 1. Further details of the combustor and the test facility are presented in Reference 2.

3.0 Instrumentation and Data Analysis Procedures

3.1 Heat Flux Measurement

The heat transfer was measured by using a thick-skin transient wall temperature method. The transient wall temperature technique uses the time history of the wall surface temperature to determine the heat flux. The inner wall surface temperature was measured using 0.060"-diameter coaxial chromel-constantan (type E) surface thermocouples. This method has the advantage that it determines both the wall temperature and the heat flux so that the film coefficient can be determined. The MEDTHERM Corporation of Huntsville, Alabama manufactured the coax thermocouples. A sketch of the coax thermocouple is shown in Figure 2. Surrounding a constantan centerwire with an insulator and a chromel tube forms the coax thermocouple. The coax gages were cemented into the model using Aremco 552 Ceramabond high temperature cement. The junction is formed at the surface by lightly sanding the wall surface across the two materials. A pretest analysis showed that the match of the thermal properties, ρ , c_p and k is suitable between 4130 Steel and type E thermocouples.

The temperature data was converted to heat flux using a one-dimensional finite difference code, which was written by UDRI personnel and used in previous experiments. The code uses an implicit finite difference form and allows the use of variable thermal conductivity (Reference 3). The surface boundary condition is the measured wall temperature. Further details of the data reduction code are given in Appendix A.

3.2 Skin Friction Measurements

A total of 16 custom-designed, two-axis skin friction gages were constructed for UDRI under a subcontract to the Virginia Siberia Trading Company. A sketch of the gage is shown in Figure 3. Of the 16 gages, 11 were installed in the model, as shown in Figure 1. The gages were 1/2" diameter x 3" long and had a 1.125" diameter mounting flange. An E-type coaxial thermocouple was installed in the center of each gage for the purpose of measuring the surface temperature, enabling the simultaneous determination of skin friction, wall temperature and heat transfer. The gage design is based on the deflection of a commercial deflection sensor manufactured by Kistler-Morse. The deflection sensor (model DSC 6) uses semiconductor strain gages to sense the deflection of the beam in two directions. Ideally, the measured bending strain on the beam is proportional to the force in the direction of the strain. The gages were filled with Dow-Corning 200[®] Silicon Fluid (1000 cS) to provide vibration damping of the sensing element, insulate the sensors from gap heating effects, and reduce the effect of pressure gradients on the indicated shear.

The Virginia Siberia Trading Company does not calibrate the skin friction gages. Therefore, the skin friction gages were calibrated by UDRI personnel by the procedures recommended by the Virginia Siberia Trading Company. Specifically, the gage was held in a fixture so that its axis was parallel to the ground, and weights (in 1 g increments) were

hung from the end of the gage using a paper cup and a piece of string. Following calibration, the nominal sensitivity of the gages was determined to be approximately 8 mV/g.

3.3 Instrument Locations

The thermal instrumentation layout was designed with guidance from UTRC/PW. A total of 63 coaxial thermocouples were installed in the bottom wall opposite the fuel injectors. The CFD heat transfer predictions showed that high heating rates occurred in the vicinity of the secondary fuel injectors, and emphasis was placed on instrumenting these areas. Because the secondary injection location on the bottom wall changes (by design) from 22" for the Mach 5.6 test to 16" for the Mach 7.0 and Mach 8.0 cases, the instrumentation layout was designed to accommodate both tests.

The positions of the coax surface thermocouples used in the bottom wall (opposite the fuel injectors) are shown in Figure 1 and listed in Table 1. Because the thermocouples were installed with cement, the gages are permanently mounted in the walls. An additional 11 surface thermocouples were installed in the bottom wall located in the center of the skin friction gages. These 11 gage locations are also shown in Figure 1 and listed in Table 2.

Originally, the coax thermocouples installed in the pilot mounting frame were intended to be the same as those used in the shock-interaction study at Wright-Patterson, indicated in Reference 1. Because a large number of cavities and holes, which were previously used as pressure taps and secondary pilots, were already present on the back side of the wall, practical considerations dictated a change in the instrumentation layout on the pilot frame. Eight locations were chosen on the pilot mounting frame, which did not suffer from large thermal interference caused by the wall voids. The holes for the thermocouples were drilled by UTRC personnel and are shown in Figure 4, with the coordinates listed in Table 3. Note that the x-coordinates in Table 3 were measured with respect to the start of the ramp.

Table 1. Positions of the Coax Thermocouples Installed in the Wall Opposite the Injectors
(UTRC Coordinates)

Gage #	x (in)	y (in)
B1	11.5	2
B2	12	0
B3	12.5	0
B4	13.5	1
B5	13.75	0
B6	14	0
B7	14.25	0
B8	14.5	0
B9	14.75	0
B10	15.33	0.5
B11	15.75	0
B12	16	0
B13	16.25	0
B14	16.5	0
B15	16.75	0
B16	17	0
B17	18	0
B18	18.5	0
B19	19	0
B20	20	0
B21	20.5	0
B22	21	0
B23	22	0
B24	27	0
B25	29	0
B26	15.5	1
B27	15.5	2
B28	16	1
B29	20	1
B30	21	1
B31	17.5	1
B32	22	1
B33	23	1
B34	24	1
B35	22.5	0.6
B36	25	1
B37	19.5	-0.5
B38	17	0.4
B39	17	0.6
B40	17	0.8
B41	17	1
B42	17	1.2
B43	17	1.4

Table 1 (continued)

B44	17	1.6
B45	16.7	1.8
B46	16.7	2
B47	22.5	-0.6
B48	22.5	-0.4
B49	22.75	0.2
B50	22.75	1.1
B51	22.75	0.9
B52	22.5	1
B53	22.75	1.3
B54	22.75	1.5
B55	22.75	1.7
B56	22.75	0.5
B57	22.75	0.75
B58	25.5	0.5
B59	25.5	1
B60	25.5	1.5
B61	25.5	2
B62	25.5	2.5
B63	22.5	0

Table 2. Positions of Combined Skin Friction/Wall Temperature Gages on the Wall Opposite the Injectors

Skin Friction Gage	Thermocouple	x (in)	y (in)
1	B64	17	-1
2	B65	20.5	1
3	B66	11.5	1
5	B67	15	-1
6	B68	13	1
7	B69	28.5	0
9	B70	24.62	0
10	B71	25.5	-1
20	B72	23.5	1
21	B73	11.5	-1
22	B74	23	-1

Table 3. Positions of Coax Thermocouples Installed in the Injector Block

Gage #	x (in)**	y (in)
101	4.05	0
102	6.09	0
103	7.25	0
104	7.5	-0.475
105	7.5	-1
106	7.5	-1.825
108	8.65	-0.425
109	8.65	-0.685

**x-coordinates are measured relative to the start of the ramp, and the y-coordinates are measured relative to the centerline

3.4 Data System

A mobile, 120 channel data acquisition system was designed for this experiment, and also was used for the previous shock interference study at Wright-Patterson AFB. The data system was based on an HP 3852A data acquisition mainframe with a 16 bit, HP 44704A high-speed digital voltmeter and five HP 44713 high speed thermocouple multiplexer cards. The HP 3852A was equipped with 4 megabytes of memory for data storage. The range of the voltmeter was set at 320 mV, corresponding to a least-count error of 5 μ V, which was much less than the background noise.

A Pentium-133 personal computer, utilizing programs written in the LABVIEW graphical program language, was used to control the HP 3852A. A GPIB card and cable were used to provide communication and data transfer between the data acquisition mainframe and the PC. Two National Instruments GPIB-130 parallel extender devices were used to extend the length of the GPIB cable to 30 meters.

A flow chart showing the data acquisition process is provided as Figure 5. The boxes on the left side of the flow chart correspond to operations on the PC side of the data system (located in the control room), while the boxes on the right correspond to actions on the HP 3852A side of the data system (on the inside of the test cell). The letters 'GPIB' denote communication between the PC and the data acquisition mainframe. The data acquisition mainframe was hand triggered at the start of the test sequence and acquired data at a rate of 100 Hz per channel for 70 seconds. The raw voltage data from the thermocouples and skin friction gages was stored in the mainframe until the end of each test. After each test, the data was transferred over the GPIB Bus to the PC where the data was converted into the proper units.

In addition to the voltage signals from the thermocouples and skin friction gages, a voltage signal from the vitiated heater total pressure gage was recorded. The purpose of this signal was to provide a common time reference to synchronize the three separate data systems (UDRI, UTRC, and SAIC) used for the tests.

3.5 Data Analysis Procedures

LABVIEW 4.0 was used to perform the preliminary data conversions. In LABVIEW, the voltages from the skin friction gages were multiplied by the appropriate linear gains to convert from voltage to shear. The thermocouple voltages and the ice point reference voltages were also converted into temperatures.

Further processing was performed on the temperature traces. Before converting to heat flux, the thermocouple data was first smoothed using a running 7-point quartic. As shown in Figure 6, the smoothing function damps out the noise in the temperature trace without changing the trace's shape. The temperature traces were then converted to heat flux in the finite difference program. The final step in the data reduction was to use a straight four point running average to further smooth the data, this allowed the length of the files to fit under the 4000 point limit for plotting in Excel Version 5.0 spreadsheet files.

3.6 Test Matrix

A total of six facility runs were made during the Mach 5.6 testing. One of the tests was a "cold flow" run with cold air running through the vitiated heater and combustor model. The other five runs were hot runs with fuel injection into the combustor. During runs 883 and 884, the model was fueled with gaseous ethylene, which was at ambient conditions. During runs 885-887, the combustor was fueled with reformed Jet A fuel. In the tests with reformed Jet A, the hot products obtained by heating Jet A fuel in a catalytic reactor were used as the fuel. This procedure simulated the regenerative cooling of the structure by Jet A fuel.

Heat transfer and skin friction data were not recorded during runs 883 and 885 due to problems in the data system hardware. For run 883, a time-out failure on the GPIB was thought to be the problem. To avoid this problem in the future, the data system was not armed until 20 seconds before the test. The second failure of the data system occurred during the first test with hot fuel (run 885). At the end of the test (before the data was transferred to the PC) the PC suffered a Windows error, resulting in the loss of data from run 885. It is thought that this failure could have been due to the large magnetic pulse which occurred when the high-current fuel heater was shut off. Magnetic shielding material was placed around the data system to counteract this effect. The data system performed without error for the rest of the runs.

4.0 Heat Transfer Correlation Procedure

In the present scramjet combustor tests, the wall temperature increases throughout the test. For this reason, characterization of the heat flux relative to the driving potential (temperature difference between the flow and the wall) is required instead of merely plotting the heat flux. With this in mind, a review of the heat flux correlation procedures used will be presented before discussing the heat flux data.

As a starting point for the data correlation, a few terms will be defined. The film coefficient, h , which normalizes the heat flux, q , by the temperature difference is defined as:

$$h = \frac{q}{(T_r - T_w)} \quad [1]$$

where, T_w , is the wall temperature and T_r , is the recovery temperature. The recovery (or adiabatic wall) temperature may be thought of as the wall temperature, in the absence of backside radiation, at which the wall heat transfer becomes zero. For low speed flows, the recovery temperature is equal to the total temperature of the flow. In high speed flows, however, part of the total energy of the flow is dissipated through viscous interactions so that the effective "potential" due to the temperature difference, $(T_r - T_w)$, is less than $(T_0 - T_w)$.

The choice of an appropriate T_r is important, particularly as the wall temperature increases, decreasing the difference between the recovery and the wall temperatures. Based on prior experience of the UDRI team, a recovery temperature of $T_r = 0.9T_0$ was selected for this experiment. The importance of choosing the correct recovery temperature is shown in Figure 7 which shows the film coefficient for a typical gage assuming $T_r = T_0$ and $T_r = 0.9T_0$. The difference in the film coefficient due to the selection of recovery temperature is significant. For the particular case shown in Figure 7, the film coefficient differed by 24 % by the end of the test.

Strictly speaking, in a flow with combustion, the specification of the exact recovery temperature requires a complete knowledge of the reacting flowfield, including the fuel mixing and the chemical kinetics up to the measurement location and is beyond the scope of the available measurements for the current experiment. In the present experiment it has been assumed that $T_r = 0.9T_0$. This assumption is based on previous experimental efforts in which the ratio T_w/T_0 was varied in order to determine the recovery temperature (Reference 4). The effect of assuming a constant recovery temperature is that the film coefficient will show a large increase if the actual recovery temperature is increased by combustion. In a reacting flow, the film coefficient based on a constant recovery temperature increases for two reasons. First, the actual heat transfer increases. Secondly, the denominator in Equation 1, $(T_r - T_w)$, is smaller than it should be because the assumed value of the recovery temperature is lower than the actual recovery temperature, which has been increased by combustion.

The Stanton number, St , is defined as :

$$St = \frac{h}{\rho_{\infty} c_{p\infty} U_{\infty}} \quad [2]$$

where ρ_{∞} , $c_{p\infty}$, and U_{∞} are selected as the free stream values of the density, specific heat and velocity, respectively. The Stanton number can be thought of as a way of normalizing the film coefficient by the total potential heating rate of the flow.

Another related topic is the peak heating in a two-dimensional shock interaction. From previous work (Reference 4), a relationship has been shown to exist between the peak pressure and film coefficient, and their corresponding reference values. This relationship can be expressed as:

$$\frac{h_{pk}}{h_{ref}} = \left(\frac{P_{pk}}{P_{ref}} \right)^{0.85}$$

or, [3]

$$\frac{P_{pk}}{P_{ref}} = \left(\frac{h_{pk}}{h_{ref}} \right)^{1.18}$$

Note that the pressure ratios in a non-reacting flow are expected to approximately track the film coefficient with the relationship in Equation 3. If the heating ratio dramatically increases above that predicted by the pressure ratio, it is an indication that the recovery temperature of the flow has been increased by combustion.

For turbulent flat plate heating, the relationship between the Stanton number and the Reynolds number can be expressed as :

$$StRe_x^{0.2} = 0.0296 \left(\frac{T_{\infty}}{T_*} \right)^{0.6} \quad [4]$$

where T_* is the reference temperature for compressible flow is expressed as:

$$T_* = T_{\infty} + 0.5(T_w - T_{\infty}) + 0.22(T_r - T_{\infty}) \quad [5]$$

Rearranging Equation 4 in terms of the film coefficient gives the following expression:

$$\frac{h}{\left(\frac{T_{\infty}}{T_*}\right)^{0.6} \mu_{\infty}} = \frac{0.0296}{x^{0.2}} c_p (Re_x / \text{ft})^{0.8} \quad [6]$$

Based on Equation 6, Neumann (Reference 1) developed a simplified correlation in which the heat function, H , defined as:

$$H \equiv \frac{h}{\left(\frac{T_{\infty}}{T_*}\right)^{0.6} \mu_{\infty}} \quad [7]$$

is plotted against of the Reynolds number per ft on a log-log plot. For the present study, the units of the film coefficient are $\text{BTU}/\text{ft}^2\text{-s-}^{\circ}\text{R}$, the units of the viscosity, μ , are $\text{lb-f-s}/\text{ft}^2$, so that the units of the heat function, H , are $\text{BTU}/\text{s}^2\text{-}^{\circ}\text{R-lbf}$. This correlation is useful in relating the results from different experiments with the same geometry and Mach number but at different flow enthalpies and Reynolds numbers.

In the previous non-reacting flow study of UTRC engine geometry at Wright-Patterson AFB, severe wall heating occurred immediately in front of the intersection of the cowl and the wall. However, because of the limited space due to coolant tubes and manifolds in the vicinity of the injector cowl it was not possible to measure the heating in the same location for the present experiment. Earlier tests at WPAFB (Reference 1) also showed that the heating there was similar to and could be compared to the heating in front of a cylinder placed normal to the flow, since the intersection of the cowl leading edge and the wall resembles a cylinder normal to the wall. The previous work suggested the use of a simplified correlation, already developed for a cylinder normal to the flow, to model heat transfer in front of the cowl (Reference 4). The correlation for the peak film coefficient in front of a cylinder is shown in Figure 8. Because the flow at the cowl/wall junction is non-reacting throughout the test (there is no fuel injected upstream of the cowl) the correlation for the heating at the cowl/wall junction is useful for predicting the peak heat flux there for the present test, even after fuel is injected downstream. Based on this correlation, the predicted peak wall heating in front of the cowl in the present experiment is $h_{pk} = 0.115 \text{ BTU}/\text{ft}^2\text{-s-}^{\circ}\text{R}$, or in terms of the heat flux to a cold wall, $q_{pk} = 185 \text{ BTU}/\text{ft}^2\text{-s}$. The value of the peak wall heat transfer in front of the cowl will be compared to the heat transfer downstream of the fuel injectors later in this report for reference purposes.

With this background, the wall temperature and heat flux measurements can now be discussed.

5.0 Results

5.1 Bottom Wall Heat Flux Measurements

In general, the coaxial thermocouples installed in the wall were robust throughout the test series. The wall surface temperature measurements for a typical run (test 884) are plotted vs. time in Figure 9 for three of the thermocouples. The temperature traces show little noise and the shape is typical for transient heating of a wall. Before $t = 35$ s, the traces all show a gradually decreasing slope that would be anticipated for a thick wall exposed to convective heating. The two thermocouples at $x = 22.75$ " and $x = 29$ ", which are downstream of the fuel injectors, show an increase in the slope after the fuel is turned on at $t = 37$ s, while the trend of the temperature trace for the thermocouple at $x = 12$ ", which is upstream of the injectors, does not change. The sudden increase and decrease of the temperature for the gage at $x = 12$ " is indicative of an unstart in the engine. More will be said about this later.

The wall temperature traces along the centerline of the combustor are shown in Figure 10 for each of the tests. The times indicated are at the start of the test and immediately before the fuel is turned off (peak wall temperature). Note that the peak wall temperature traces are nearly identical up to $x = 20$ ". Downstream of this location, the traces for the last two tests, in which reformed Jet A fuel was injected through the secondary injectors at $x = 22$ ", were notably different from the trace for test 884, which injected gaseous ethylene through the secondary injectors.

In Figures 11 and 12, the peak wall temperatures are plotted for all of the coaxial thermocouples for runs 884 and 886. It is evident that there is some spread in the lateral direction at axial measurement locations where there are multiple sensors. The lateral variation of the wall temperatures can be expected due to the three-dimensional nature of the flowfield. Another reason for the variation is that, in most cases, the temperatures and the indicated heat fluxes were higher for the thermocouples that were installed in the skin friction gages than for gages in the wall located nearby. Figure 13 shows the temperature traces for the two thermocouples installed in skin friction gages at $x = 11.5$ ", $y = \pm 1$ ", and the thermocouple installed at $x = 12$ ", $y = 0$ ". Note the gages installed in the skin friction gages read higher than the gages installed at $x = 12$ " and $x = 12.5$ ". In addition, there is a substantial difference between the two gages at $x = 11.5$ ", $y = \pm 1$ ". The reasons for these differences are not known for certain. Two possible explanations, however, are extraneous thermoelectric effects due to installation of the gages in the skin friction gages, and gap heating in the gap between the skin friction gage element and surrounding housing. A third possibility is that there actually is a significant lateral variation in the heater across the combustor width. While the apparent variation between the thermocouples in the gages and those mounted in the walls is a cause of some concern, the effects on the conclusions are not significant.

The heat fluxes calculated from the wall temperatures shown in Figure 9 are plotted vs. time in Figure 14. The heat flux histories illustrate the transient nature of the

heat flux. The heat flux increases dramatically after the fuel is turned on for the two downstream thermocouples and then decreases as the wall temperature increases and the "driving potential" ($T_r - T_w$) decreases. The heat flux for the upstream thermocouple is relatively constant until the unstart at $t = 48$ s, where it increases dramatically due to the unstart. A detailed plot of the heat flux during the unstart for the gage at $x = 12$ " is shown in Figure 15, which shows that the unstart occurs over many data points and rapidly increases the heat flux by a factor of over 2. The effect of the unstart was also shown by the other gages in the upstream section of the combustor in addition to the UTRC test documentary video and wall pressure measurements.

Figure 16 shows the film coefficient for the gage at $x = 12$ " during each of the tests. Although the test duration was longer than anticipated, the measured wall heat flux expressed as the film coefficient is steady for 50 seconds. This is important from the standpoint of the thermal modeling because the wall heating expressed in terms of the film coefficient should be relatively steady throughout the test. If the film coefficient had dropped off toward the end of the test it would have been an indication of an inadequate thermal model. The flatness of the curves in Figure 16, therefore, is taken as evidence of the acceptability of the thermal model for the wall.

For the present experiment, the heat fluxes in the combustor with no fuel injection are compared to the results from the test at WPAFB in Figures 17 and 18. Figure 17 shows the reference heat flux (measured at $x = 12$ ", $y = 0$ ") expressed as a heat function (Equation 7), plotted along with the reference heating for the previous experiment at WPAFB. The reference heat flux in the present test is about 10-15% lower than the value predicted by the correlation from the previous experiment. In terms of the film coefficient, the reference heating averaged $0.035 \text{ BTU/ft}^2\text{-s}$ for the three tests. Expressed in terms of the heat flux to a cold wall ($T_w = 500 \text{ }^\circ\text{R}$), $q_{ref} = 56 \text{ BTU/ft}^2\text{-s}$. Figure 18 shows the peak heating (expressed as a heat function) along the combustor centerline in the region of peak heating due to the reflection of the shocks from the pilots. The peak of the measured heat flux along the centerline with no injection occurred at $x = 16.75$ " for each of the tests. Based on the fit of the data obtained in the previous test, the measured peak heating is slightly greater than expected. The ratio of the peak to the reference heat function during the period of no fuel injection was about 1.7.

The heat transfer expressed as the film coefficient is plotted for all gage locations along the bottom wall in Figures 19-21 showing data for the three tests during periods with fuel off and fuel on. The film coefficient for the three tests were calculated from Equation 1 using the measured wall temperatures and heat fluxes along with the recovery temperatures listed in Table 4. Recall that the reference temperature is calculated assuming that $T_r = 0.9T_0$, where T_0 is the combustor inlet total temperature (determined by UTRC). For reference purposes, the heating level expected in front of the injector cowl is also shown. The heat flux was higher with fuel injection at locations downstream of $x = 15.75$ " for all of the tests. The film coefficient along the centerline at $x = 16.75$ " increased from 1.7 to 2.7 with the addition of the fuel. The results for the two tests with reformed Jet A fuel (tests 886-887) show that the film coefficient is lower than the expected peak heating

at the junction of the cowl and the wall over most of the combustor. Recall that the maximum expected heating in front of the cowl is in a non-reacting flow.

Table 4. Recovery Temperatures Used in the Calculation of the Film Coefficient in Figures 19 -21

Test	time (s)	Fuel off		time (s)	Fuel on	
		T_0 (°R)	T_r (°R)		T_0 (°R)	T_r (°R)
884	27	2425	2183	51	2420	2178
886	27	2350	2115	51	2365	2129
887	23	2341	2107	50	2353	2118

In contrast to the two cases with reformed Jet A fuel, the heat transfer for the test with gaseous ethylene fuel (run 884) rapidly increased several inches downstream of the secondary injectors at $x = 22$ ", exceeding the cowl heating level. At the last measurement location, the film coefficient increased by a factor of 12.7 after the fuel was turned on, while it only increased by a factor of 3 for the cases with reformed Jet A fuel.

Using the relationship between the film coefficient and the pressures from Equation 3, Figures 22-24 show the ratio of the local pressure to the reference pressure and the ratio of the film coefficient raised to the 1.176 power, which is the relationship between film coefficient and pressure rise in a shock along the centerline. The plots for the two runs with the reformed Jet A fuel (runs 886 and 887 in Figures 23-24) show that the pressure ratio and the film coefficient ratio are roughly the same throughout the length of the combustor, implying that the secondary fuel injected at $x = 22$ " did not react upstream of $x = 29$ " during these tests.

Note that the absence of any evidence of combustion along the instrumented section of the bottom wall does not preclude the possibility of the fuel burning downstream along the wall, nor does it say anything about the fuel burning elsewhere in the combustor. In fact, because of the high mean velocity through the combustor, it would not be surprising that the reacted products from the fuel injected on one side of the combustor do penetrate to the opposite wall of the combustor. If fuel reacts on one side of the combustor only, the pressure will increase on both sides of the combustor and the flow field would be thermally stratified, with the heated products flowing along the one wall and cooler gas flowing along the other.

In contrast to the two runs with reformed Jet A fuel, the film coefficient ratio for run 884 (Figure 22) increased dramatically several inches downstream of the injectors, implying that the recovery temperature was increased by the combustion of the fuel from the secondary injectors.

To summarize, on the bottom wall of the combustor (opposite the main pilot/injectors) the heat transfer was observed to increase downstream of the main fuel injector location on the opposite wall for all three tests. Additionally, P/P_{ref} along the bottom wall was roughly equal to the h/h_{ref} . It is thought that the cause of the observed

heat transfer increase along the bottom wall is due to the pressure rise, which was caused by shocks and the reaction of the fuel injected from the other side of the combustor.

Another measure of the wall heat transfer in a combustor is the local increase in the film coefficient at each point due to fuel addition. The film coefficient augmentation ratio, $h_{fuel-on}/h_{fuel-off}$, is one way of representing this increase. Figure 25 shows the augmentation ratio, $h_{fuel-on}/h_{fuel-off}$, at each measurement location for the three tests. Adding fuel increased the film coefficient by a factor of less than 5.5 for the two tests with reformed Jet A fuel (tests 886 and 887). In test 884, the film augmentation ratio increased dramatically for the last two measurement locations. It is thought that this large increase is due to an increase in the recovery temperature caused by the reaction of the fuel.

Looking ahead to the Mach 7-8 tests, the secondary injector location will move upstream to $x = 16$ ", so that there will be more gages downstream of the fuel injection site. In addition, because the local static temperatures will be higher, any ignition delay effects should be reduced.

5.2 Injector Wall Heat Transfer

The heat transfer on the injector block expressed as the film coefficient is shown in Figures 26-33 for the three tests. The locations of the gages are shown in Figure 4. For comparison, the level of the maximum heating expected in front of the cowl/wall junction (predicted from correlation of experimental data from the experiment at WPAFB) is also shown in each of the plots. Recall that the film coefficients are based on using the combustor inlet total temperature to calculate the recovery temperature. The plots are shown for each gage on the injector block as a function of time. Figure 26 shows the film coefficient for the gage at $x = 4.05$ ", $y = 0$ " (Gage 101 in Figure 4). The measured heating rate at this location was much lower than predicted heating in front of the cowl and was essentially flat, showing no effect of the of fuel injection throughout the entire test. The one exception was run 884 around 48 seconds, the peak in this run was caused by the unstart.

Figure 27 shows the film coefficient for the next gage downstream along centerline of the injector block (gage 102 at $x = 6.09$ ", $y = 0$ "). The data for the two runs which used reformed Jet A (run 886 and 887) showed no effect of fuel injection throughout the test. The data from the test which used ethylene (run 884) does show that the heat flux increased after fuel injection. It is thought that this increase was due to an increase in local pressure. The effect of the unstart is also seen for this gage in run 884.

Figure 28 shows the film coefficient for gage 103 ($x = 7.25$ ", $y = 0$ "), which is on the centerline 0.34" downstream of the injectors. The heat flux for all three gages increases as the fuel is turned on. Although the heat flux doubles for the cases with reformed Jet-A fuel and more than triples with for the case with ethylene, the heating level at this location with fuel injection, was less than the predicted heating in front of the cowl/wall junction.

In Figures 29-31 the heat transfer is plotted for the row of gages at $x = 7.5$ " downstream of the start of the pilot ramps (gages 103, 104, and 105). At each gage location, the measured heat transfer increased after the fuel was turned on. The test-to-test variation in the heat transfer at this instrument row was significant, with the highest heat transfer occurring for run 884. The level of the heating at the gage which was closest to the centerline ($y = 0.48$ ") was less than the predicted peak heating in front of the cowl for the two tests with reformed Jet A fuel, and was slightly greater than this value for test 884, which used gaseous ethylene fuel. At the outer two locations ($y = 1$ " and $y = 1.83$ ") the heat flux was higher than the predicted cowl heating for all of the tests, with the highest heating rates occurring in run 884.

Figures 32-33 show the film coefficient for the two gages at $x = 8.65$ " (gages 108 and 109). For each of the runs, the maximum measured heating at this axial station was lower than that measured at the $x = 7.5$ " axial station. As was the case at the other measurement stations, the flux was greatest for run 884, which shows heating slightly above the expected heating in front of the cowl, while the heating for the other two runs was less than this level over most of the test. In addition, the two runs with reformed Jet A fuel exhibited a pronounced dip in the film coefficient immediately after injection of the fuel was initiated, showing that the wall was cooled. It is thought that the wall cooling was caused by the injection of cold fuel trapped between the fuel heater and the secondary injector orifice. The observation of the wall cooling by the fuel points out a major advantage of the use of surface thermocouples; that is, the rapid identification of events which alter the wall heating. It has also been shown that thermocouples can rapidly pick up transients such as the unstart in run 884, and the fuel-on transients for the runs with the heated fuel.

The film coefficient augmentation ratios, $h_{fuel-on}/h_{fuel-off}$, at each of the measurement locations on the injector block are listed in Table 5. Figure 34 graphically shows the lateral distribution of the film coefficient augmentation ratios, $h_{fuel-on}/h_{fuel-off}$, measured downstream of the injectors at $x = 7.25$ " and $x = 8.65$ ". At each of the measurement points the flux was highest for the test with ethylene (test 884). The data for $x = 7.25$ ", which is represented by the closed symbols, shows that the lowest heat flux occurred at $y = 0.48$ " (gage 104). It is interesting to note that this gage is located almost directly downstream of the secondary injectors. The highest heat flux occurred at $y = 1$ " for the test with ethylene (run 884). For the tests with reformed Jet A, there was little difference in the heat fluxes at $y = 1$ " and $y = 1.83$ ". At the downstream row of lateral gages at $x = 8.65$ " the gages were closely spaced ($y = 0.48$ " and $y = 0.69$ ") and little difference was observed between the heat fluxes at this axial location. It should be noted that more measurements were planned in the injector region; however, it was not possible to mount any more gages in the injector block because of the large number abandoned pilot injector holes which were already in the injector block.

Table 5. Film Coefficient Augmentation Ratios $h_{fuel-on}/h_{fuel-off}$ for the Gages on the Injector Side of the Combustor

Gage #	x (in)	y (in)	Test 884	Test 886	Test 887
101	4.05	0	0.97	1.01	1.04
102	6.09	0	2.25	1.08	1.26
103	7.25	0	3.15	1.81	2.19
104	7.5	0.48	5.69	2.81	3.40
105	7.5	1.0	10.30	5.43	6.90
106	7.5	1.83	8.26	5.49	7.01
108	8.65	0.43	4.89	2.86	3.64
109	8.65	0.69	5.25	2.41	3.21

On the basis of the pressure traces along the length of the combustor downstream of the injectors, it is thought that the fuel from either the primary injectors or the secondary injectors reacted (the pressure rise is coming from combustion). Further interpretation of the heat transfer in the injector region requires a detailed knowledge of the wall pressures in this region for each test; however, on the basis of the higher heat fluxes for the ethylene test it is thought that some of the fuel may have reacted in the injector region. The pressure distributions along the wall with the pilots (not shown) show that the peak pressure occurs downstream of the instrumented region downstream of the pilots, so that it is quite possible that the maximum heating on the injector wall occurred further downstream than the last measurement station. For this reason, it would be useful to have more information on the wall heating at locations further downstream. A limited number of coaxial thermocouples (4 at last count) are available for measurements at points further downstream. In addition, there are 14 channels available on the existing data acquisition system for more thermocouples. More measurements would require ordering thermocouples. In view of the long lead time on this instrumentation, a decision should be made soon on the acquisition of more surface thermocouples.

5.3 Skin Friction Measurements

Skin friction measurements were taken for four runs in addition to one run with cold air only. Before discussing the skin friction data, it is useful to review the events leading to tunnel operation. Figure 35 shows the voltage from the total pressure transducer during the four runs. During the cold flow run, the air to the vitiated heater was ramped from zero mass flow to the amount of air used by the vitiated heater during the heated runs, and kept constant. During the hot runs, the data acquisition system was turned on shortly after flow of the air to the vitiated heater was established. Note that the heater pressure at the start of the hot runs was the same as the plateau in the cold flow test. Ideally, the data system should have been on for the opening of the air valve, however, this was not practical considering the long total test time and the storage limits in the data system. After the cold air flow was established through the heater, hydrogen and oxygen were added to the heater and ignited, increasing the total pressure. A short time later, the ejector was turned on.

Offsets in the skin friction data were accounted for by subtracting the average skin friction level at the start of the test from all of the readings, thus setting the skin friction to zero at the start of the test. This procedure allows the outputs from the gages to be related back to the condition of no flow through the combustor. It adds the shear measured in the cold flow test to that measured in the hot flow test, which starts at the same condition as the steady portion of the cold flow test. As will be shown later, for most of the gages the skin friction in the cold flow tests was much less than that in the hot flow tests.

The measured skin friction expressed as wall shear in lbf/ft^2 is shown in Figures 36-46 for each of the gages during the cold flow tests. Two traces appear on each of the plots; P denotes shear in the primary flow direction, while S denotes the measured shear in the secondary direction. The sign convention that was used is that the shear in the primary direction is positive in the downstream direction, and the shear in the secondary direction is positive to the right while looking downstream in the combustor. In the early seconds of the run the air flow is ramped up from zero to its maximum level. Between 20-30 seconds the ejector was turned on, and its effect is to decrease the back pressure on the combustor. The effect of ejector operation is seen in some of the gages downstream of $x = 15$ ". The time before the ejector is turned on corresponds to the start of the tests for the hot runs. For later analysis, an average shear level was defined for each of the gages by averaging the shear between 10 and 18 seconds. This is shown in Tables 6 and 7 for the two separate directions.

Table 6. The Average Shear Force During the Cold Flow Test (Primary Axis)

Gage #	x (in)	y (in)	Shear (lbf/ft^2 -s)
A1	11.5	1	2.54
A2	11.5	-1	0.74
A3	13	1	2.63
A4	15	-1	-0.07
A5	17	-1	0.19
A6	20.5	1	-7.76
A7	23	-1	-6.98
A8	23.5	0	2.30
A9	24.62	0	-0.04
A10	25.5	-1	2.24
A11	28.5	0	9.80

Table 7. The Average Shear Force During the Cold Flow Test (Secondary Axis)

Gage #	x (in)	y (in)	Shear (lbf/ft ² -s)
A1	11.5	1	-0.32
A2	11.5	-1	-2.02
A3	13	1	0.33
A4	15	-1	-0.75
A5	17	-1	-0.51
A6	20.5	1	-3.92
A7	23	-1	-3.27
A8	23.5	0	0.20
A9	24.62	0	-0.20
A10	25.5	-1	0.36
A11	28.5	0	8.67

The skin friction for run 884 is shown in Figures 47-57 for each of the gages. Note that the shear in these plots is total shear, formed by subtracting the offset at the start of each test from each of the measurements and then adding the appropriate value from Table 6 or 7 corresponding to the shear with cold air flowing through the combustor. For most of the gages, cold flow offset is small relative to the output with the heater and combustor on. The output from the three gages that are furthest upstream show a monotonic trend throughout most of the test, which is an expected trend since the first three skin friction gages are located upstream of the injectors and should not be influenced by fuel injection. The two gages at $x = 11.5$ " are symmetrically located about the centerline of the combustor and as such should measure the same values of shear. The data show that after 20 seconds the shear indicated by one of the gages increases while the shear on the other gage decreases, with the gage at $x = 11.5$ ", $y = -1$ " increasing by a factor of 45% between $t = 20$ and 48 seconds.

During test 884, an unstart occurred at $t = 48$ seconds. After the unstart, the gages at $x = 11.5$ ", $y = 1$ " and $x = 13$ ", $y = 1$ " (see Figures 47 and 49) recovered rapidly after the unstart, while the gage at $x = 11.5$ ", $y = -1$ " did not stop oscillating until after the test was over. Also note that the output of the first gage in the primary direction returned to the same baseline at the end of the test while there was some shift of the baseline at the end of the test for the other two gages.

Examining the output of the gage at $x = 15$ ", $y = 1$ " (see Figure 50), it is seen that the output steadily dropped throughout the test and showed a substantial shift in the baseline at the end of the test. It is thought that this may have been due to thermal effects on the displacement sensor. An increase (or decrease) in the temperature at the strain gage location can change the resistance of the strain gage, and thus, the output of the skin friction gage.

Further downstream, the gage at $x = 17$ " (see Figure 51) showed a separate step in the output, apparently due to the fuel injection. Also, note that the amplitude of the fluctuations in the shear increased after 40 seconds. While the gage at $x = 17$ " was fast to

respond to the transients when the vitiated heater and fuel were turned on, its response to the end of the test was slow (the test was over at 60 seconds).

Downstream of the $x = 17''$ position, the relationship between the gage behavior and what was happening in the tunnel is less clear. The behavior of the gage at $20.5''$ (Figure 52), which is $1.5''$ upstream of the secondary injectors, is puzzling, in that the output of the gage turned negative after the fuel was turned on, then increased, decreased, and continued to rise after the test was over. The gage at $x = 23''$ (Figure 53) showed little response until after the fuel was turned on. The output of the gage at $x = 23.5''$ (Figure 54) showed little output on the primary axis, and continually increased after the test was over. In addition, the output on the secondary axis was greater than that on the primary axis. The gage at $x = 24.62''$ shows higher output on the secondary axis than the primary axis. This is an unexpected result, particularly considering that the gage is located on a symmetry line on the centerline of the combustor. The output of the two gages at the end of the combustor (Figures 56 and 57) shows that the shear along the primary axis sharply decreased with time after the fuel was turned on. Again, it is thought that the drop may have been due to thermal effects.

For completeness, the skin friction for run 886 is shown in Figures 58-68 for each gage, and the skin friction for run 887 is shown in Figures 69-79. Several points should be made here. First, the gage output trends in the primary direction up to $x = 17''$ appear to be the same for all three tests. This is illustrated in Figures 80-81 for two of the gages by the composite plots of the shear in the primary direction at $x = 11.5''$, $y = 1''$ and $x = 15''$. For the gages downstream of $x = 17''$, the traces for the last two runs 886-887 show differences with test 884; however, the general shape and magnitude of the shear along the primary axis are approximately the same for the two hot runs.

Because heat transfer and skin friction are both transport phenomena, it is useful to compare them. As a starting point, the Reynolds analogy between the skin friction and Stanton number may be written as:

$$St = \frac{f_r C_f}{2} \quad [8]$$

or,

$$\frac{2h}{\rho_\infty c_{p\infty} u_\infty} = f_r \frac{\tau}{\frac{1}{2} \rho u_\infty^2} \quad [9]$$

where τ is the shear in lbf/ft^2 , h is the film coefficient in $\text{BTU/ft}^2\text{-s-}^\circ\text{R}$, and f_r is the Reynolds analogy factor.

The Reynolds analogy is true only if both St and C_f are based on the local properties. For consistency, St and C_f were based on the combustor inlet freestream

conditions. Several formulations exist for the Reynolds analogy factor including the Colburn relationship ($f_r = Pr^{-2/3}$) and the von Karman relationship (Reference 5) which sets the approximate range of f_r between 1.0 and 1.25.

The Stanton number and the skin friction coefficient, based on combustor inlet conditions, during run 886 are shown in Figures 82-91. For reference purposes, a curve for $2St$ is included in each of the plots, corresponding to $f_r = 1$. The first two gages were upstream of any interference from the ramp. For the first two gages, C_f was significantly greater than $2St$. For all other gages $2St > C_f$. Note that separation and stagnation regions are two types of flow fields in which the shear decreases relative to the heat flux.

Two further points should be made about the use of Reynolds analogy. First, Reynolds analogy has not been proved for supersonic combustor flowfields. Secondly, in comparing the heat transfer to the skin friction it is important to use the local properties to evaluate C_f and St . The relationship between shear and film coefficient in Equation 9 can be simplified to:

$$\frac{\tau}{h} = \frac{1}{f_r} \frac{u}{c_p} \quad [10]$$

or, for an ideal gas:

$$\frac{\tau}{h} = \frac{1}{f_r} M \sqrt{T} \left(\frac{\gamma - 1}{\sqrt{\gamma}} \right) \sqrt{\frac{1}{R}} \quad [11]$$

Therefore, the expected ratio between shear and film coefficient is a function of the molecular weight, temperature, Mach number, and γ . Recall that the current picture of the operation of the combustor is that the fuel along the wall opposite the injectors does not react in the immediate vicinity of the injectors. However, the pressure does change, as a result of the combustion on the other side of the combustor and the shock waves. As the pressure changes so does the Mach number and temperature in the combustor. It can be shown that a pressure rise caused by either a shock wave or an isentropic deceleration will decrease the product of $M\sqrt{T}$, thus decreasing the expected ratio between the shear and film coefficient. Further interpretation of the relationship between shear and heat transfer depends on a detailed knowledge of the properties used in Equation 11 along the combustor.

In test 886 the outputs from four of the gages, which are located at $x = 20.5"$, $x = 24.62"$, $x = 25.5"$, and $x = 23.5"$, showed little response in comparison to the response of the thermocouples, and are thus regarded as suspect. The output of the gage at $x = 15"$ steadily dropped off while the Stanton number was constant. Six of the gages appear to track the events (vitrated heater on, fuel on, fuel off) of the test. These "good" gages are the ones that are located at $x = 11.5"$, $y = \pm 1"$, $x = 13"$, $x = 17"$, $x = 23"$, and $x = 28.5"$. The output of the gage at $x = 23"$ appears to be about the expected magnitude on the basis

of Reynolds analogy but has a sign difference. The skin friction levels for the six "good" gages that appear to change along with the Stanton number range from $C_f = 0.0015$ to 0.0075 .

5.4 Loss of the Silicon Oil in the Skin Friction Gage Cavity

Two factors work against retention of the silicon oil in the cavity. First, the thermal diffusivity of the silicon oil is extremely low. The low thermal diffusivity of the silicon oil is advantageous from the standpoint of reducing heat conduction through the oil to the strain gages; however, it also causes a rapid rise in the surface temperature of the oil. This is illustrated in Figure 92 which shows the surface temperature of the silicon oil when exposed to a constant heat flux of $10 \text{ BTU/ft}^2\text{-s}$, assuming the oil is semi-infinite and assuming constant properties. The point of Figure 92 is that the oil at the surface of the gage rapidly heats, even when exposed to low heat fluxes. The actual surface temperature will be lower due to conduction to the metal surrounding the gap. Figure 93 shows the temperature distribution through the wall for a typical gage during run 886. Although the vapor pressure of the oil is extremely low (10 mm Hg at 1000°R) there are other potential problems associated with the use of silicon oil at high temperatures. The flash point for the fluid is 600°F . Above this temperature a combustible mixture can form above the fluid.

After the tests at UTRC, a small sample of the silicon oil was poured into a pan which was already heated on an ordinary electric kitchen stove. The oil immediately started to give off a thick smoke. The pan was removed from the stove immediately. The residue left in the pan was a solid gummy substance, not liquid oil. Admittedly, the conditions of this quick test were different than the actual conditions that the oil in the skin friction gage is exposed to. However, the test illustrates that there are potential problems associated with the use of the silicon oil at high temperatures. In particular, there is the possibility of combustion of the oil, or the formation of a solid substance, which could prevent the movement of the sensing element. Also, since one of the purposes of the silicon oil is to prevent pressure gradient effects, the loss or conversion of the silicon oil to a solid, would make the skin friction measurements susceptible to the effect of pressure gradients in the direction of the measurement. The potential problems with the silicon oil will only get worse in the upcoming Mach 7-8 tests, which will have much higher heating throughout the test.

6.0 Data Files from the Mach 5.6 Tests

Data files have been archived and are available for time histories of heat transfer, wall temperature, and skin friction. The files are in the form of a time history of the measurement with time increasing with the number of rows. Further details are given in the following sections for each of the types of files.

6.1 Heat Transfer and Temperature Data Files

The reduced heat transfer data is plotted as a function of time for the 3 tests with combustion (runs 884, 886, and 887). There are 12 data files. Each of the files is in Microsoft Excel *.txt format. The filename convention is as follows:

First 2 letters: tp = top (injector wall)
bt = bottom wall (opposite wall)

Next 3 numbers = run number

Next 2 letters: ta = Temperature in °R
fa = Flux in BTU/ft²-s

Example: tp884fa.txt = Heat flux data for gages on the injector side during run 884

A small section of a data file (bt884fa.txt) is shown in Figure 94 for illustrative purposes. The file layout is in order of increasing time along the columns, and increasing *x* and *y* gages coordinates along the rows. The first seven rows of the files comprise the channel information for each of the gages including the data channel, gage number, gage type, and coordinates. The signal from the vitiated heater total pressure, recorded as gage 222 for the purpose of providing a common time scale, is also present as a data column in each of the files.

The heat flux data files were transmitted to Pratt and Whitney through the local representative during the week of January 15, 1997. Since then it was found that the *x* coordinate for one of the gages (gage 69 which is the thermocouple inside of the last skin friction gage) is incorrect in the files transmitted to PW/UTRC. The correct *x* coordinate for gage 69 is 28.5", not 25.5".

6.2 Skin Friction Data Files

Two data files were created for each test run; one corresponding to the measured primary axis shear, and one corresponding to secondary axis shear. In addition to the hot flow tests, there was one test with cold flow through the tunnel, for a total of eight files for the skin friction. The file format is the same type (Excel *.txt) as the temperature and heat flux files. The filename convention is as follows:

First 4 letters: 'U88*' for the hot flow tests, where * = '4', '6', or '7'
'cold' for the cold flow test

Next letter: P for primary axis (shear along the main flow path)
S for secondary axis (perpendicular to the main flow path)

Last two letters: CF

Example: u884PCF.txt = the skin friction along the primary axis for run 884.

Like the heat flux files, the channel gain information for each gage is listed along its coordinates. The values of skin friction are in units of lb/ft^2 .

7.0 Status of the Instrumentation and Data System

The data system was left connected to the model in anticipation of completing the Mach 7-8 testing in early January 1997. The Mach 7-8 testing did not take place in January because of a water leak in the UTRC vitiated heater nozzle. In the meantime, UTRC is proceeding with other tests. At the request of UDRI, the instrumented bottom wall section of the combustor was removed from the combustor, keeping the wires intact and tied to the data system. In addition, UDRI requested that the bottom combustor wall section not be tipped in order to avoid spilling any oil out of the skin friction gages and enabling inspection of the gages.

It is strongly recommended that several days be allowed for the examination of the skin friction gages before replacing the instrumented bottom wall in the combustor. This would allow verification of the current gage orientation, examination, re-calibration, and refilling of the gages with silicon oil (if required). In addition, note that there are four spare gages available for replacement of gages that appear to be suspect.

8.0 Summary and Conclusions

This report describes the experimental analysis and procedures used in acquiring and reducing the thermal load data during tests of a hydrocarbon-fueled scramjet combustor at United Technologies Research Center (UTRC). Wall temperature, heat transfer, and skin friction measurements were made for three tests at Mach 5.6 flight enthalpies. The goal of the study was to map the heat transfer and skin friction in the UTRC Scramjet combustor. The combustor was heavily instrumented with coaxial thermocouples on the wall opposite the injectors. The tests were conducted with both unheated gaseous ethylene and the heated products from the endothermic reaction of Jet A, which was passed through a catalytic reactor to simulate regenerative cooling of the structure.

A total of 82 coaxial thermocouples and 11 skin friction gages were used in this study. Most of the heat flux measurements and all of the skin friction measurements were on the wall that was opposite the main fuel injectors. A limited number of gages (8) were placed on the injector wall in the nearfield of the pilots.

The use of coaxial thermocouple gages for the measurement of detailed heat transfer measurement of the heat transfer in scramjet combustors was demonstrated for 50 second tests. The coaxial gages were shown to be a rapid indication of the localized wall heating. As a result, they were effective in determining where combustion occurred. In addition, it was shown that the coaxial thermocouple could be an effective indicator of an unstart condition in the engine.

The results for the non-reacting flow (before fuel was turned on) were compared to the results from the previous study of the same injector configuration at WPAFB. The results showed that the WPAFB study predicted the level of the peak heat transfer in the reflected shock-interaction region opposite the pilots. The level of the peak heating in this region was determined to be 1.7 times the reference heating level with fuel off, and 2.7 with fuel addition.

On the bottom wall of the combustor, the heat transfer was observed to increase downstream of the main fuel injectors, located on the opposite wall, for all three tests. Because P/P_{ref} along the bottom wall was proportional to h/h_{ref} , it is thought that the cause of the observed heat transfer increase was solely due to the pressure rise, which was caused by shock waves and the reaction of the fuel injected on the other side of the combustor. The increase in the film coefficient ratio, $h_{fuel-on}/h_{fuel-off}$, was less than 5.5 for the two tests with reformed Jet A fuel over the entire instrumented area of the combustor. In the test with gaseous ethylene fuel, the film coefficient ratio increased dramatically for the last two measurement locations. It is thought that this large increase was due to an increase in the recovery temperature caused by the reaction of the fuel.

Based on the Pratt and Whitney CFD predictions, the heat transfer on the wall opposite the injectors show that the level of the heating was lower than expected with the

heat transfer being proportional to the pressure. On the basis of the previous test at WPAFB, a correlation was developed for the peak heating in front of the cowl/wall junction. The results for the two tests with reformed Jet A fuel showed that the film coefficient was lower than the level of the peak heating predicted in front of the cowl/wall intersection ($h = 0.115 \text{ BTU/ft}^2\text{-s-}^\circ\text{R}$) over most of the combustor. In contrast, the heat transfer for the test with gaseous ethylene fuel predicted cowl heating several inches downstream of the secondary injectors where it is thought that the fuel from the secondary injectors reacted.

The majority of the gages that were located downstream of the secondary fuel injectors were in the near field of the injectors. It is thought that there was an ignition delay for the reformed Jet A fuel, so that the fuel from the secondary injectors reacted downstream of the instrumentation. For the upcoming Mach 7-8 tests, the secondary injection station will be moved upstream six inches, so that a longer section of the combustor downstream of the injectors will be instrumented. In addition, the higher static temperatures for these tests should ensure earlier ignition of the fuel.

A limited number of coaxial thermocouples (8) on the injector wall showed that the peak heat flux levels, expressed as the film coefficient, were higher than the heat flux on the wall opposite the injectors. The heating was highest at the row of gages 0.59" downstream of the secondary injectors. The test-to-test variation in the heat flux in this region was significant with the highest heating rates measured during the test with gaseous ethylene fuel. The peak heat measured film coefficient based on combustor inlet recovery temperature in this region ranged from $h = 0.14\text{-}0.18 \text{ BTU/ft}^2\text{-s-}^\circ\text{R}$ for the tests with reformed Jet A fuel to $0.25 \text{ BTU/ft}^2\text{-s-}^\circ\text{R}$ for the test with gaseous ethylene fuel.

The effect of an unstart was shown to dramatically increase the heat flux. Measurements in the injector region showed an increase in the heat flux by a factor of three. Of course the implications on structural integrity due to this condition may not be as serious as the potential problems with the inlet flow, performance, and vehicle control which would occur in the event of an unstart.

A total of 11 combined skin friction-heat transfer gages were mounted on the wall opposite the injectors. The results from each gage were presented as shear force vs. time. The results from the skin friction show that the output from most of the gages were repeatable in the sense that the trends shown by the each gage were approximately the same from test to test. The output from four of the gages showed little response in comparison to the response of the thermocouples, and are thus regarded as suspect. The output from several of the other gages steadily increased or decreased through the test.

Six of the gages appeared to roughly track the operational events (vitiated heater on, fuel on, fuel off) of the test. The skin friction levels for the six "good" gages appeared to change along with the Stanton number range from $C_f = 0.0015$ to 0.0075 . However, there was considerable drift in the skin friction measurements relative to the changes in the

film coefficient during the test. It is thought that this drift was due to thermal effects on the strain gages on the displacement sensor.

A first-order analysis of the heating of the silicon oil which was used in the skin friction gages showed that there are potential problems with oil heating in the long-duration high-enthalpy tests. Because of the low thermal diffusivity, the temperature at the oil-air interface increases rapidly. Although the vapor pressure of the oil is extremely low, there are potential problems with the reaction of the silicon oil with oxygen at elevated temperatures for long duration testing. Specifically, there is the possibility of combustion of the oil, or the formation of a solid substance, which could prevent the movement of the sensing element.

9.0 Recommendations

In preparation for the upcoming Mach 7-8 tests, it is recommended that several days be allowed for the examination of the skin friction gages before replacing the instrumented bottom wall in the combustor. This would allow verification of the current gage orientation, examination, re-calibration, and refilling of the gages with silicon oil (if required).

It is recommended that further analysis be given to the subject of the thermal effects on the gage response, in particular, to determine whether thermal effects could be responsible for the trends seen during the tests.

Another issue is the thermal response and subsequent degradation of the silicon oil in the gages. There is concern about whether the oil near the surface of the gage is doing what it is supposed to do. We need to inquire whether the oil drastically changes in properties or vanishes a short time after the start of each test.

A total of four coax thermocouple gages exist which could be located at other locations in the combustor before the next series of tests. In addition, there are 14 channels available on the HP data acquisition system. More measurements would require ordering thermocouples. Certainly more measurements would be of interest on the main injector side of the combustor and at locations further downstream on the opposite wall. However, because of the lead time on this instrumentation, a decision should be made soon on the acquisition of more surface thermocouples.

10.0 References

1. Neumann, R. D. et al (1998), "Characterization of Combustor Thermal and Acoustic Loads in a Non-Reacting Supersonic Flow," AFRL-PR-WP-TR-1998-2005.
2. Kay, I. W. and Salvador, C., "Scramjet Component Technology Program Phase II Engine Component Development Contract," R96-5.101.0013-9.1/57.
3. Stouffer, S. D. (1995), "The Effect of Flow Structure on Heat Transfer and Combustion in a Supersonic Combustion Ramjet Combustor," Ph.D. Dissertation, Mechanical Engineering, Virginia Polytechnic Institute and State University, Blacksburg, VA.
4. Hayes, J. R., and Neumann, R. D. (1986), "Introduction to the Aerodynamic Heating Analysis of Supersonic Missiles," Chapter 3 in *Progress in Astronautics and Aeronautics*, Vol. 142.
5. van Driest, E. R. (1956), "The Problem of Aerodynamic Heating," *Aeronautical Engineering Review*, October 1956.

11.0 Appendix A: Conversion of Temperature to Heat Flux

The following section presents the details of the methodology used in the conversion of the wall temperature to heat flux and is reprinted from Reference 3.

Conversion of Surface Temperature History to Heat Flux

Most of the previous research which used the conversion of surface temperature to heat transfer has been associated with short run time facilities (shock tubes) and used assumptions of constant thermal properties, and a semi-infinite solid. With these assumptions, the methods of Vidal^[121] or Cook and Felderman^[122] can be used to determine the heat flux. Kidd^[123] shows that the time which a wall of thickness, l , and conductivity, k , can be considered semi-infinite can be determined from the following relationship: $t < \left(\frac{l^2}{3.2k} \right)$. Therefore for the 1/2 inch thick walls used in the combustor, the wall can be considered semi-infinite for 13 and 4 seconds for the stainless steel and carbon steel walls, respectively. For the case of longer run times the semi-infinite assumption is not valid. Therefore other methods must be employed to extract the heat flux from the surface temperature.

Kidd^[123] used a finite-difference method which does not assume semi-infinite walls to determine the wall heat transfer from surface thermocouple measurements. A similar approach was used for this study. The development and validation of this code for a case with temperature-dependent thermal properties will be presented in the sections below.

B.1 Code Development

The non-linear, heat conduction problem with temperature-dependent thermal properties is shown in equation B-1.

$$\frac{\partial}{\partial x} \left(k \frac{\partial T}{\partial x} \right) = \rho C \frac{\partial T}{\partial t} \quad (\text{B-1})$$

Over a large temperature range, the density, specific heat, and the thermal conductivity are functions of temperature, which make equation B-1 nonlinear. The one-dimensional heat conduction equation was rewritten in

the following form which neglects the variation of thermal conductivity with x , but allows k , C , and ρ to vary with temperature.

$$k \frac{\partial^2 T}{\partial x^2} = \rho C \frac{\partial T}{\partial t} \quad (\text{B-2})$$

Equation B-2 was then written in the common implicit finite-difference form which is shown in equation B-3 and corresponds to the grid representation shown in Fig. B.1

$$K_{i-1}T_{i-1}^{n+1} + (K_{i-1} + K_{i+1})T_i^{n+1} + K_{i+1}T_{i+1}^{n+1} = \frac{(\rho C)_i \Delta x^2}{\Delta t} (T_i^{n+1} - T_i^n) \quad (\text{B-3})$$

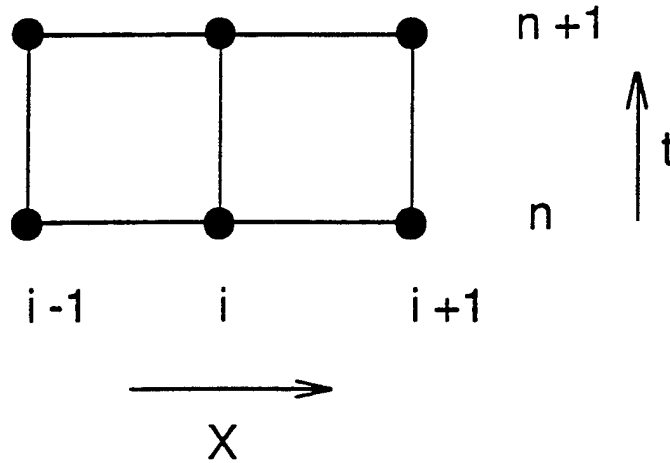


Figure B.1 Computational Grid for Finite-Difference Code

In equation B-3 the superscript is used to denote increments of time and the subscripts are used to denote spatial increments. For simplicity constant Δx and Δt were used for the finite difference grid. The thermal properties were curve-fitted to account for variation with temperature. The terms $K_{i\pm 1}$ represent an effective conductivity between node i and the adjacent nodes. As suggested by Patankar^[124] the thermal resistance was used to determine the effective thermal conductivity between two nodes. Therefore, the terms $K_{i\pm 1}$ can be determined by equation B-4:

$$K_{j\pm 1} = \frac{2k_i k_{j\pm 1}}{k_i + k_{j\pm 1}} \quad (\text{B-4})$$

Considering equation B-3 again, the thermal conductivity terms are multiplied by the temperatures at time $n+1$, while the density and the specific heat are multiplied by the temperature at both times n and $n+1$. Therefore, the effective thermal conductivity was evaluated at the temperatures at time $n+1$ and the product of density and specific heat is evaluated at times n and $n+1$ and then averaged. In equation B-3 the thermal properties used in the calculation of the temperatures at time $n+1$ are dependent on the temperature at time $n+1$. Therefore, equation B-3 was solved using the properties at time n first. Then the estimate of temperature at time $n+1$ was used to update the thermal properties and allow a second determination the temperature at time $n+1$. This process was repeated four more times at each time step. Experience obtained while developing the code has shown that, by the last iteration, the calculated temperatures at time $n+1$ are the same as that calculated in the preceding iteration.

The boundary conditions used for the code were a specified internal wall temperature (from the surface thermocouple measurement) and an insulated outer wall. The outer wall was not actually insulated in this study, but, for the materials and run times used in this study, the amount of heat transfer from the outer wall during the test was insignificant.

The result of solving equation B-3 is the determination of the temperature distribution across the wall as a function of time. To properly determine the heat transfer, the entire temperature history up to the test point of interest was required. After obtaining the temperature distribution, the heat transfer can be calculated from equation (B-5):

$$q = \frac{K_0}{\Delta x} (T_0^{n+1} - T_1^{n+1}) + \frac{\rho C \Delta x}{2} \frac{(T_0^{n+1} - T_0^n)}{\Delta t} \quad (\text{B-5})$$

where T_0 is the measured internal wall temperature. The first term in the equation B-5 is due to the temperature gradient in the metal and the second term is due to thermal capacity of the wall material. As the grid spacing decreases the second term decreases compared to the first term. For the grid

spacing used during this study the contribution of the second term was less than one percent of the total wall heat transfer.

Several equally spaced grids were tried and a spacing of 50 nodes over the 12.7 mm wall was selected. With this spacing the determination of the heat flux was rapid. Typically less than one-half second on the Convex C-2 vector computer at NASA was required per thermocouple for a ten second test.

B.2 Code Validation

After creating the finite difference code it was necessary to determine how well it models the heat flux. An analytical solution of the non-linear problem of heat transfer with temperature-dependent thermal properties was used to validate the finite difference code. First the analytical closed-form solution was used to determine the surface temperature history caused by a known heat flux. Then this surface temperature history was used as the input temperature history to the finite difference heat conduction code. The calculated heat flux was then compared to the known heat flux which was used as an input to the analytical solution.

The equation for the one-dimensional heat conduction problem with temperature-dependent thermal properties was shown in equation B-1. If k , ρ , or C vary as a function of temperature then equation B-1 is non-linear. The Kirchhoff transformation^[125] was used to linearize equation B-1 for the variation of the conductivity with temperature. The Kirchhoff transformation is shown in equation B-6.

$$U = \int_{T_o}^T \frac{k(\eta)}{k_o} d\eta \quad (\text{B-6})$$

Further details of the Kirchhoff Transformation can be found in reference 126.

A test case for the validation was designed with the properties of the Kirchhoff transformation in mind. The problem was that of one-dimensional conduction with one side adiabatic and a constant flux (4.54 MW/m^2) to the other side. A hypothetical material with thermal properties which varied linearly with temperature as shown in equations B-7 to B-9 was used to allow

variation of the thermal conductivity and specific heat while maintaining constant α .

$$k = k_0 (1 + \beta T) \quad (\text{B-7})$$

$$C = C_0 (1 + \beta T) \quad (\text{B-8})$$

$$\rho = \text{constant} \quad (\text{B-9})$$

The coefficients k_0 , C_0 , and ρ in equation B-7 and B-8 were chosen to represent the properties of stainless steel at room temperature. The only thing that is artificial about the 'material' used for the validation is that the same linear dependence with temperature was used for both the conductivity and specific heat. In general the variation with temperature of the conductivity and specific heat are not the same.

After applying the Kirchoff transformation to the boundary conditions they become:

$$k_0 \frac{\partial U}{\partial x} = q_0 \quad \text{at } x = l \quad (\text{B-10})$$

$$k_0 \frac{\partial U}{\partial x} = 0 \quad \text{at } x = 0 \quad (\text{B-11})$$

where q_0 is the specified heat flux.

The solution for the heated surface temperature is given in equations

$$\text{B-12 and B-13: } U = \frac{q_0}{k_0} \left[\frac{\alpha t}{L} + L \left(\frac{1}{3} - \frac{2}{\pi^2} \sum_{n=1}^{\infty} \left(\frac{1}{n^2} e^{-\alpha n^2 \pi^2 t / L^2} \right) \right) \right] \quad (\text{B-12})$$

$$U = (T - T_0) + \frac{\beta}{2} (T^2 - T_0^2) \quad (\text{B-13})$$

The wall temperature calculated from the analytical solution is shown in Fig. B.2. This temperature trace was sampled at 20 Hz and 5 Hz and was used as the boundary condition for the finite difference code. The numerically calculated heat fluxes are also plotted in Fig. B.2. After an initial 12 % overshoot, the calculated values of the heat flux quickly settled to the known input flux. The heat flux calculated from the 20 Hz temperature trace settles faster than that calculated from the 5 Hz data trace. However, even at the 5 Hz data rate, which was the experimental data rate, the finite difference code adequately models the problem of transient conduction with temperature-dependent thermal properties, if the heat flux is relatively steady with time.

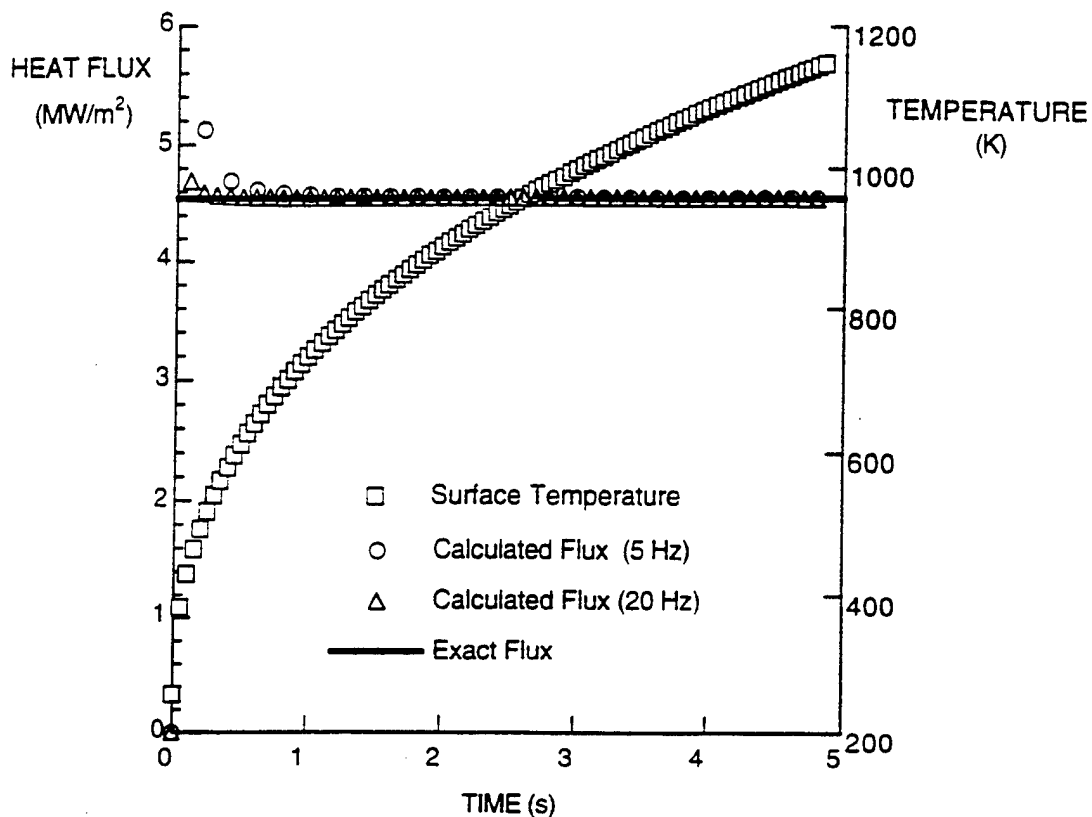


Figure B.2 Validation of the Finite-Difference Code.

B.3 Conversion of Wall Temperature From the Heat Flux

A modified version of the code was used to calculate the wall temperature corresponding to a known surface heat flux. The modified code used a known heat flux history flux as the boundary condition at the internal wall surface instead of the fixed temperature boundary condition.

B.4 Uncertainty Sources in the Hot Wall Heat Flux

The results of the test case presented above show that the heat flux can be accurately predicted at times greater than four data cycles after the start of a large transient. If the region near a transient is avoided, the errors due to the code are negligible. The major term in the heat flux calculation

(equation B-5) is $q = \frac{K_0}{\Delta x} (T_0^{n+1} - T_1^{n+1})$ thus, the only sources of uncertainty are the temperature measurement and thermal conductivity. The thermal properties for the steel were found from handbooks and had an uncertainty of $\pm 5\%$.

The uncertainty of the temperature measurement was determined in Appendix A, and had a total uncertainty of $T = \left[\pm 0.75 + \frac{0.64}{T} \right] \%$. The first term of the temperature is the bias uncertainty of the thermocouple caused by calibration. The effect of the bias uncertainty is a constant shift of the temperature vs. time curve. In other words the temperature is within a $\pm 0.75 \%$ band. Thus the bias term of temperature measurement causes a small error in the thermal properties. However, the uncertainty in the thermal properties is much larger than this term, so that it can be neglected in comparison. The second term in the temperature uncertainty is due to the quantization uncertainty which is random, and oscillates between positive and negative values. Furthermore, the magnitude of this term decreased as the temperature difference between the surface and the first node increased.

An examination of the temperature difference of the surface temperature and the first node for several of the tests showed that the magnitude of the temperature difference was about 20 K. at four data cycles after the fuel on transient. Thus the uncertainty of the heat flux due to the temperature uncertainty was $\approx (0.64/20)$ or $\pm 3 \%$ of the heat flux.





The total uncertainty of the hot wall heat flux is the RMS sum of the uncertainty due to the conductivity and the temperatures and is $\pm 5.8 \%$ of the heat flux.

References for Appendix A

121. Vidal, R. J. (1956), "A Resistance Thermometer for Transient Surface Temperature Measurements," ARS Meeting , Buffalo, N.Y., September 1956.
122. Cook , W. J., and Felderman, E. J. (1966), "Reduction of Data from Thin-Film Heat Transfer Gages: A Concise Numerical Technique," *AIAA Journal*, Vol. 4, No. 3.
123. Kidd, C. T. (1990), "Coaxial Surface Thermocouples: Analytical and Experimental Considerations For Aerothermal Heat-Flux Measurement Applications," ISA Paper #90-126.
124. Pantakar, S. V. (1980), *Numerical Heat Transfer and Fluid Flow*, Hemisphere, Washington DC.
125. Kirchhoff, G. (1894), *Vorlesungen über die Theorie der Wärme*, Barth, Leipzig.
126. Ozisik, M. N. (1979), *Heat Conduction*, Wiley, New York.

12.0 Appendix B: Figures

KEY:

 = Skin Friction Gage
 = Existing Holes
 = Kulite
 = Coax TC

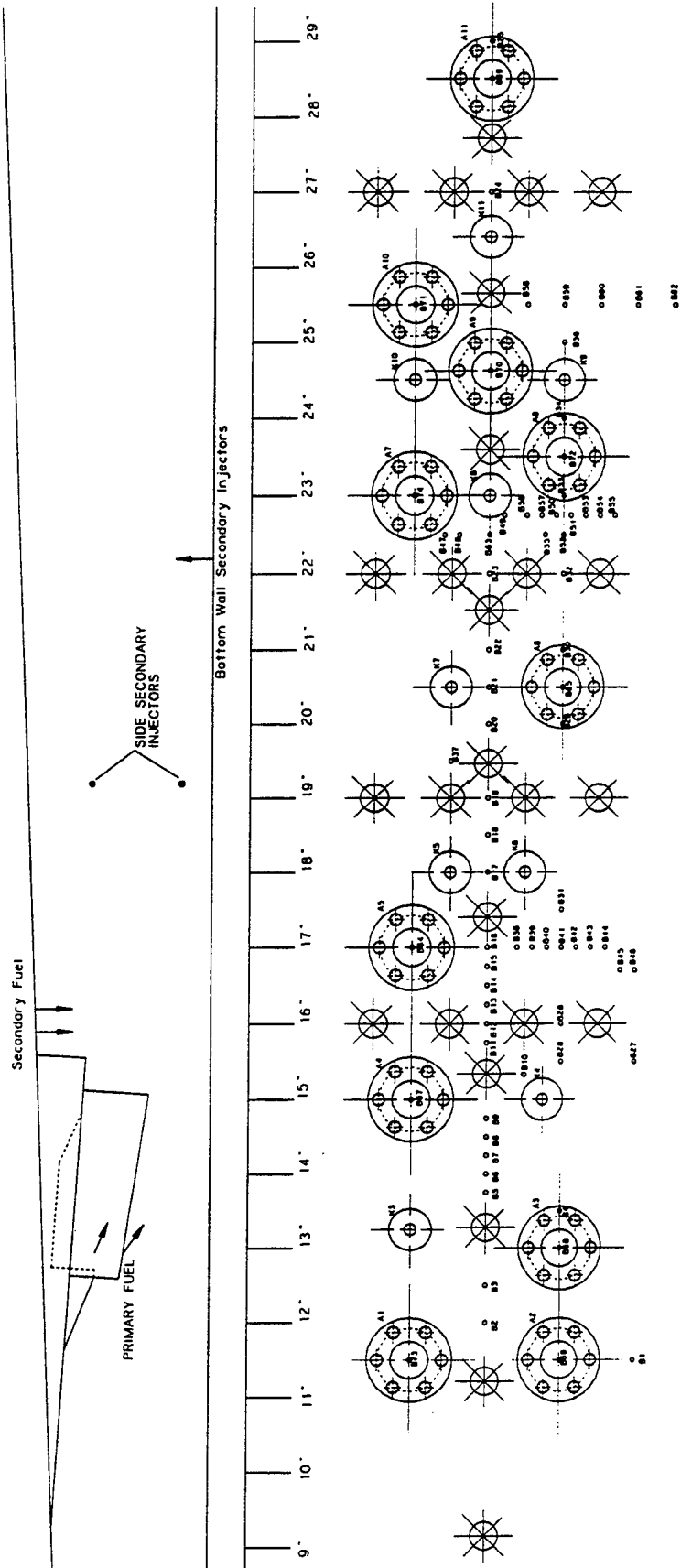


Figure 1. Layout of Heat Flux and Skin Friction Instrumentation for the Mach 5.6 Tests

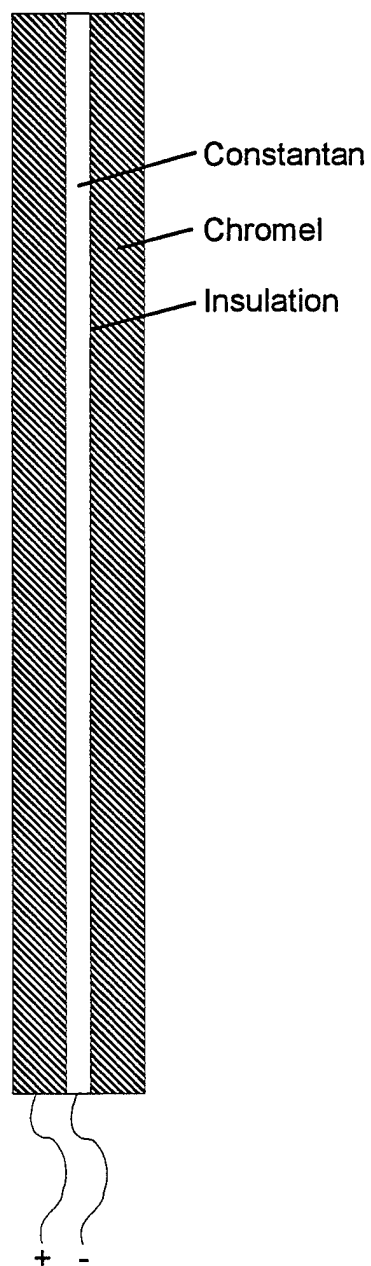


Figure 2. Sketch of Coaxial Thermocouple

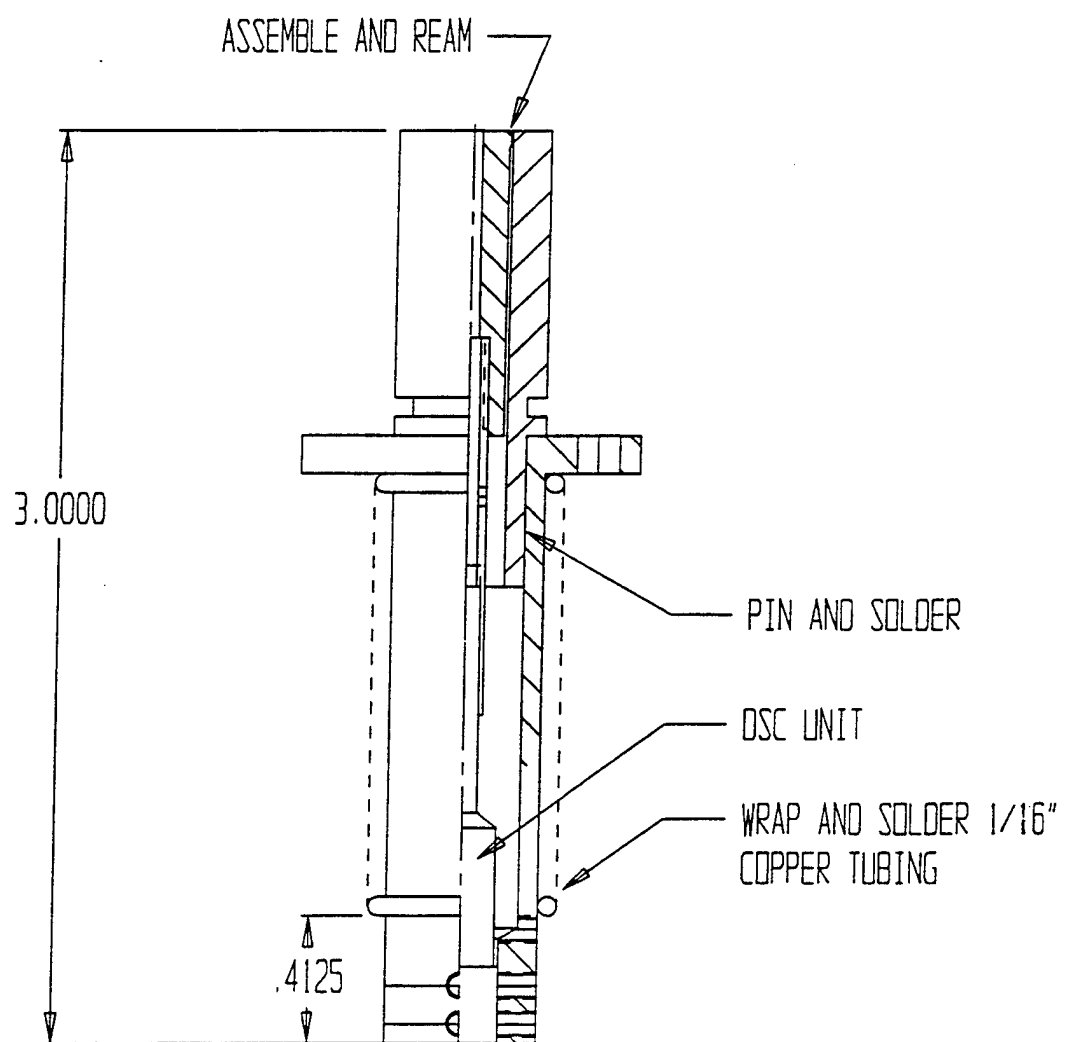


Figure 3. Sketch of the Skin Friction Gage

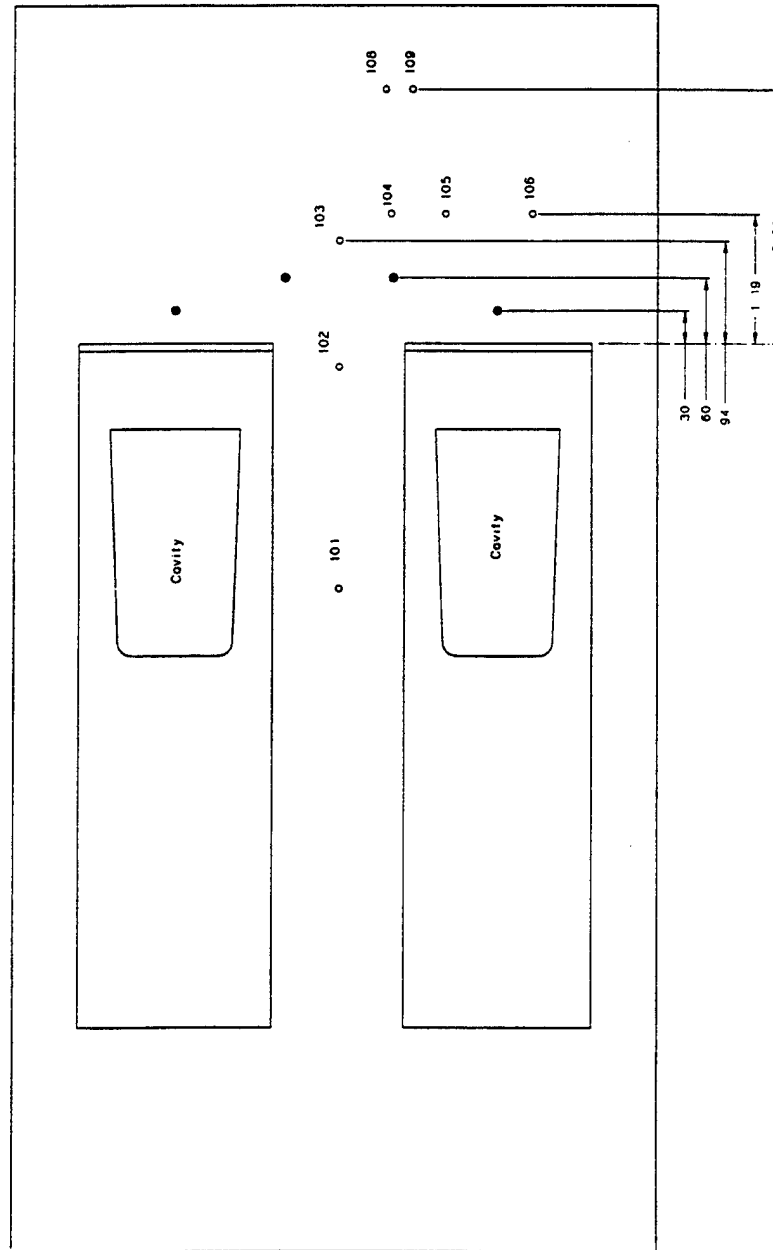


Figure 4. Coaxial Thermocouple Locations on the Pilot Mounting Frame

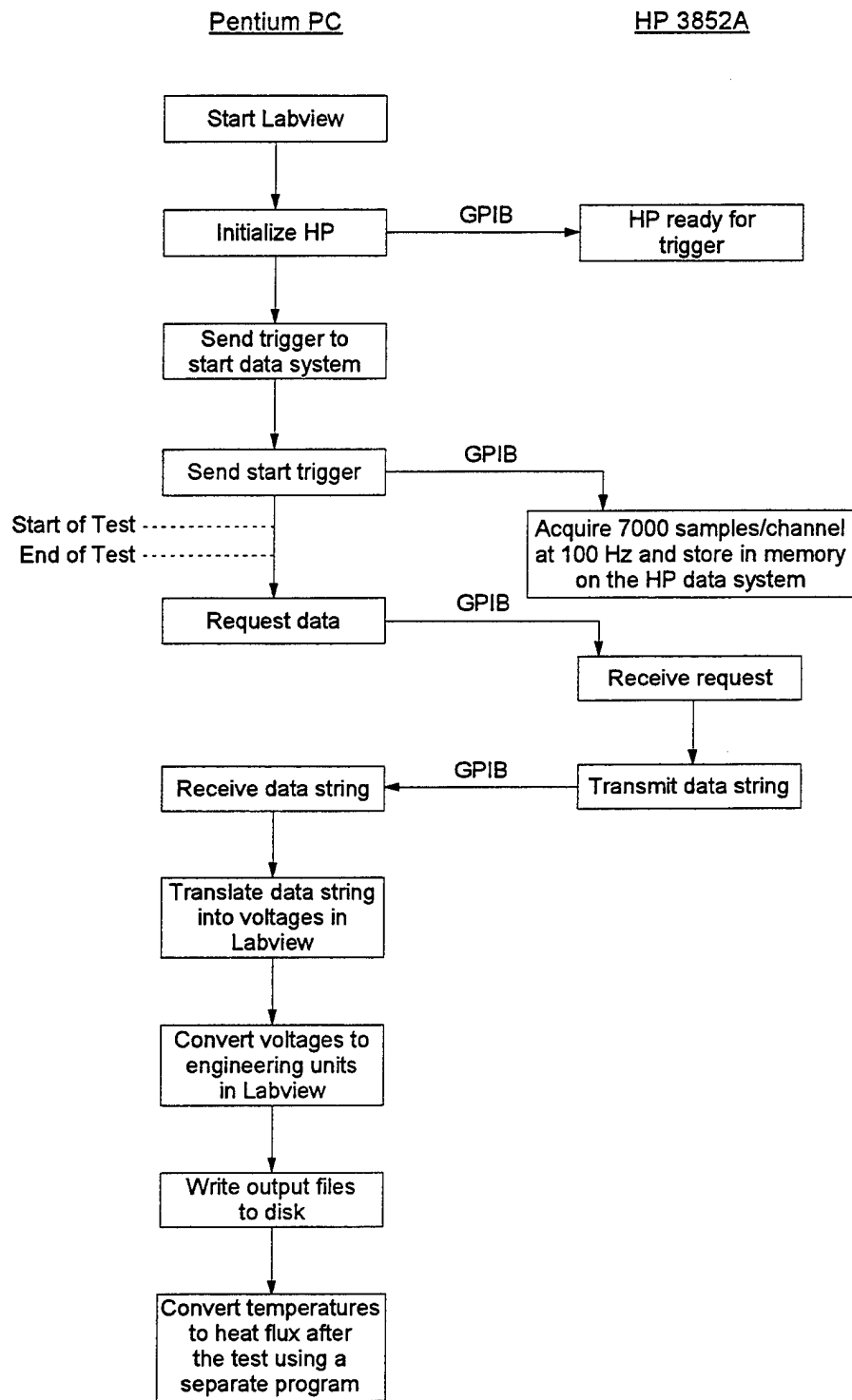


Figure 5. A Flow Chart of the Data Acquisition Process

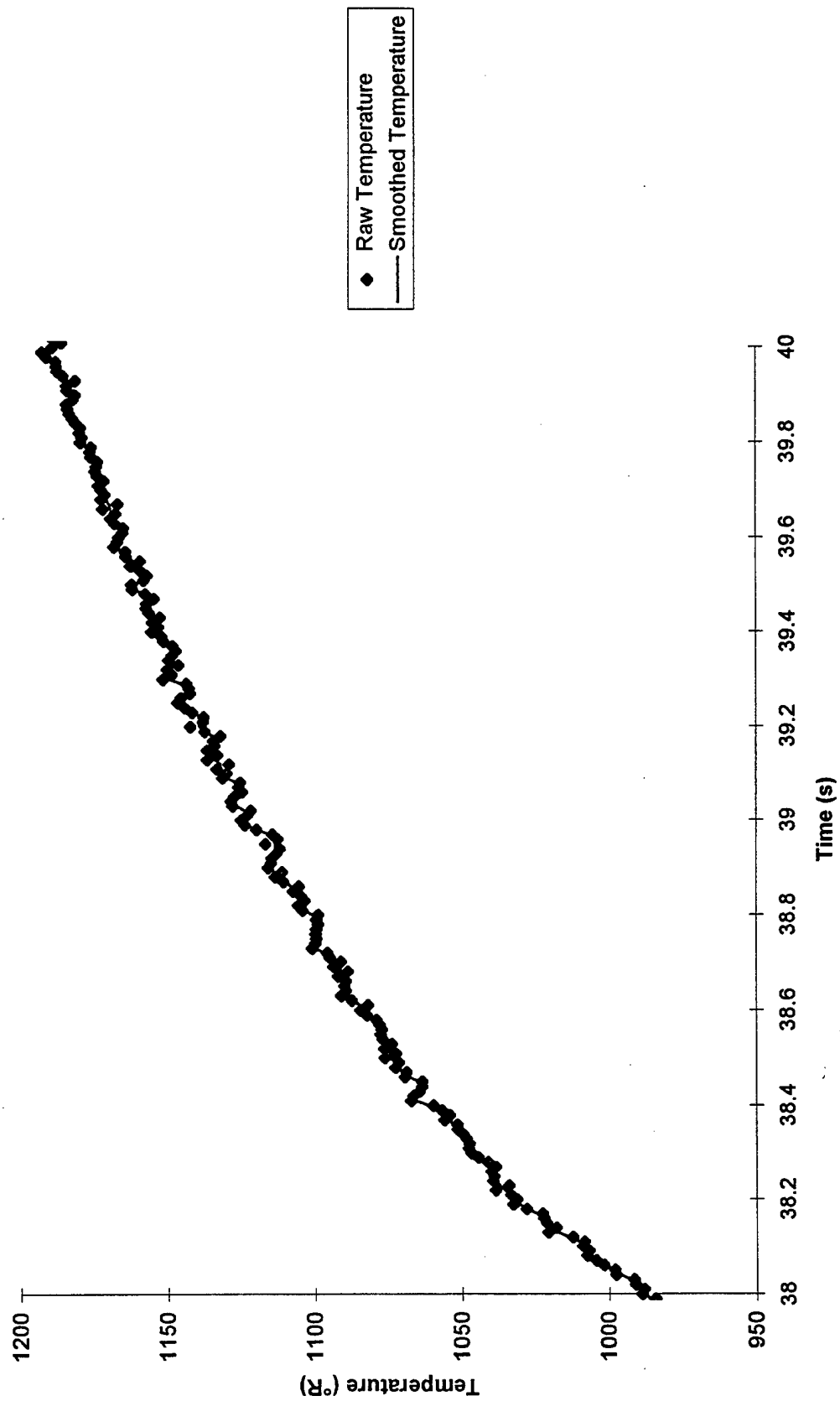


Figure 6. Raw and Smoothed Temperature Traces for a Typical Thermocouple

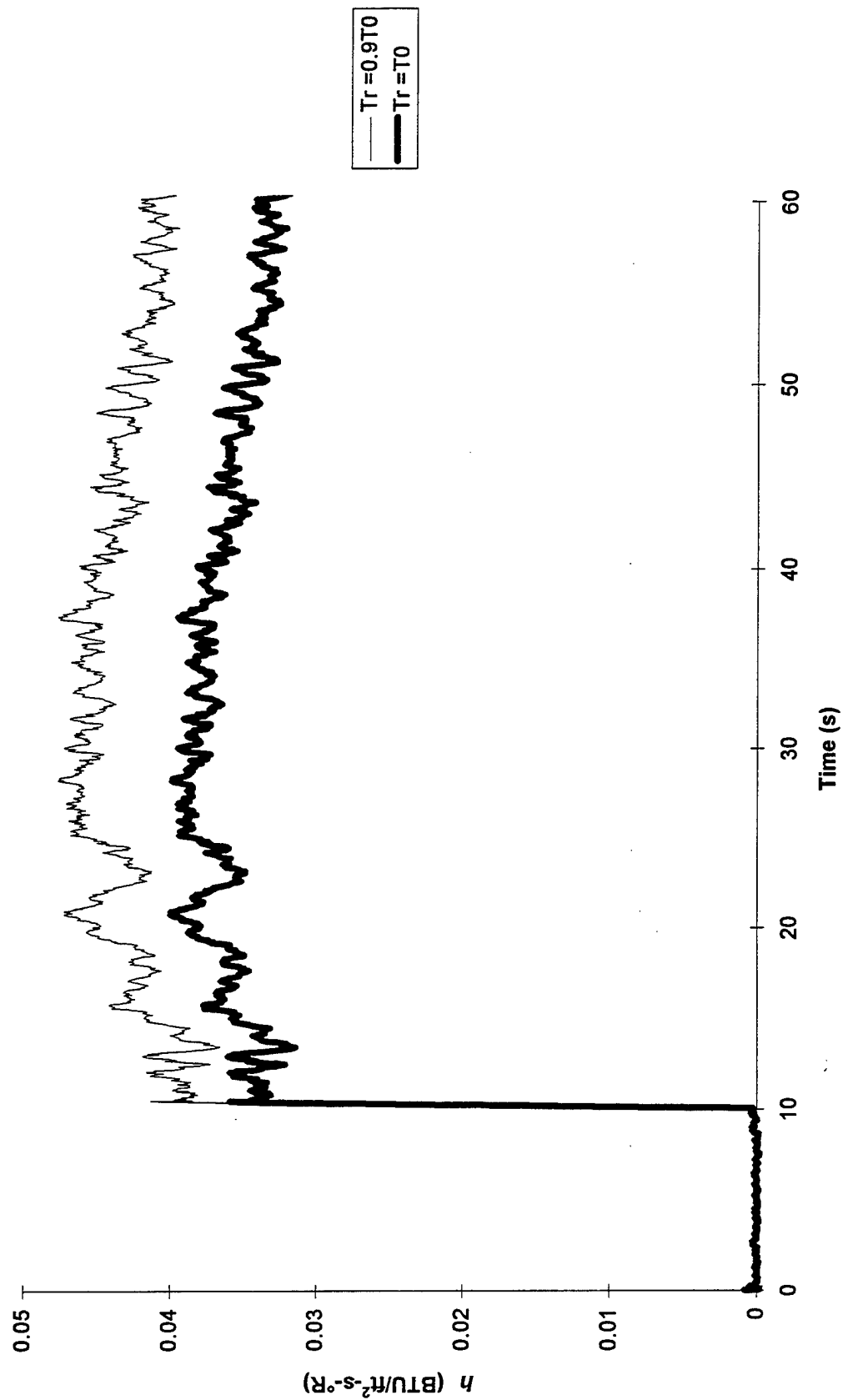


Figure 7. Effect of the Recovery Temperature on the Stanton Number (Test 886, $x = 11.5''$, $y = 1''$)

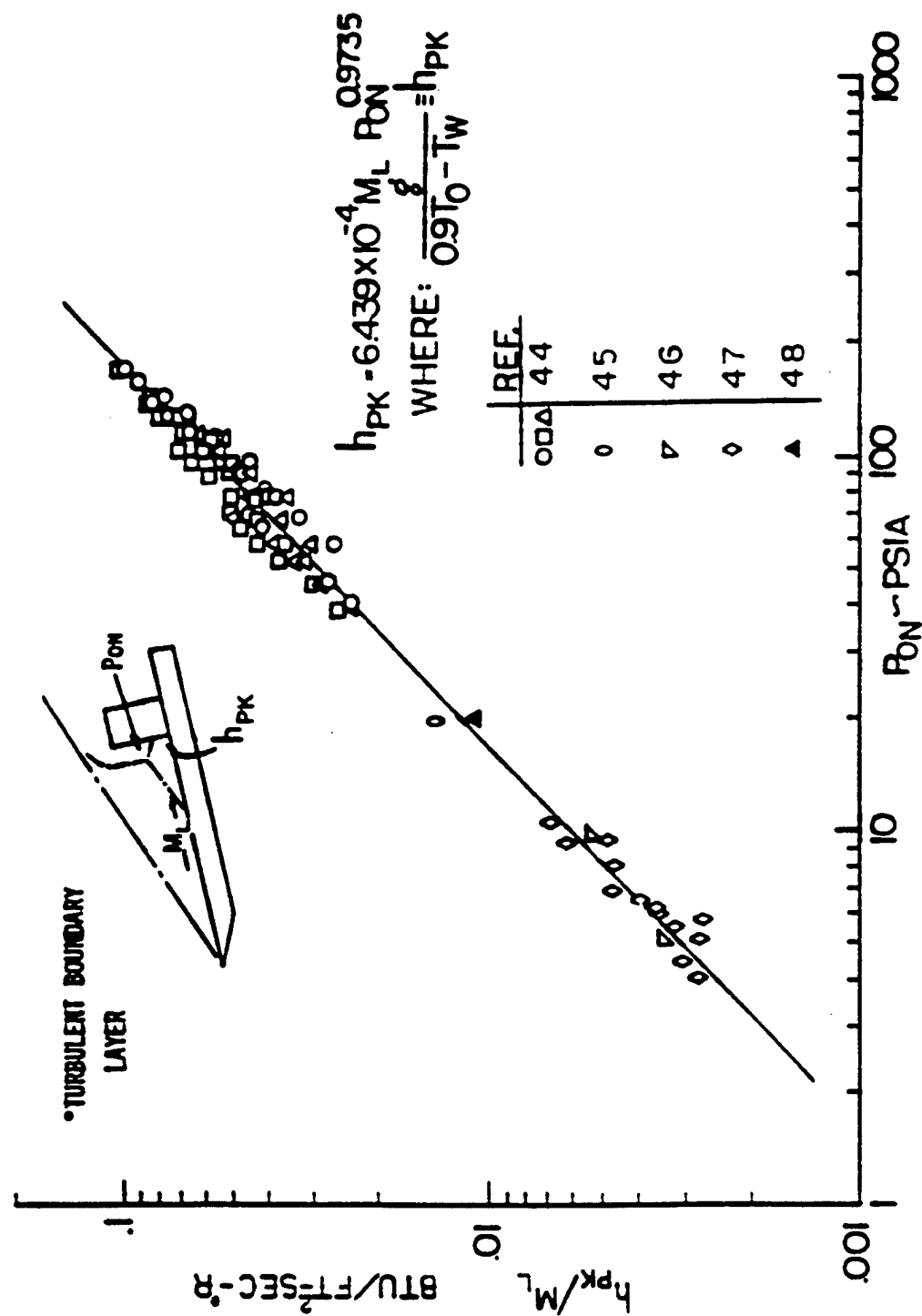


Figure 8. Correlation of the Peak Heating in Front of a Cylinder-Wall Junction



Figure 9. Wall Temperatures at Selected Locations During Run 884

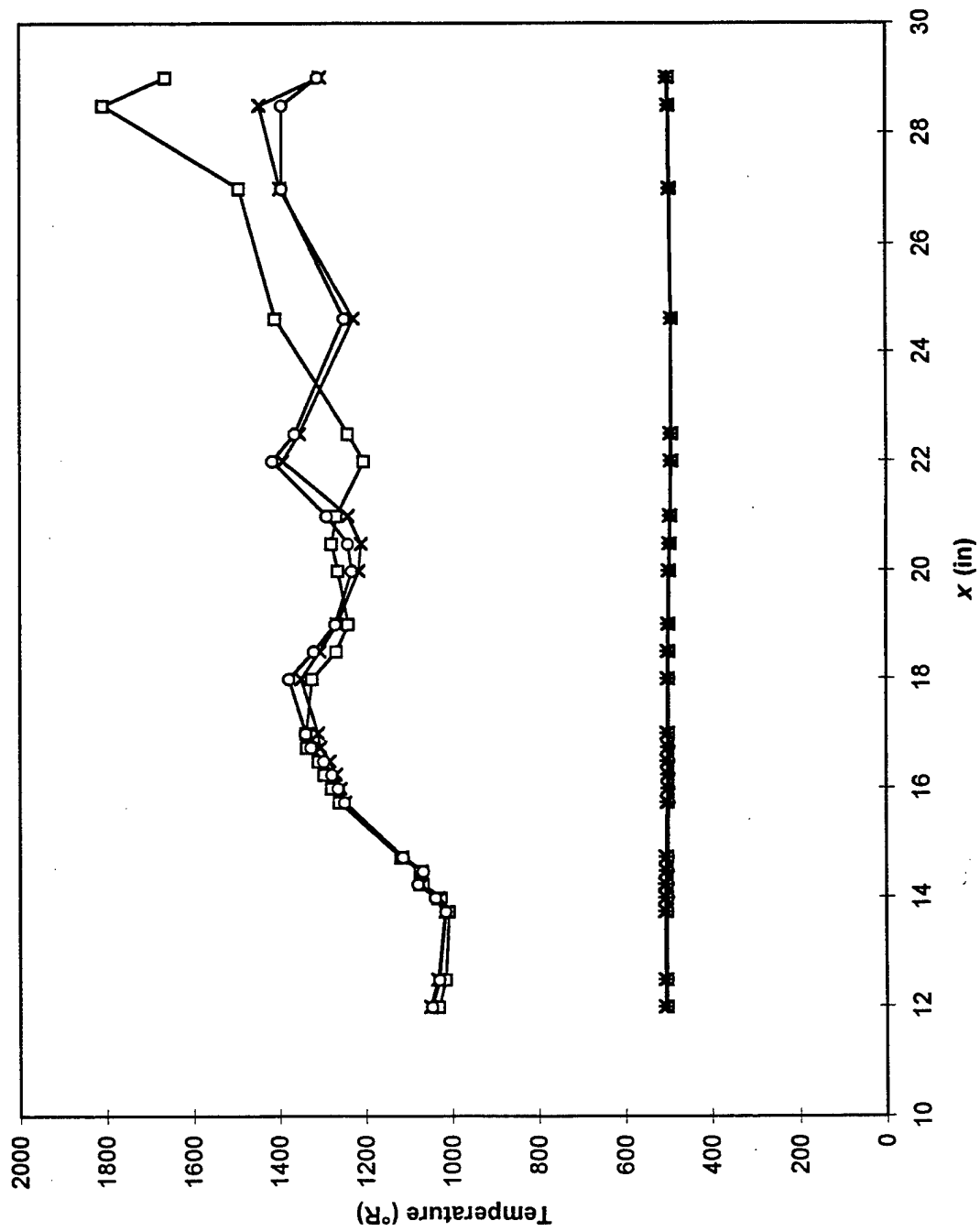


Figure 10. Initial and Peak Temperatures Along the Centerline of the Bottom Wall

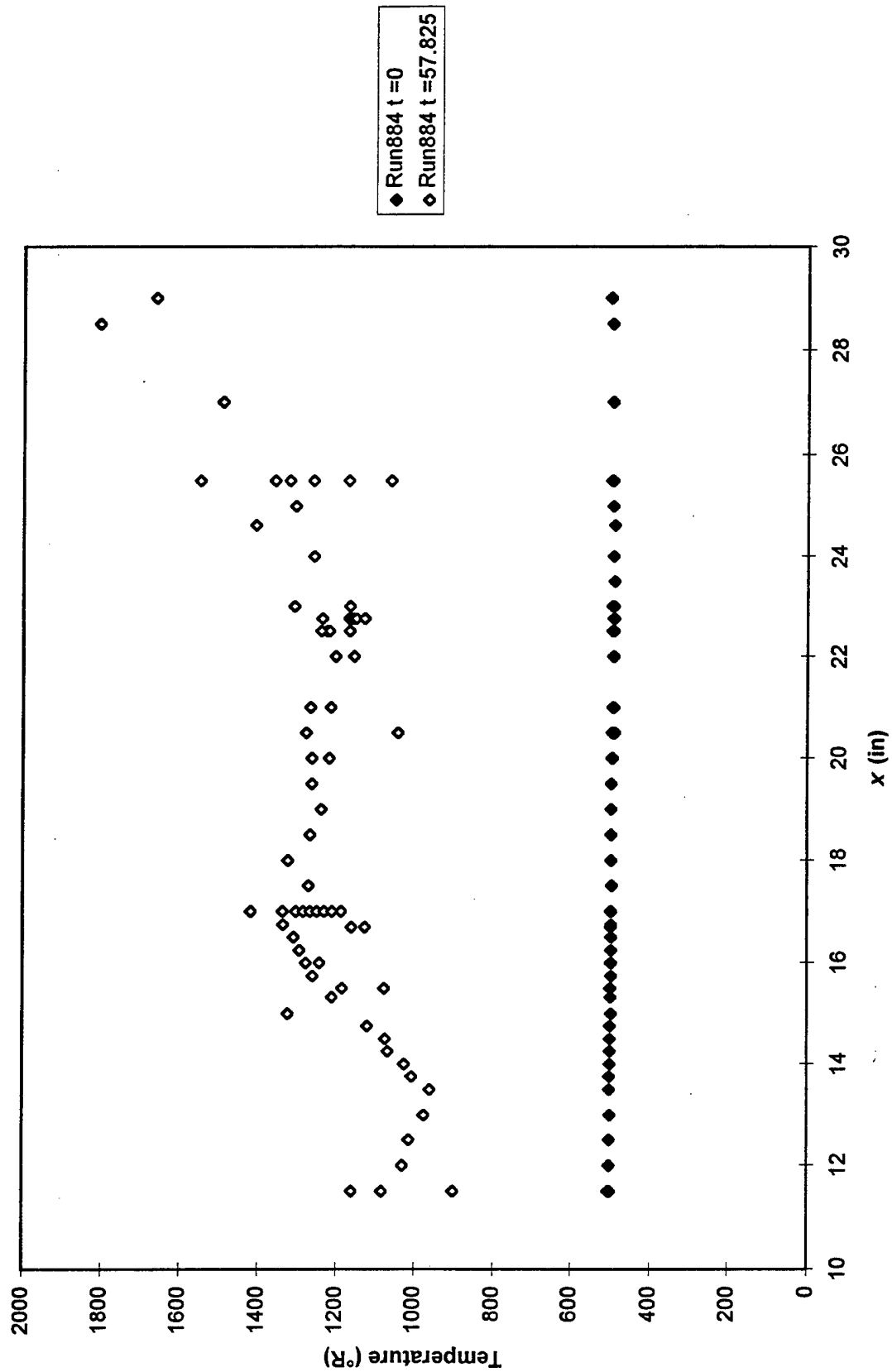


Figure 11. Initial and Peak Temperatures on the Bottom Wall During Run 884

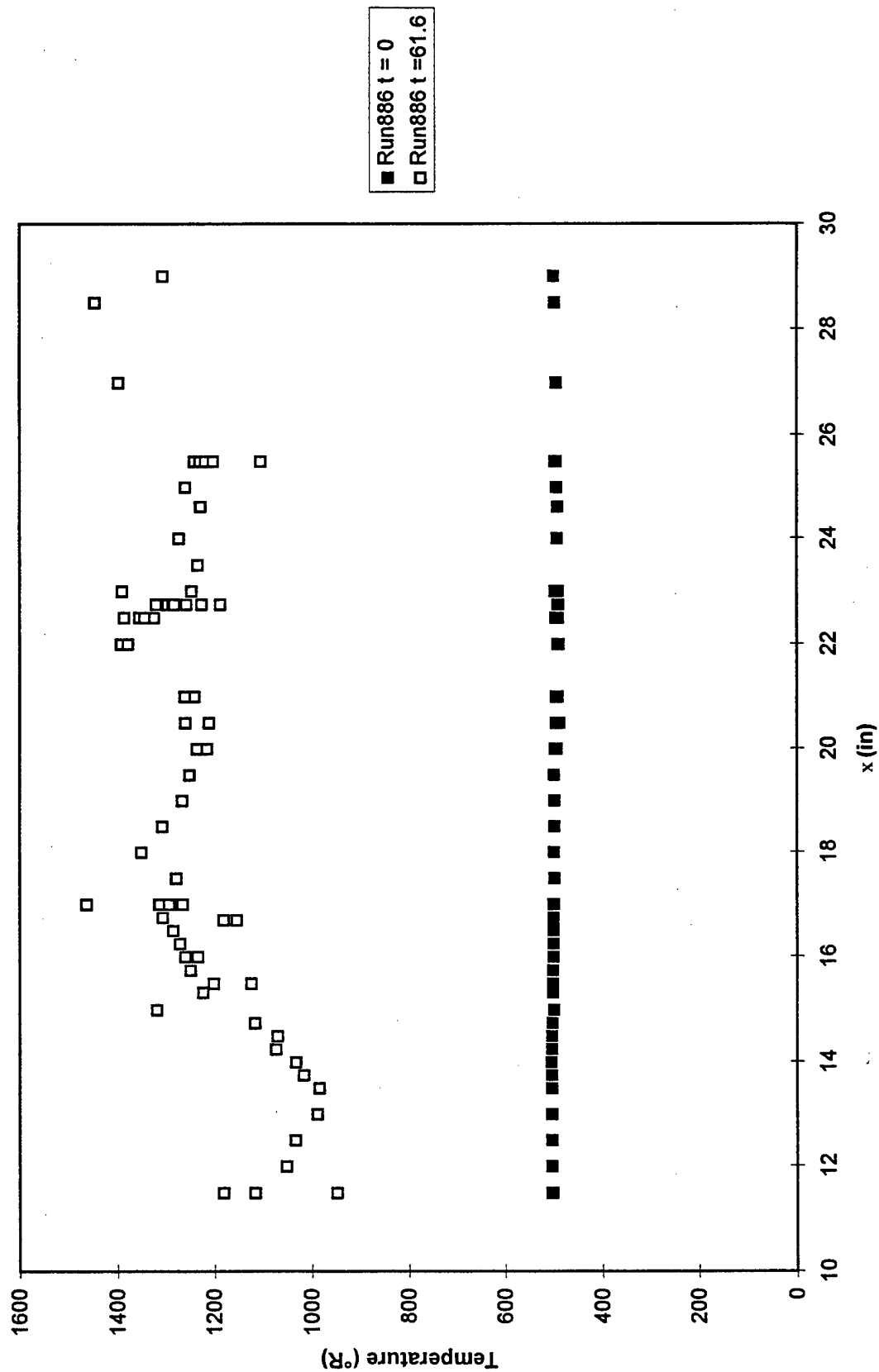


Figure 12. Initial and Peak Temperatures on the Bottom Wall During Run 886

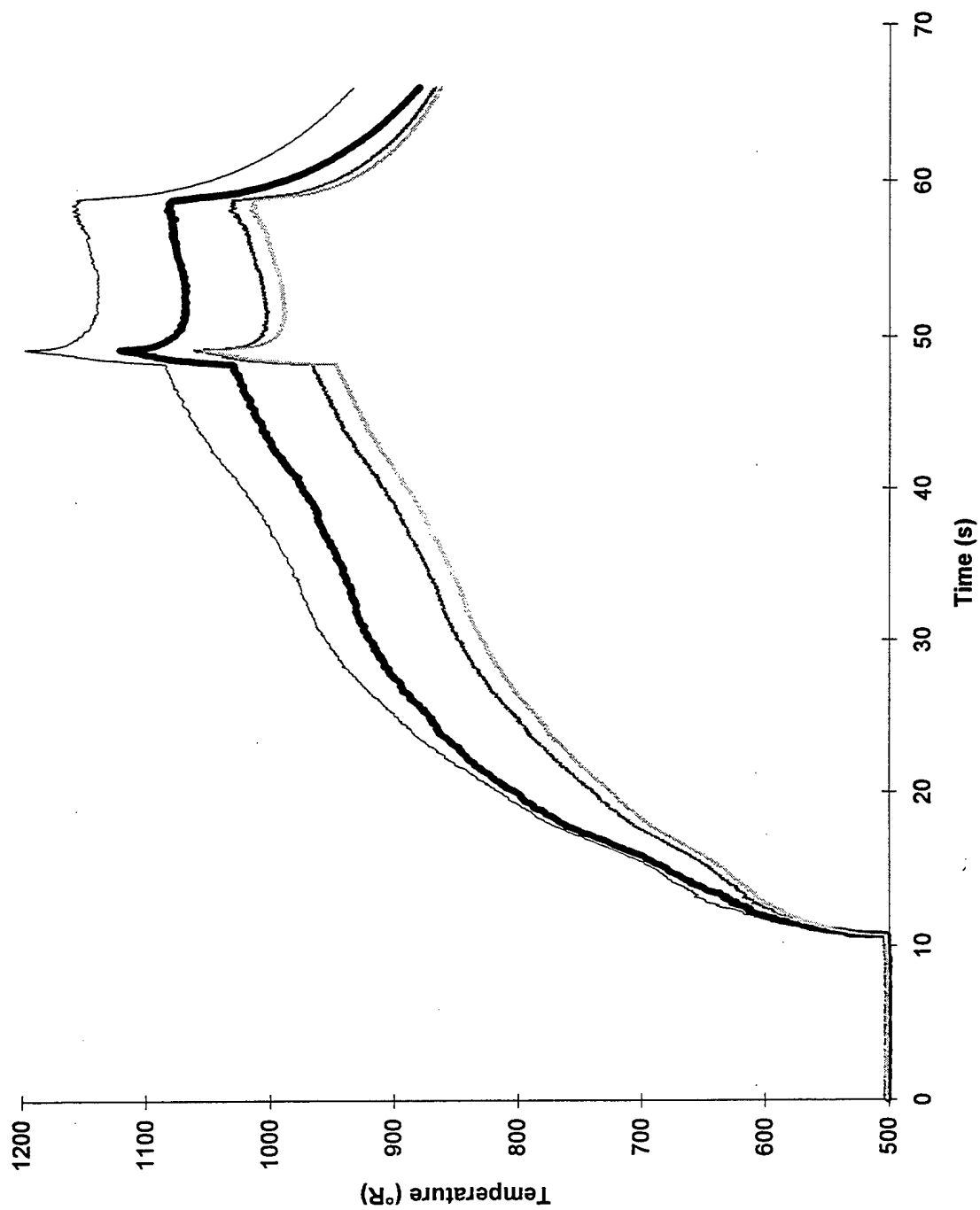


Figure 13. Wall Temperatures Upstream of the Shock Interaction in Run 884

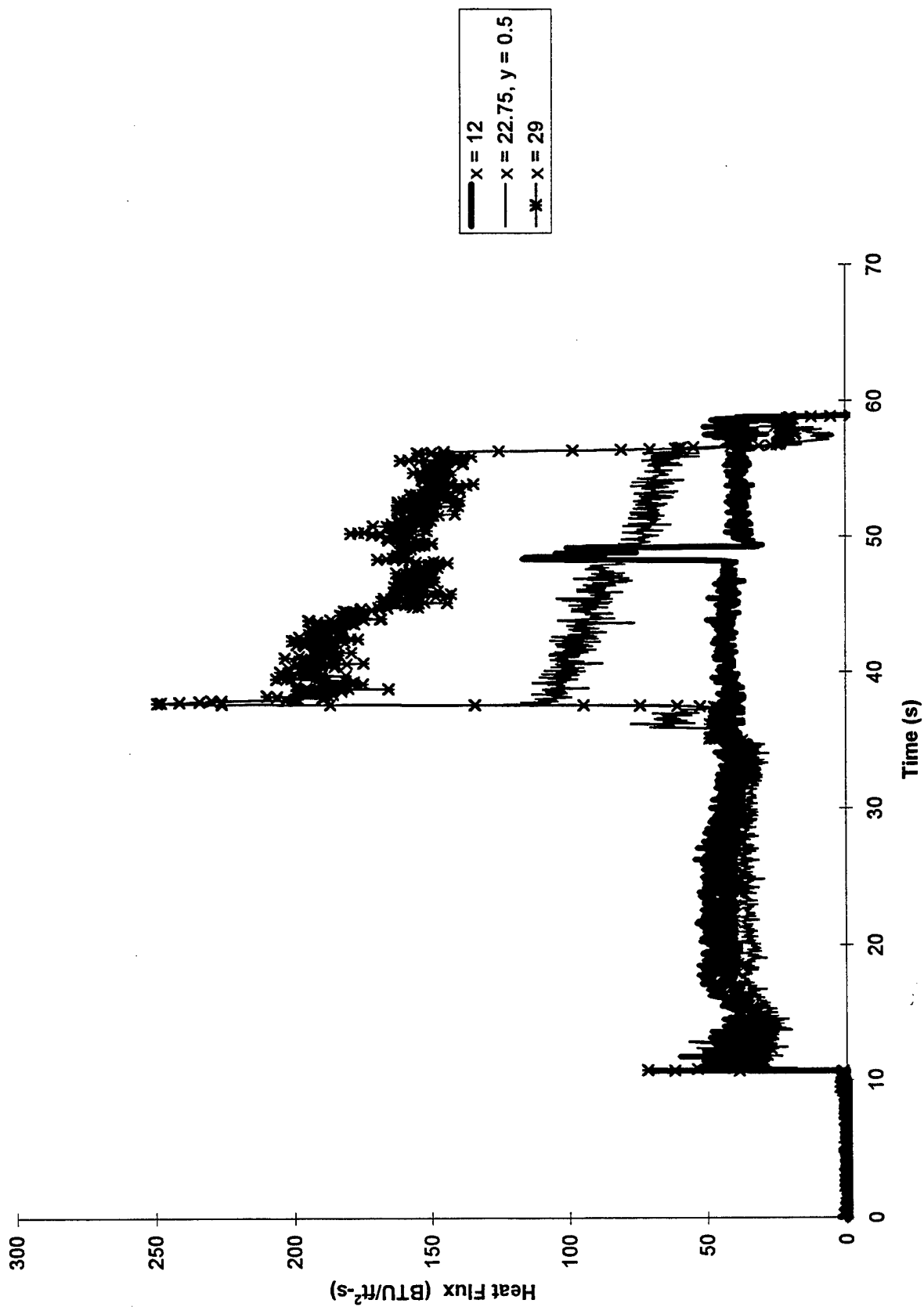


Figure 14. Heat Fluxes at Selected Locations During Run 884

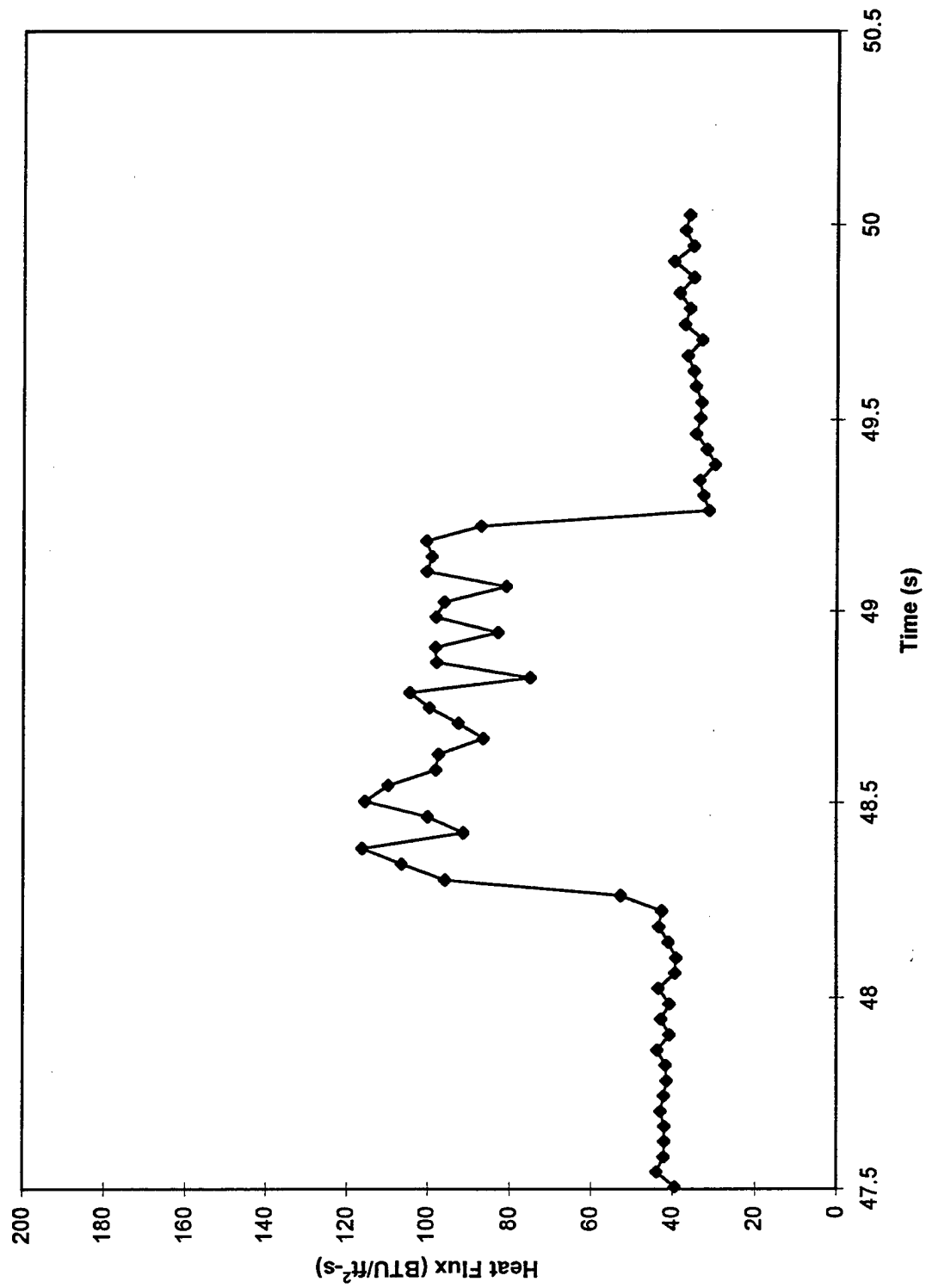


Figure 15. Detail of Unstart During Run 884 for the Gage at $x = 12$ "

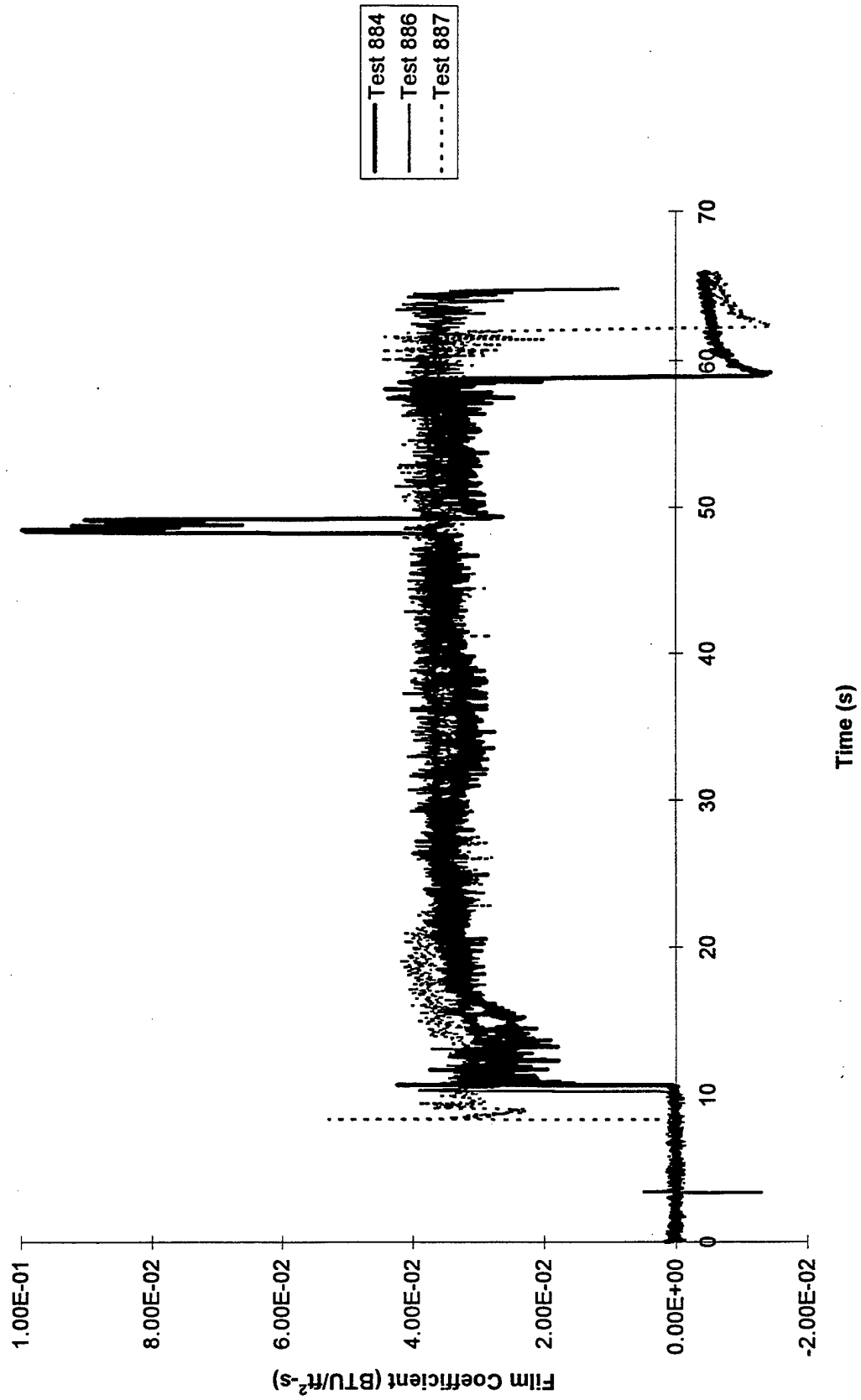


Figure 16. Film Coefficient for the Gage at $x = 12''$

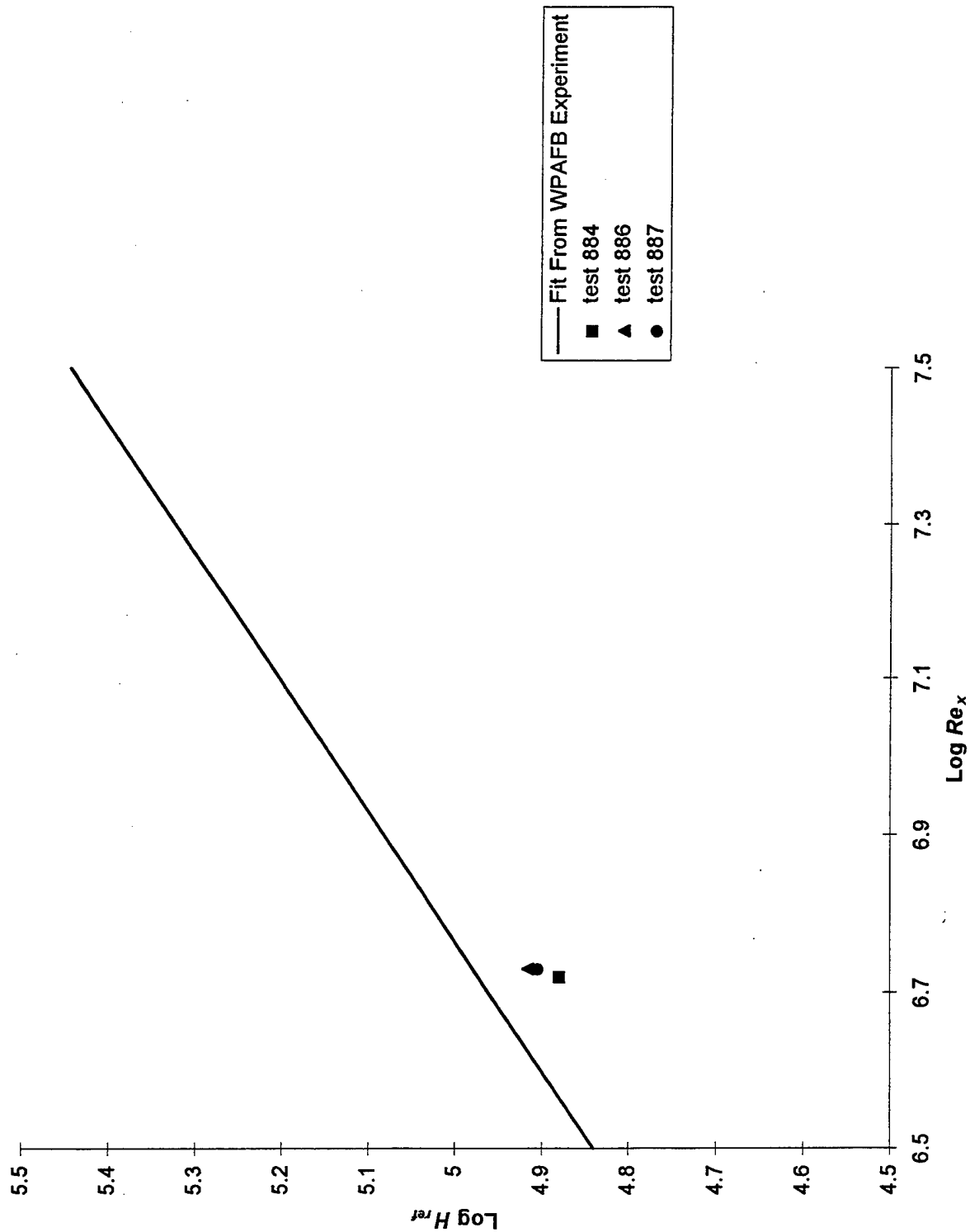


Figure 17. Comparison of Reference Heating to the Reference Heating in the Experiment at WPAFB

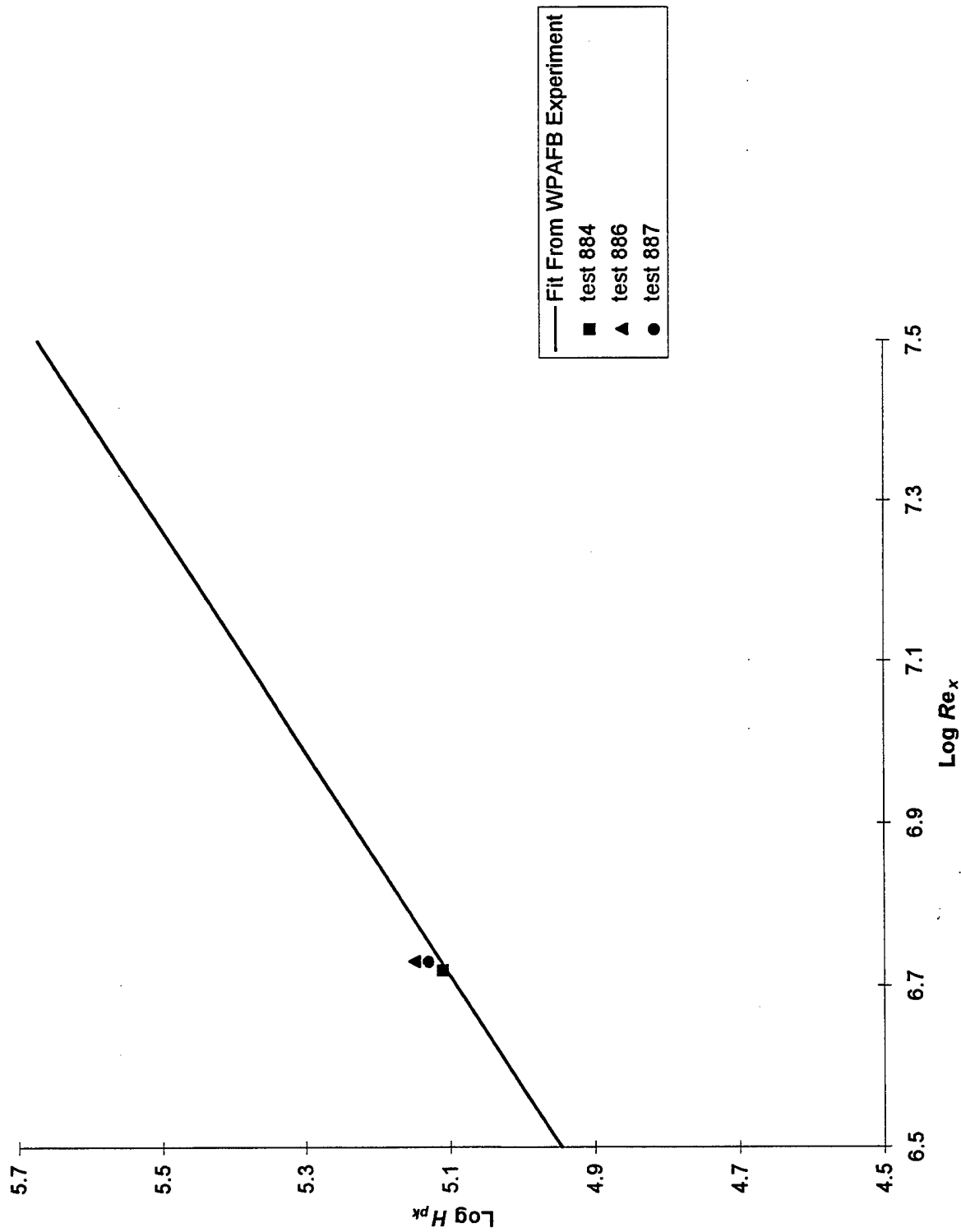


Figure 18. Comparison of Peak Heating in the Shock Interaction Region to the Peak Heating in the Experiment at WPAFB (No Fuel)

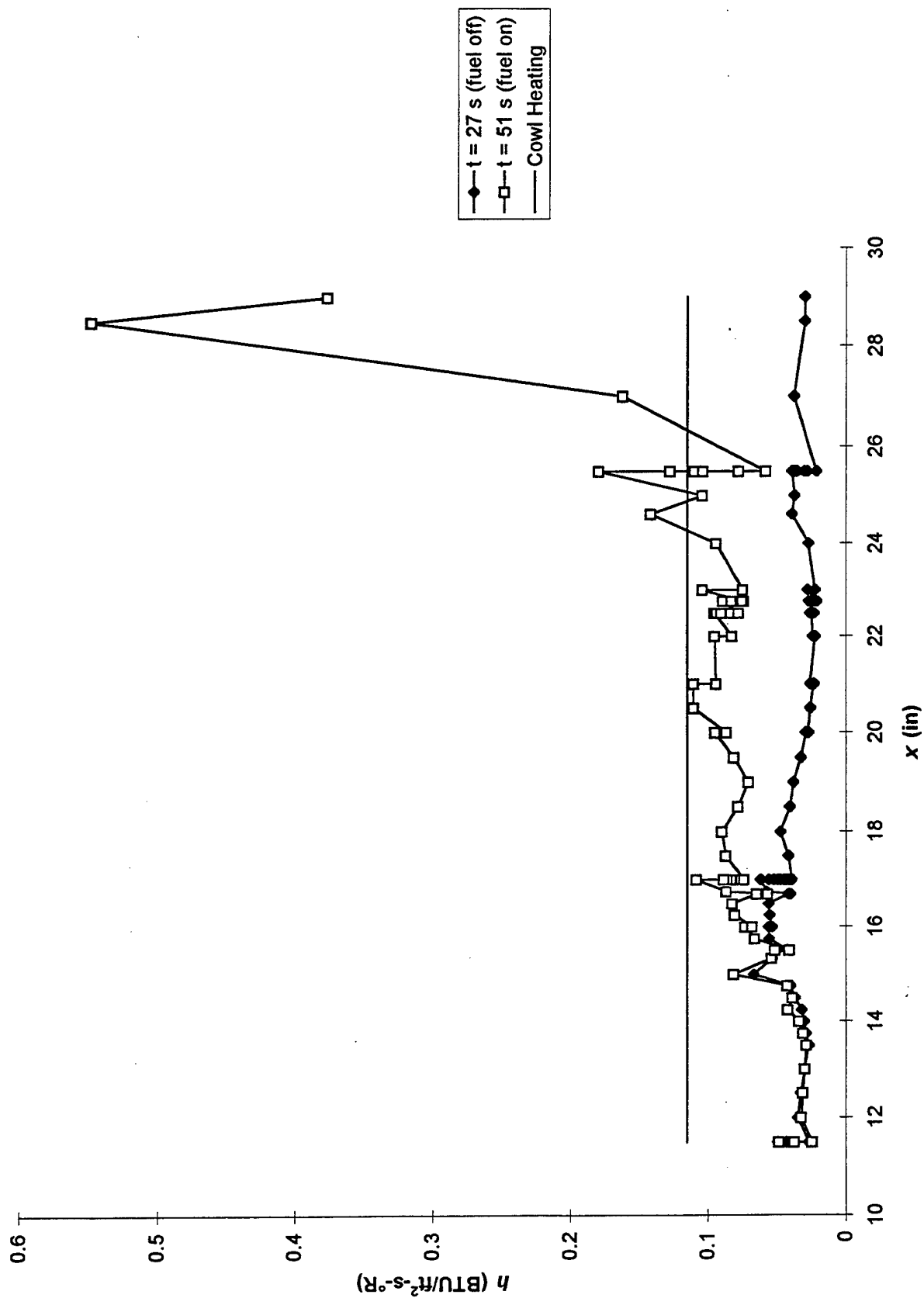


Figure 19. Film Coefficient Along the Bottom Wall in Test 884

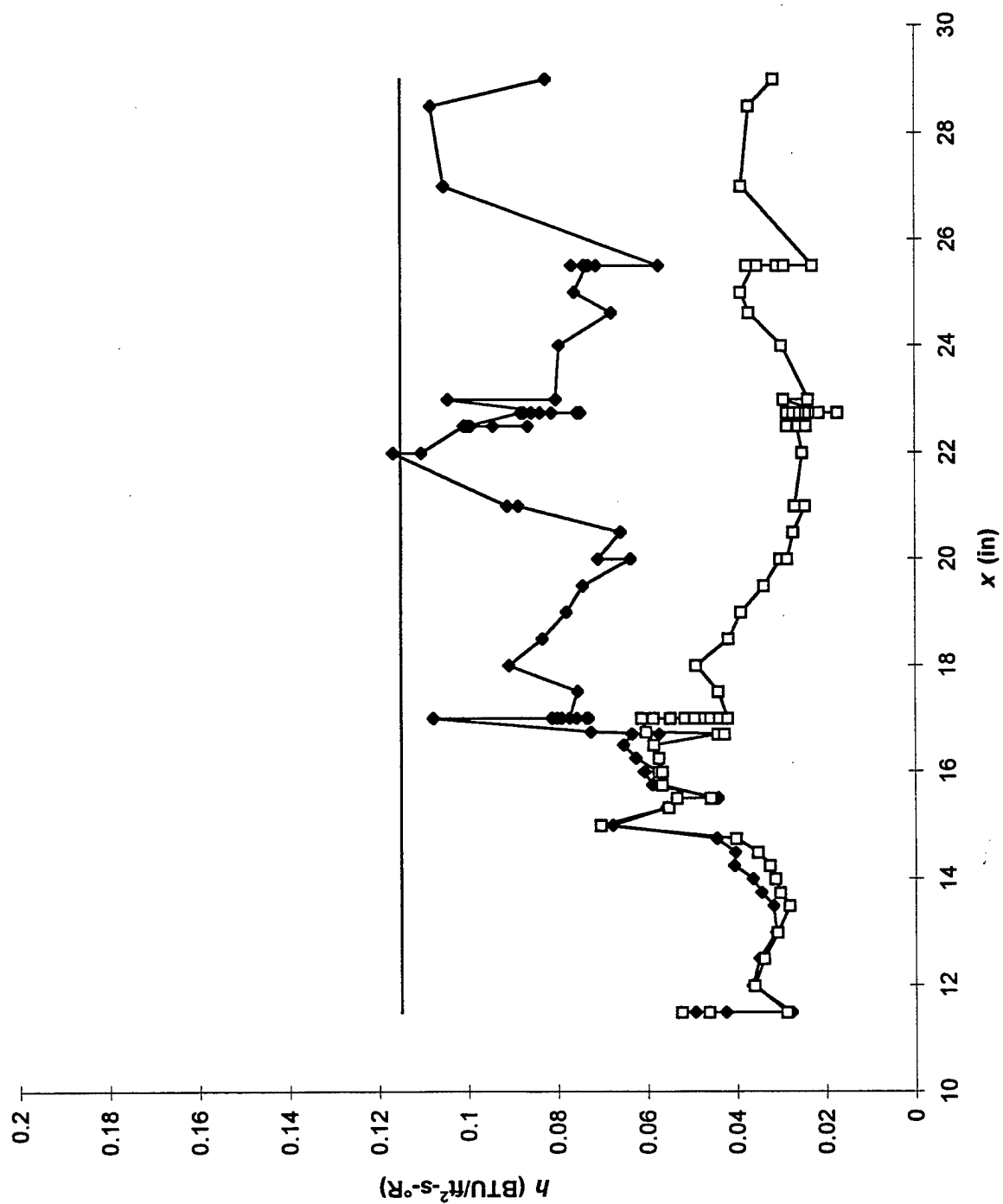


Figure 20. Film Coefficient Along the Bottom Wall in Test 886

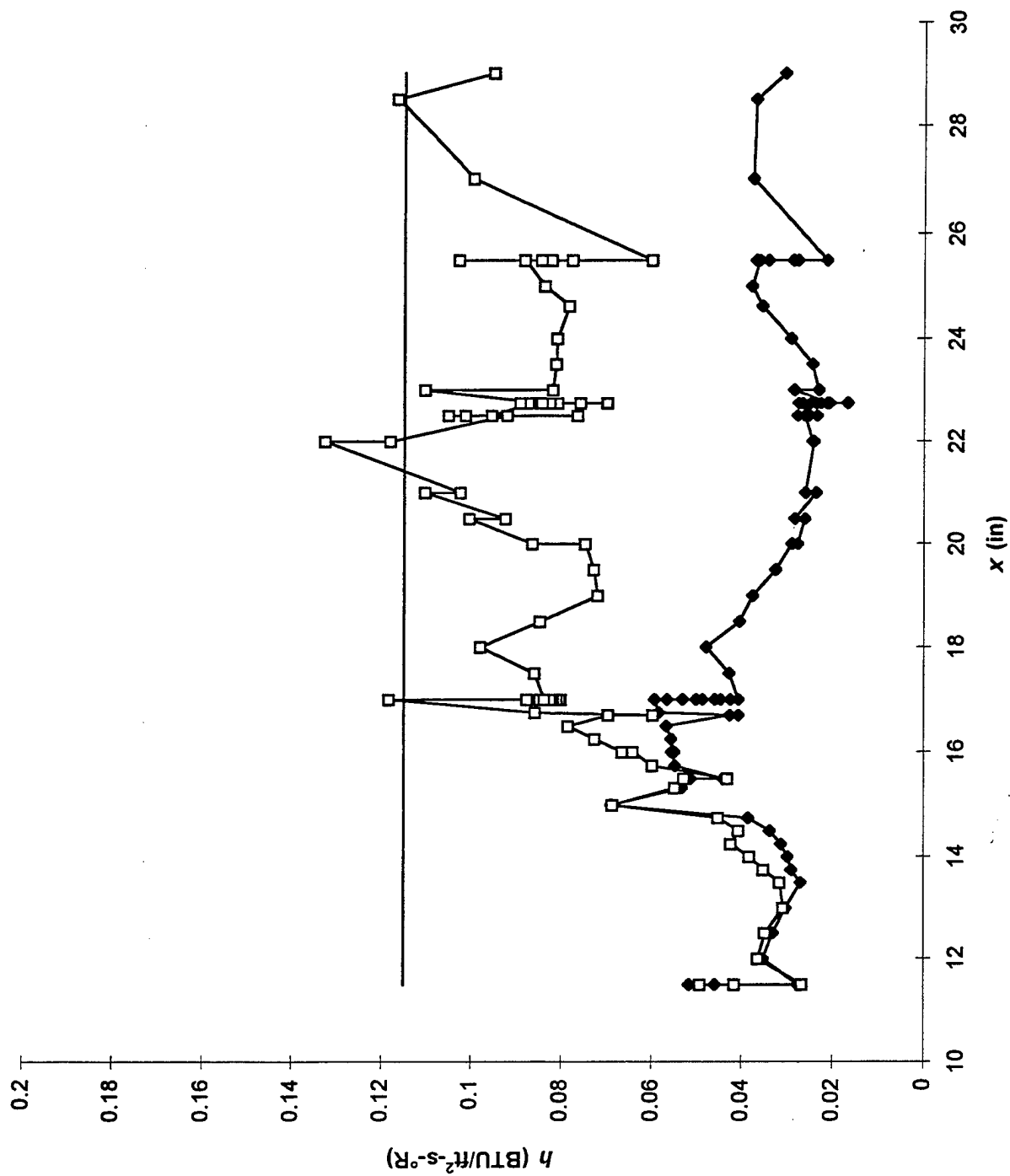


Figure 21. Film Coefficient Along the Bottom Wall in Test 887

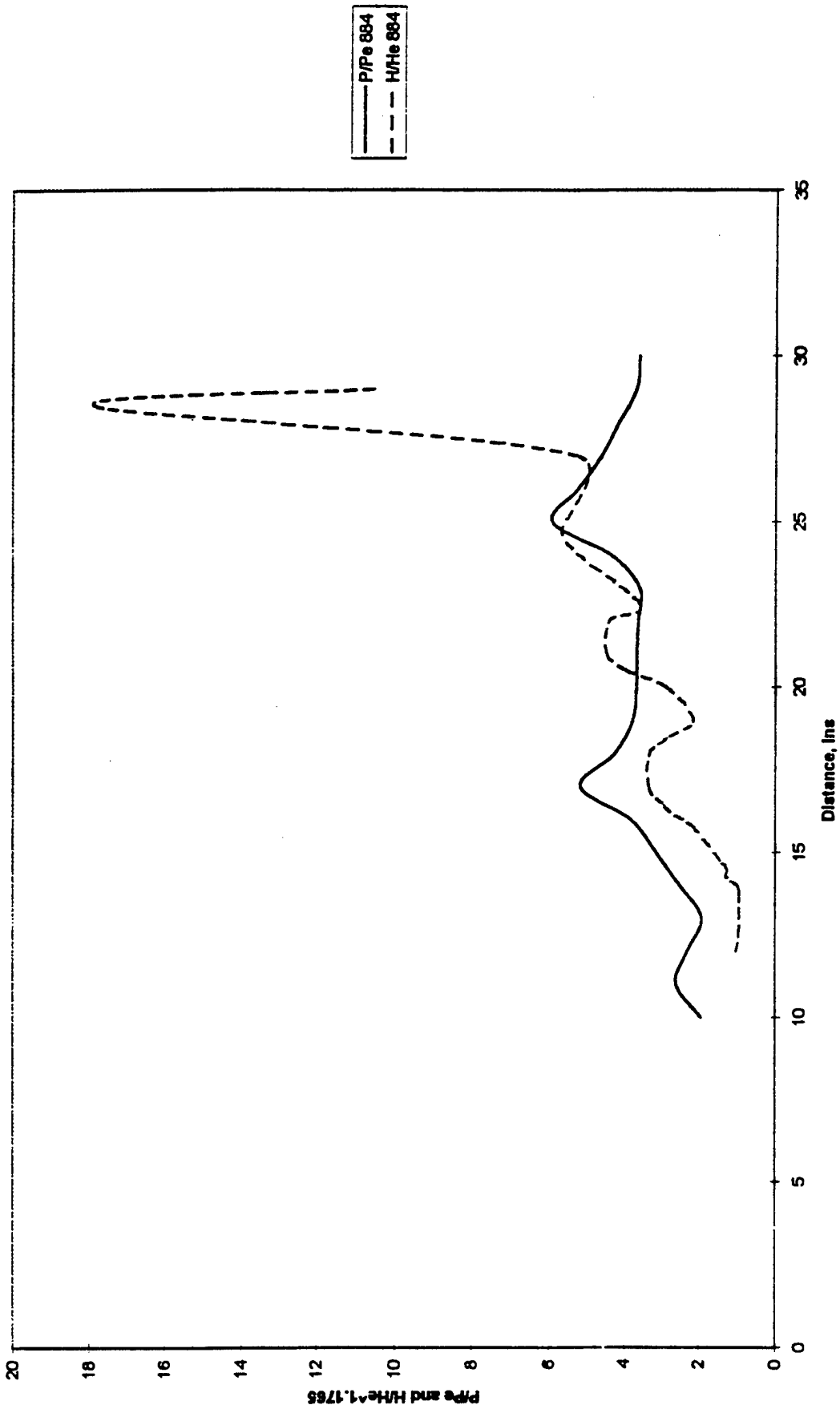


Figure 22. Pressure and Film Coefficient Ratios Along the Centerline in Test 884

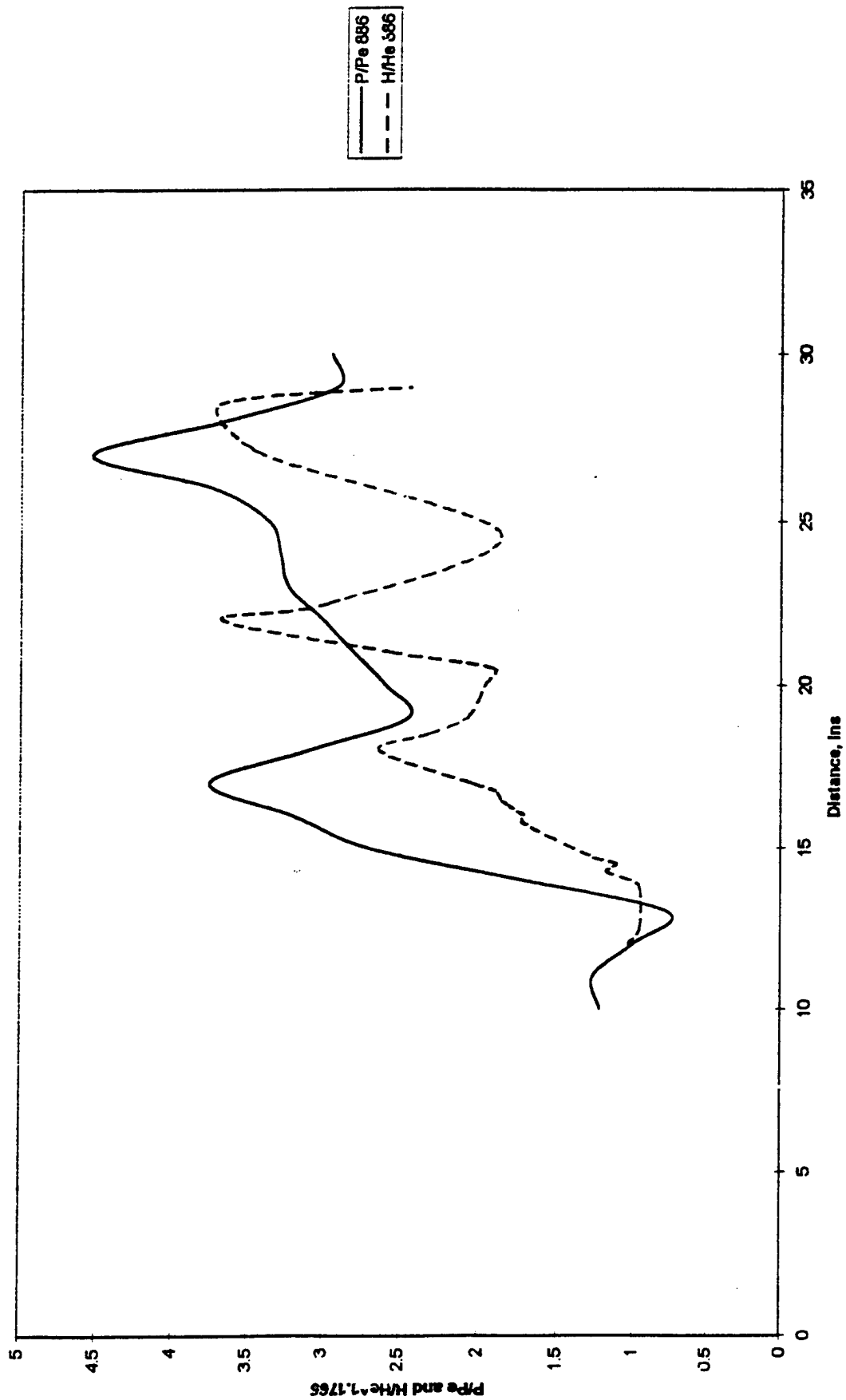


Figure 23. Pressure and Film Coefficient Ratios Along the Centerline in Test 886

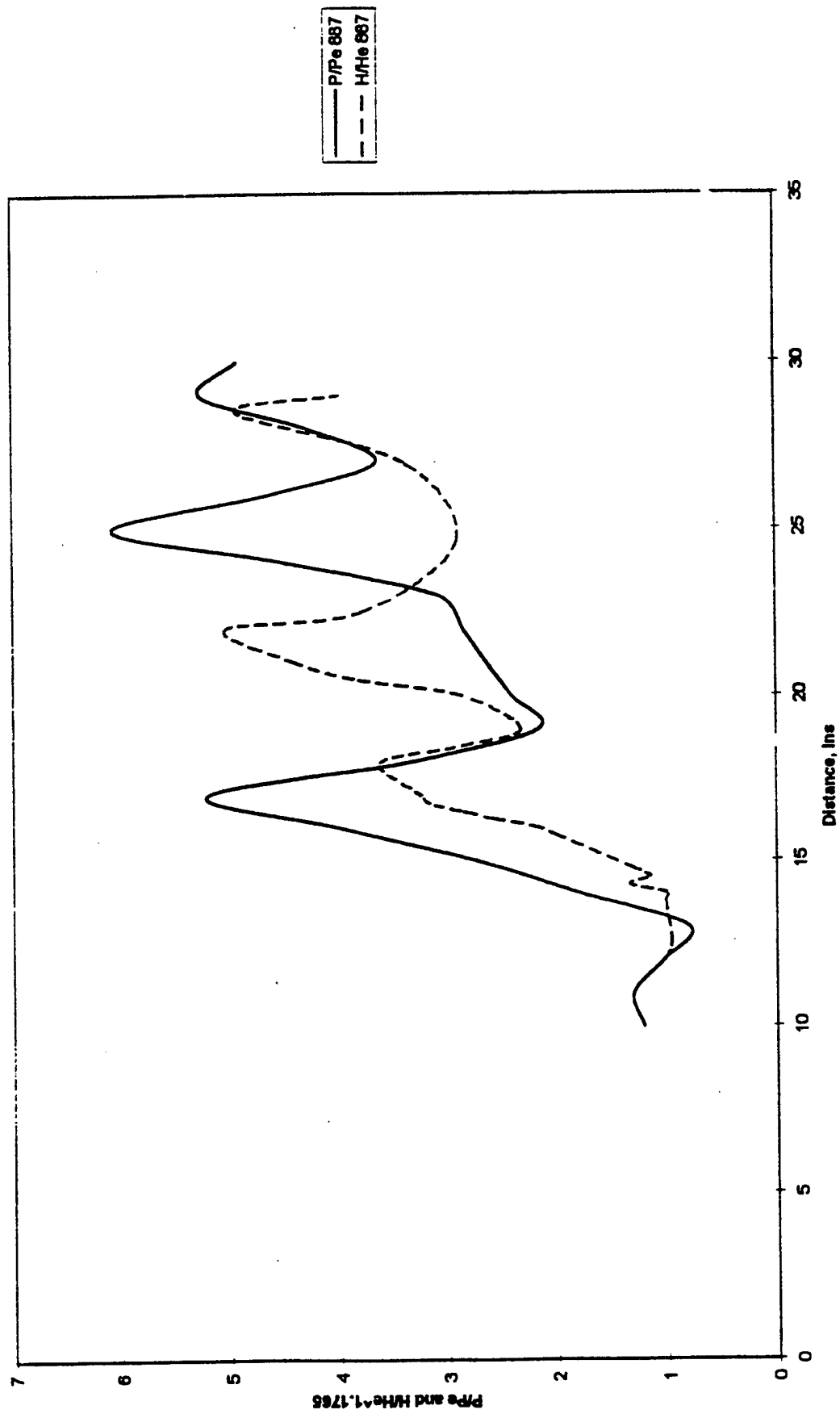


Figure 24. Pressure and Film Coefficient Ratios Along the Centerline in Test 887

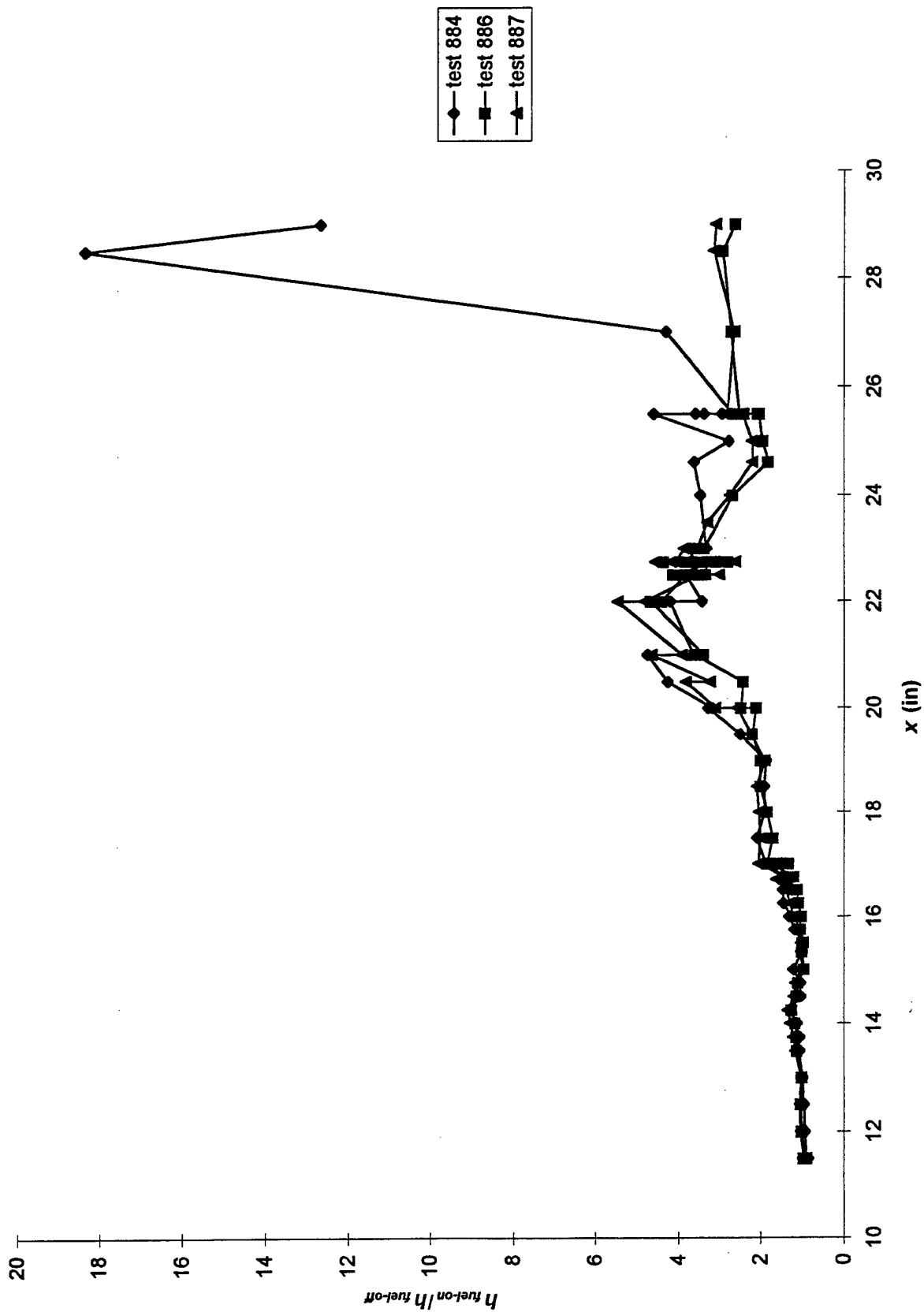


Figure 25. Ratio of $h_{fuel-on}/h_{fuel-off}$ Along the Wall Opposite the Injector

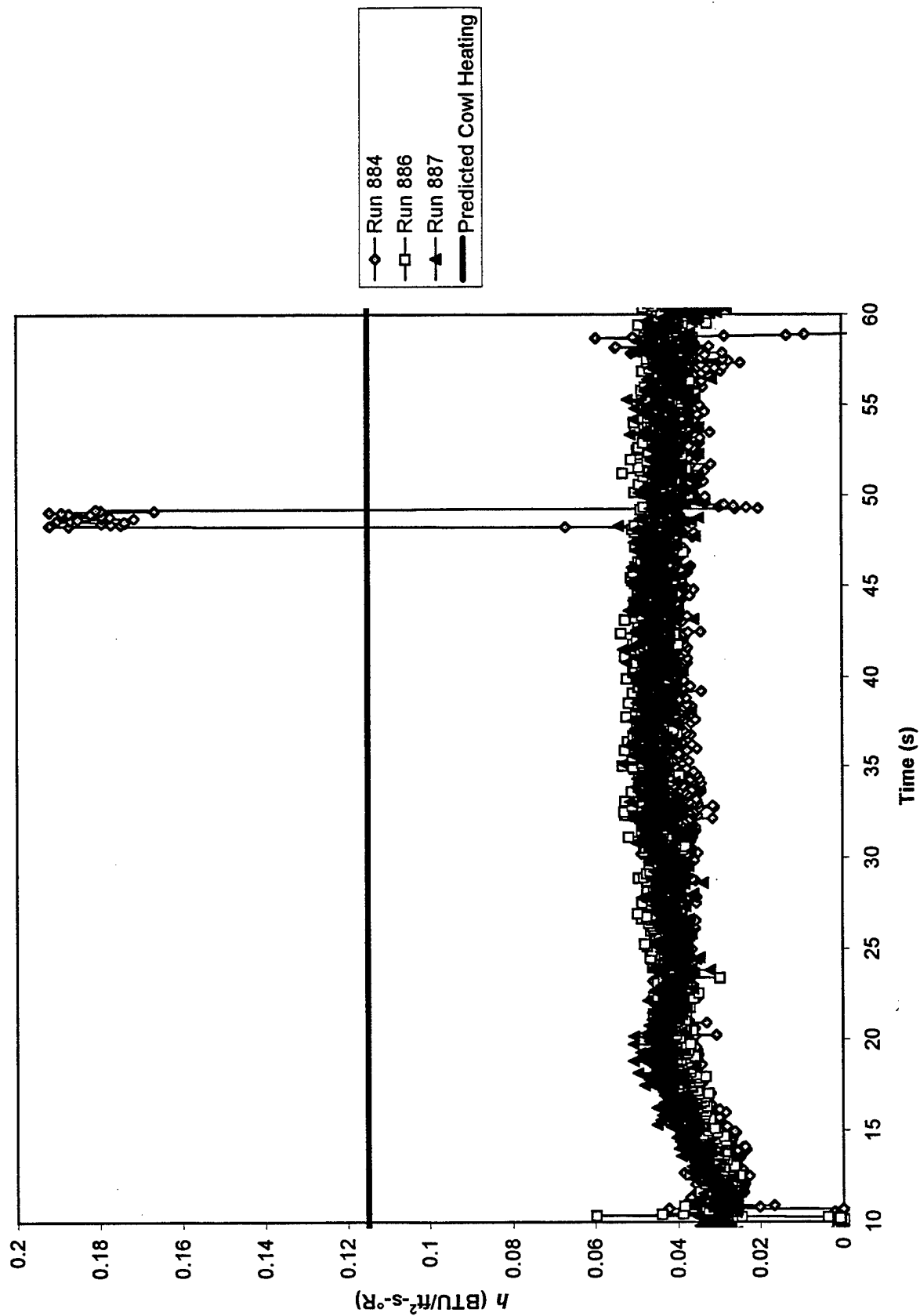


Figure 26: Film Coefficients for Gage 101 ($x = 4.05''$, $y = 0''$)

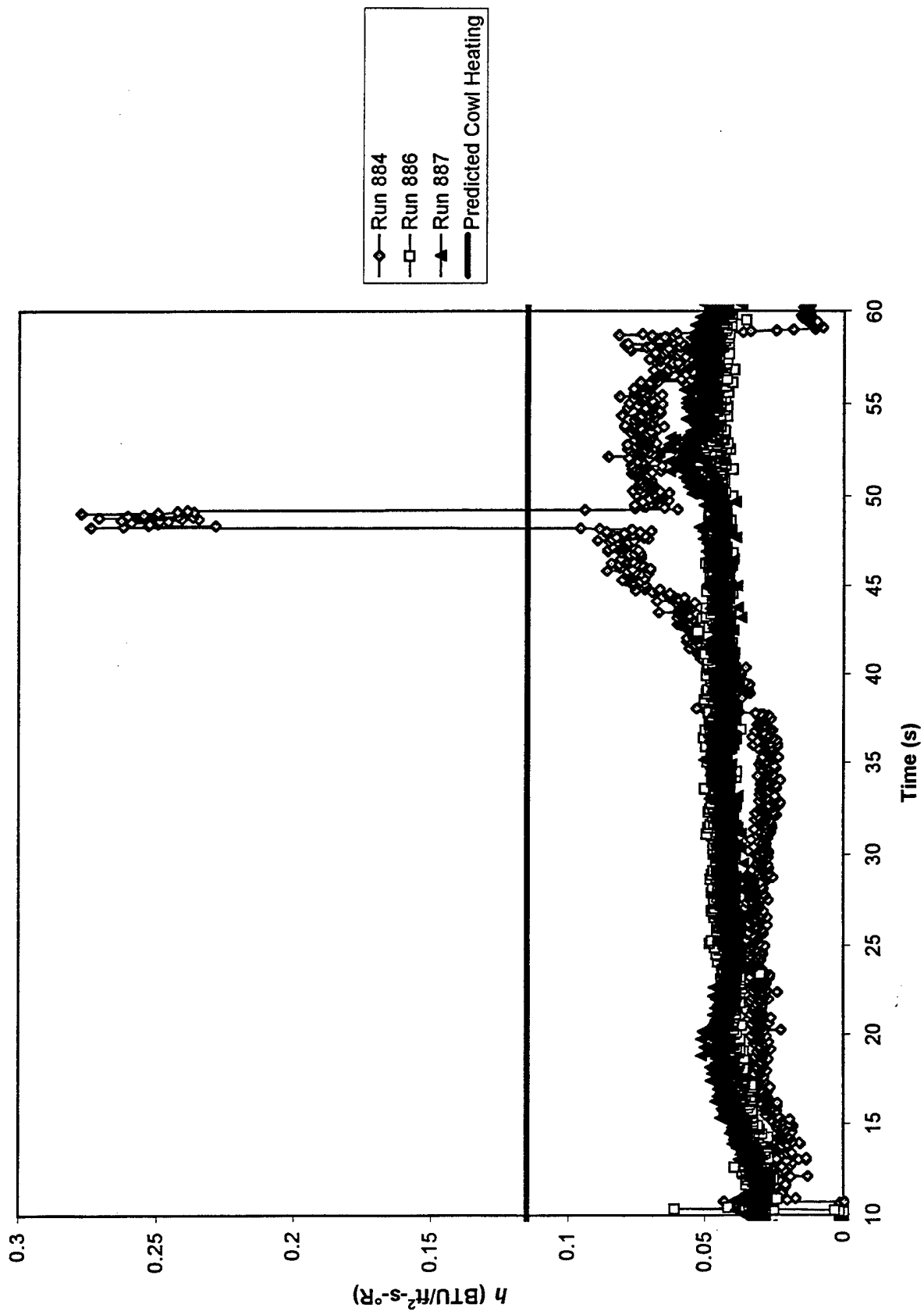


Figure 27: Film Coefficients for Gage 102 ($x = 6.09''$, $y = 0''$)

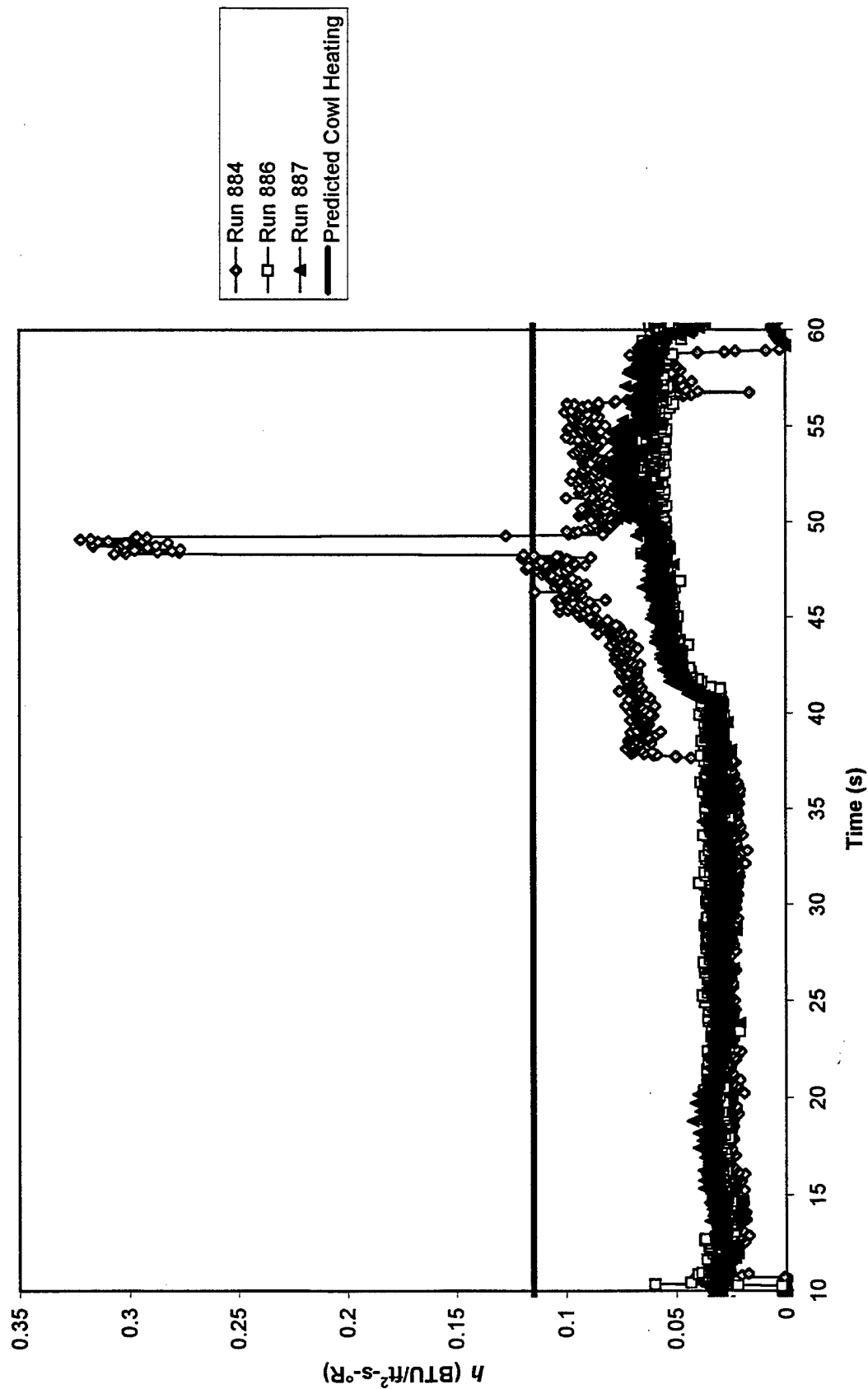


Figure 28: Film Coefficients for Gage 103 ($x = 7.25''$, $y = 0''$)

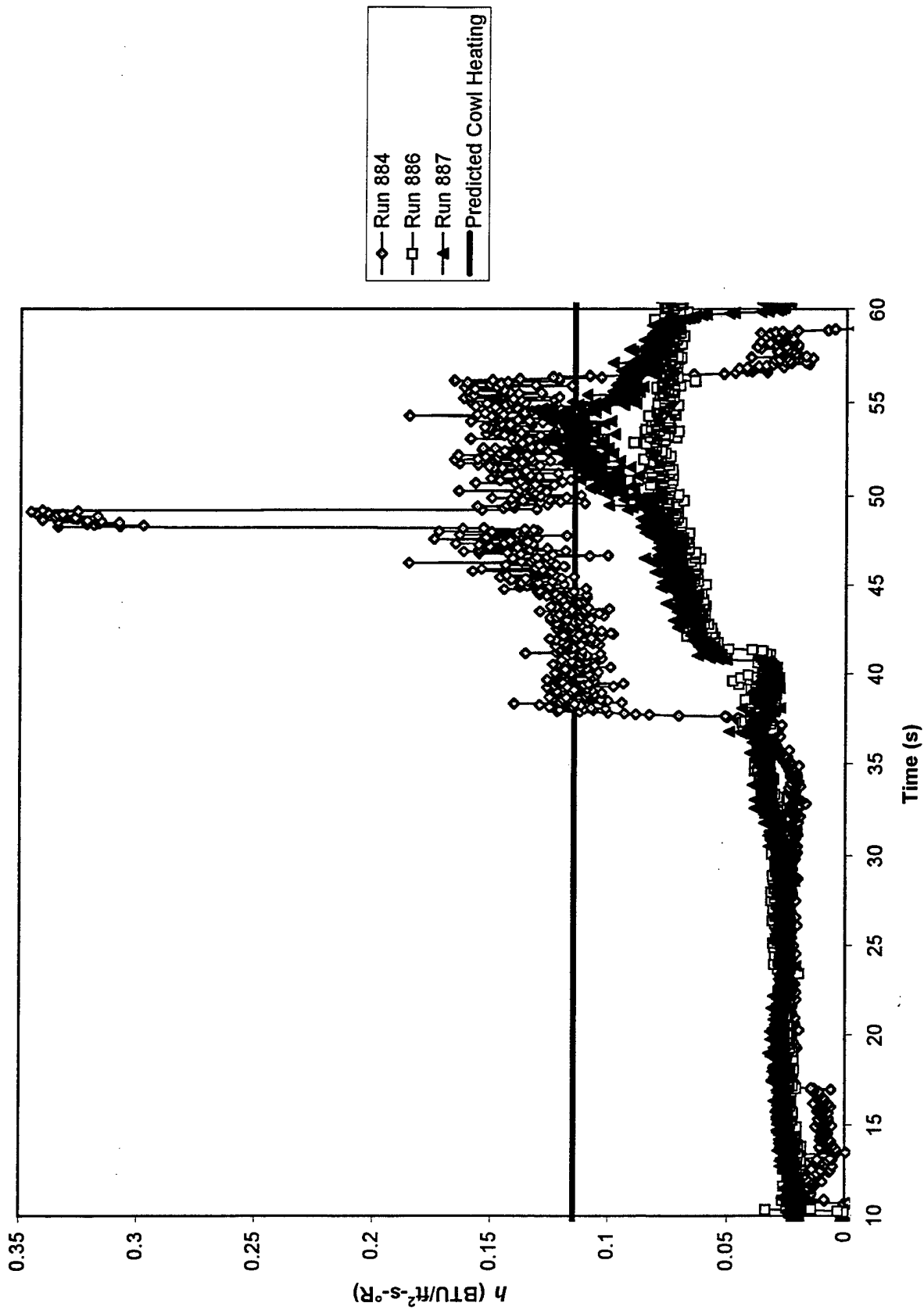


Figure 29: Film Coefficients for Gage 104 ($x = 7.5''$, $y = 0.48''$)

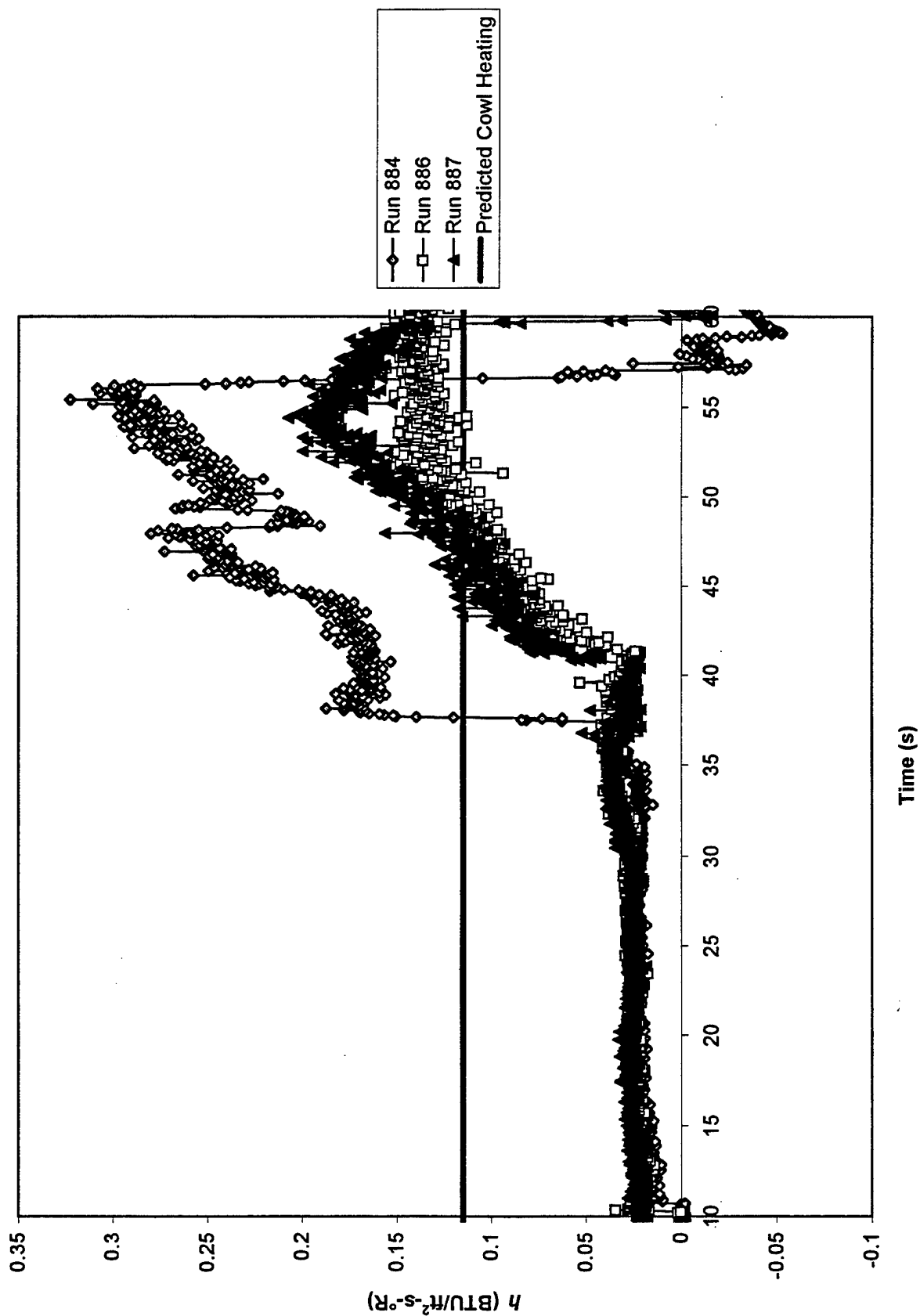


Figure 30: Film Coefficients for Gage 105 ($x = 7.5''$, $y = 1.0''$)

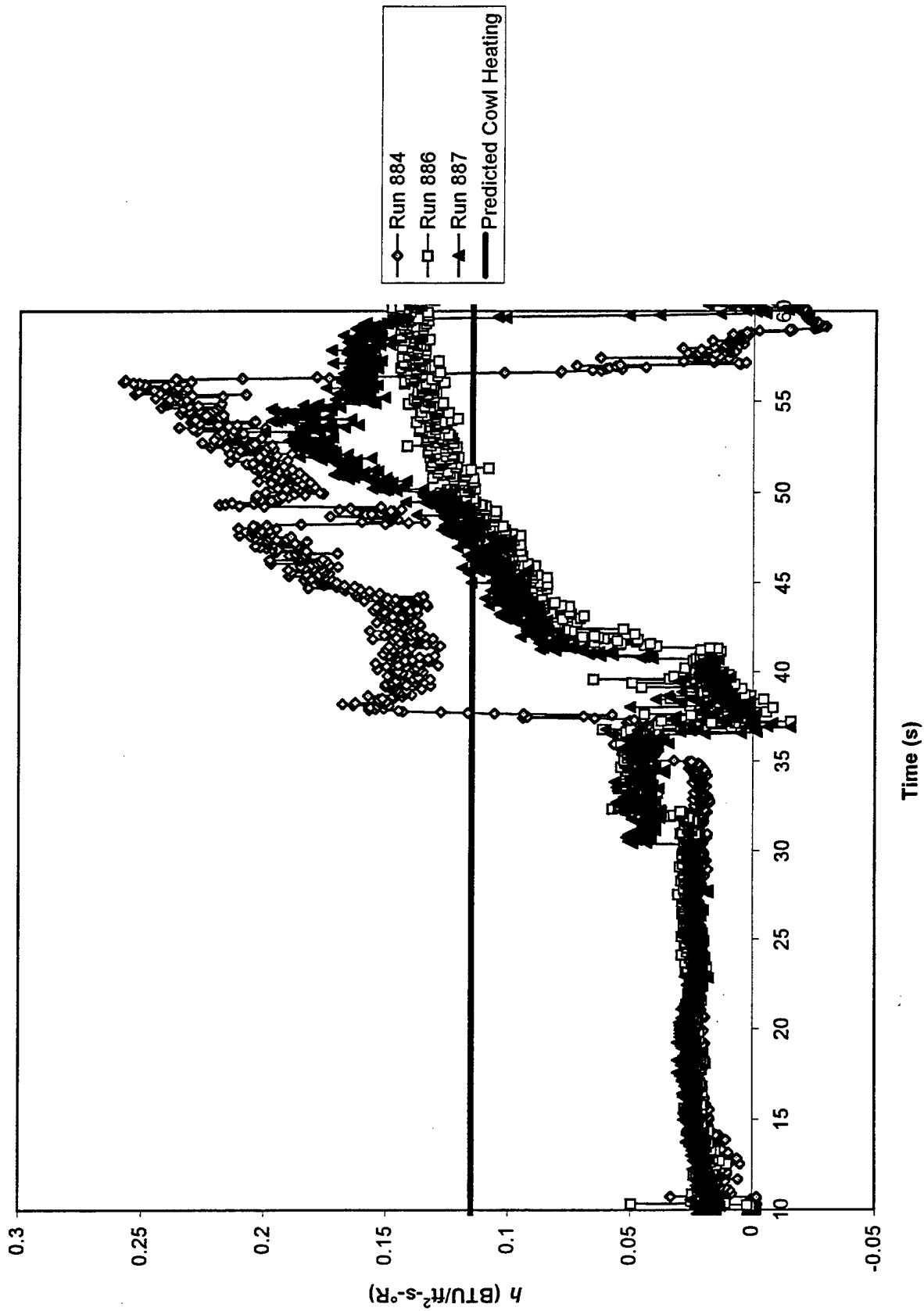


Figure 31: Film Coefficients for Gage 106 ($x = 7.5''$, $y = 1.83''$)

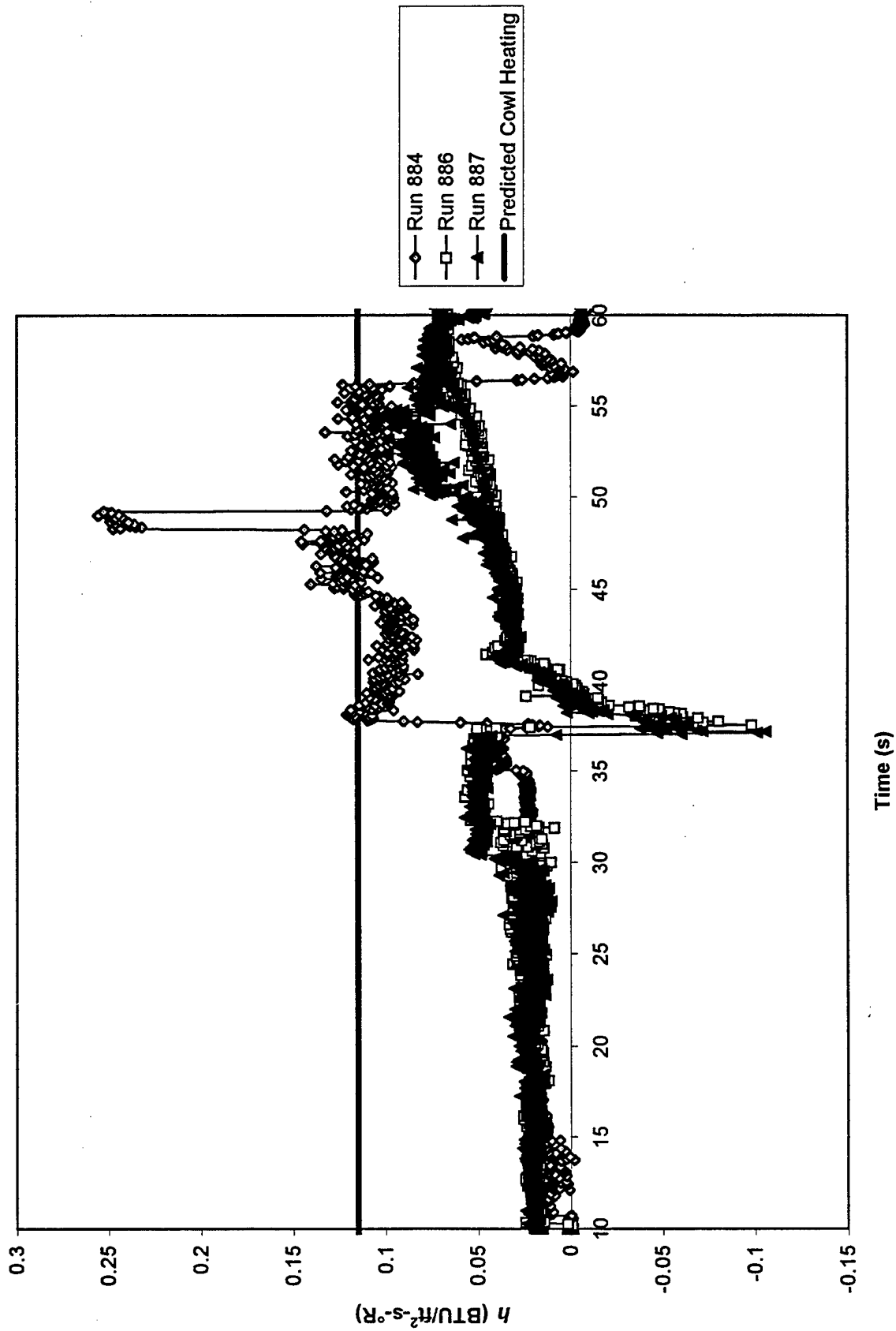


Figure 32: Film Coefficients for Gage 108 ($x = 8.65''$, $y = 0.43''$)

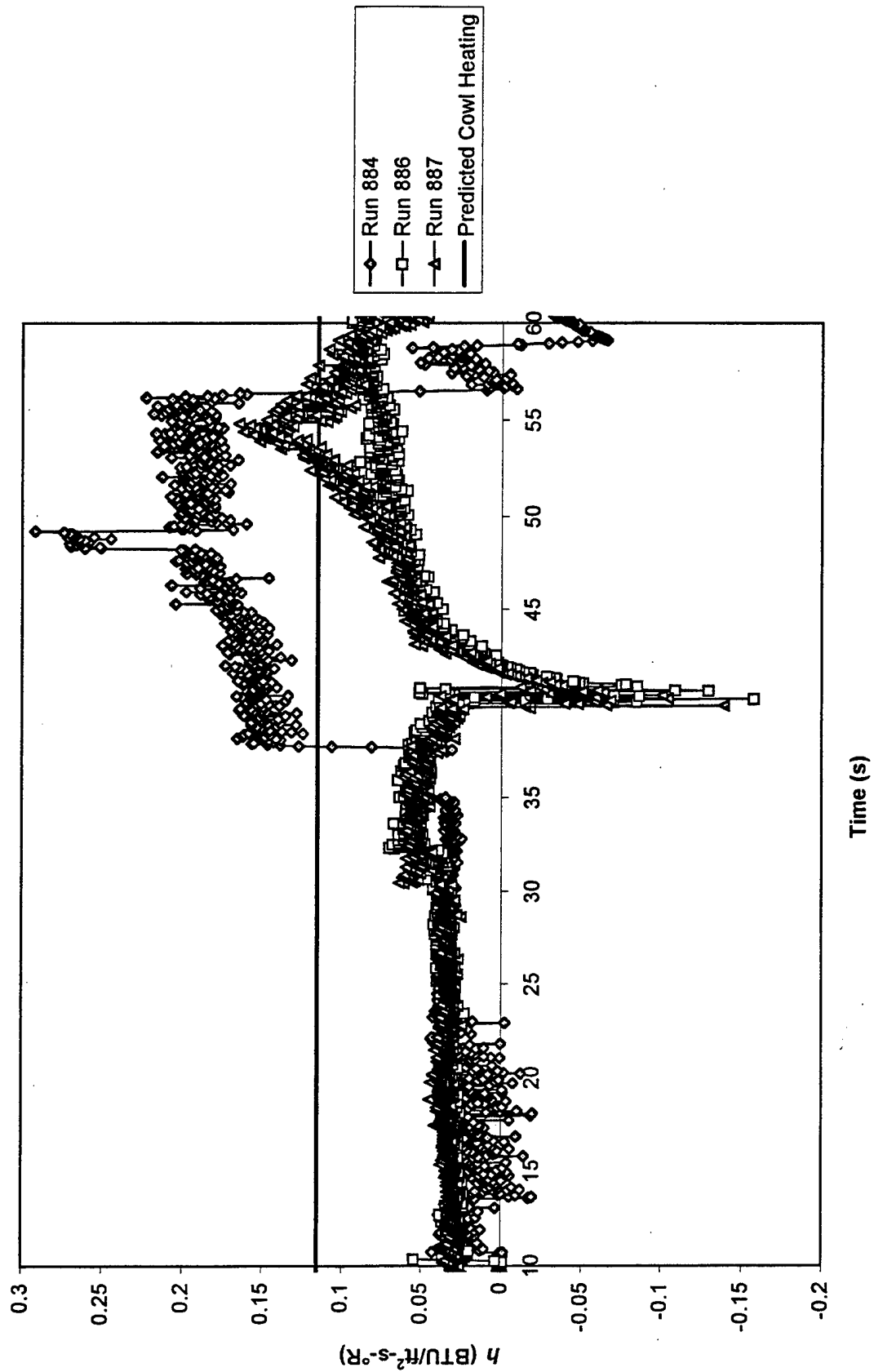


Figure 33: Film Coefficients for Gage 109 ($x = 8.65''$, $y = 0.69''$)

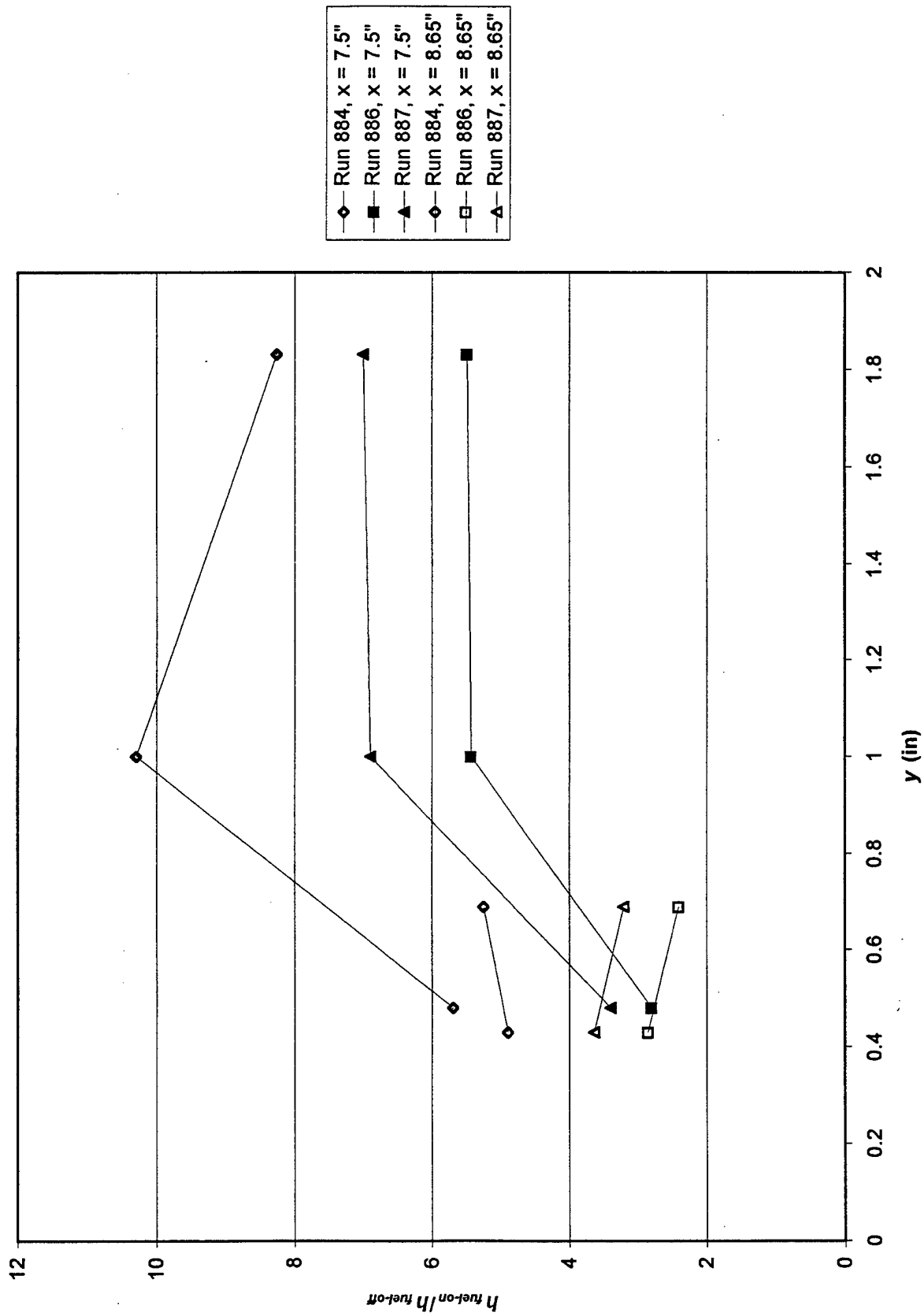


Figure 34: Lateral Distribution of the Heat Flux Augmentation Ratio $h_{fuel-on}/h_{fuel-off}$ Downstream of the Injectors

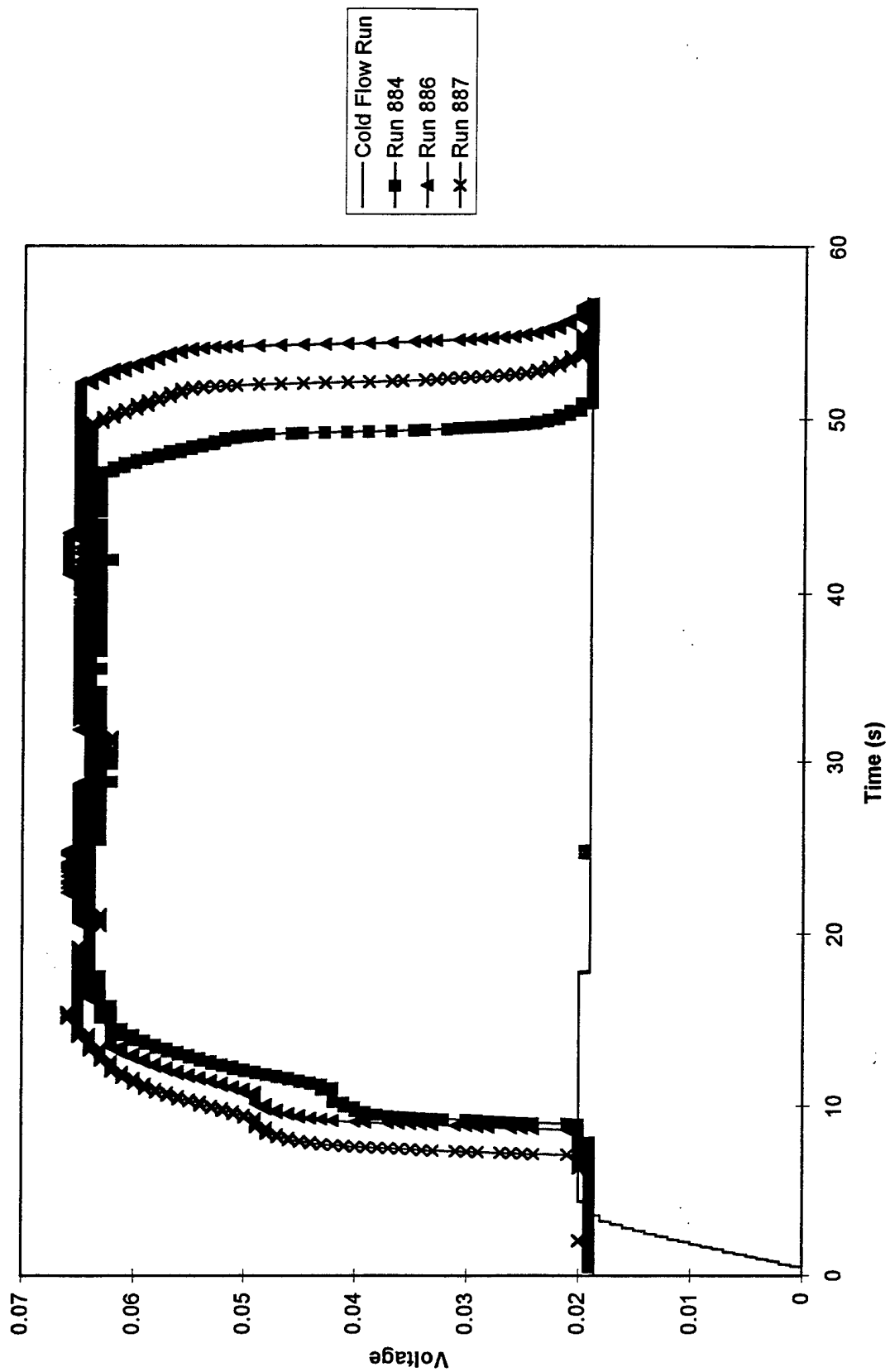


Figure 35. Voltage from the Vitiated Heater Total Pressure Transducer

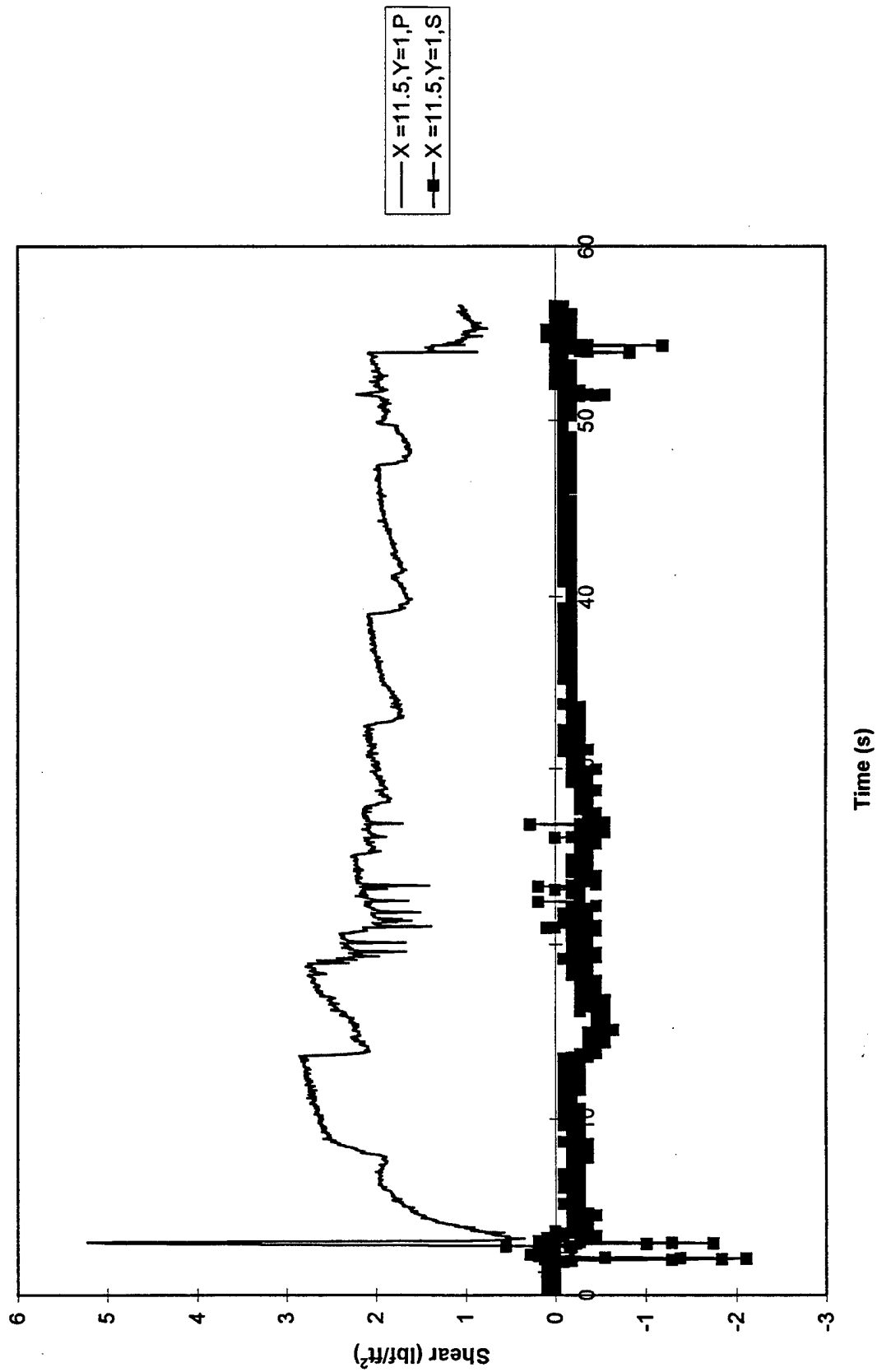


Figure 36. Skin Friction at $x = 11.5"$, $y = 1"$ During the Cold Flow Test

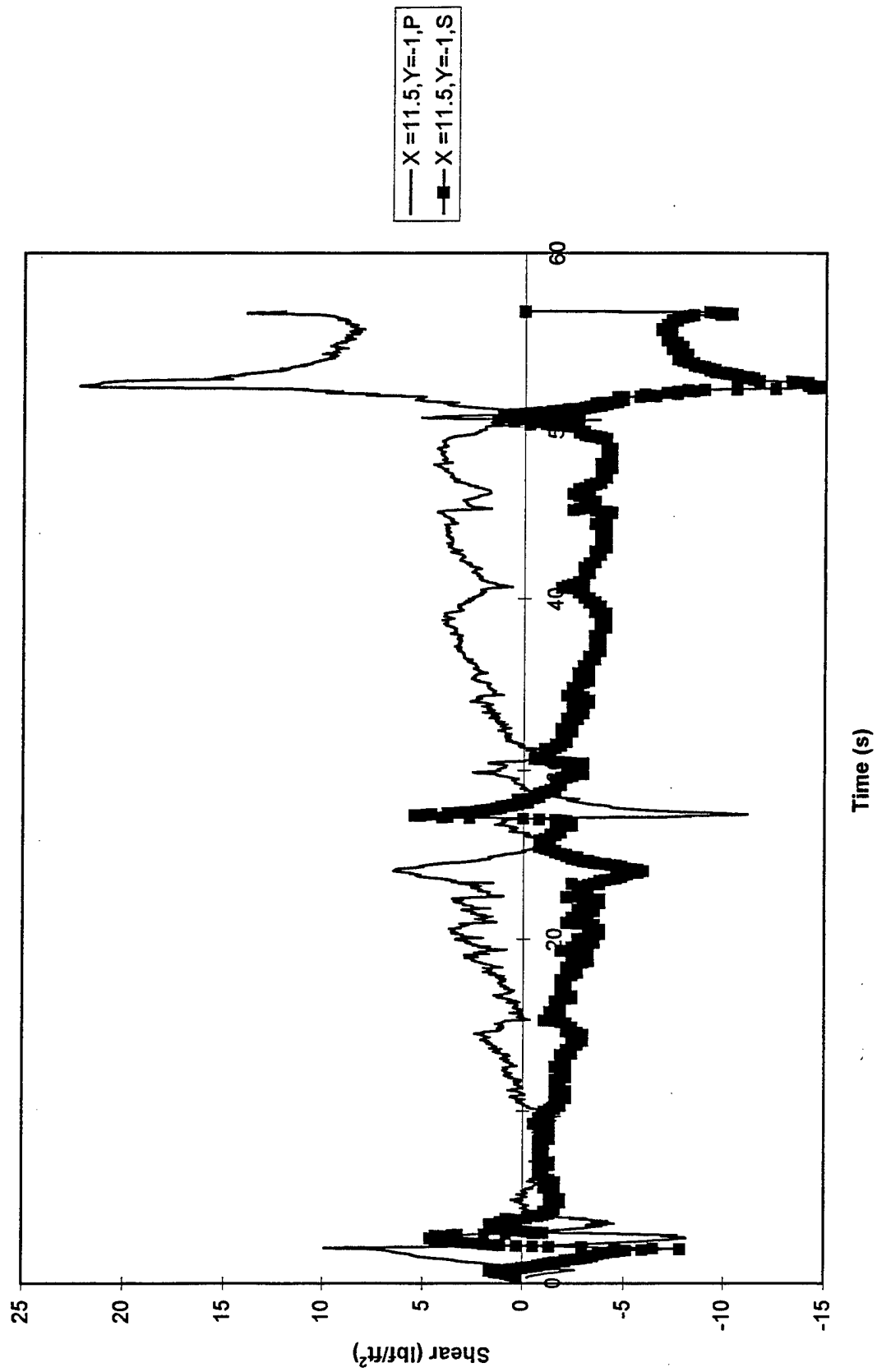


Figure 37. Skin Friction at $x = 11.5"$, $y = -1"$ During the Cold Flow Test

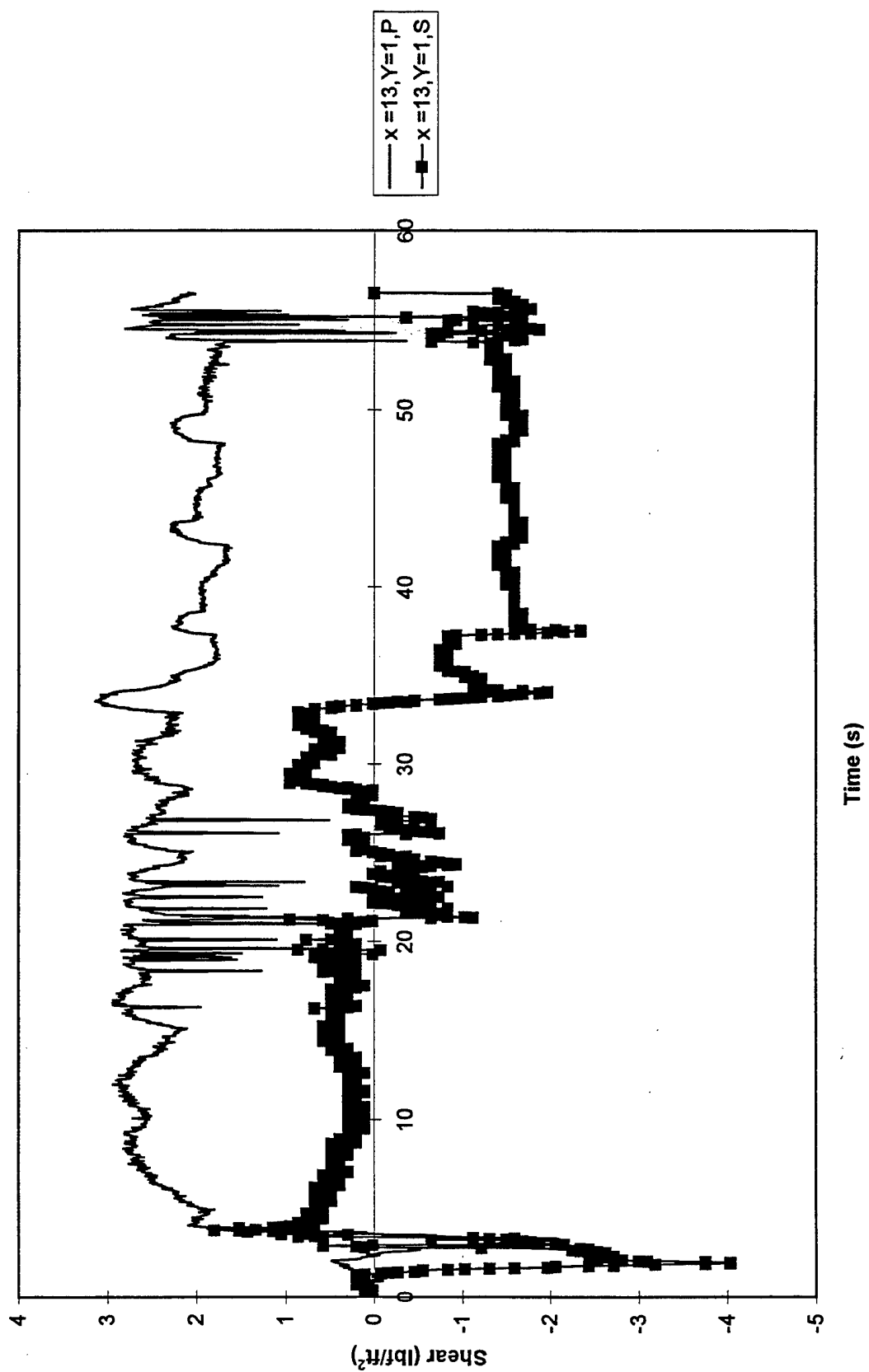


Figure 38. Skin Friction at $x = 13''$, $y = 1''$ During the Cold Flow Test

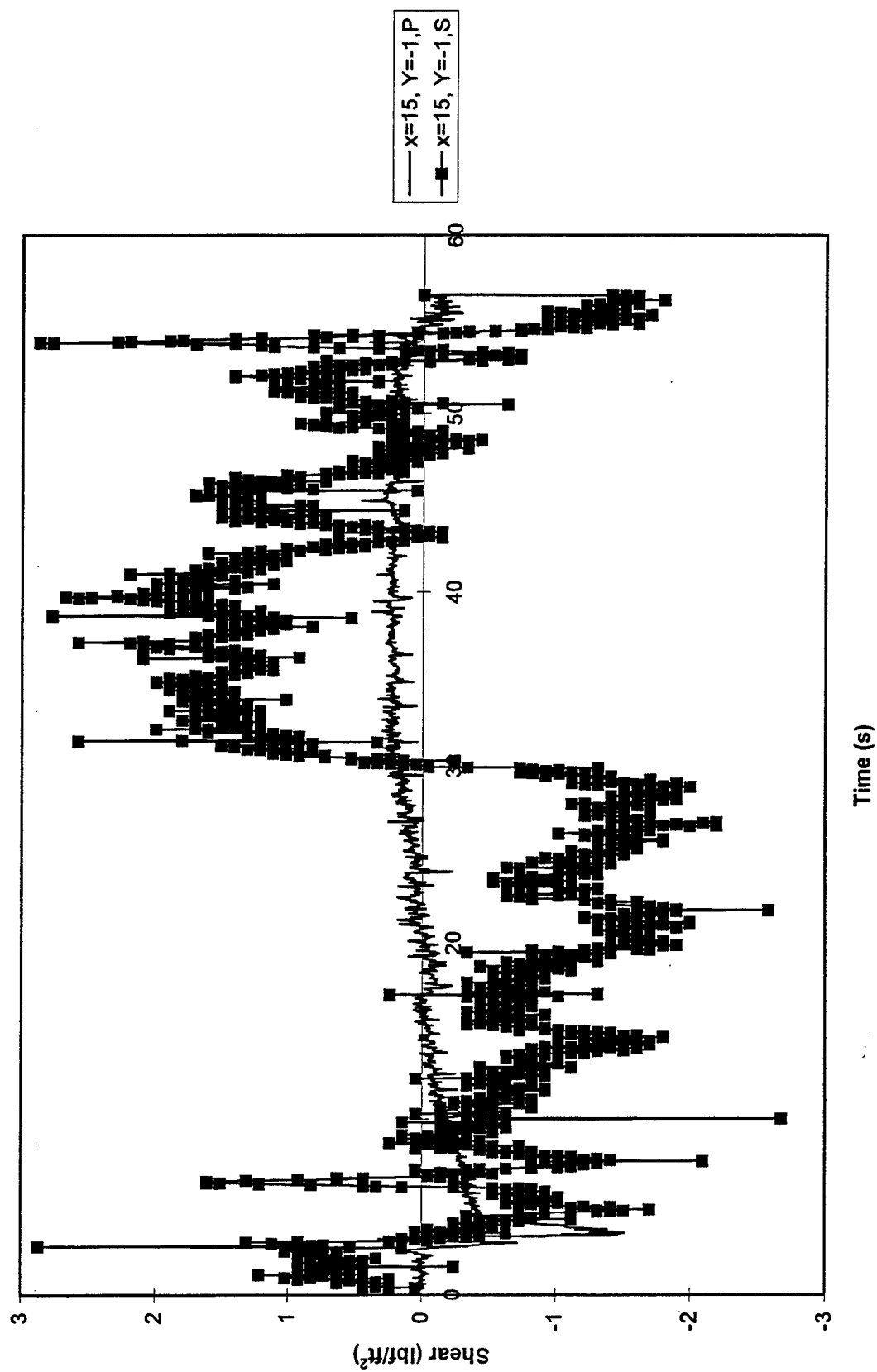


Figure 39. Skin Friction at $x = 15''$, $y = -1''$ During the Cold Flow Test

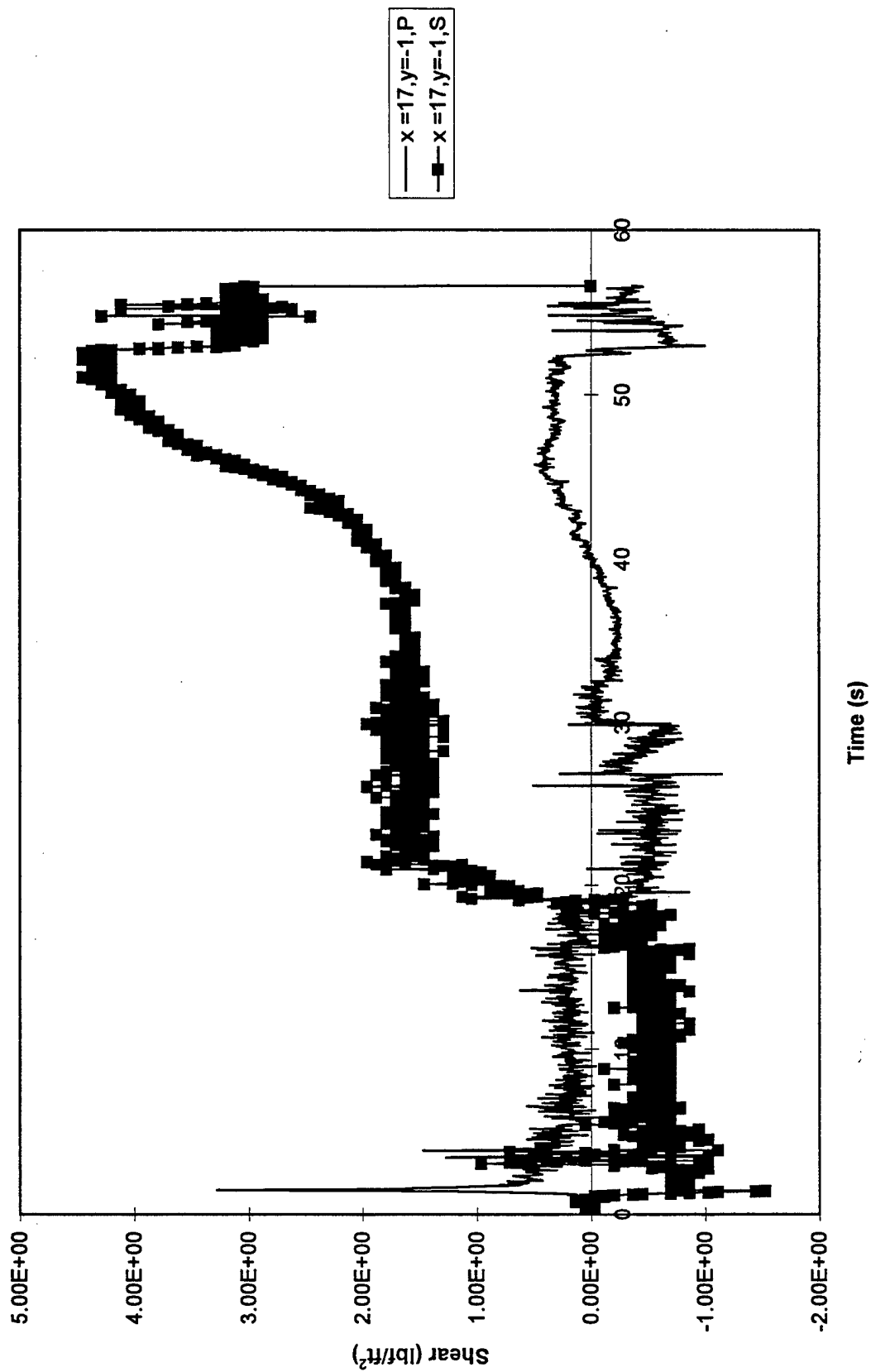


Figure 40. Skin Friction at $x = 17''$, $y = -1''$ During the Cold Flow Test

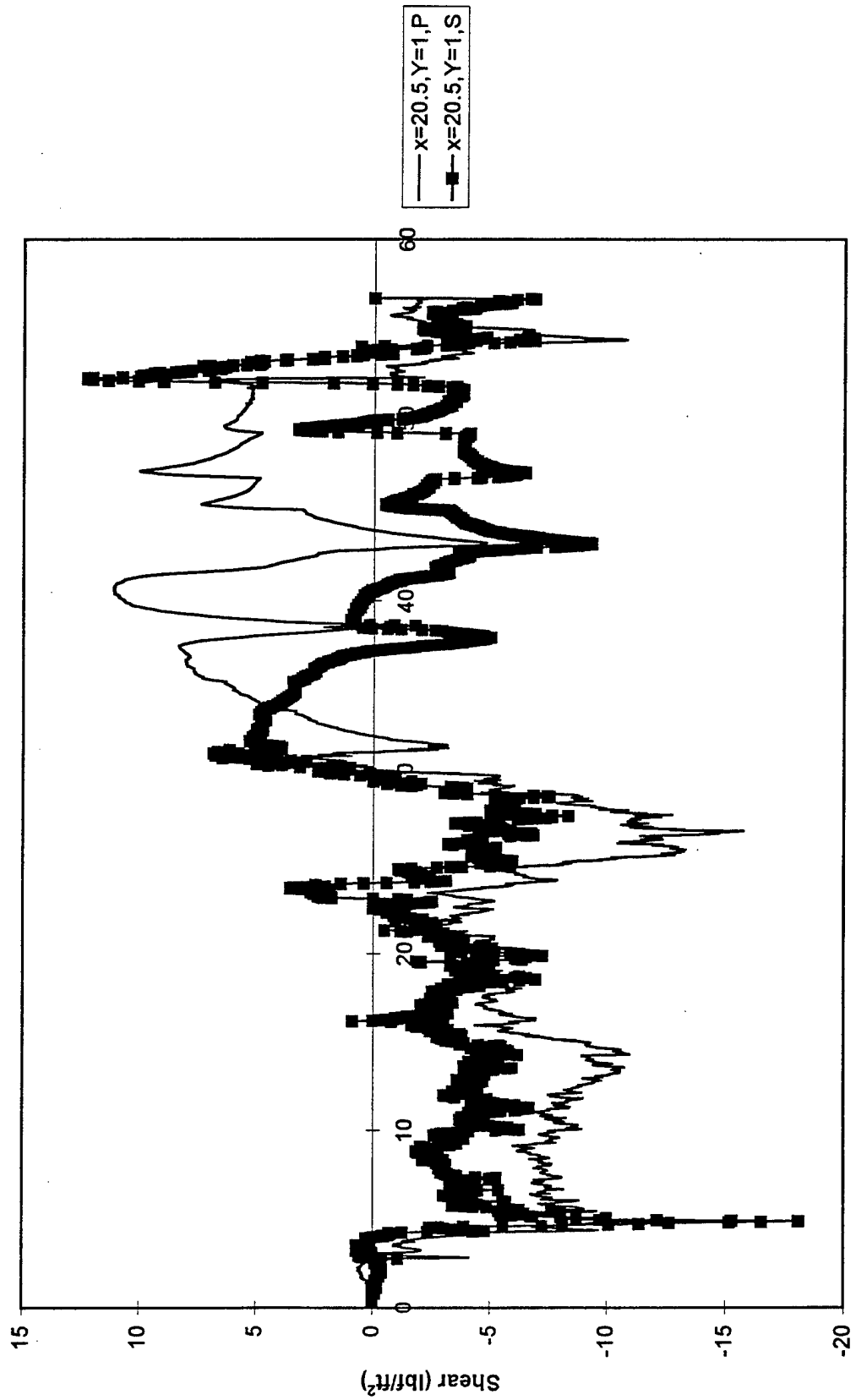


Figure 41. Skin Friction at $x = 20.5''$, $y = 1''$ During the Cold Flow Test

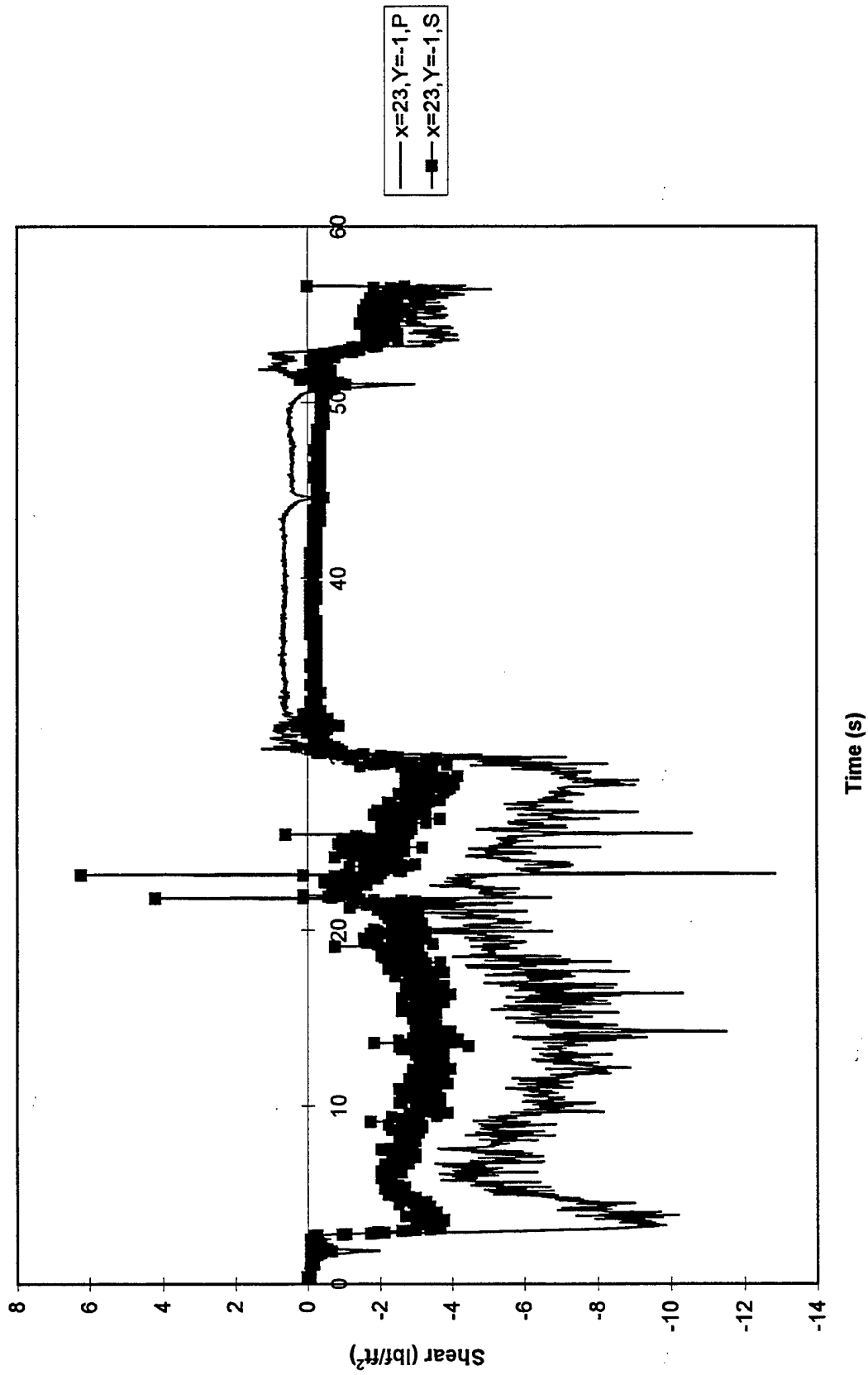


Figure 42. Skin Friction at $x = 23"$, $y = -1"$ During the Cold Flow Test

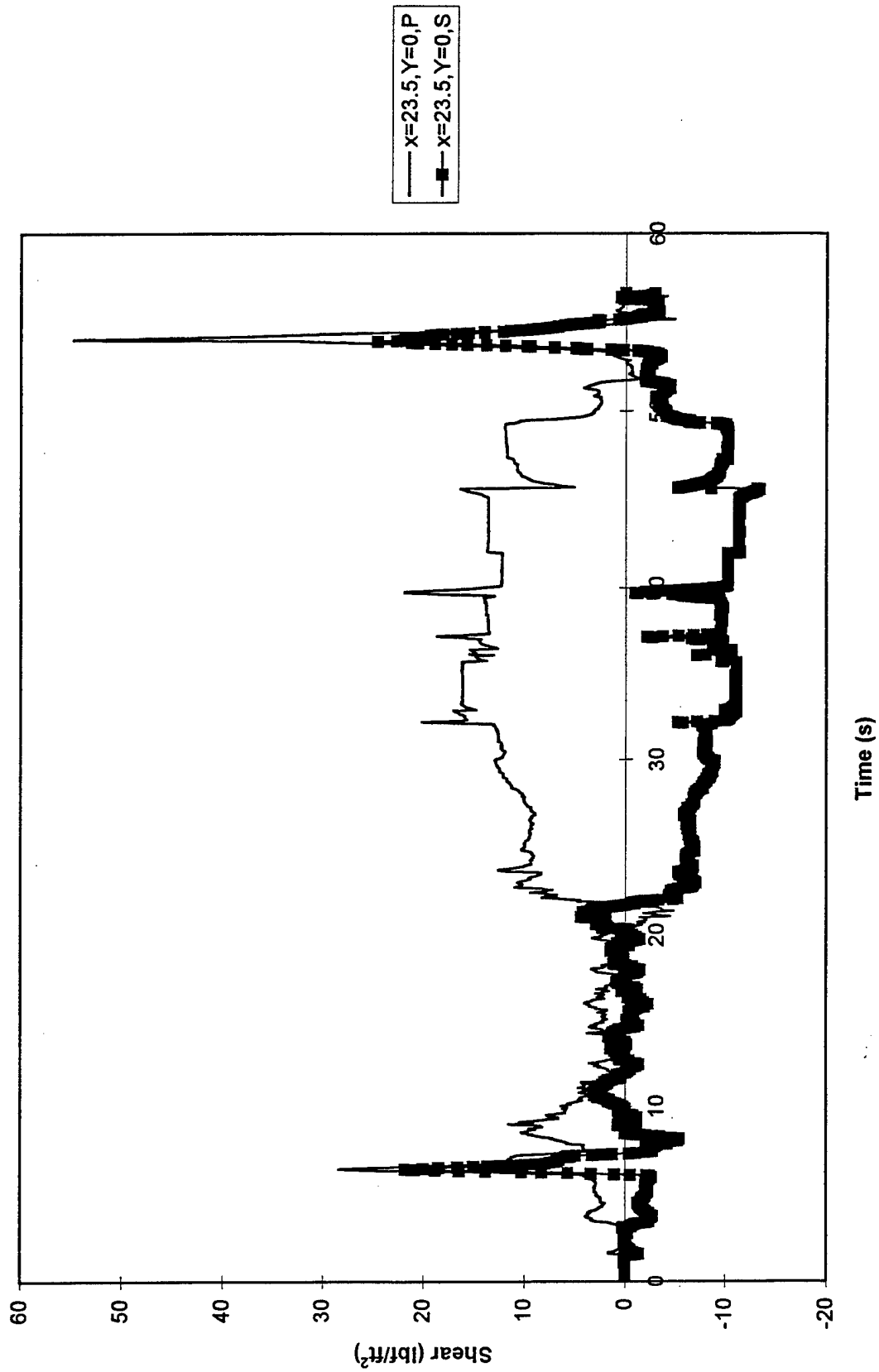


Figure 43. Skin Friction at $x = 23.5''$, $y = 0''$ During the Cold Flow Test

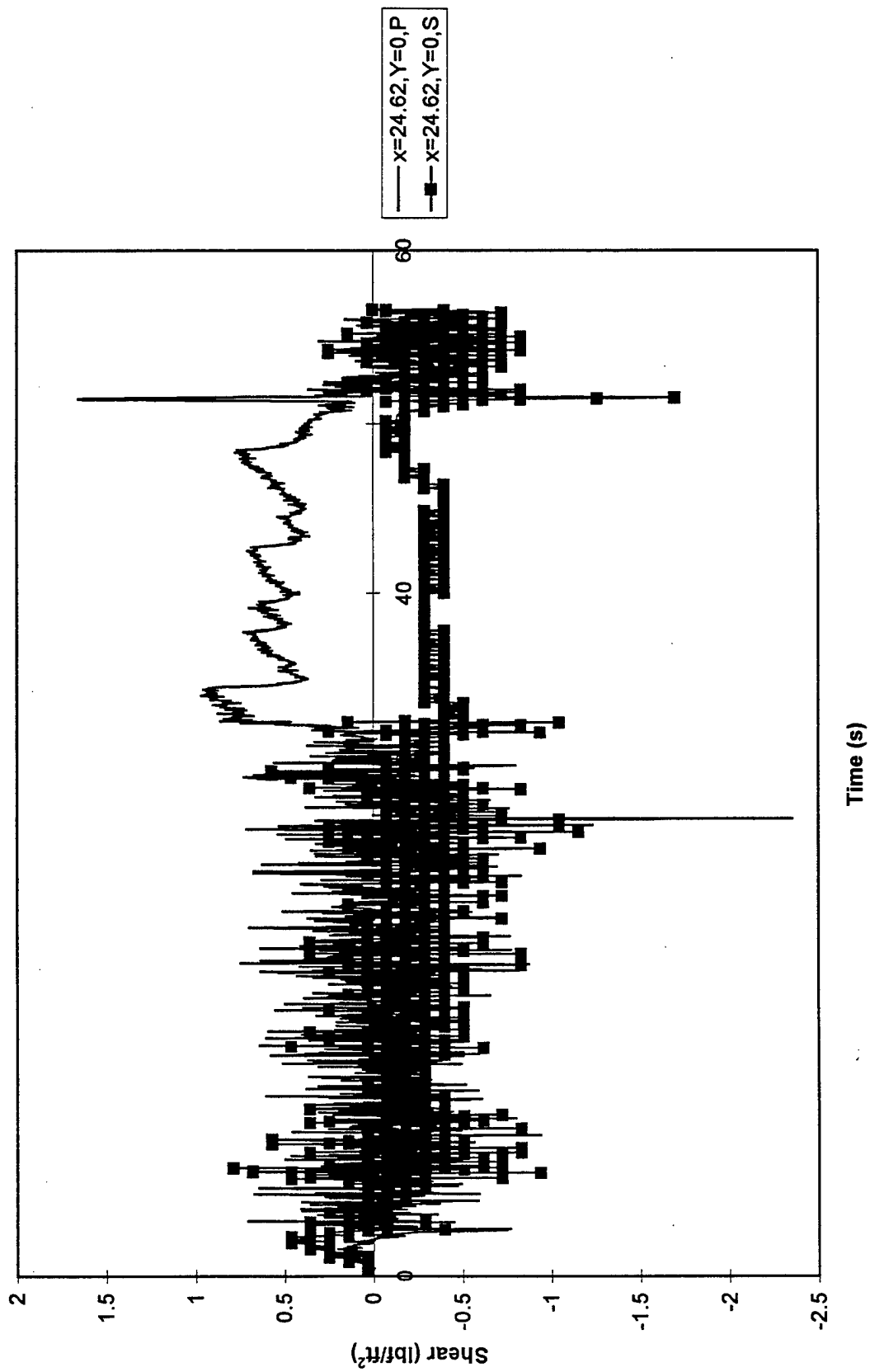


Figure 44. Skin Friction at $x = 24.6''$, $y = 0''$ During the Cold Flow Test

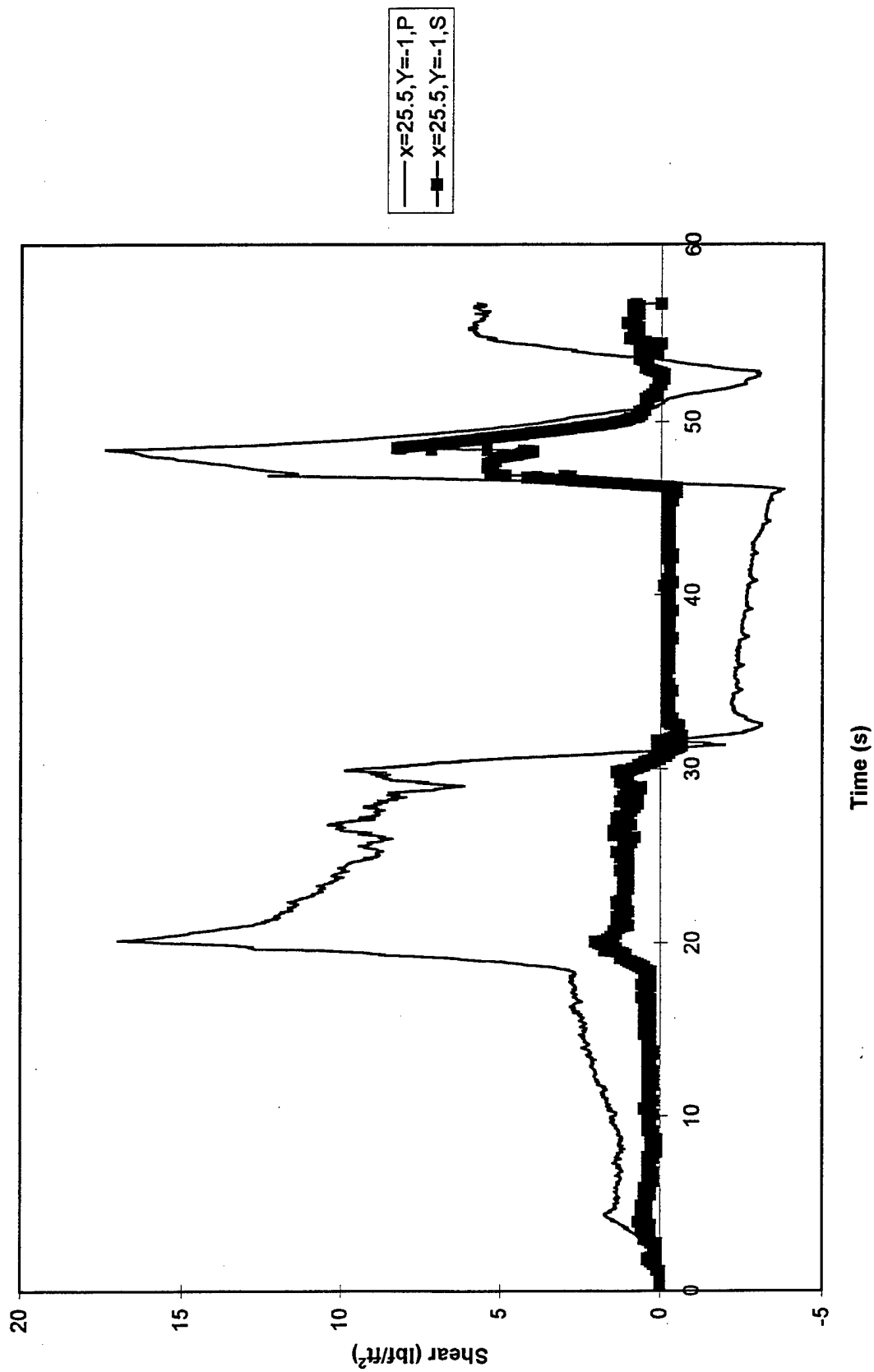


Figure 45. Skin Friction at $x = 25.5"$, $y = -1"$ During the Cold Flow Test

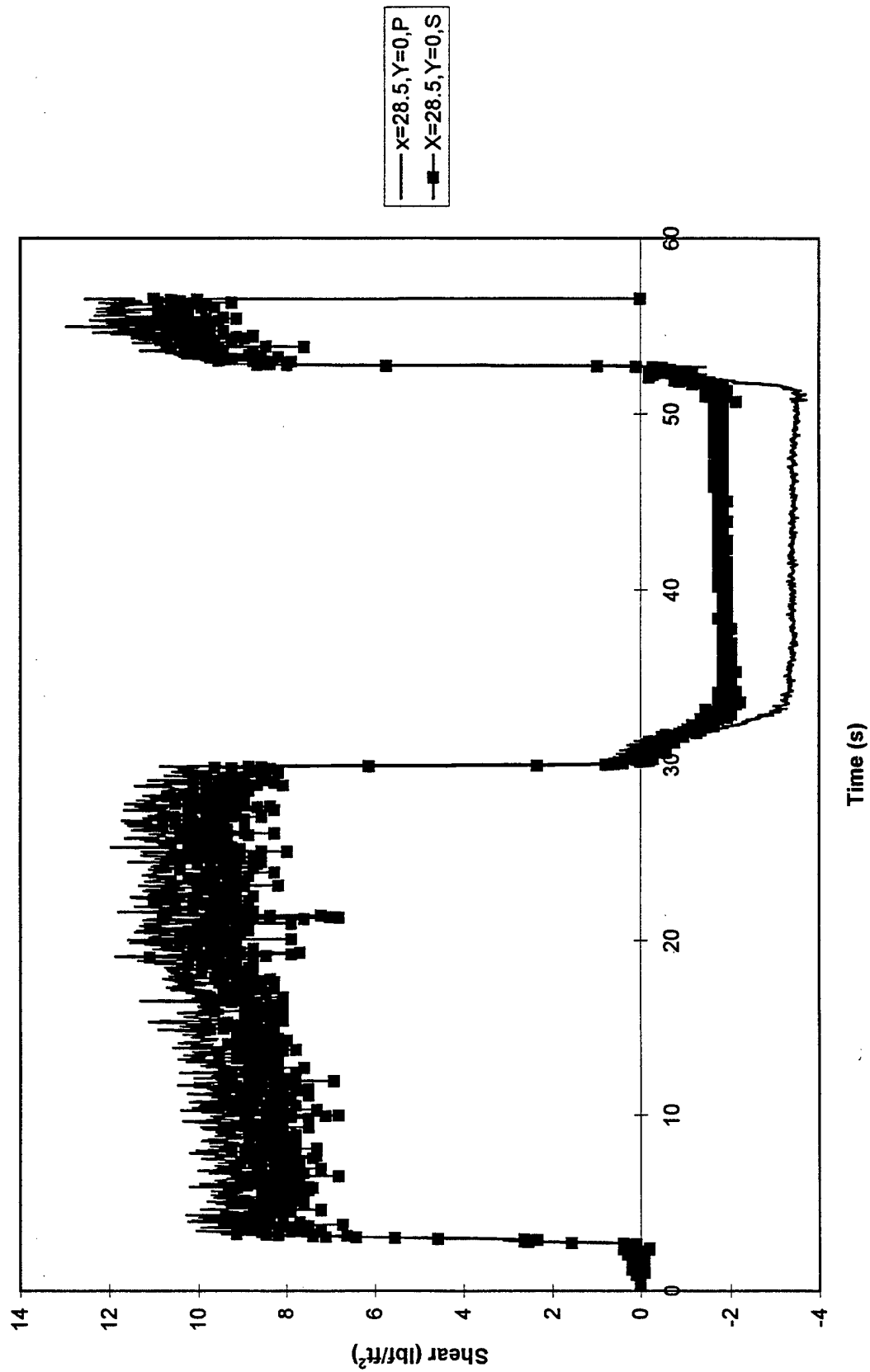


Figure 46. Skin Friction at $x = 28.5''$, $y = 0''$ During the Cold Flow Test

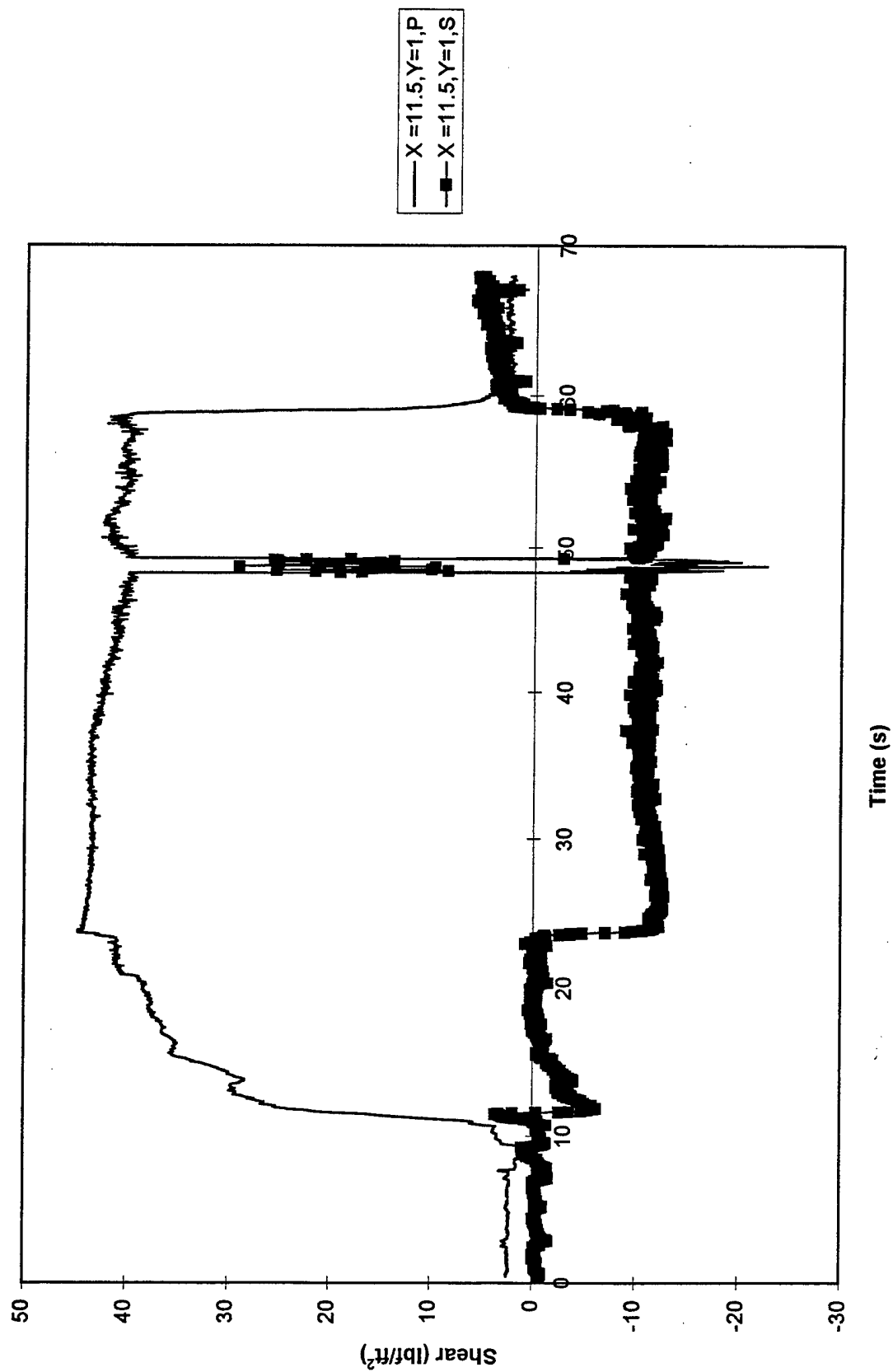


Figure 47. Skin Friction at $x = 11.5"$, $y = 1"$ During Test 884

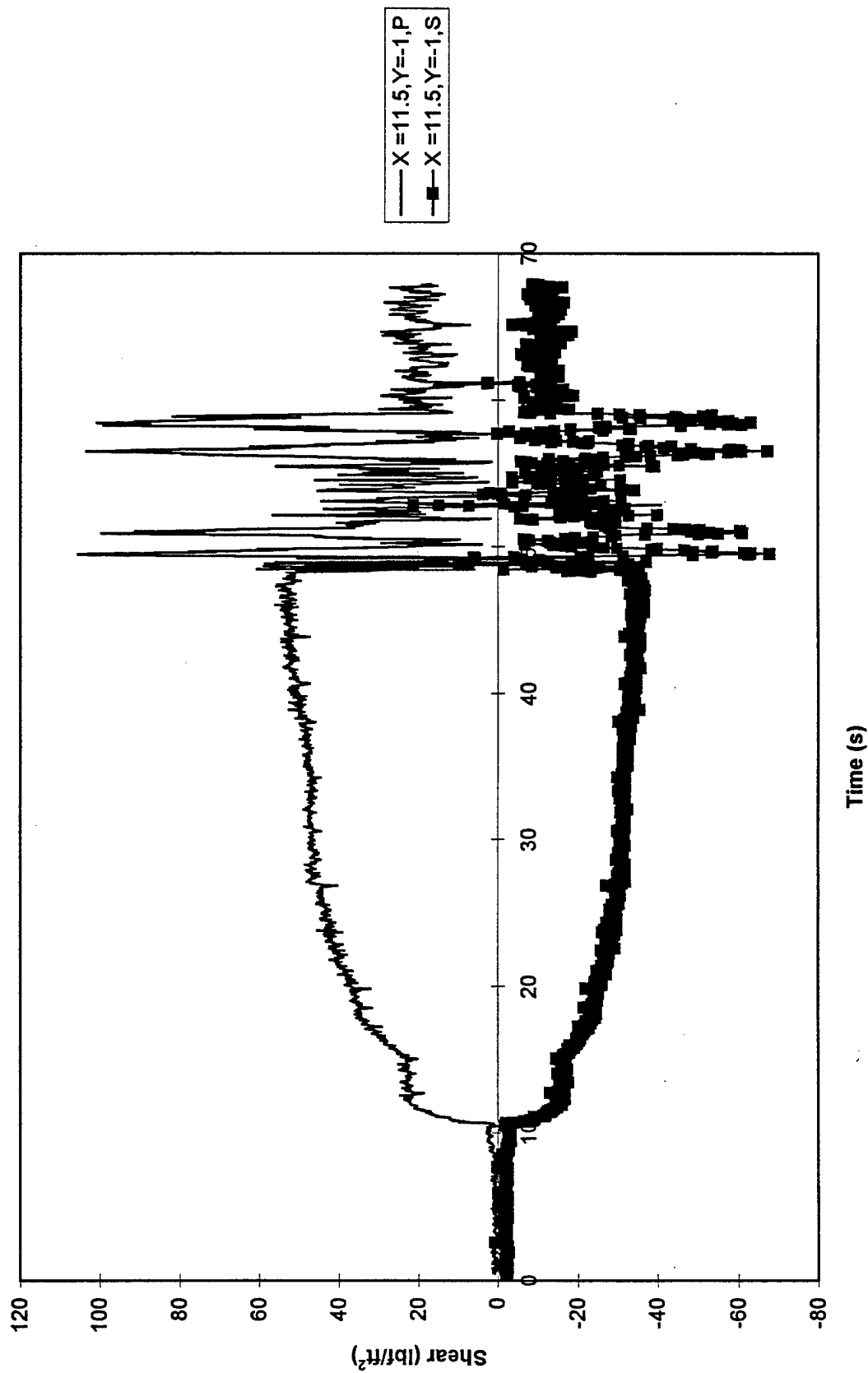


Figure 48. Skin Friction at $x = 11.5"$, $y = -1"$ During Test 884

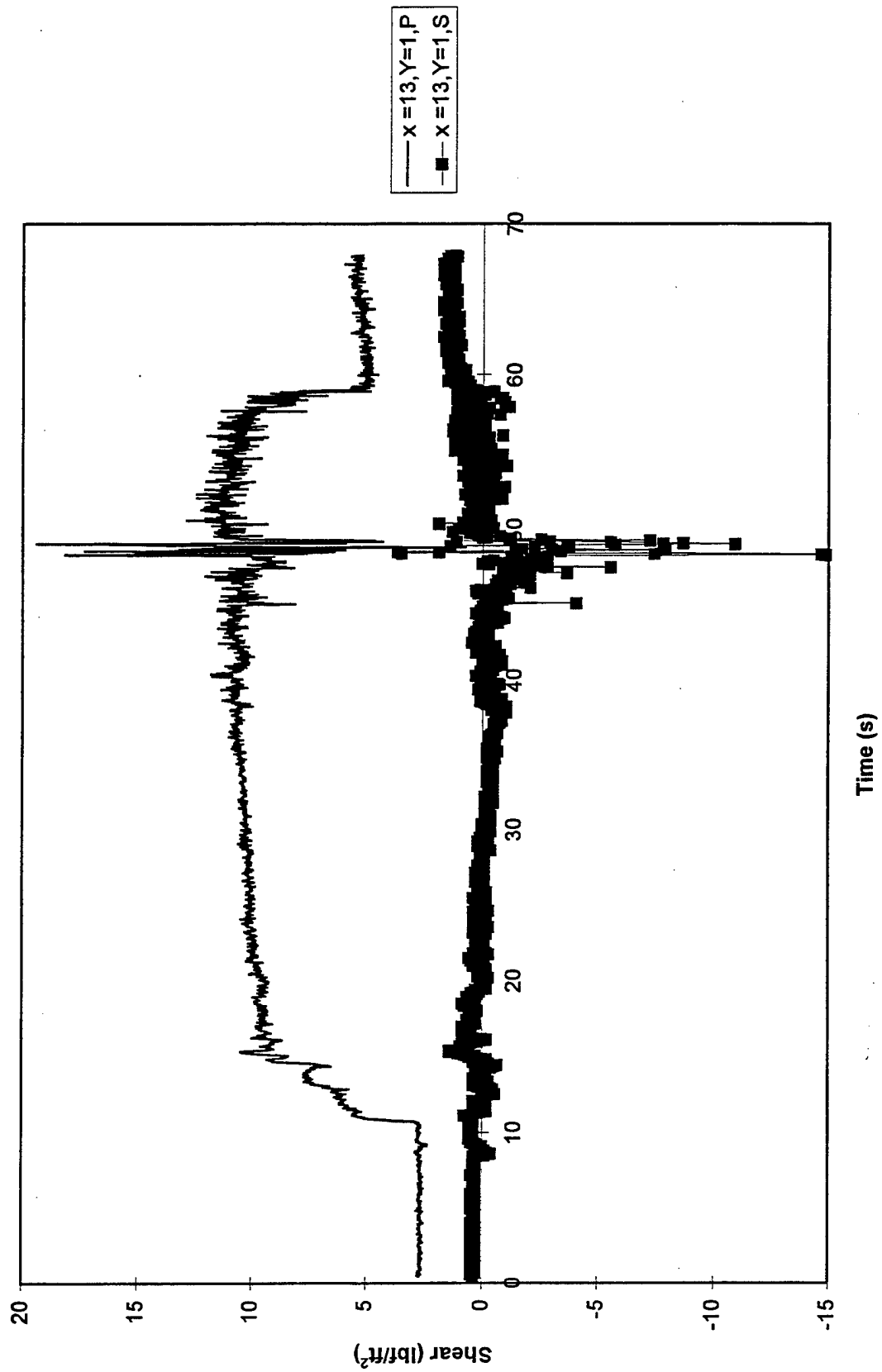


Figure 49. Skin Friction at $x = 13''$, $y = 1''$ During Test 884

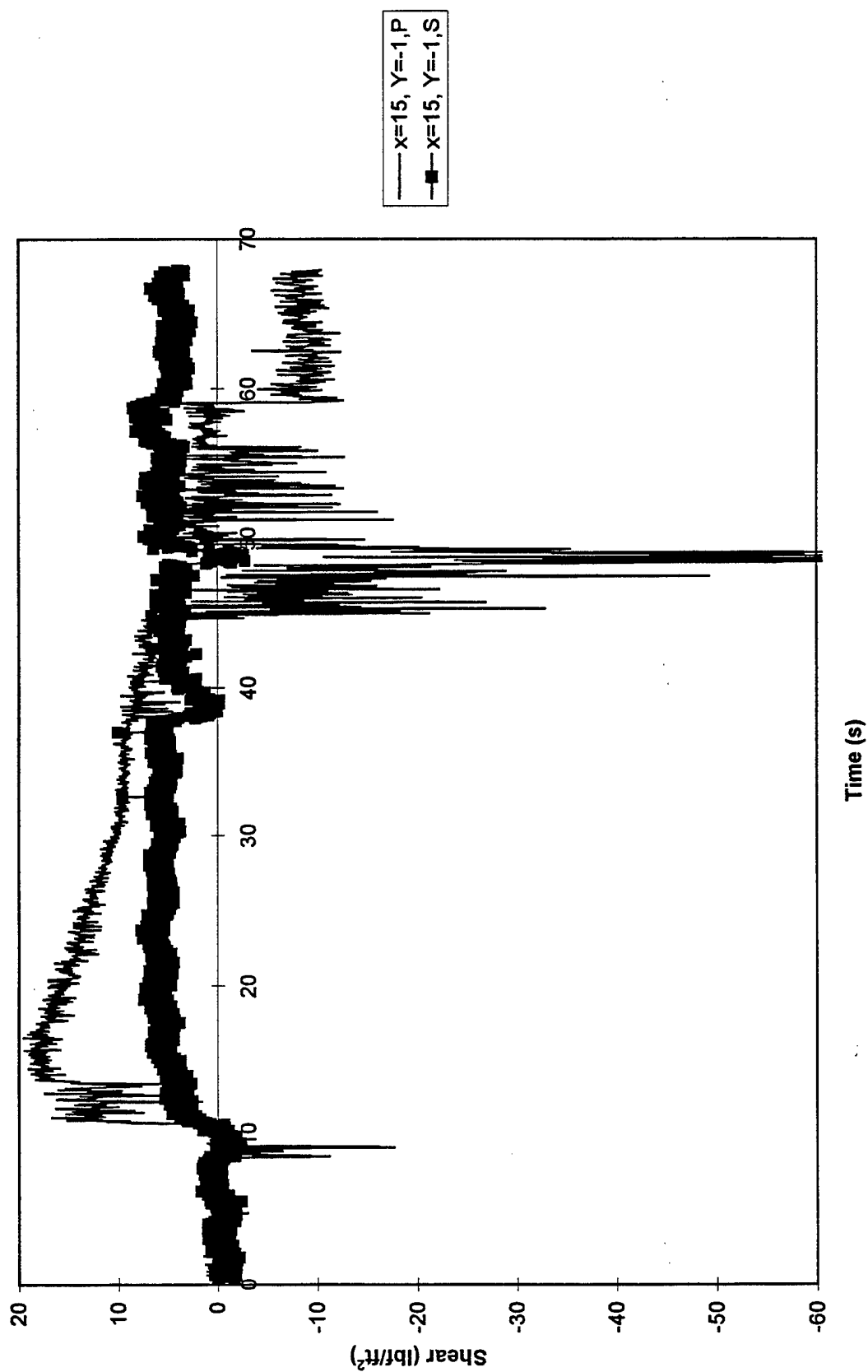


Figure 50. Skin Friction at $x = 15"$, $y = -1"$ During Test 884

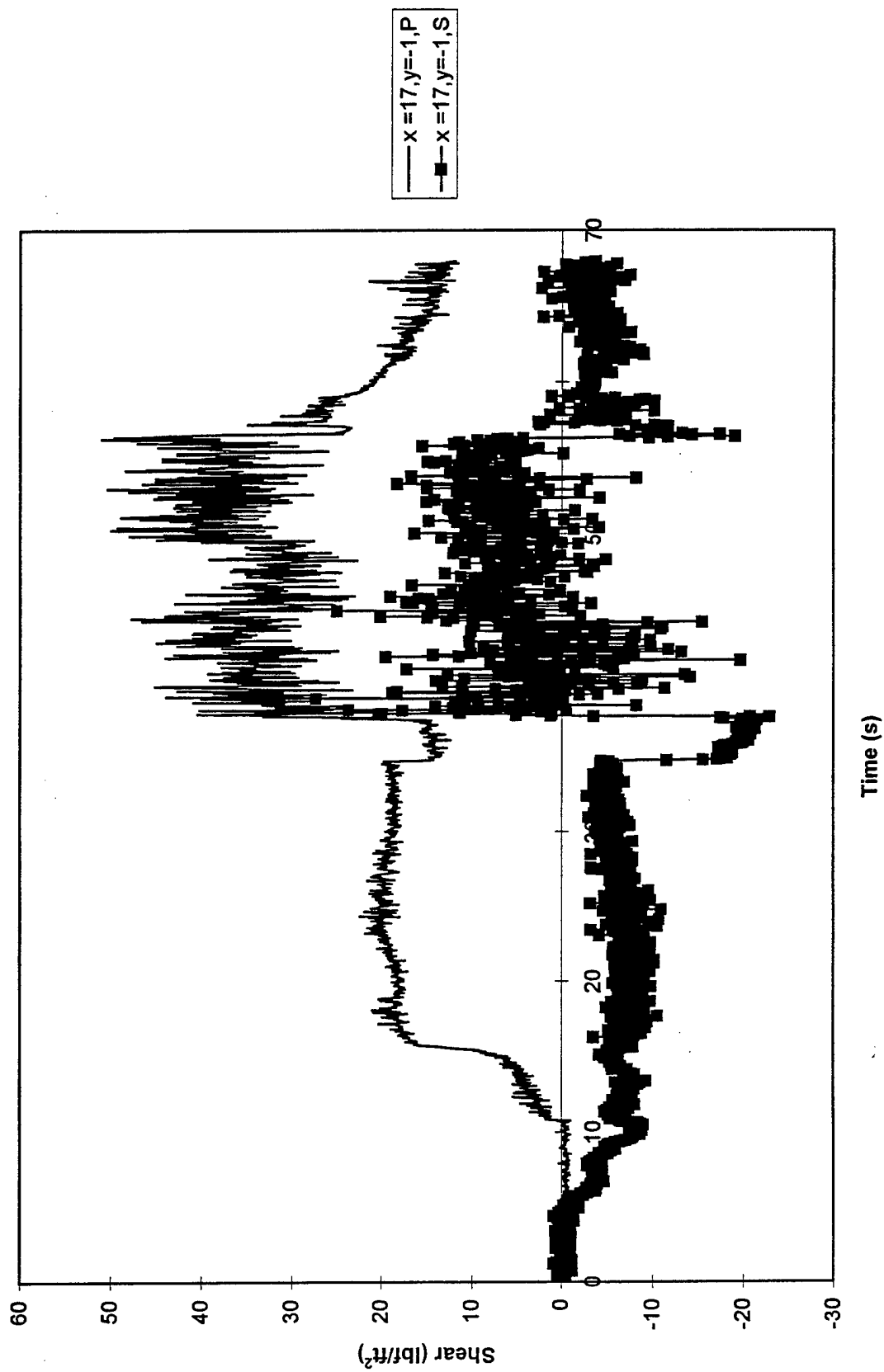


Figure 51. Skin Friction at $x = 17"$, $y = -1"$ During Test 884

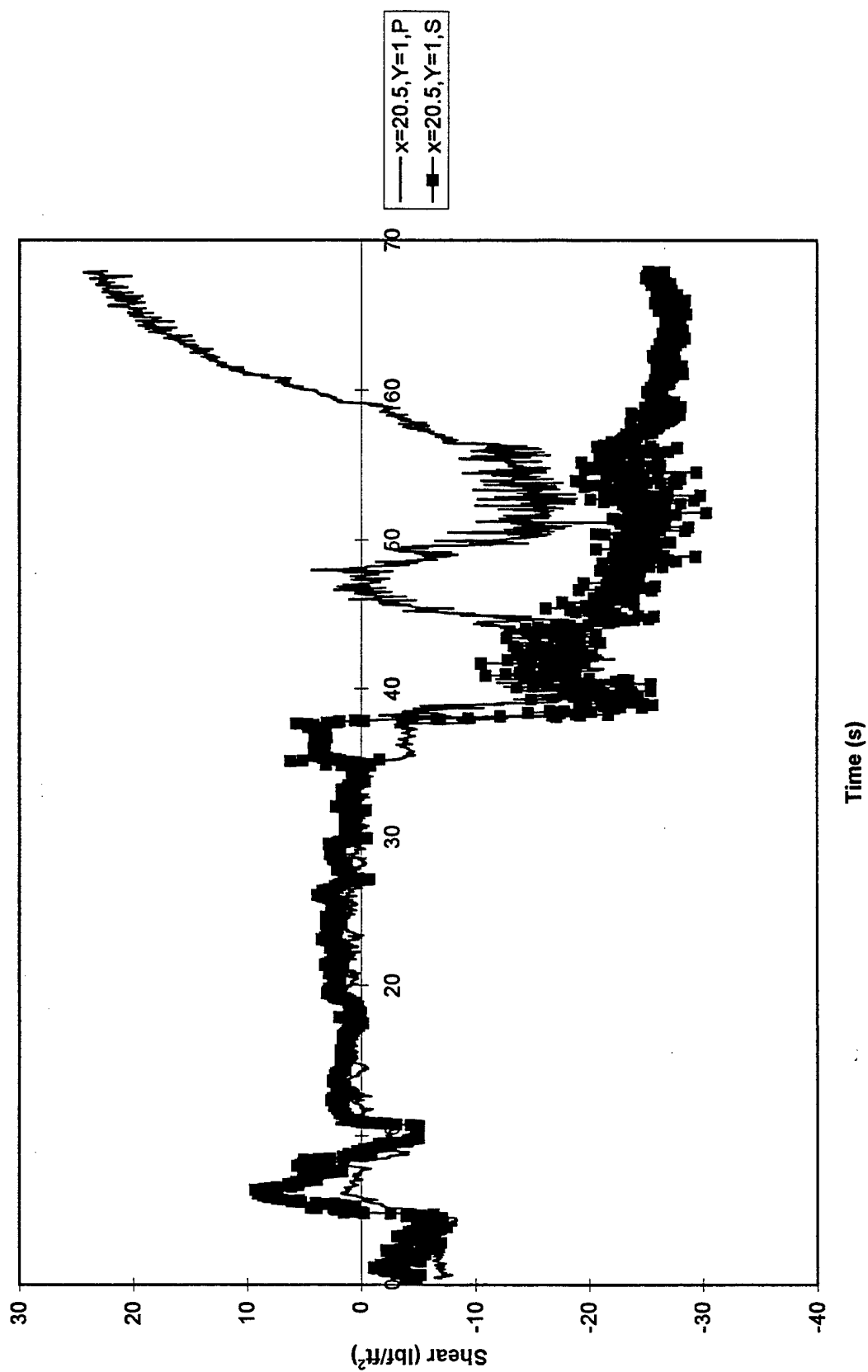


Figure 52. Skin Friction at $x = 20.5"$, $y = 1"$ During Test 884

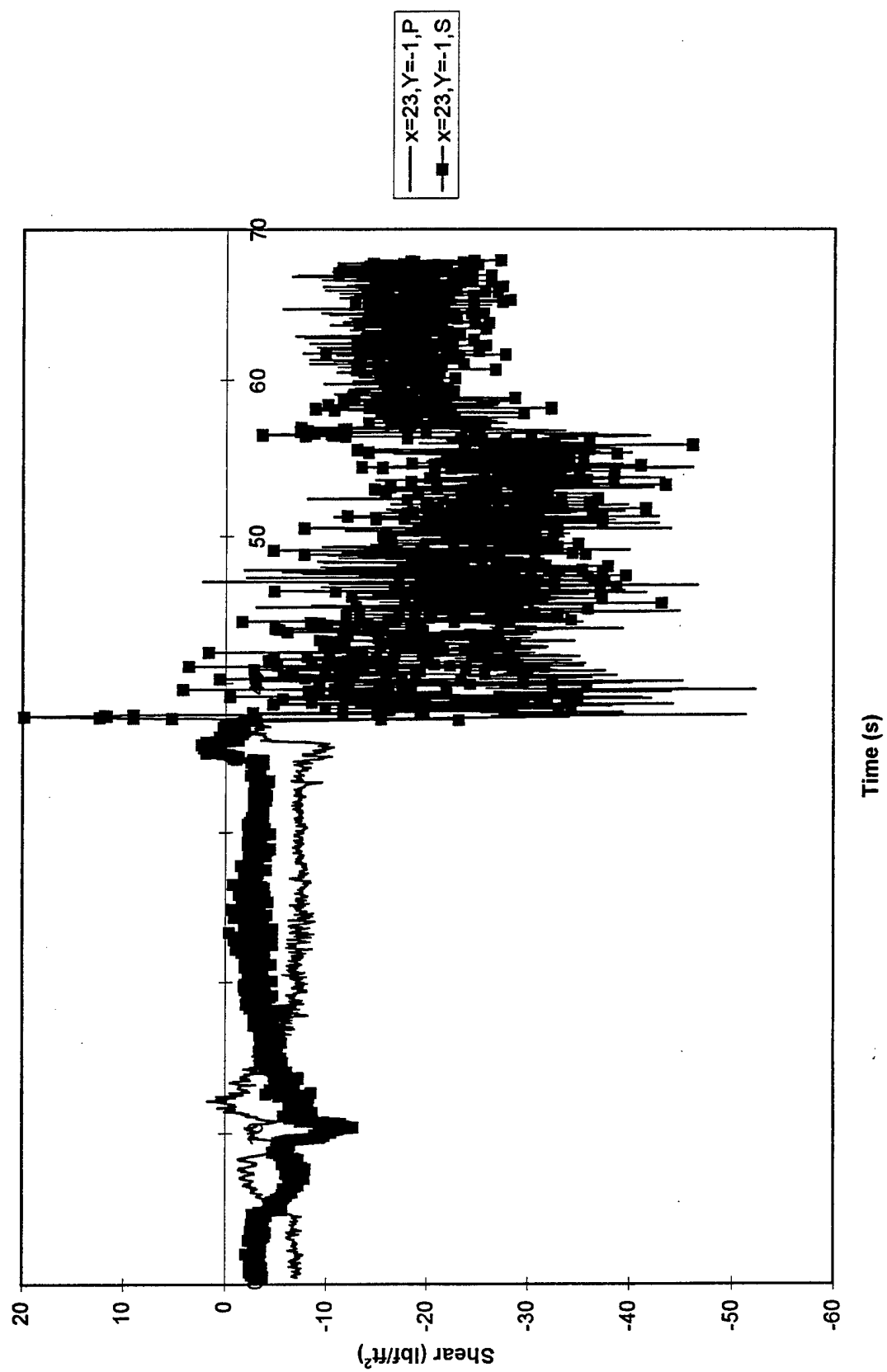


Figure 53. Skin Friction at $x = 23"$, $y = -1"$ During Test 884

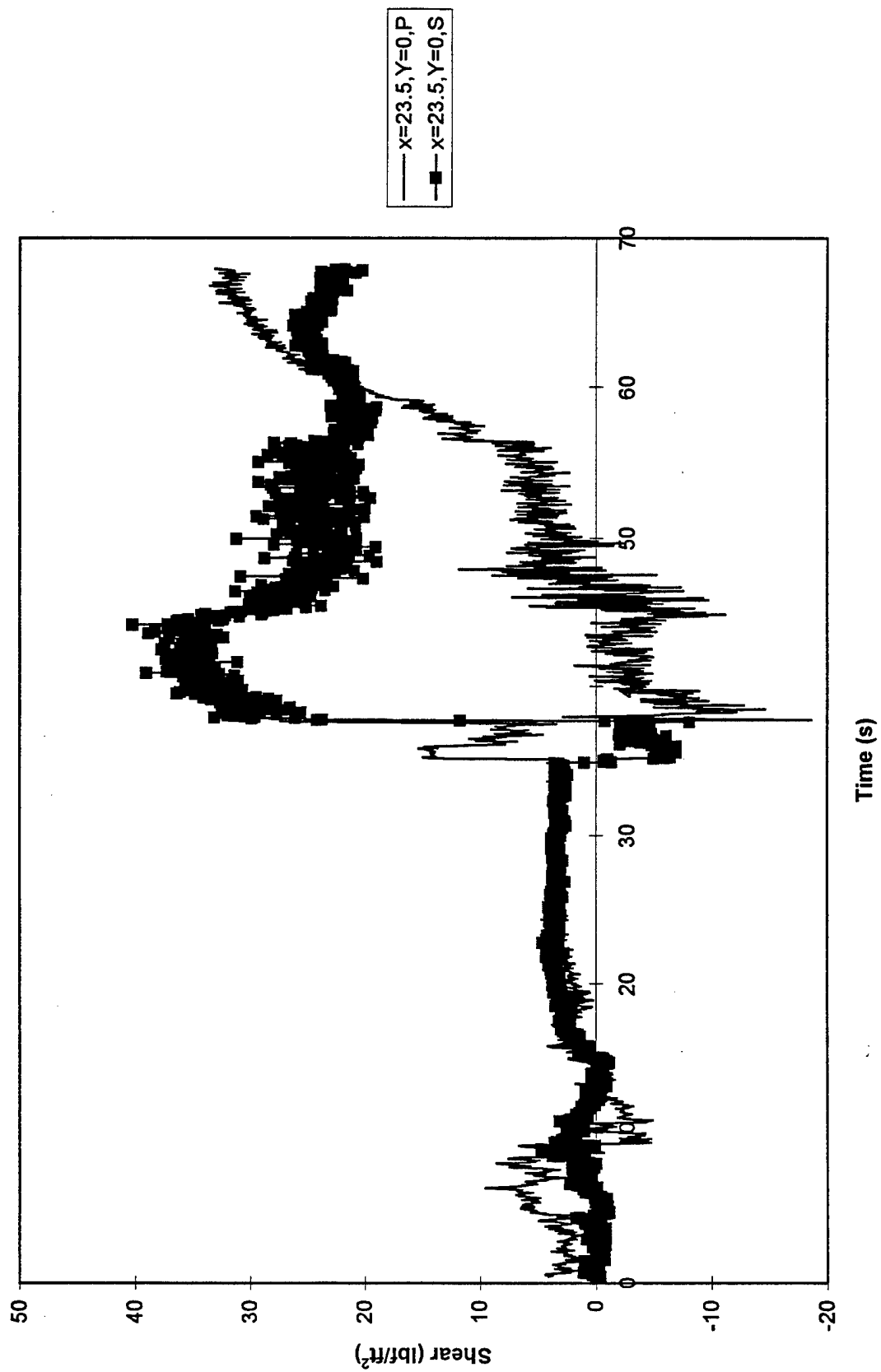


Figure 54. Skin Friction at $x = 23.5"$, $y = 0"$ During Test 884

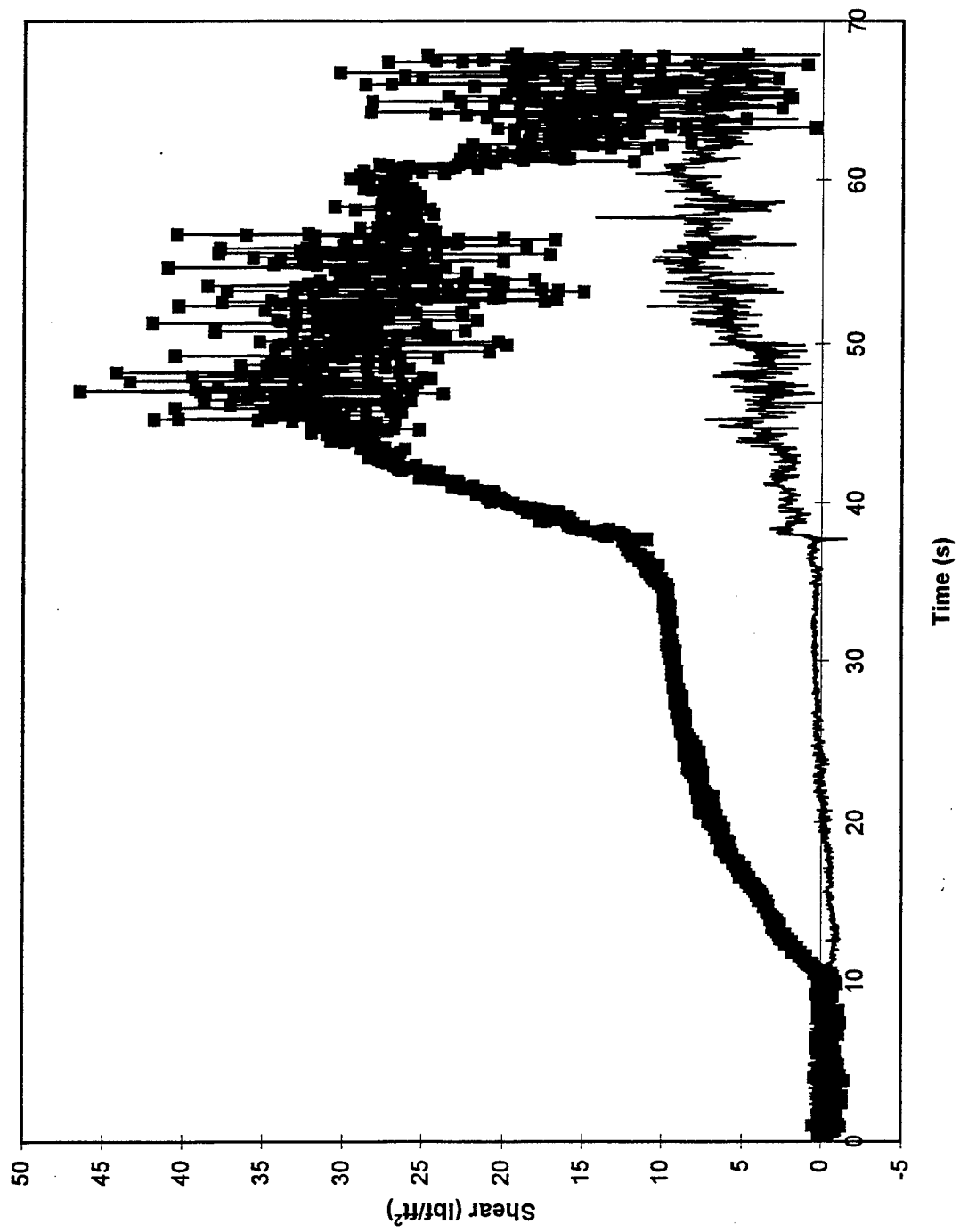


Figure 55. Skin Friction at $x = 24.6''$, $y = 0''$ During Test 884

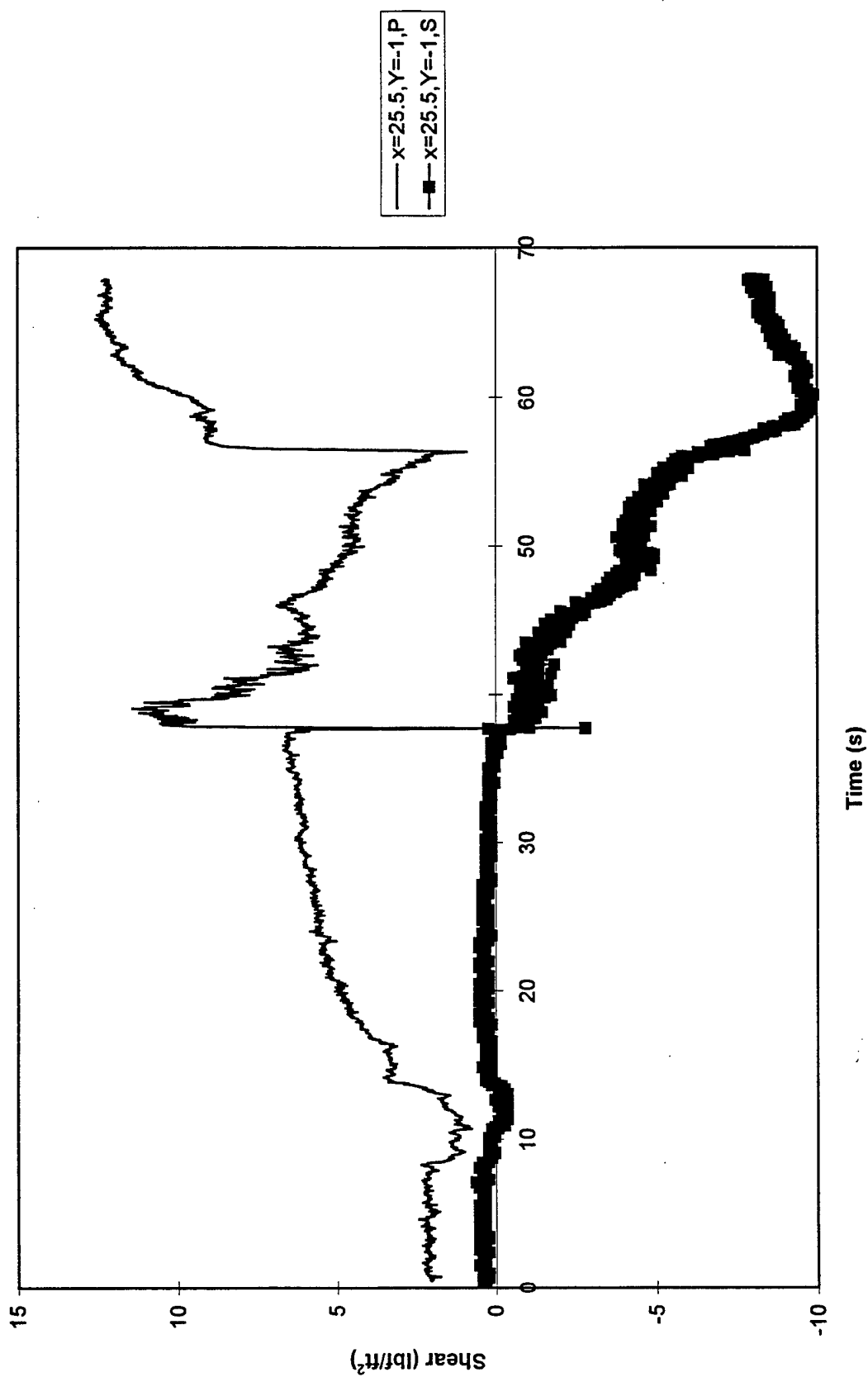


Figure 56. Skin Friction at $x = 25.5"$, $y = -1"$ During Test 884

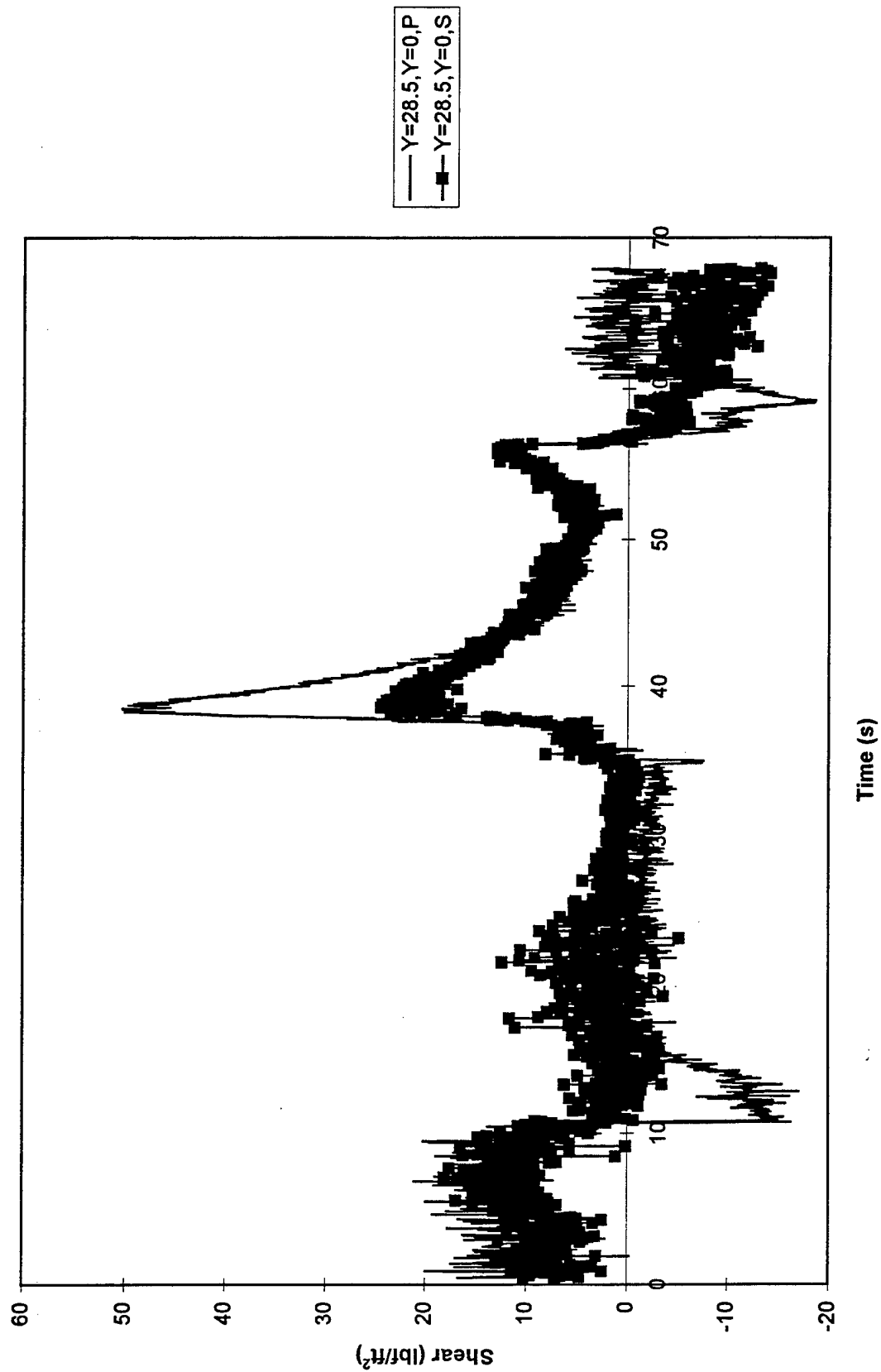


Figure 57. Skin Friction at $x = 28.5''$, $y = 0''$ During Test 884

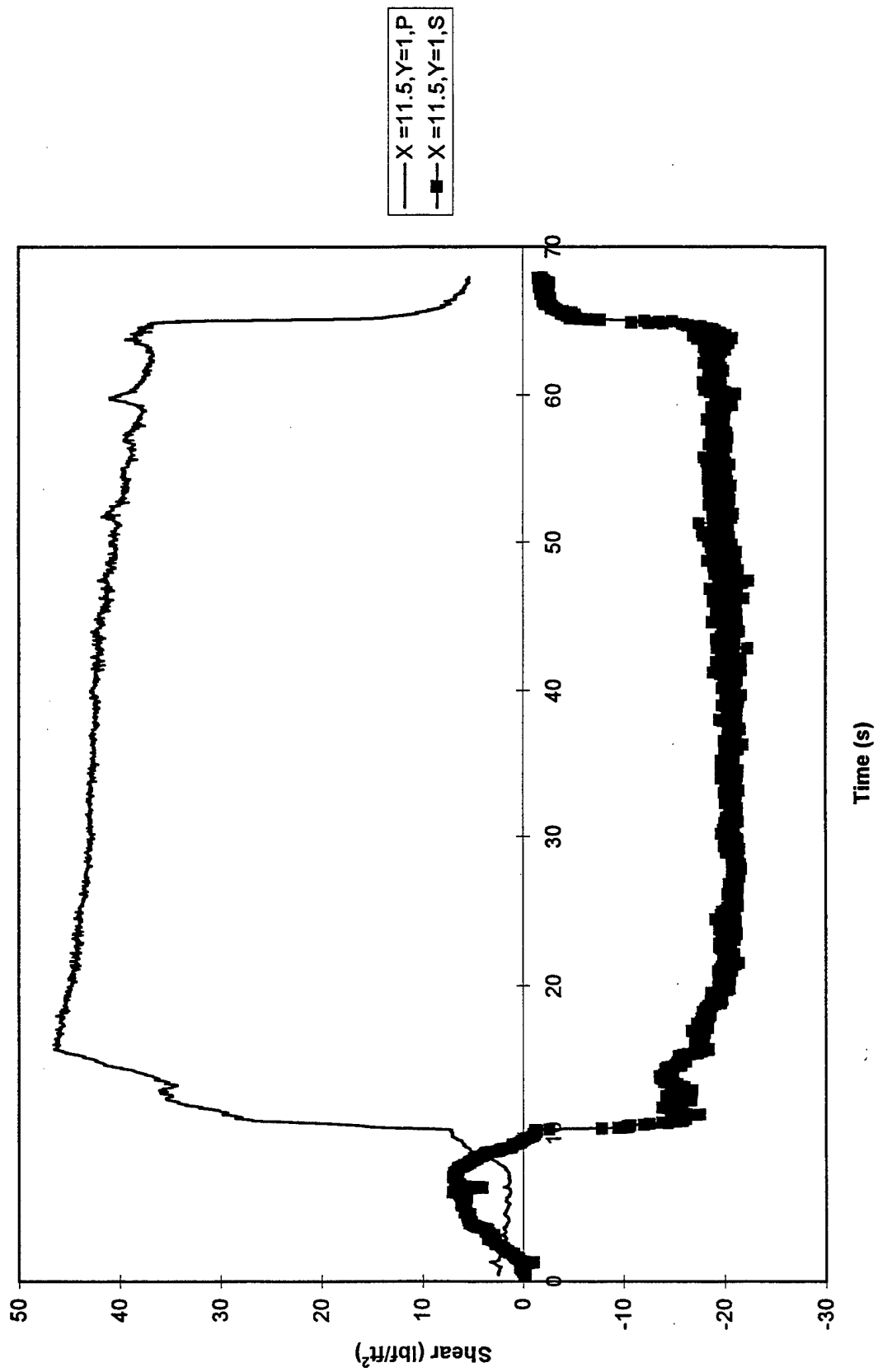


Figure 58. Skin Friction at $x = 11.5$, $y = 1$ " During Test 886

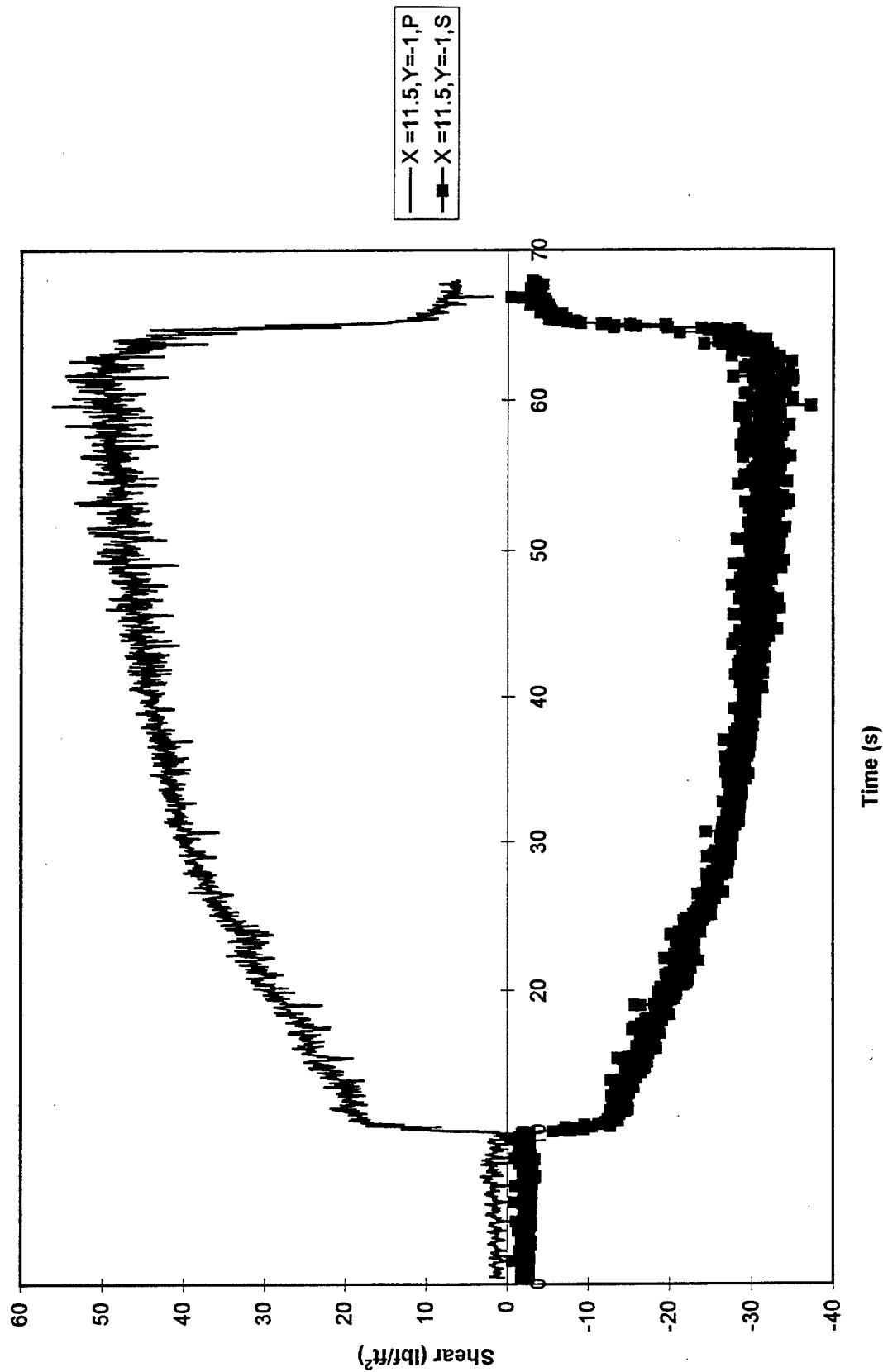


Figure 59. Skin Friction at $x = 11.5"$, $y = -1"$ During Test 886

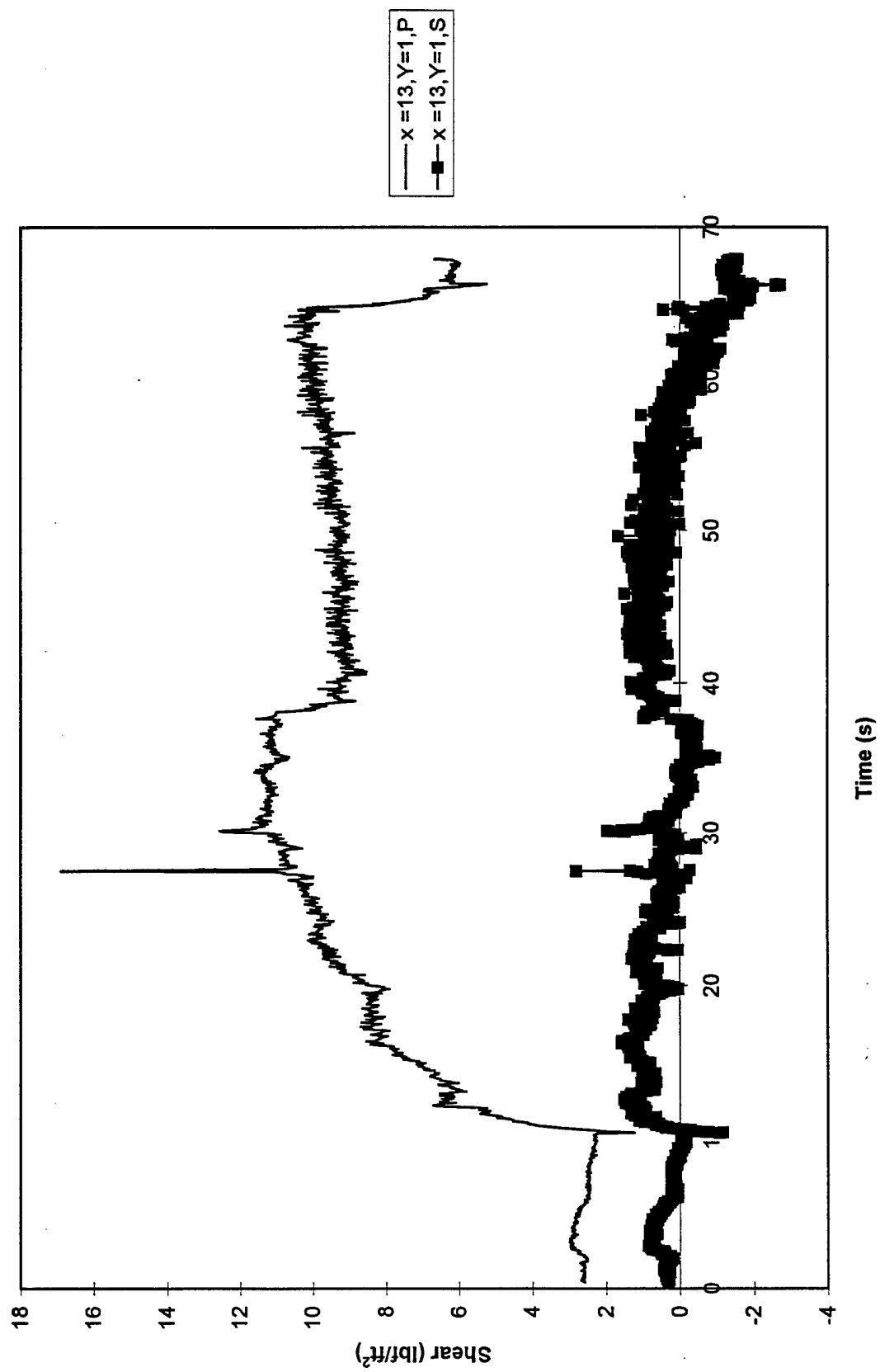


Figure 60. Skin Friction at $x = 13''$, $y = 1''$ During Test 886

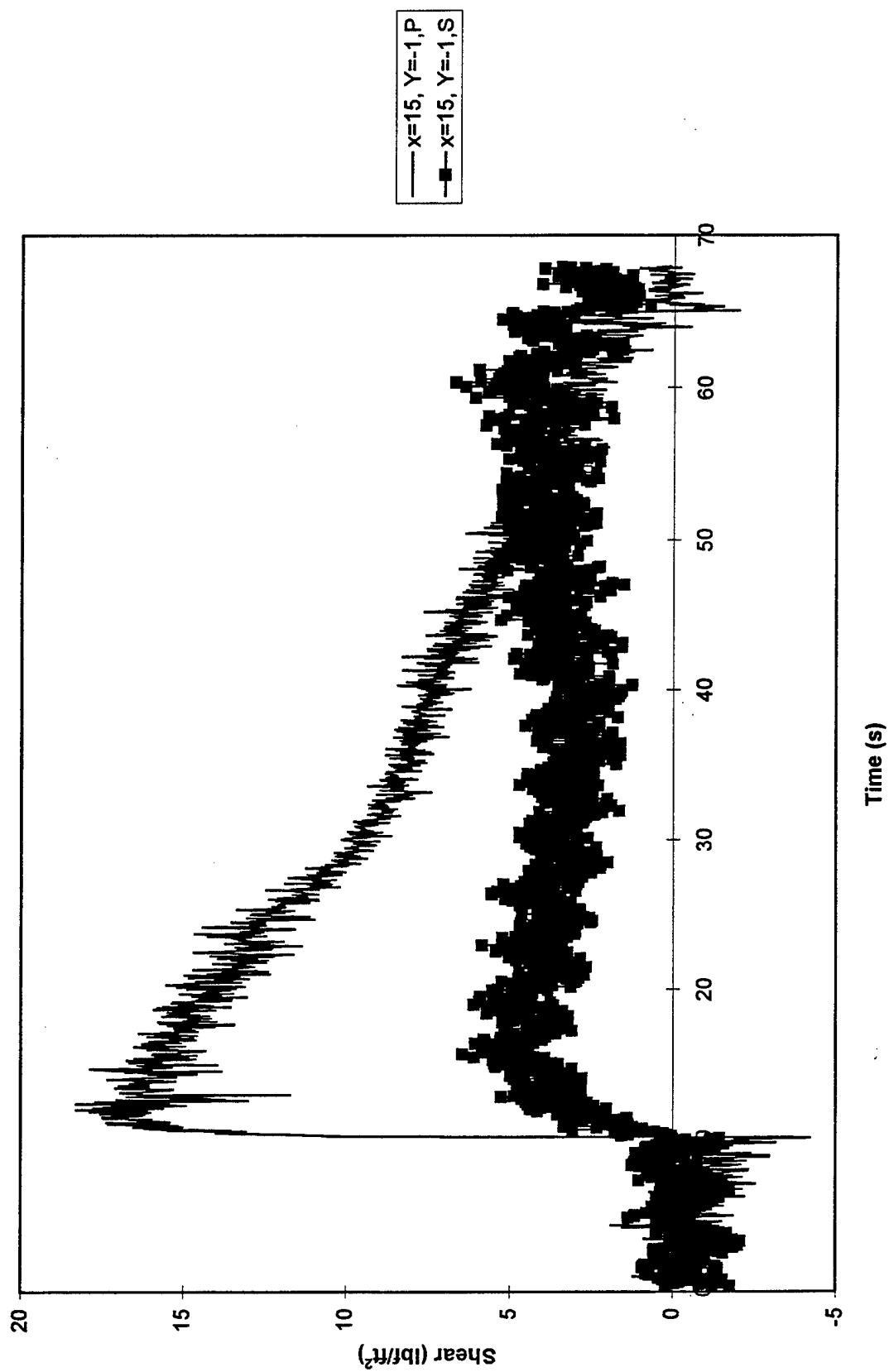


Figure 61. Skin Friction at $x = 15"$, $y = -1"$ During Test 886

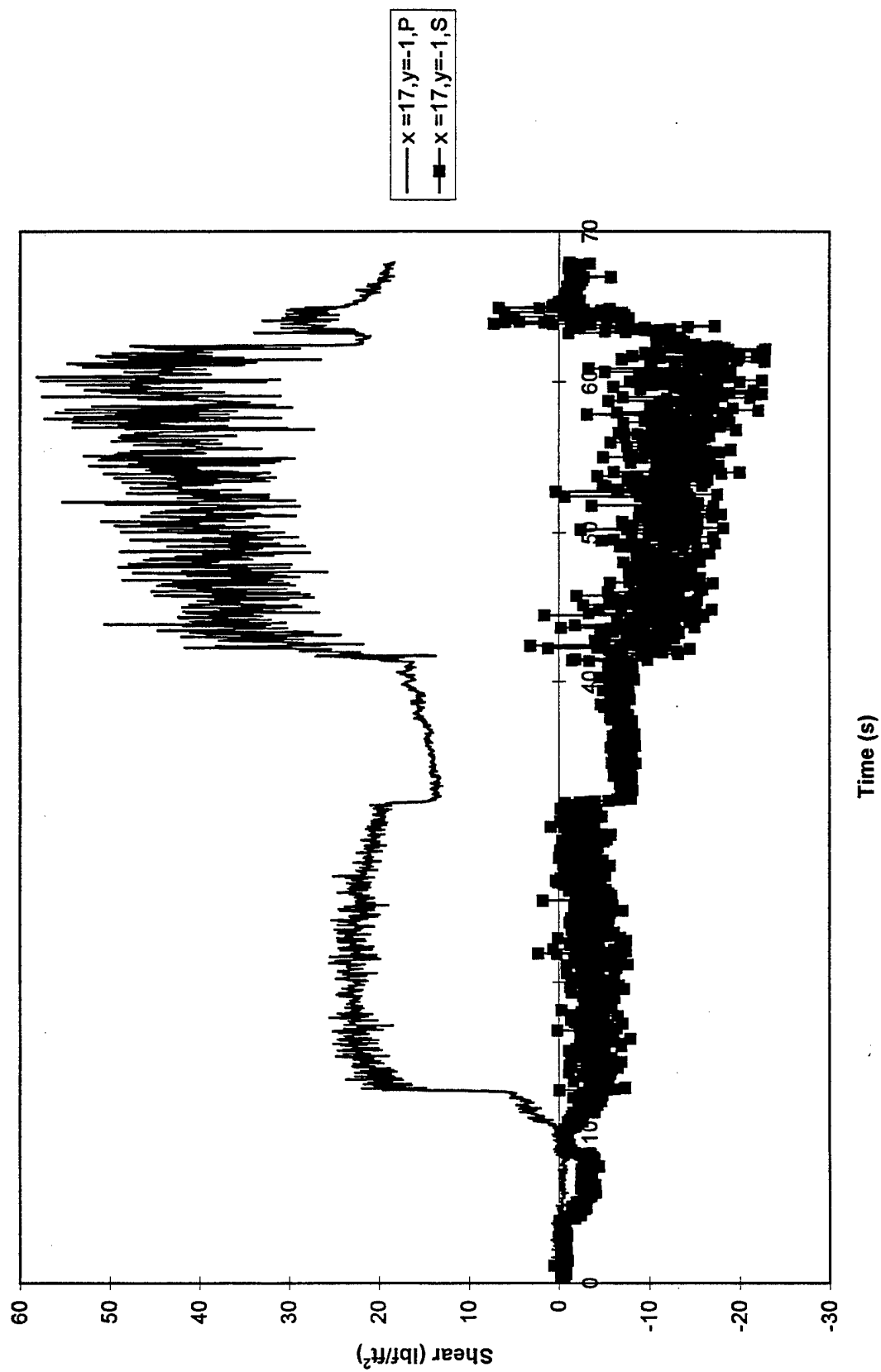


Figure 62. Skin Friction at $x = 17''$, $y = -1''$ During Test 886

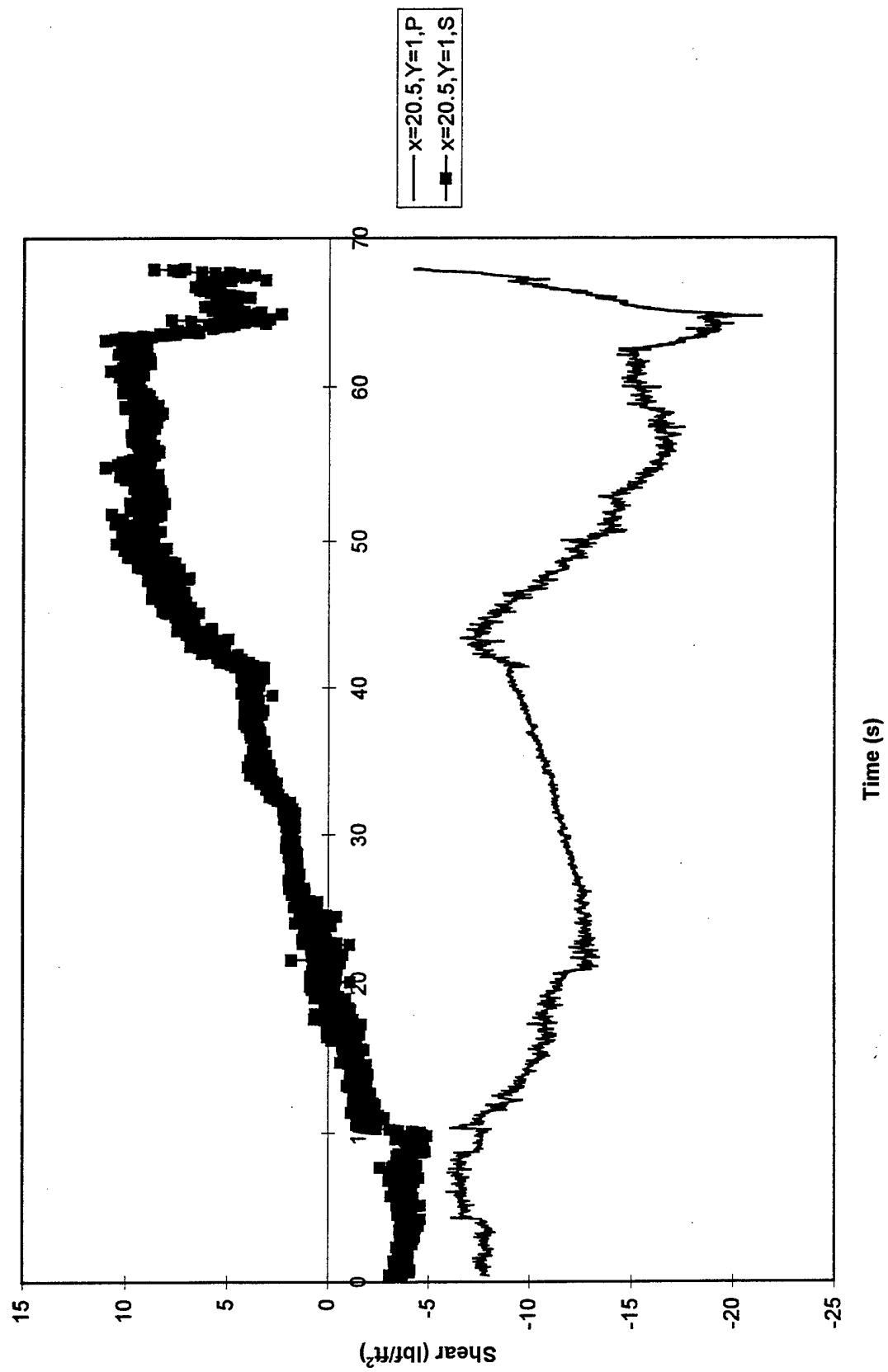


Figure 63. Skin Friction at $x = 20.5"$, $y = 1"$ During Test 886

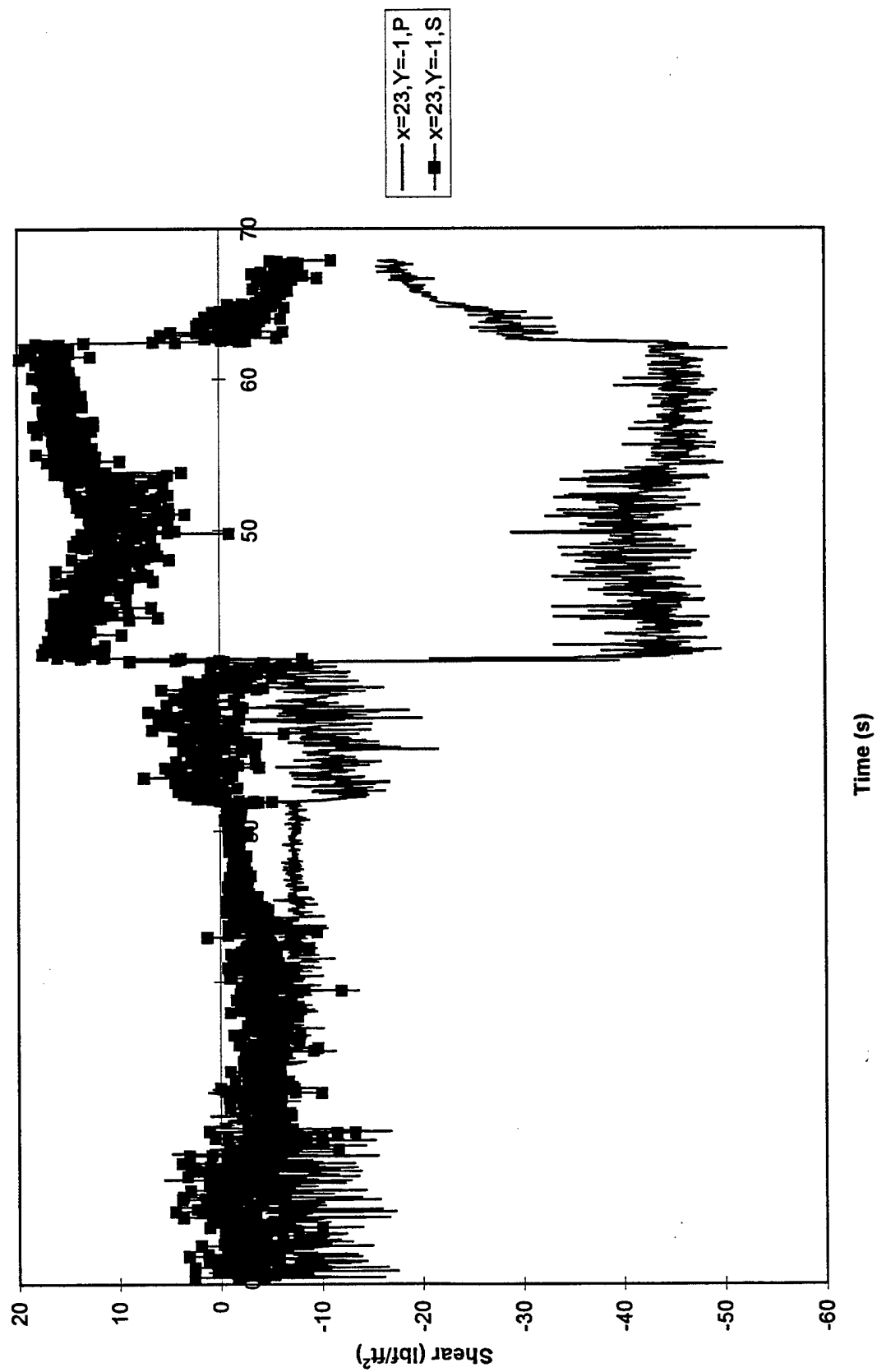
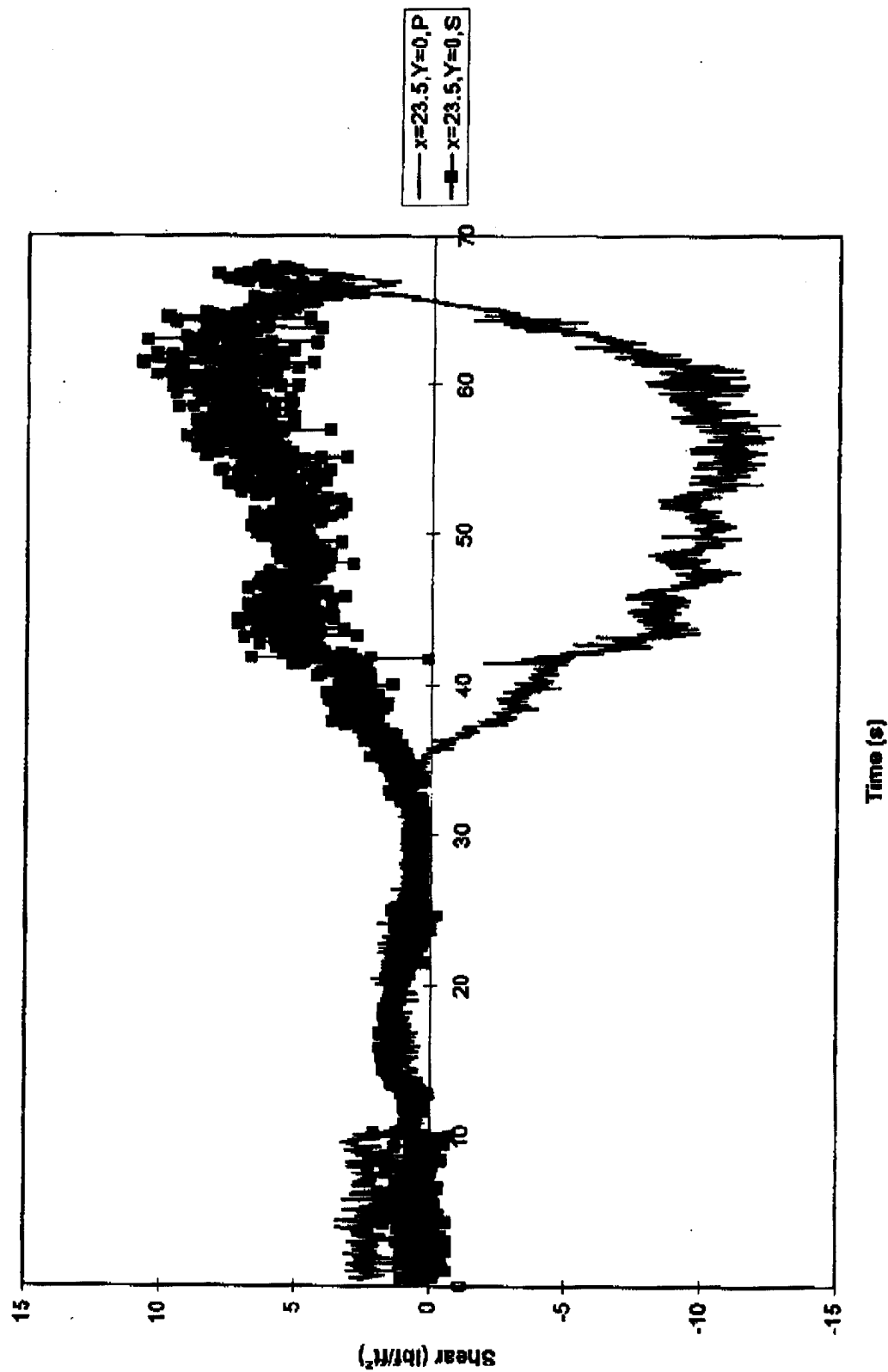


Figure 64. Skin Friction at $x = 23"$, $y = -1"$ During Test 886

Figure 65. Skin Friction at $x = 23.5''$, $y = 0''$ During Test 886

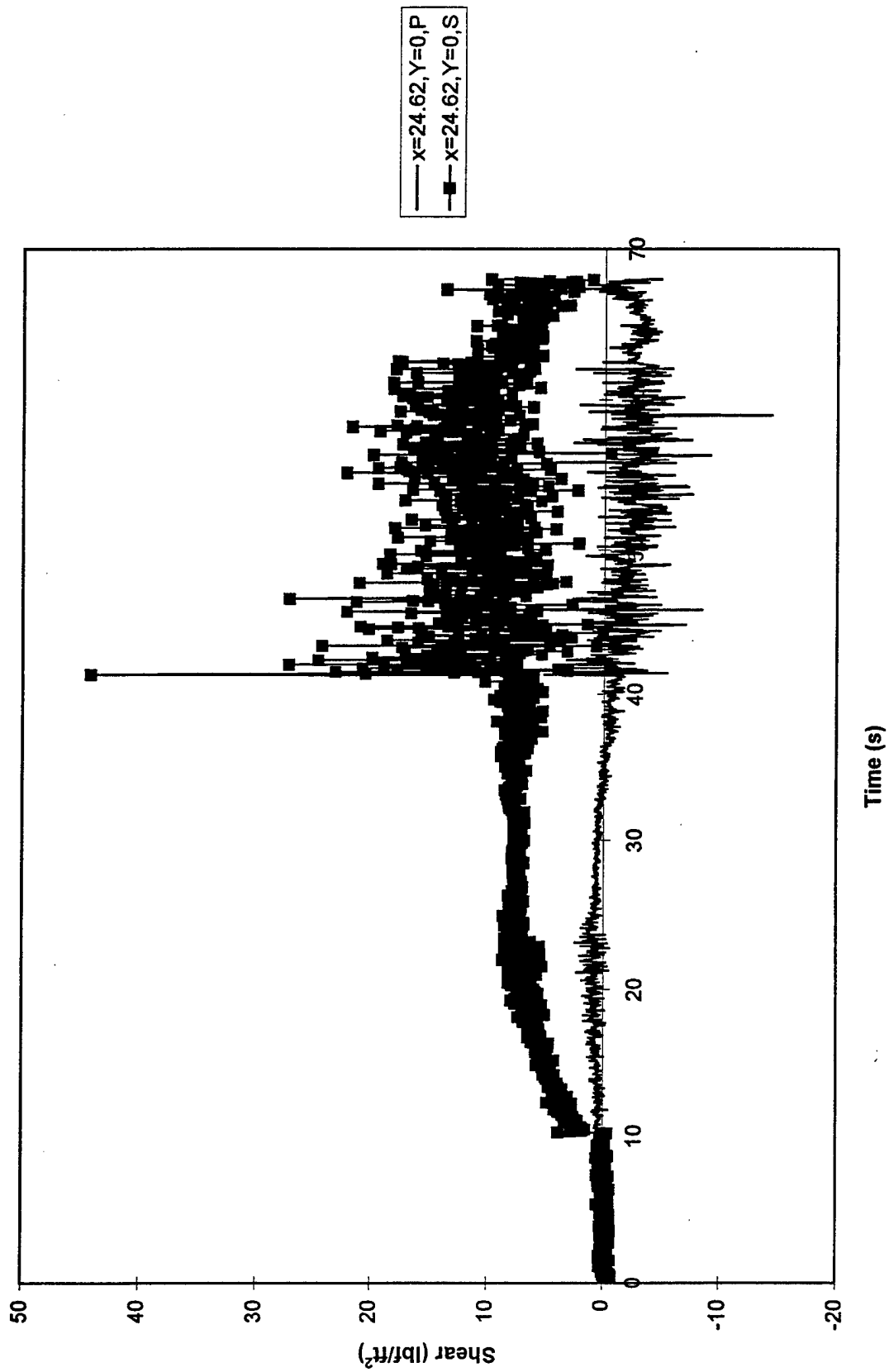


Figure 66. Skin Friction at $x = 24.6''$, $y = 0''$ During Test 886

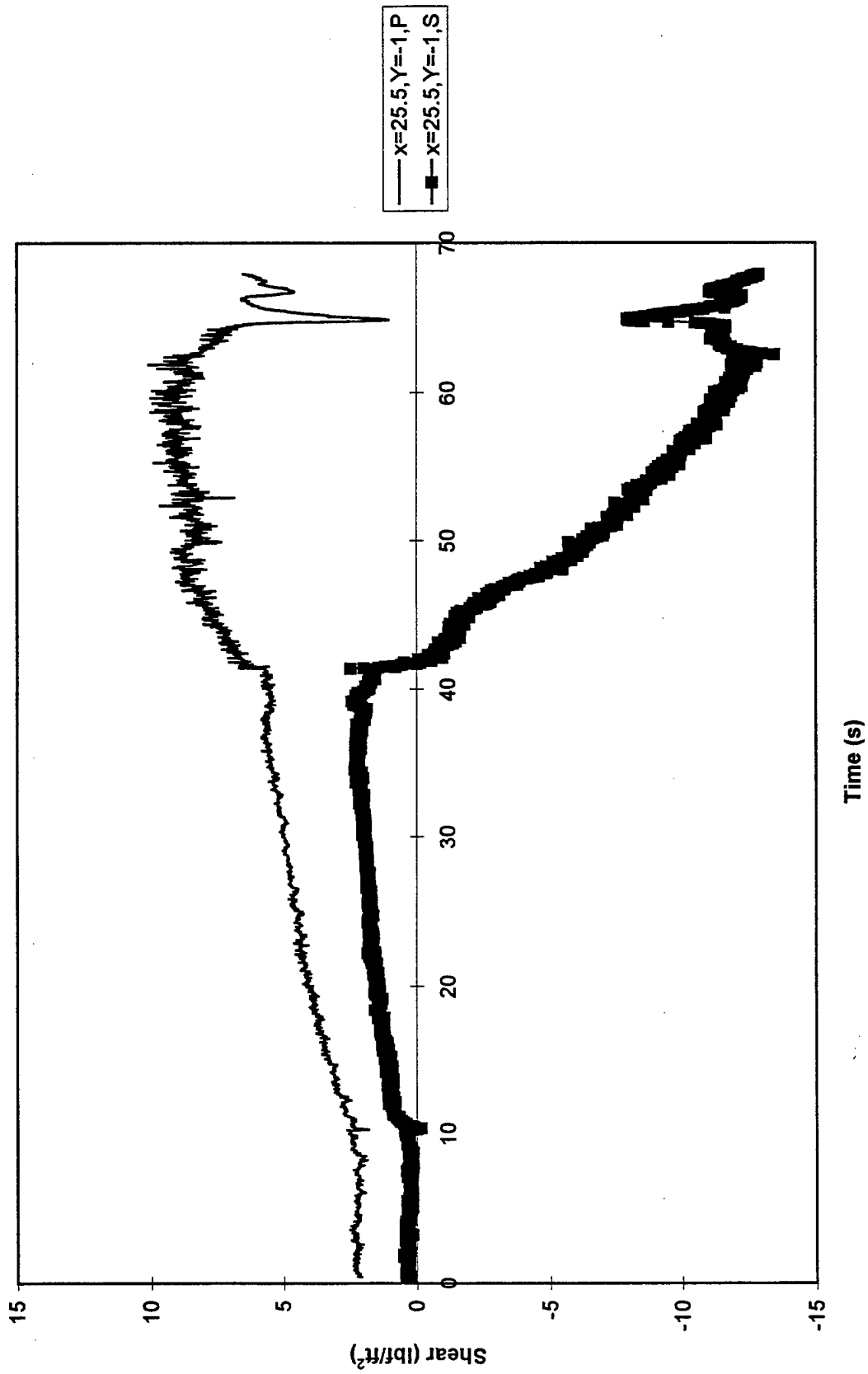


Figure 67. Skin Friction at $x = 25.5"$, $y = -1"$ During Test 886

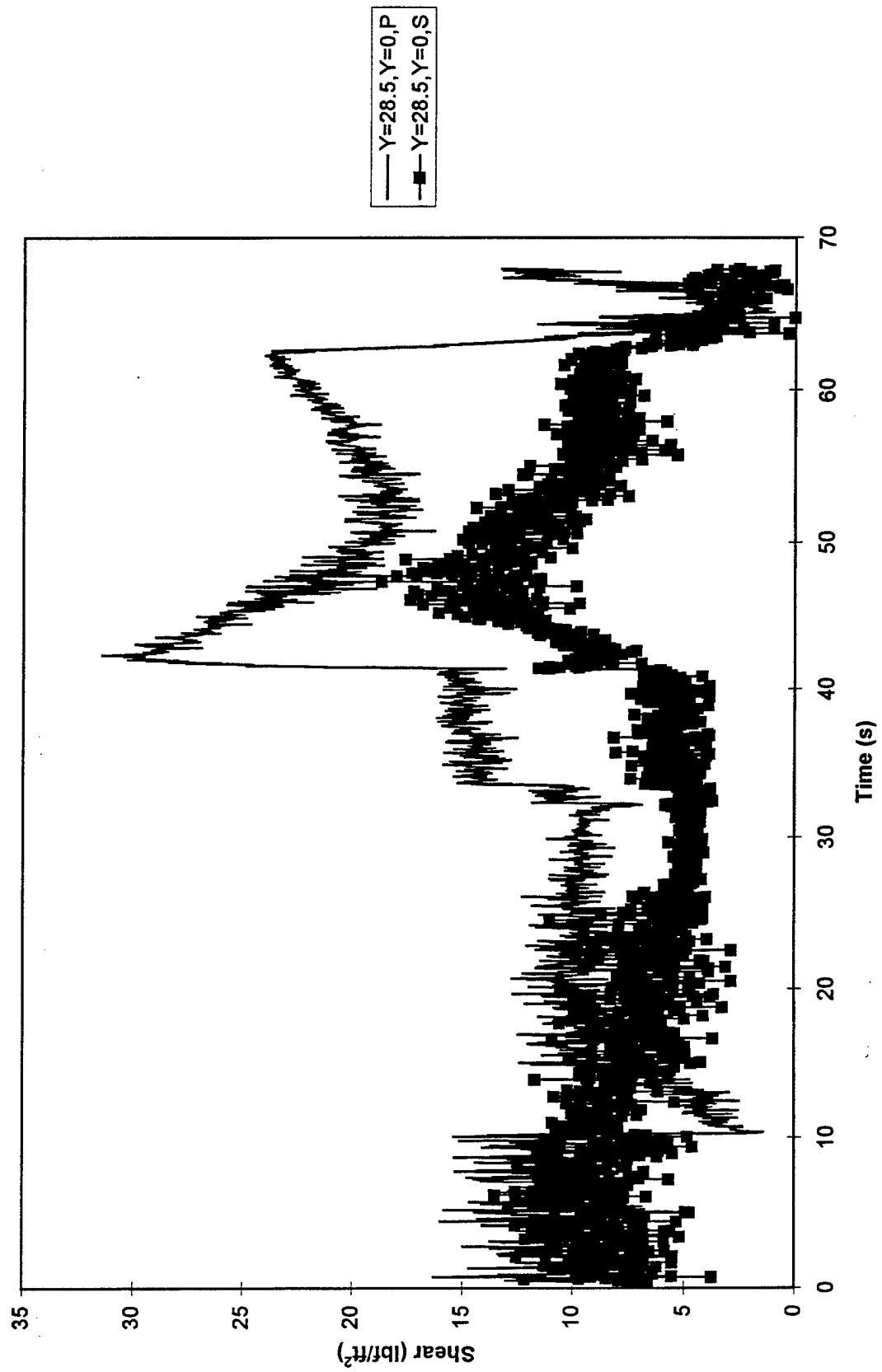


Figure 68. Skin Friction at $x = 28.5"$, $y = 0"$ During Test 886

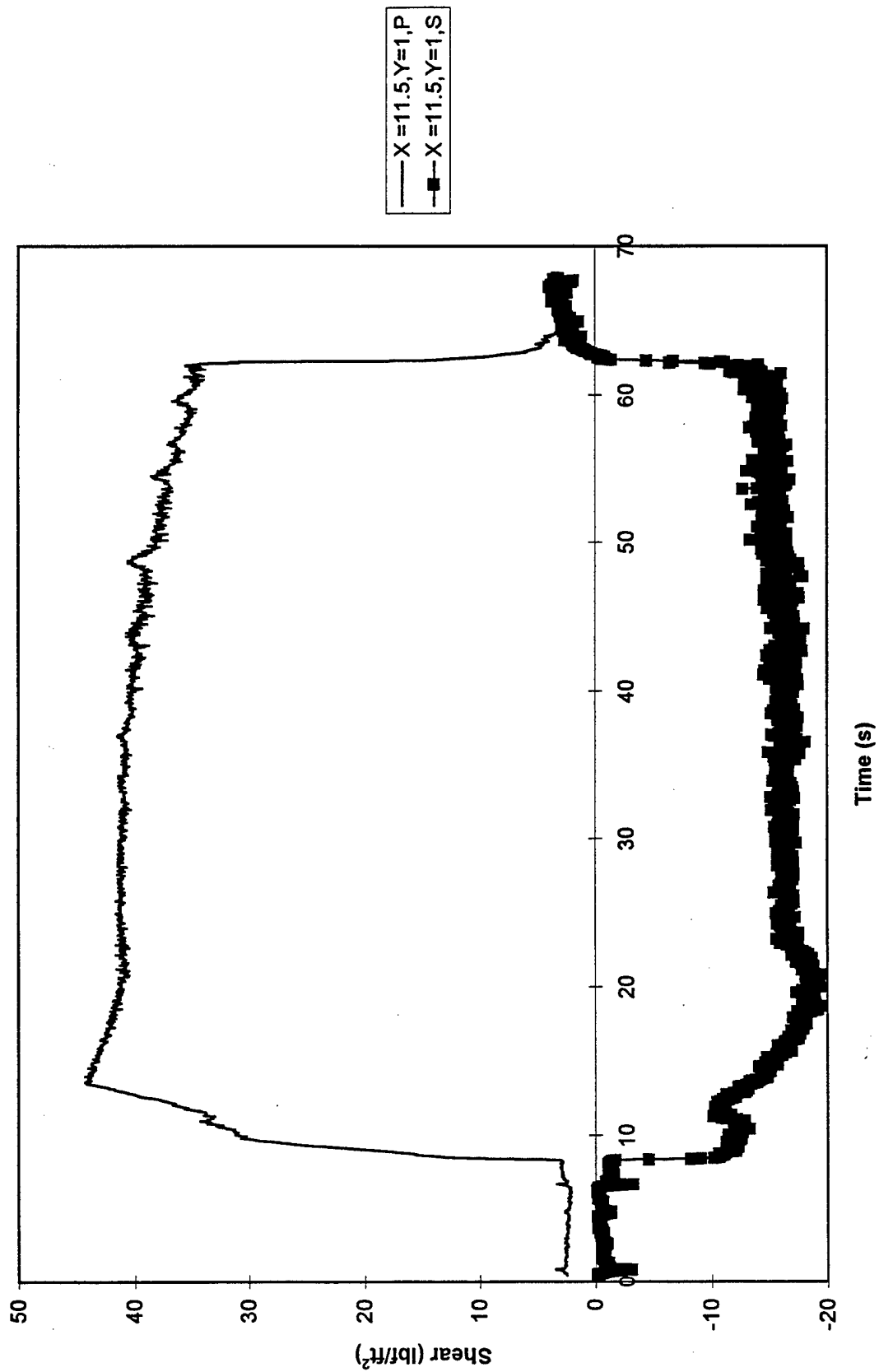


Figure 69. Skin Friction at $x = 11.5"$, $y = 1"$ During Test 887

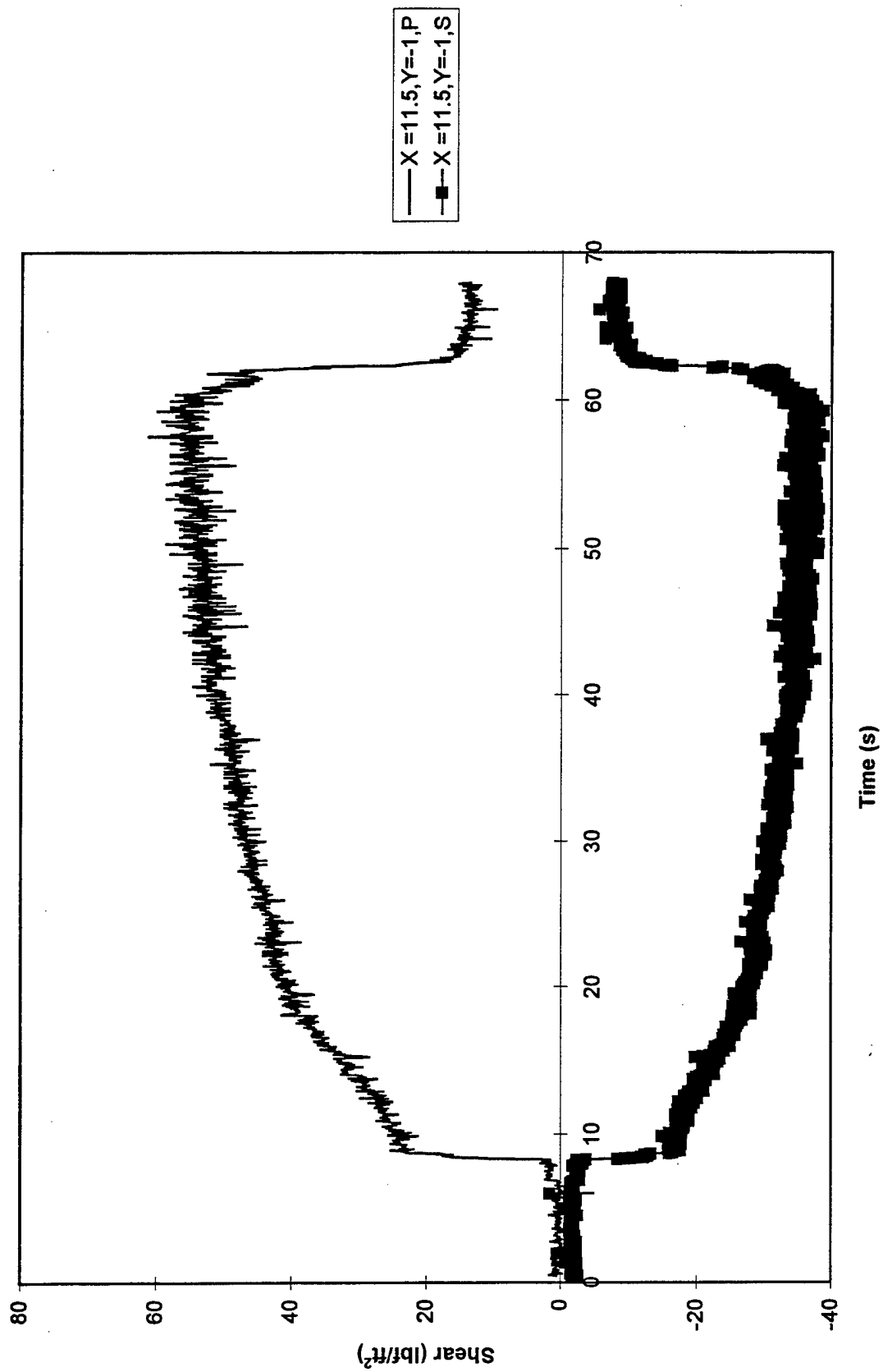


Figure 70. Skin Friction at $x = 11.5"$, $y = -1"$ During Test 887

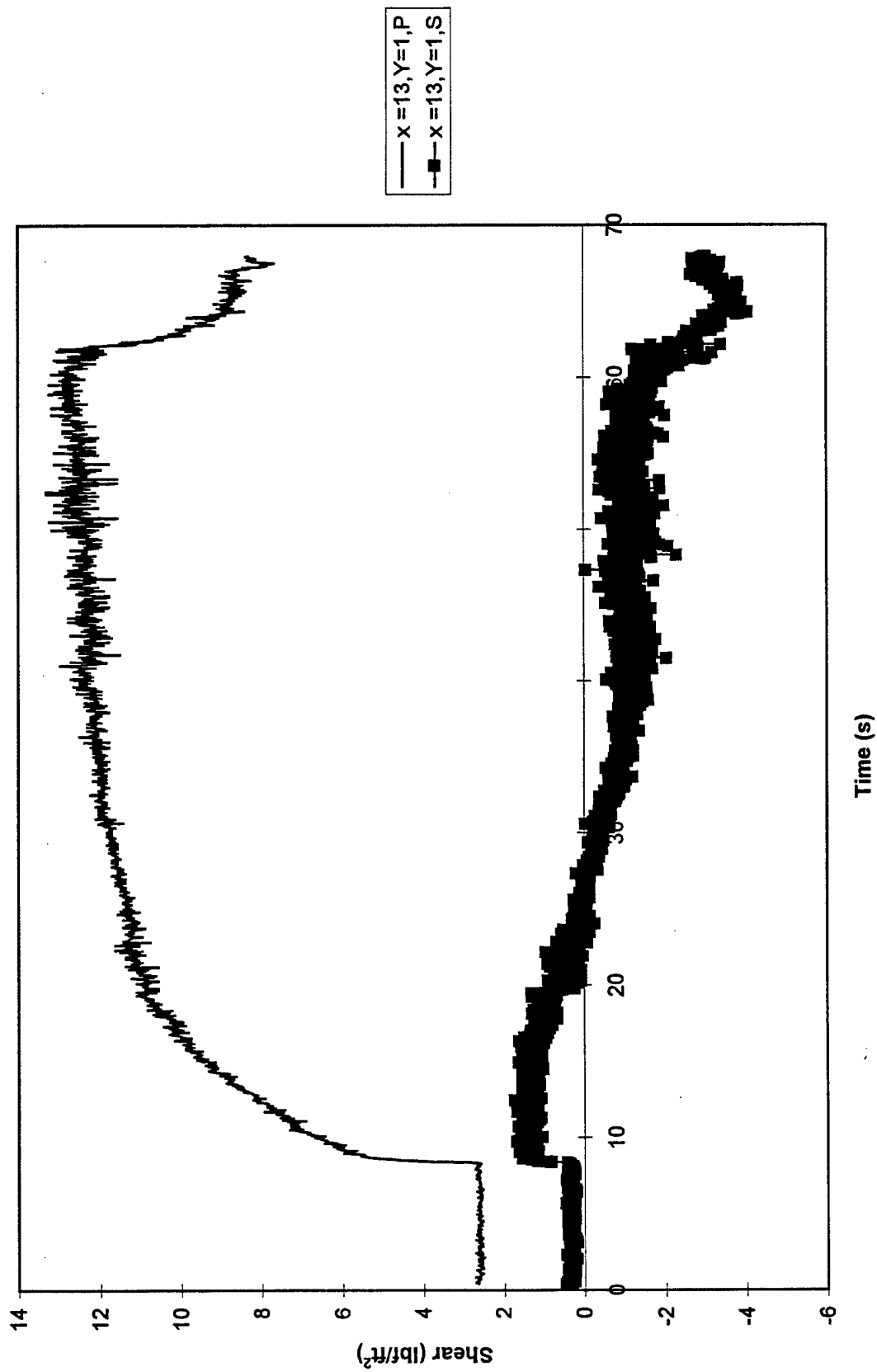


Figure 71. Skin Friction at $x = 13''$, $y = 1''$ During Test 887

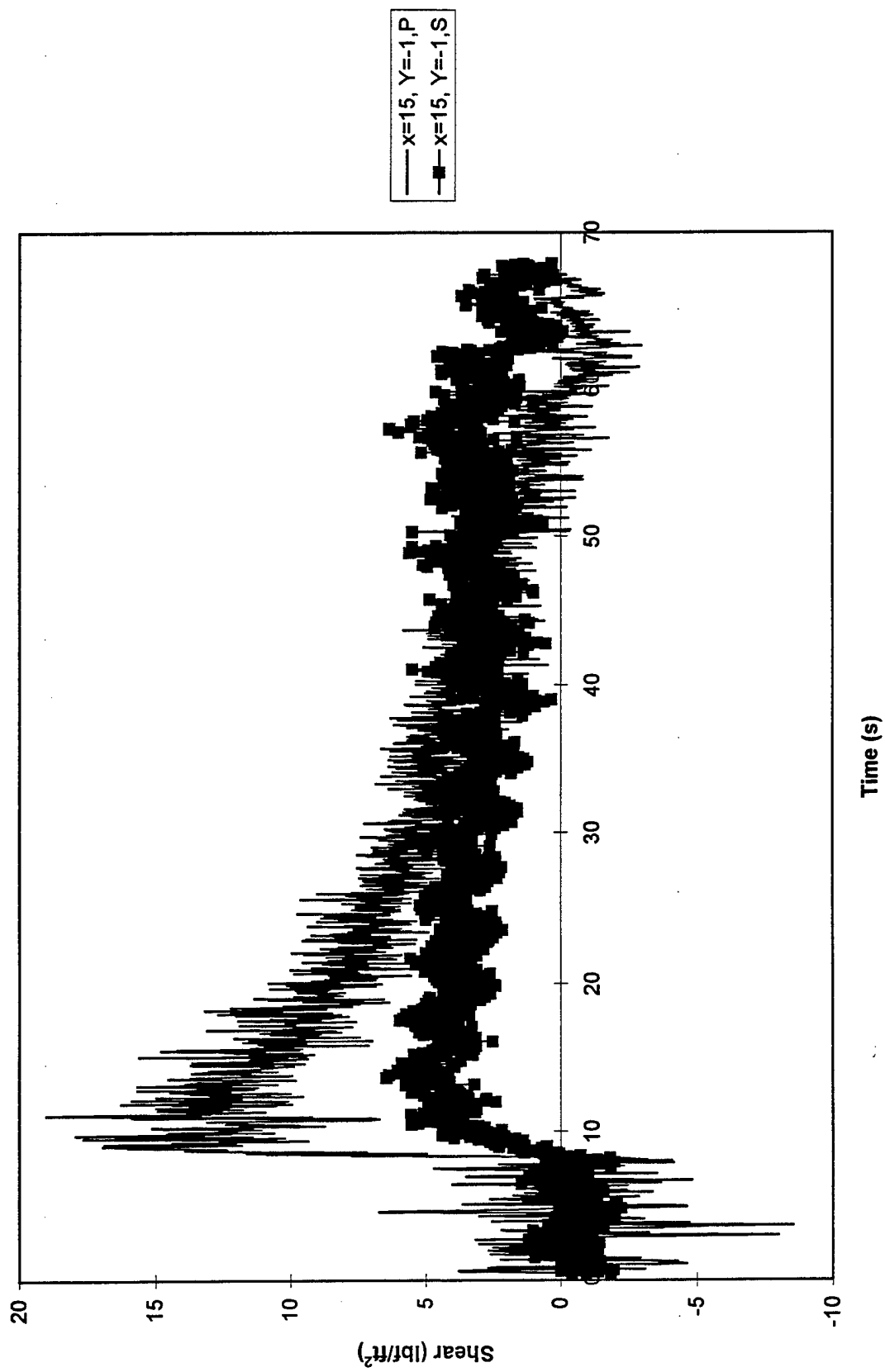


Figure 72. Skin Friction at $x = 15"$, $y = -1"$ During Test 887

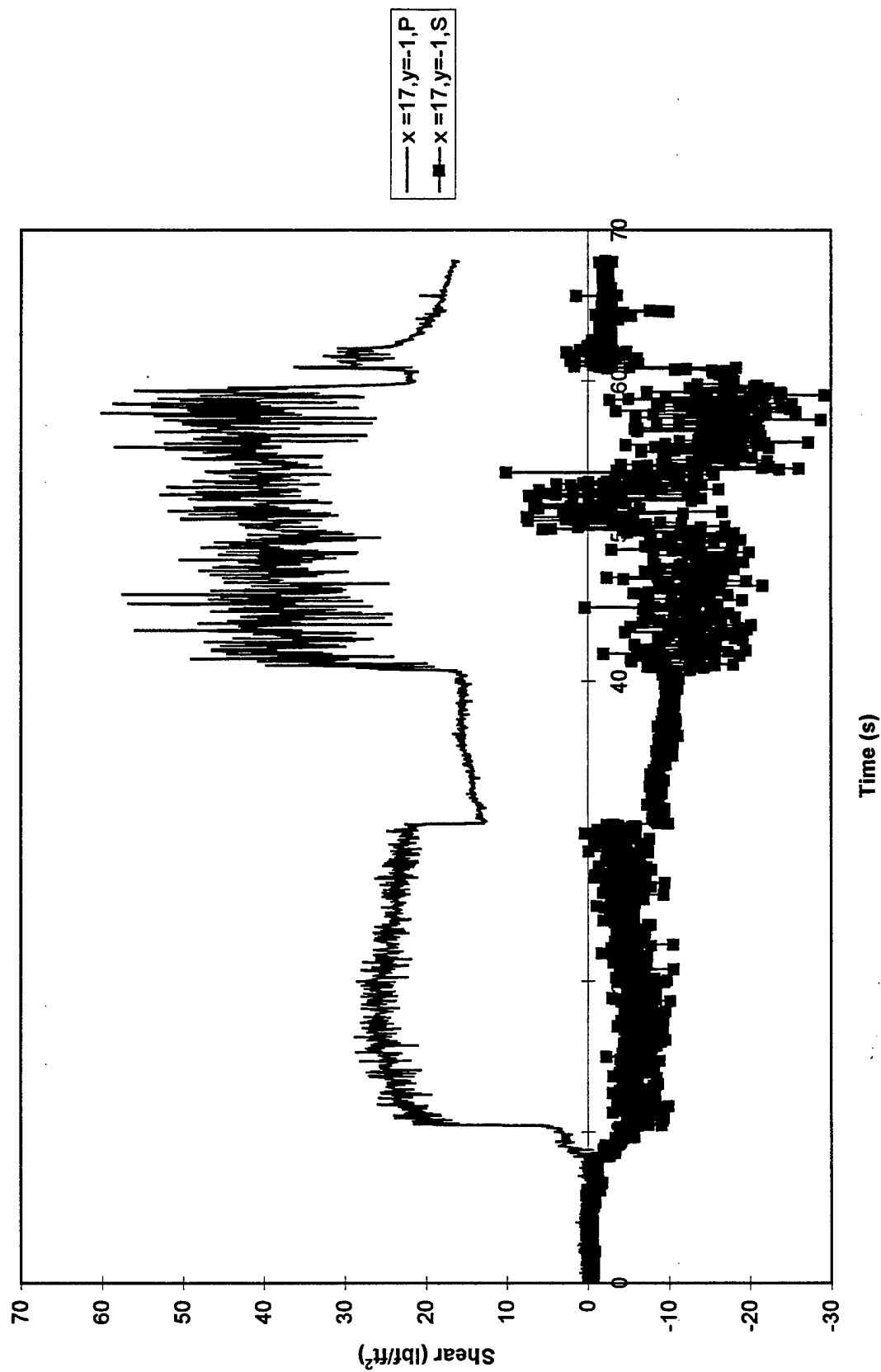


Figure 73. Skin Friction at $x = 17''$, $y = -1''$ During Test 887

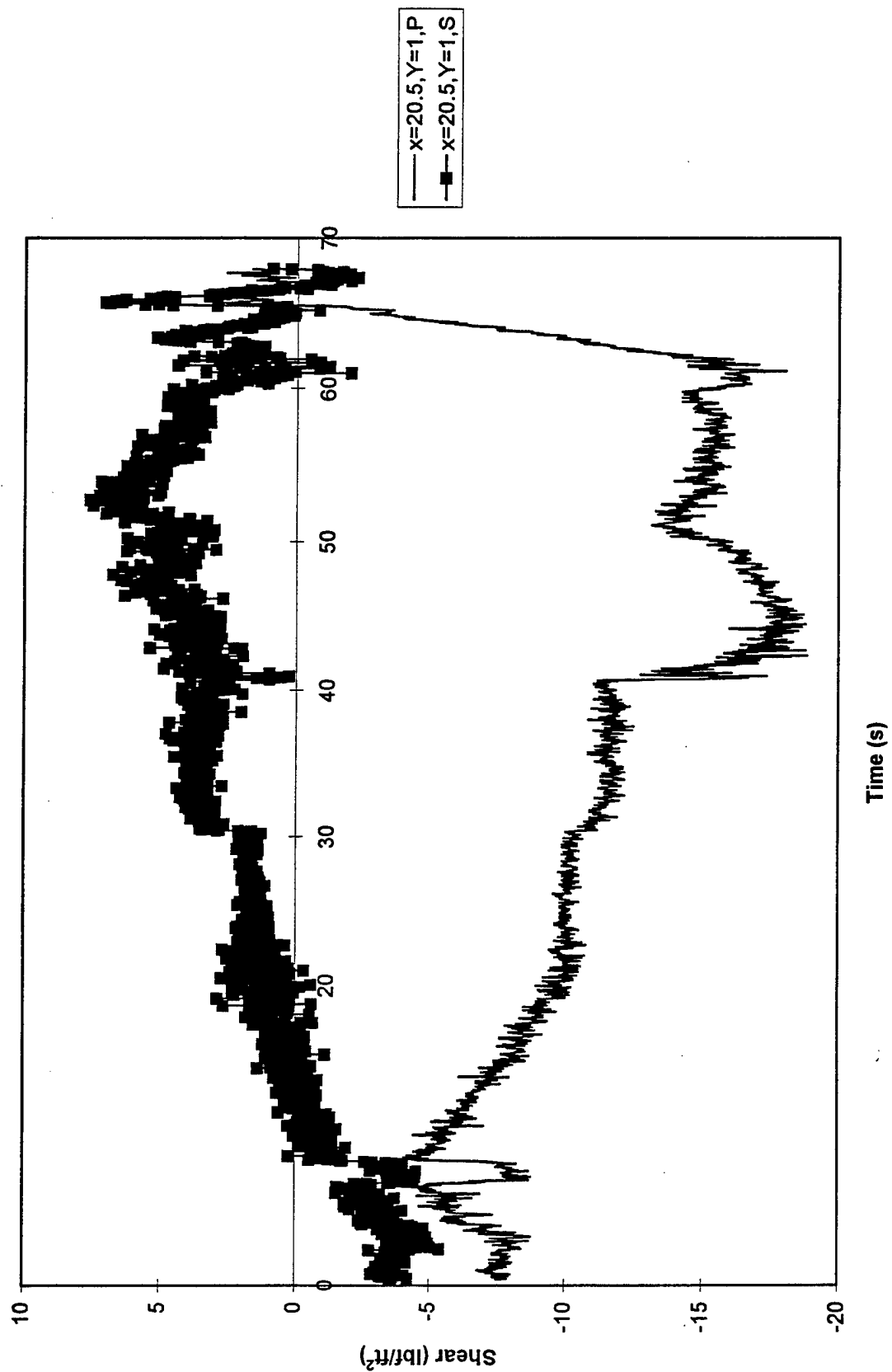


Figure 74. Skin Friction at $x = 20.5$ ", $y = 1$ " During Test 887

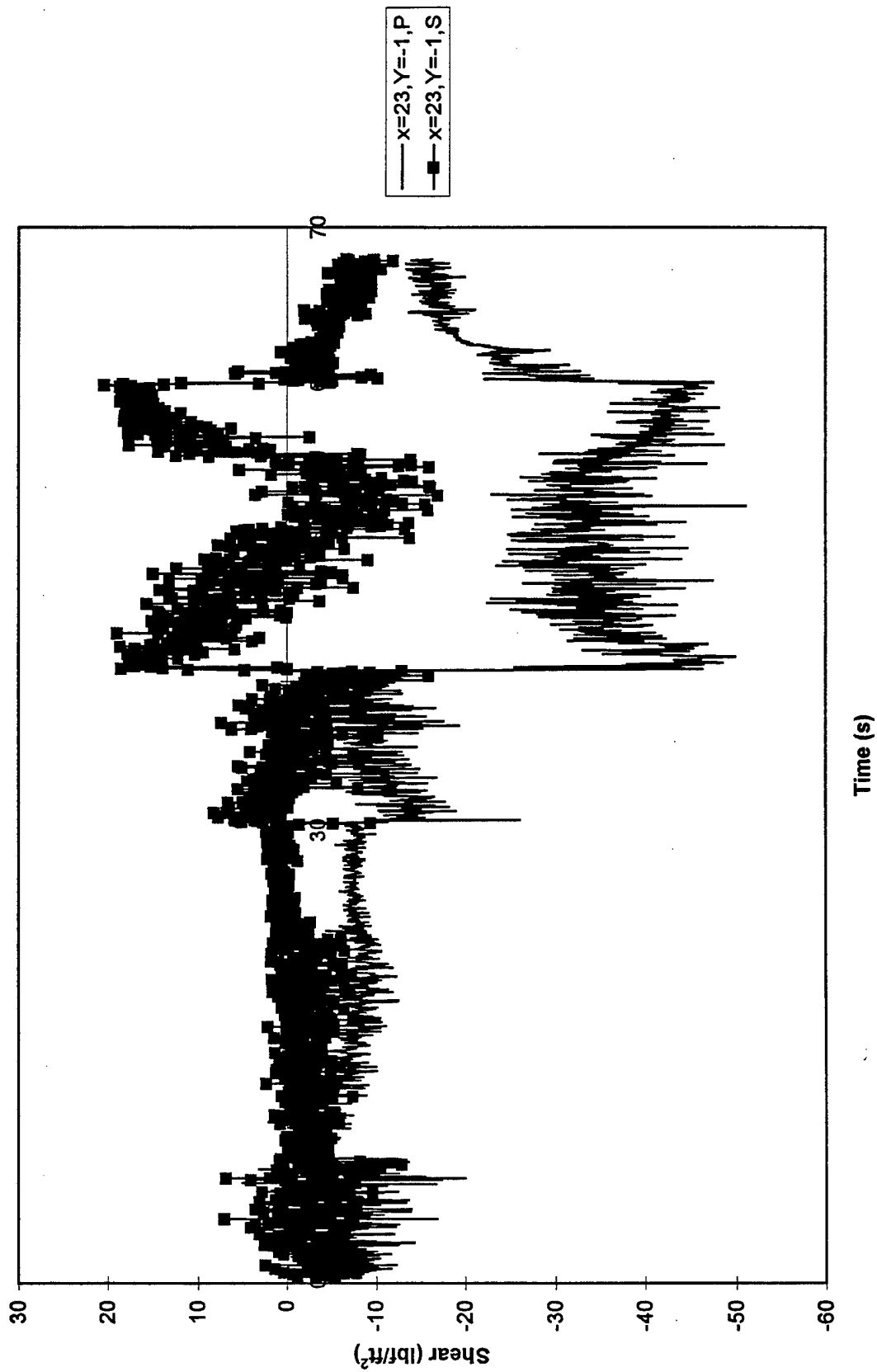


Figure 75. Skin Friction at $x = 23"$, $y = -1"$ During Test 887

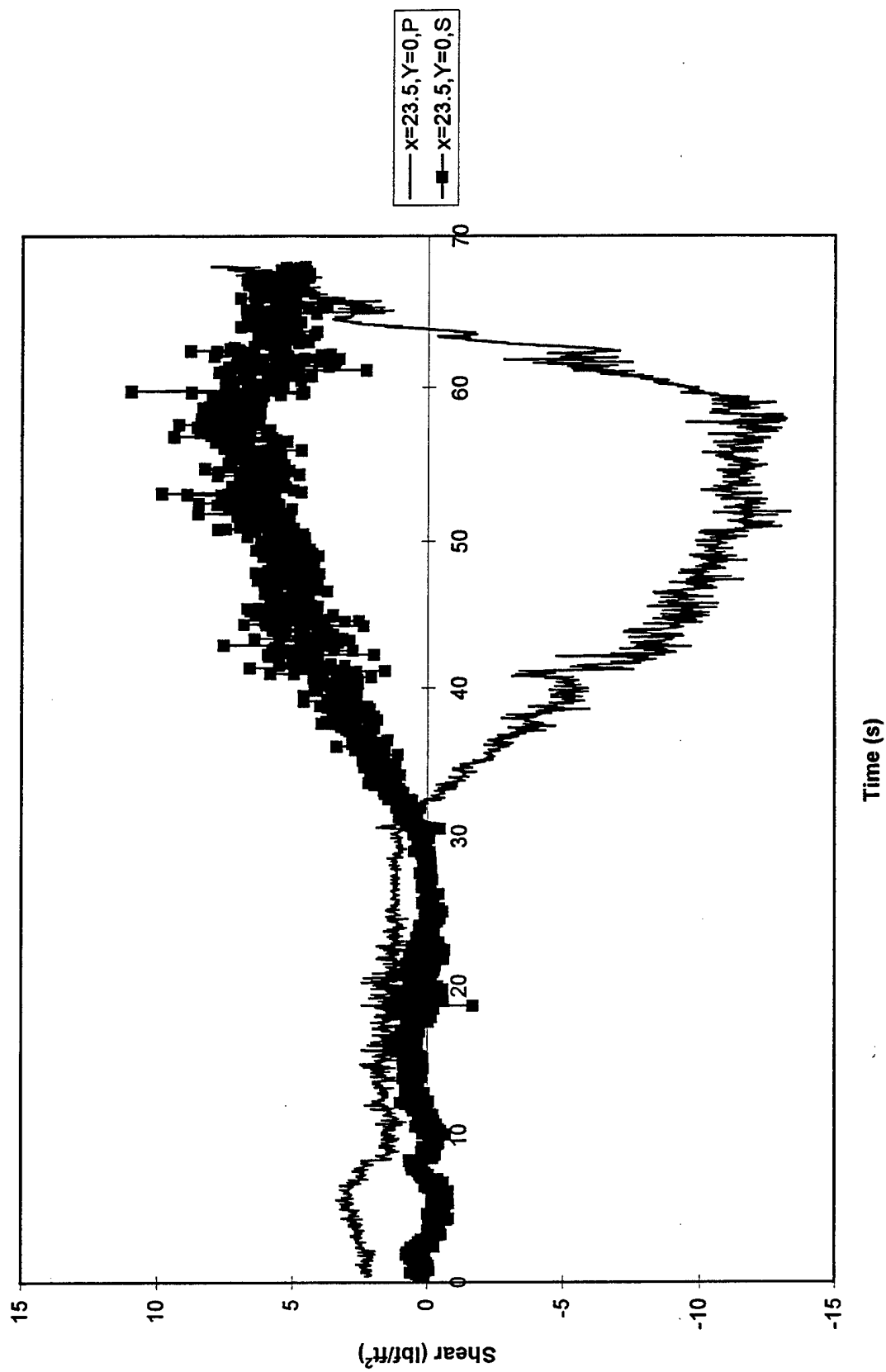


Figure 76. Skin Friction at $x = 23.5$ ", $y = 0$ " During Test 887

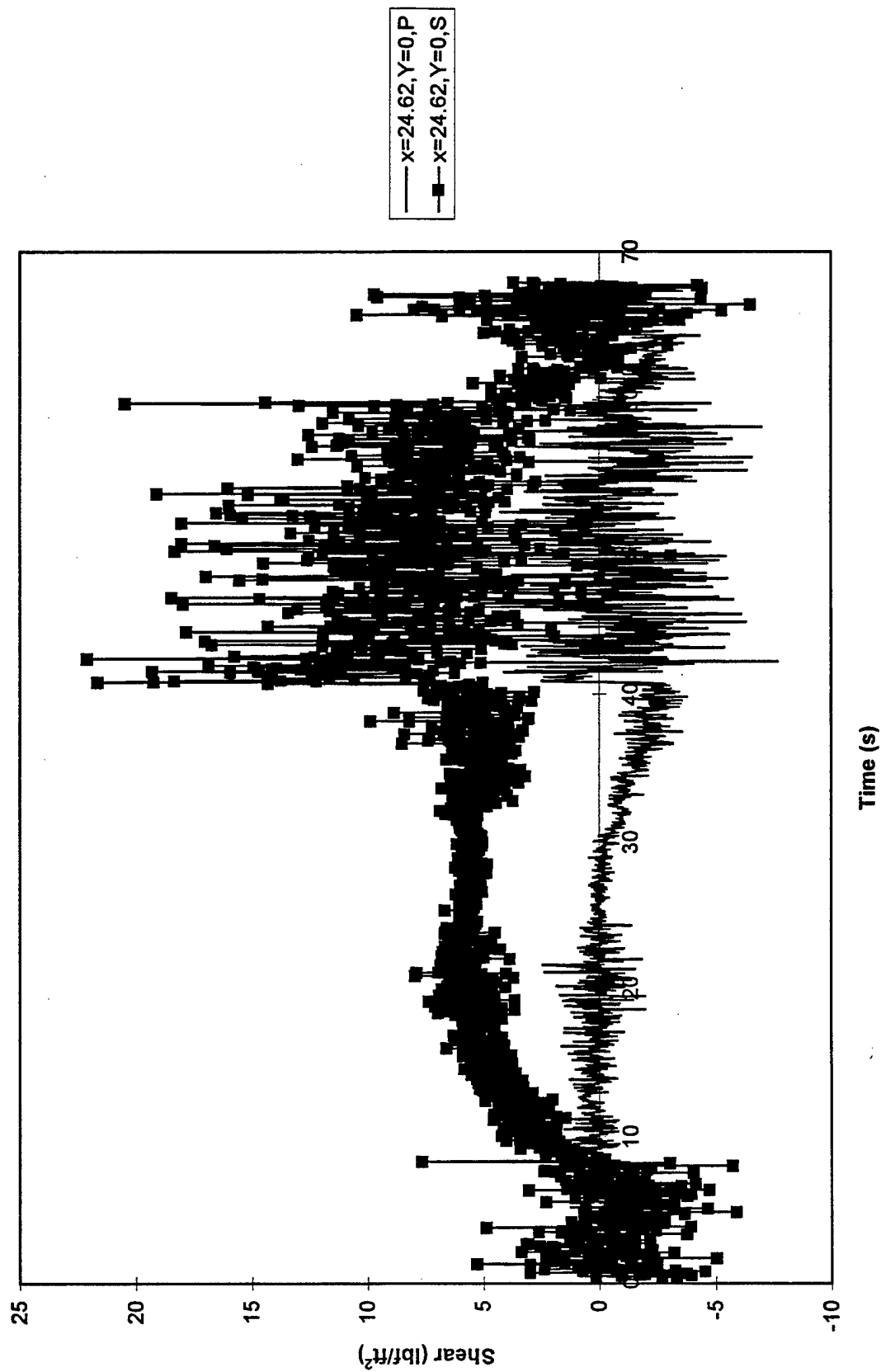


Figure 77. Skin Friction at $x = 24.6''$, $y = 0''$ During Test 887

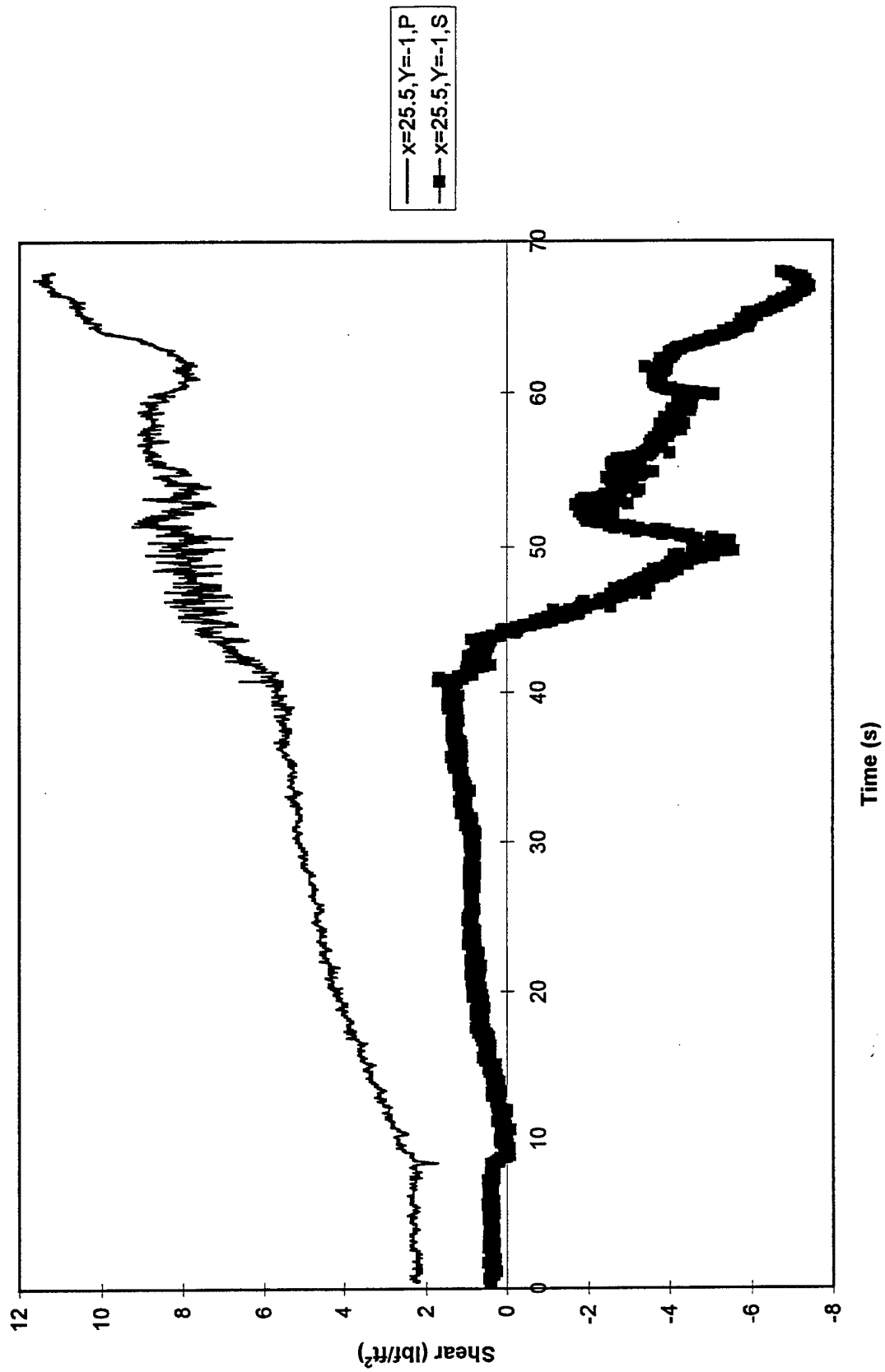


Figure 78. Skin Friction at $x = 25.5"$, $y = -1"$ During Test 887

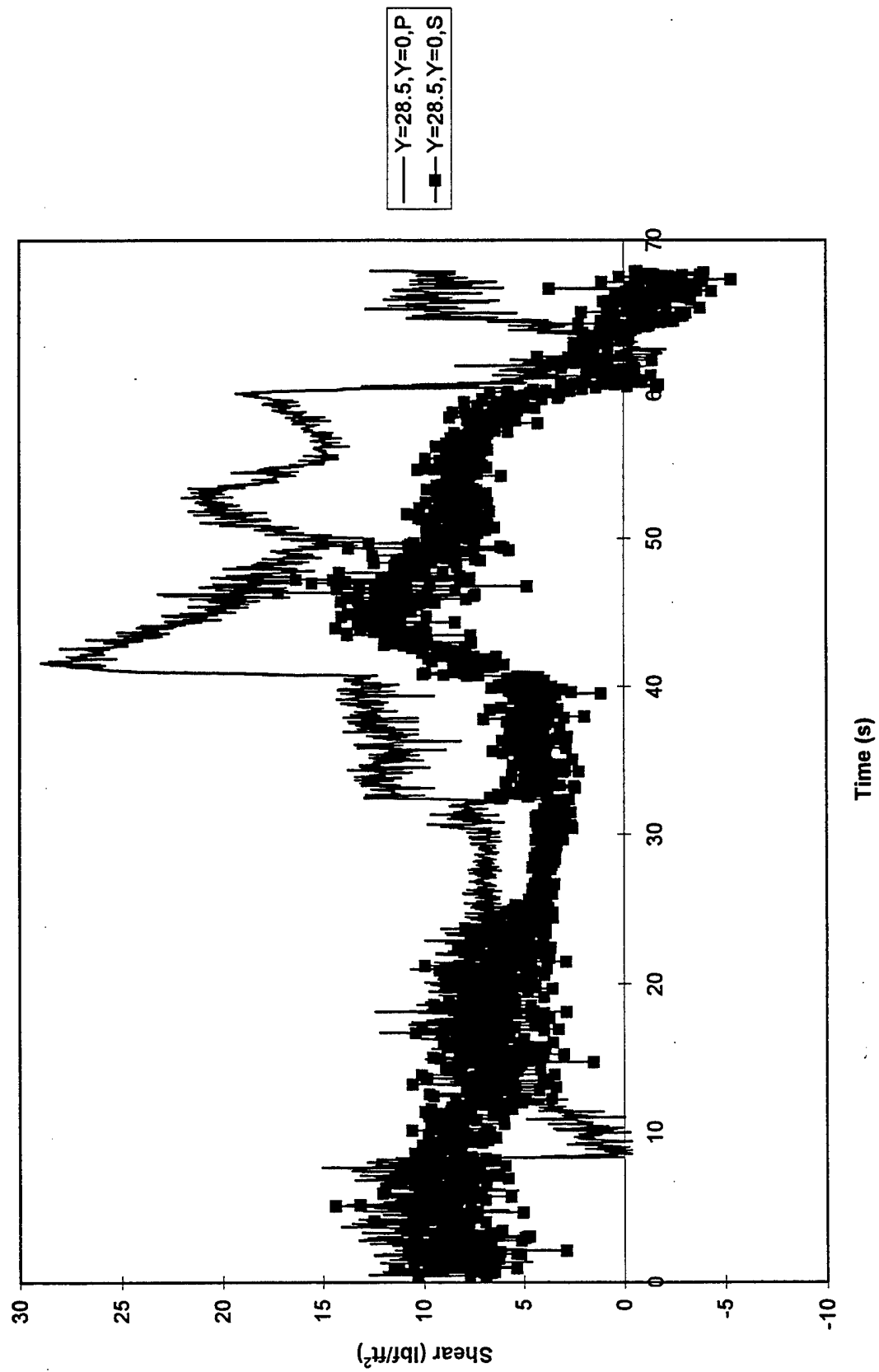


Figure 79. Skin Friction at $x = 28.5"$, $y = 0"$ During Test 887

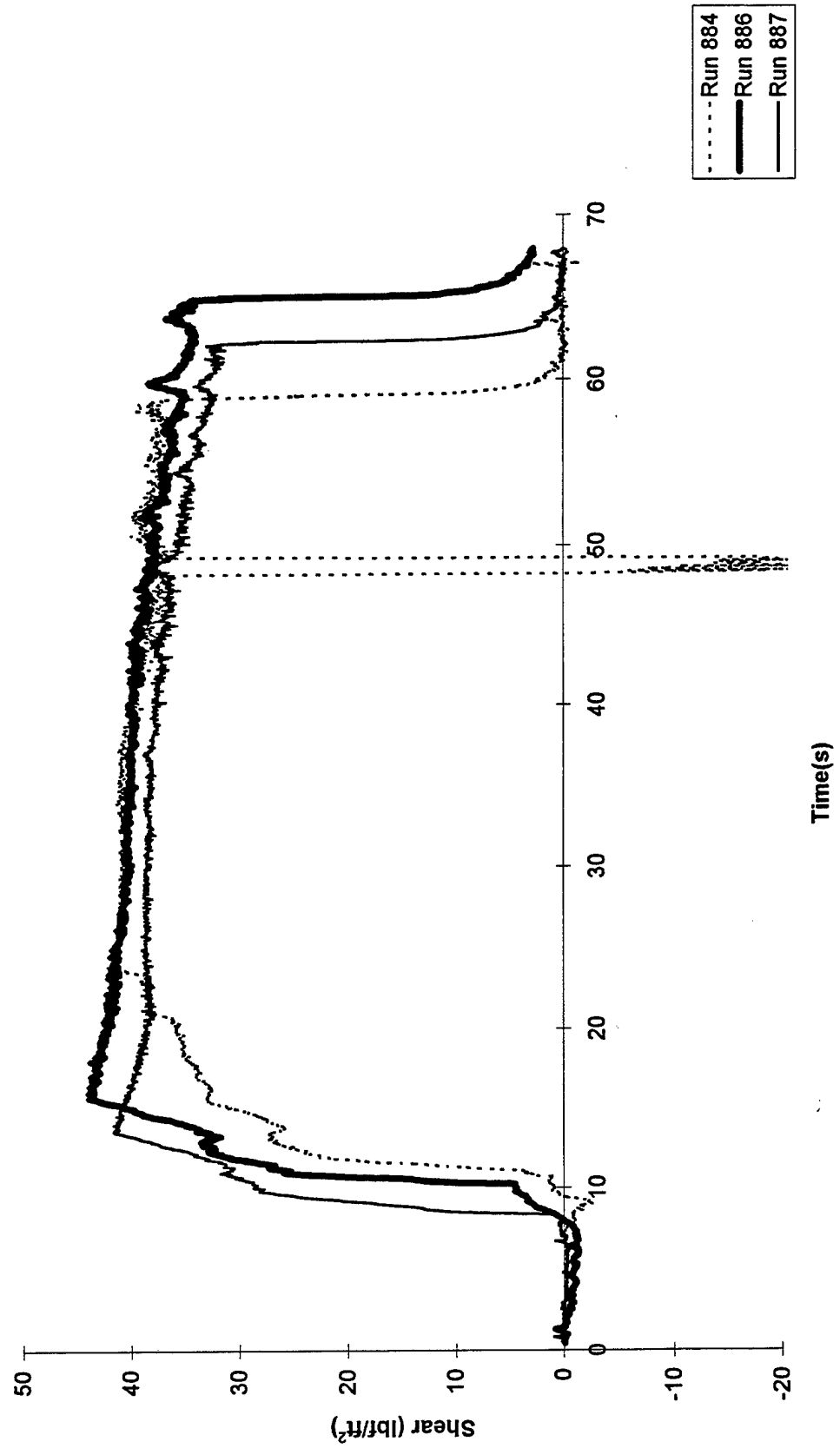


Figure 80. The Skin Friction at $x = 11.5''$, $y = 1''$

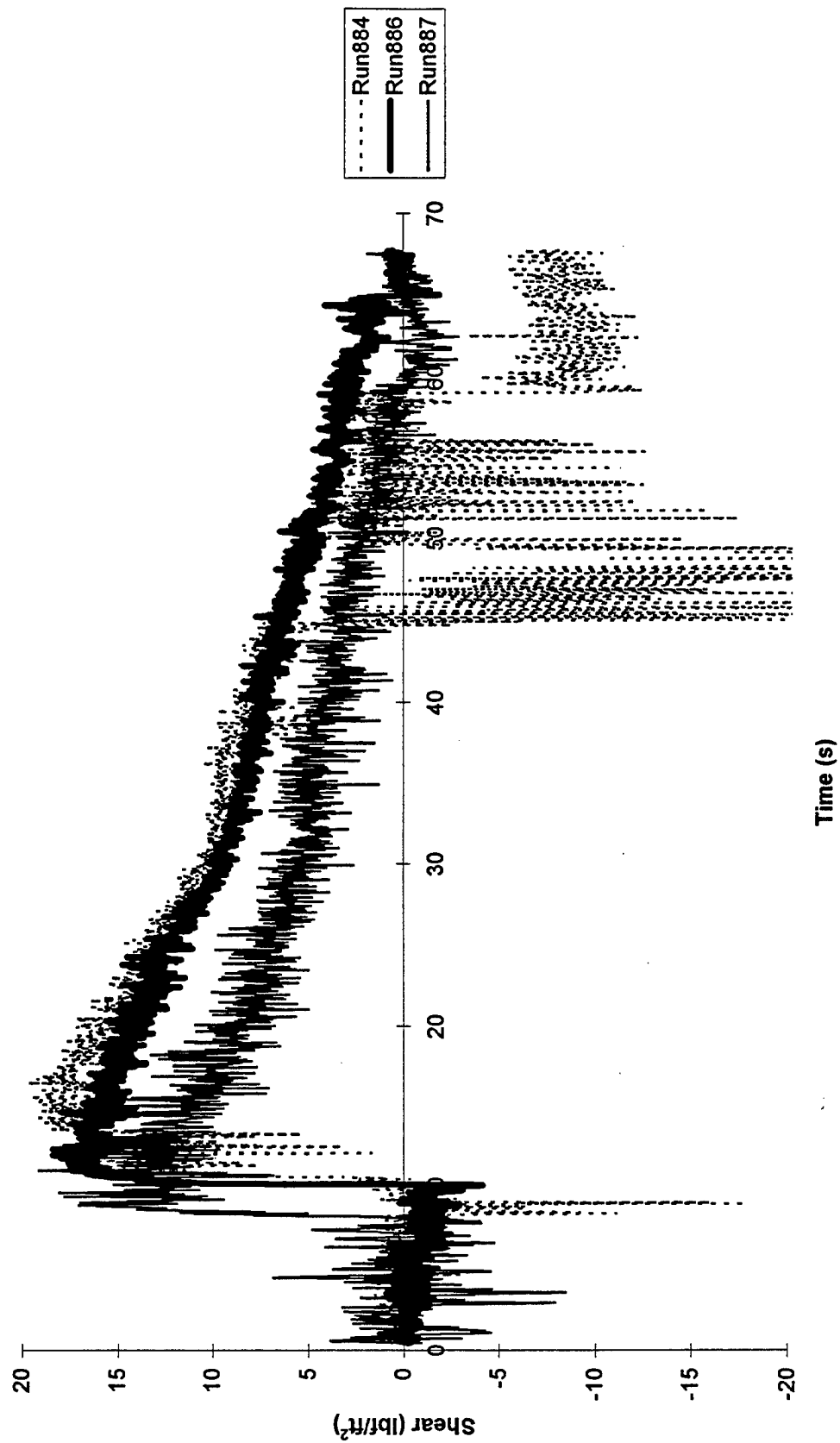


Figure 81. The Skin Friction at $x = 15''$

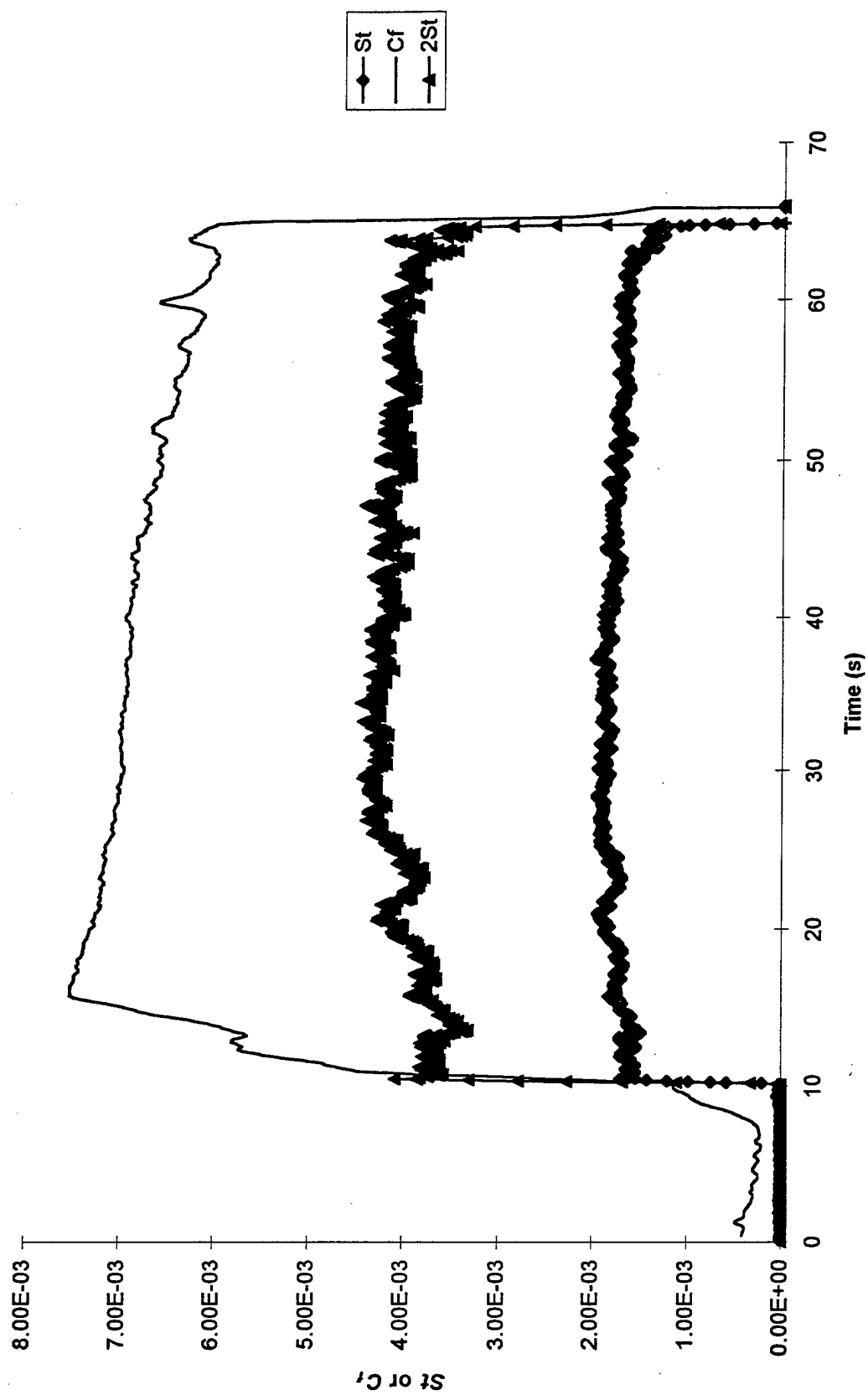


Figure 82. Comparison of Skin Friction and Heat Transfer at $x = 11.5''$, $y = 1''$ During Run 886

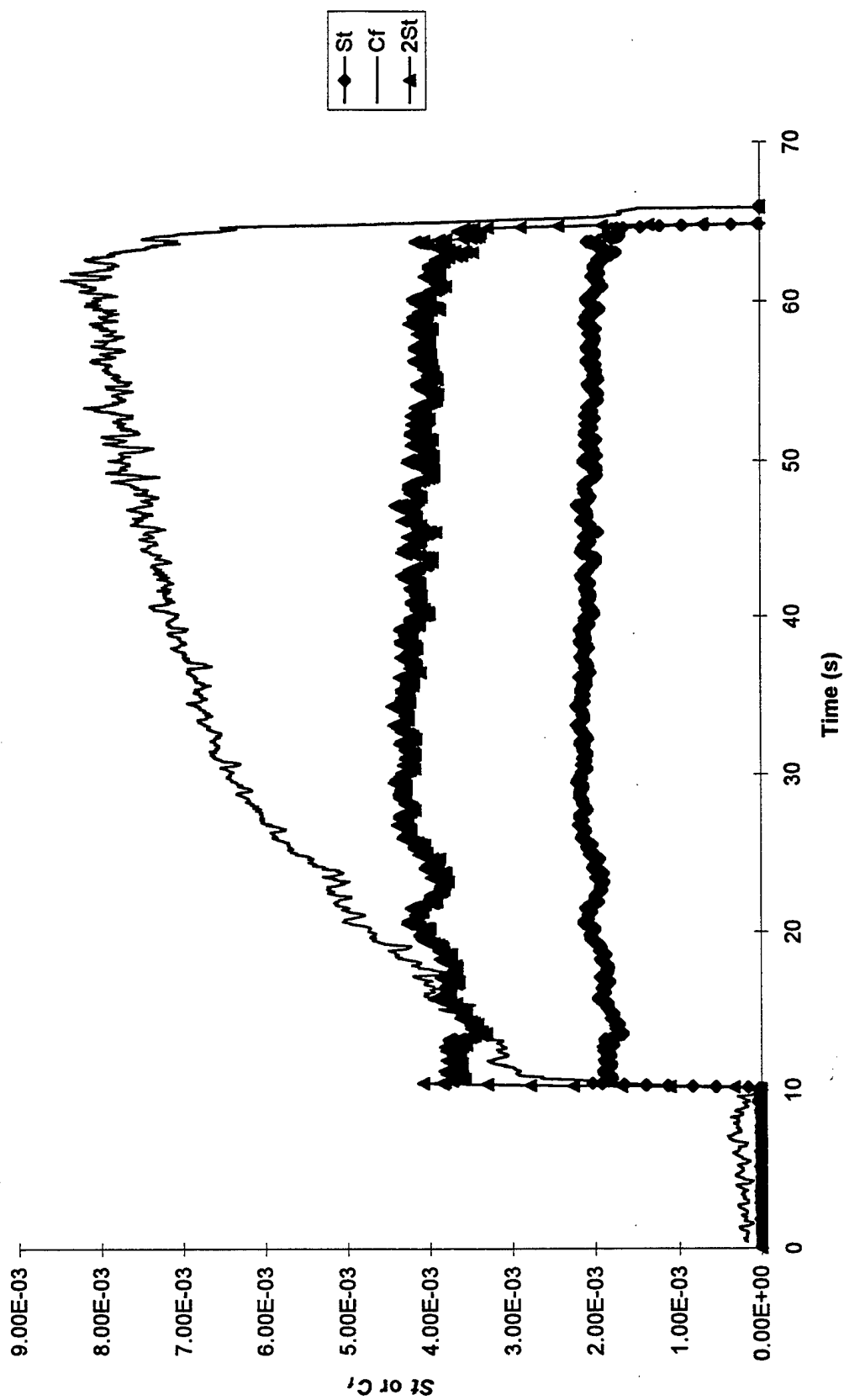


Figure 83. Comparison of Skin Friction and Heat Transfer at $x = 11.5''$, $y = -1''$ During Run 886

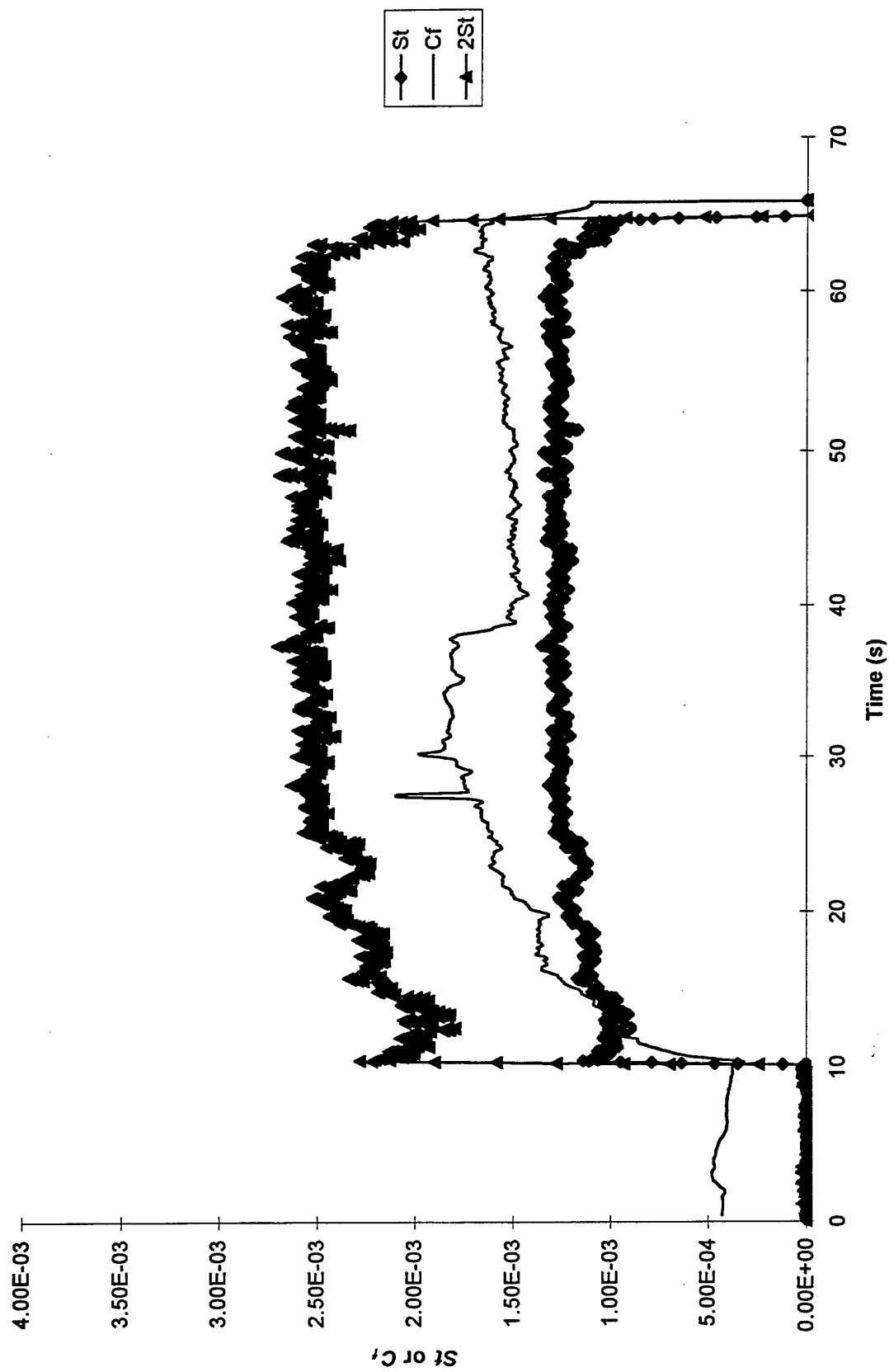


Figure 84. Comparison of Skin Friction and Heat Transfer at $x = 13''$, $y = 1''$ During Run 886

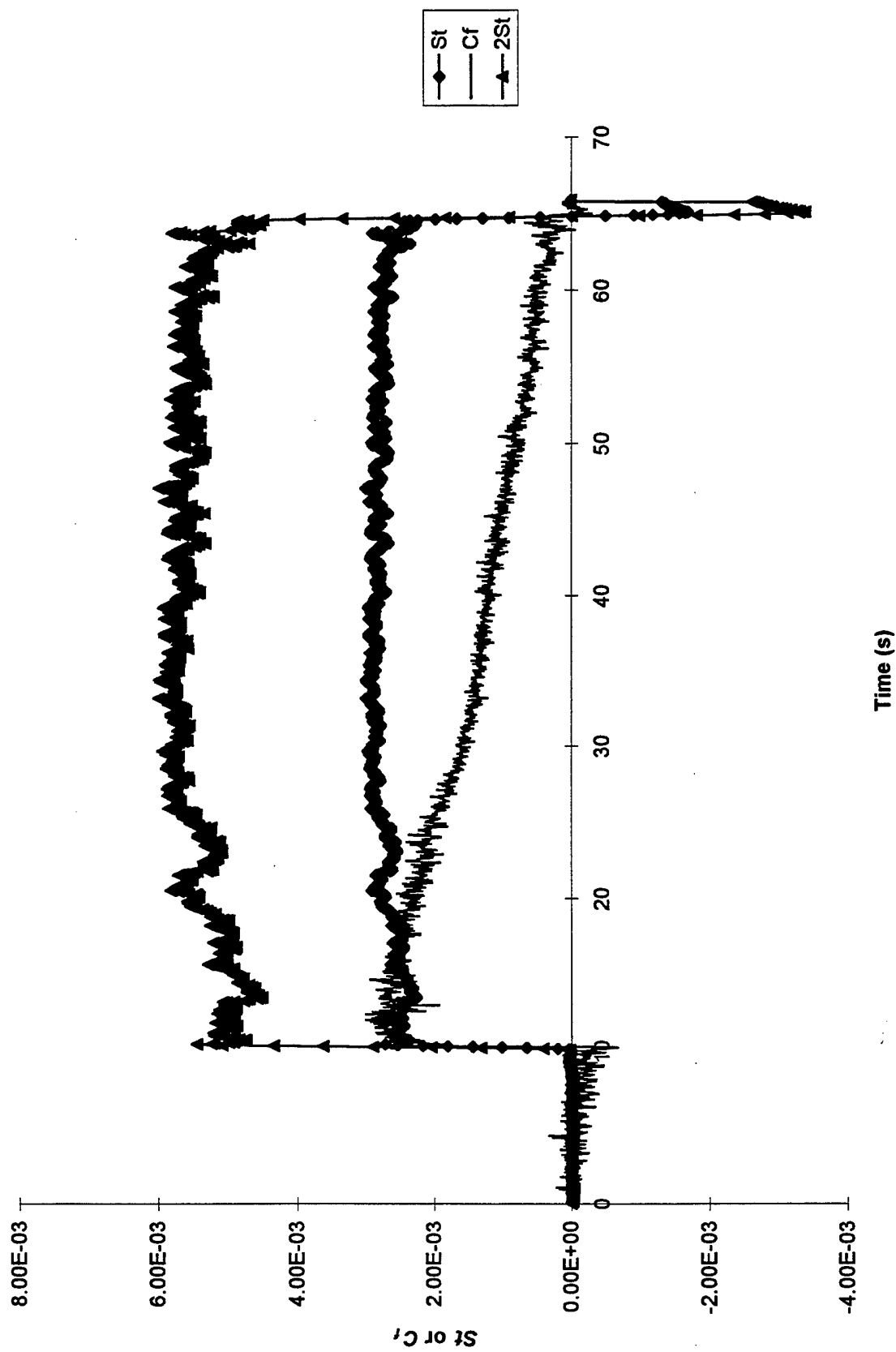


Figure 85. Comparison of Skin Friction and Heat Transfer at $x = 15''$, $y = -1''$ During Run 886

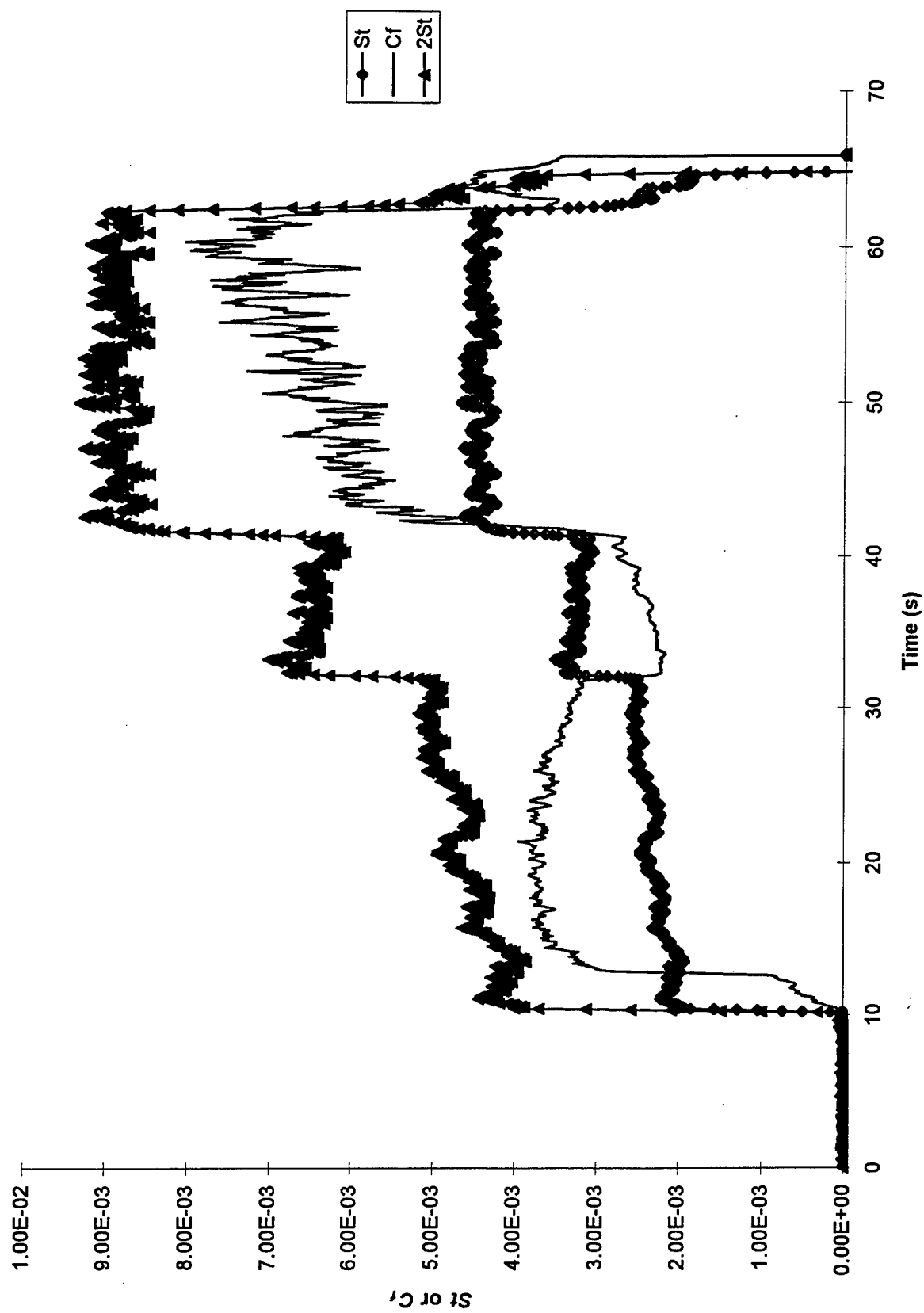


Figure 86. Comparison of Skin Friction and Heat Transfer at $x = 17''$, $y = -1''$ During Run 886

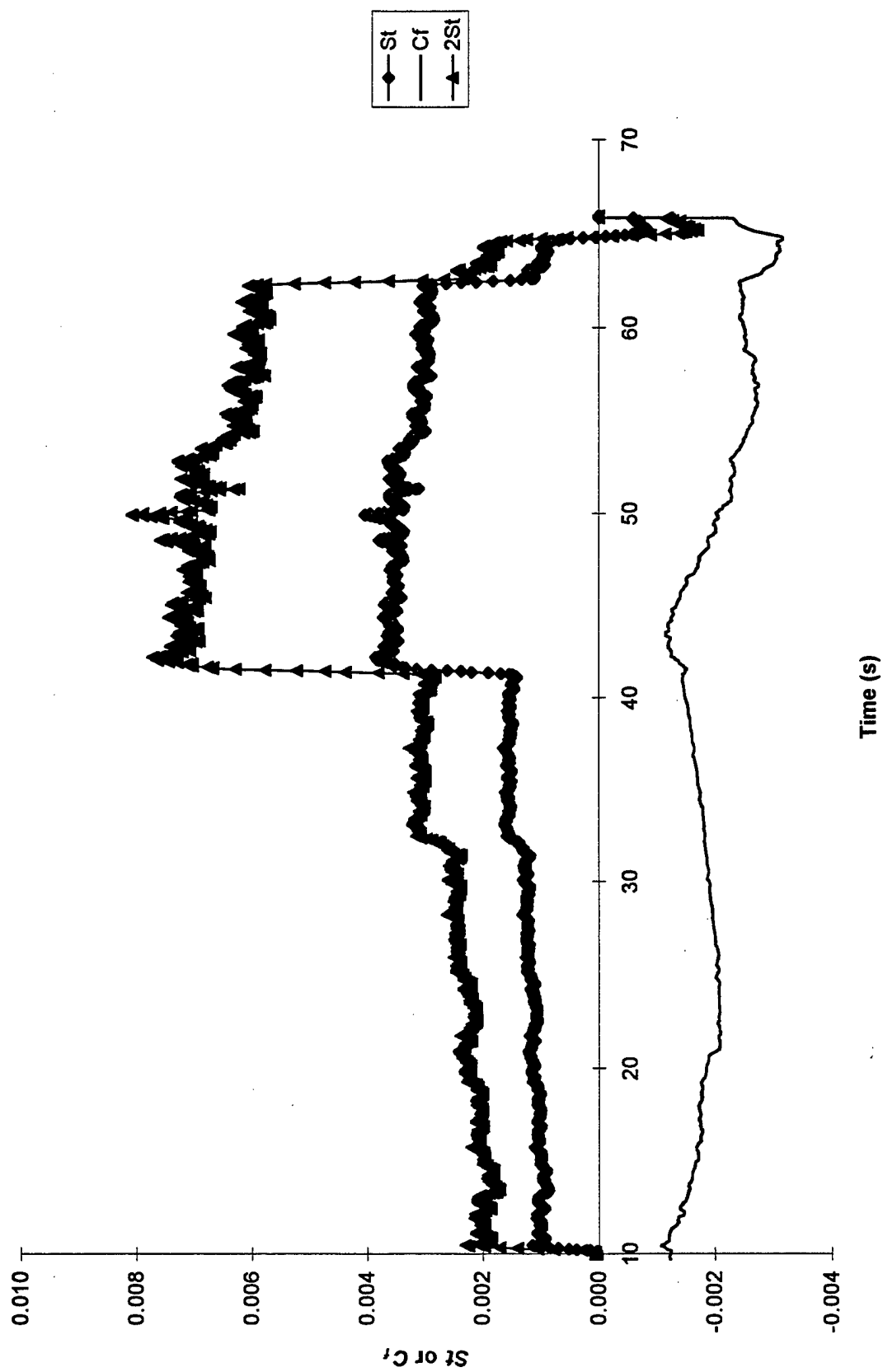


Figure 87. Comparison of Skin Friction and Heat Transfer at $x = 20.5''$, $y = 1''$ During Run 886

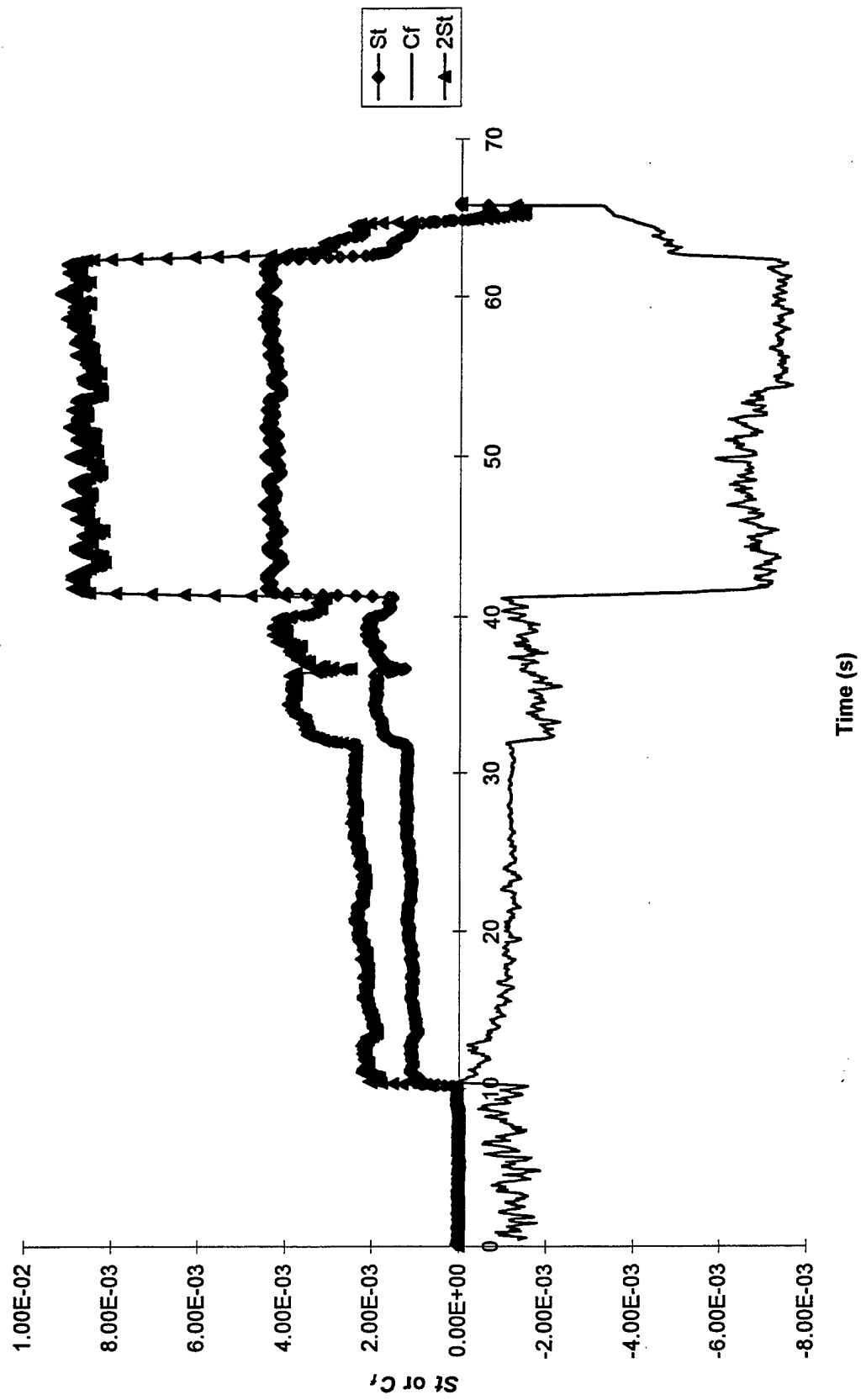


Figure 88. Comparison of Skin Friction and Heat Transfer at $x = 23''$, $y = -1''$ During Run 886

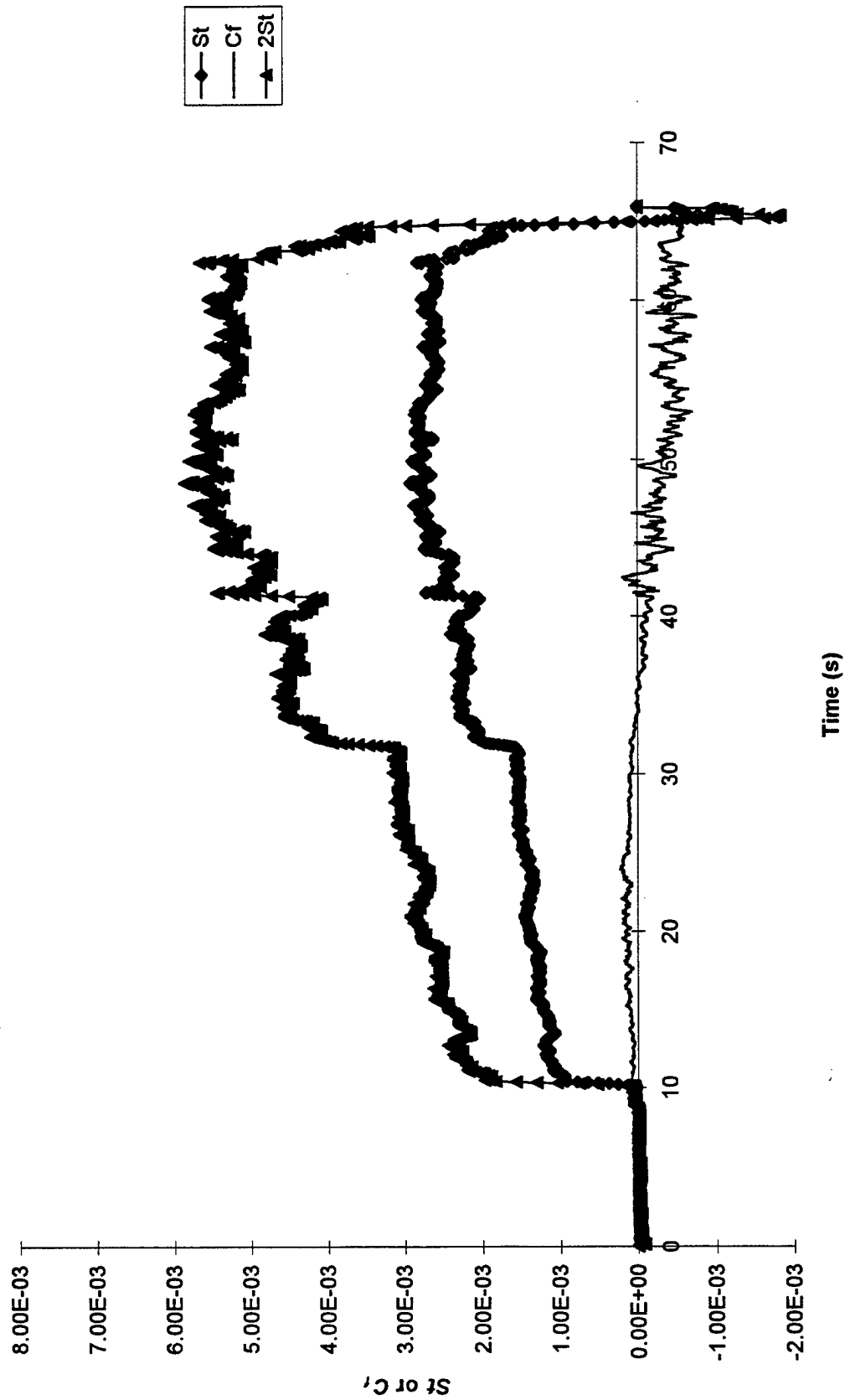


Figure 89. Comparison of Skin Friction and Heat Transfer at $x = 24.6''$, $y = 0''$ During Run 886

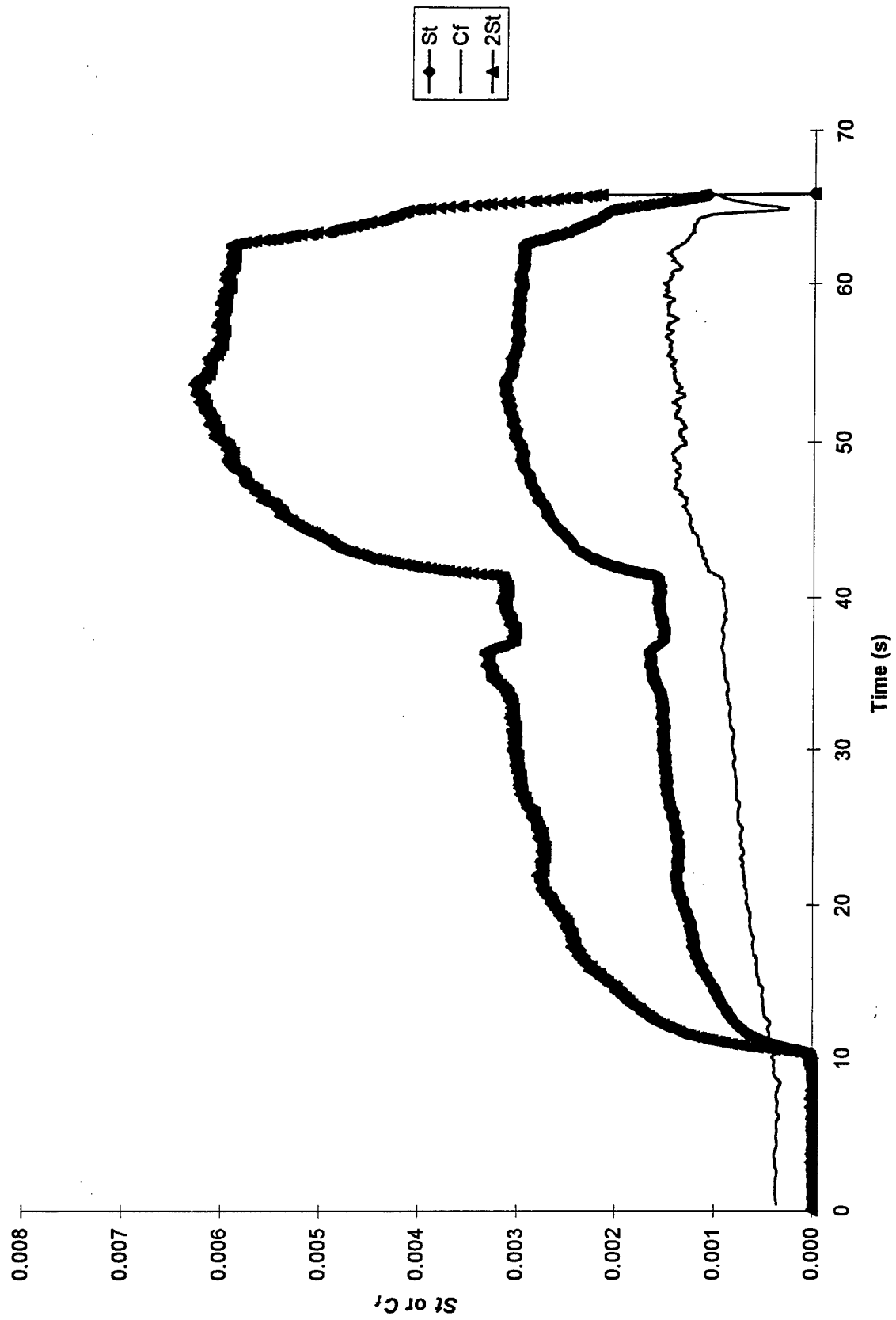


Figure 90. Comparison of Skin Friction and Heat Transfer at $x = 25.5''$, $y = -1''$ During Run 886

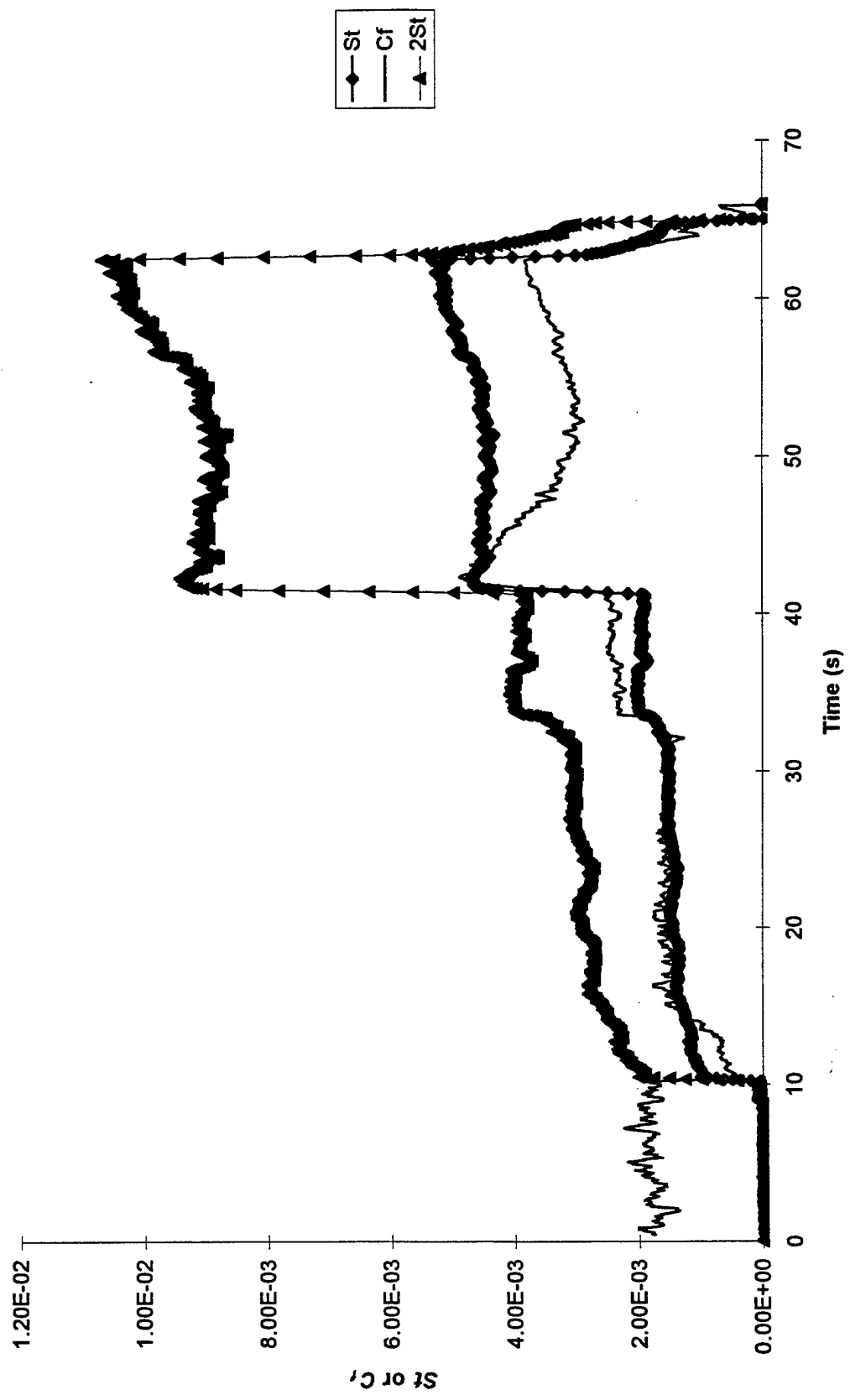


Figure 91. Comparison of Skin Friction and Heat Transfer at $x = 28.5''$, $y = 0''$ During Run 886

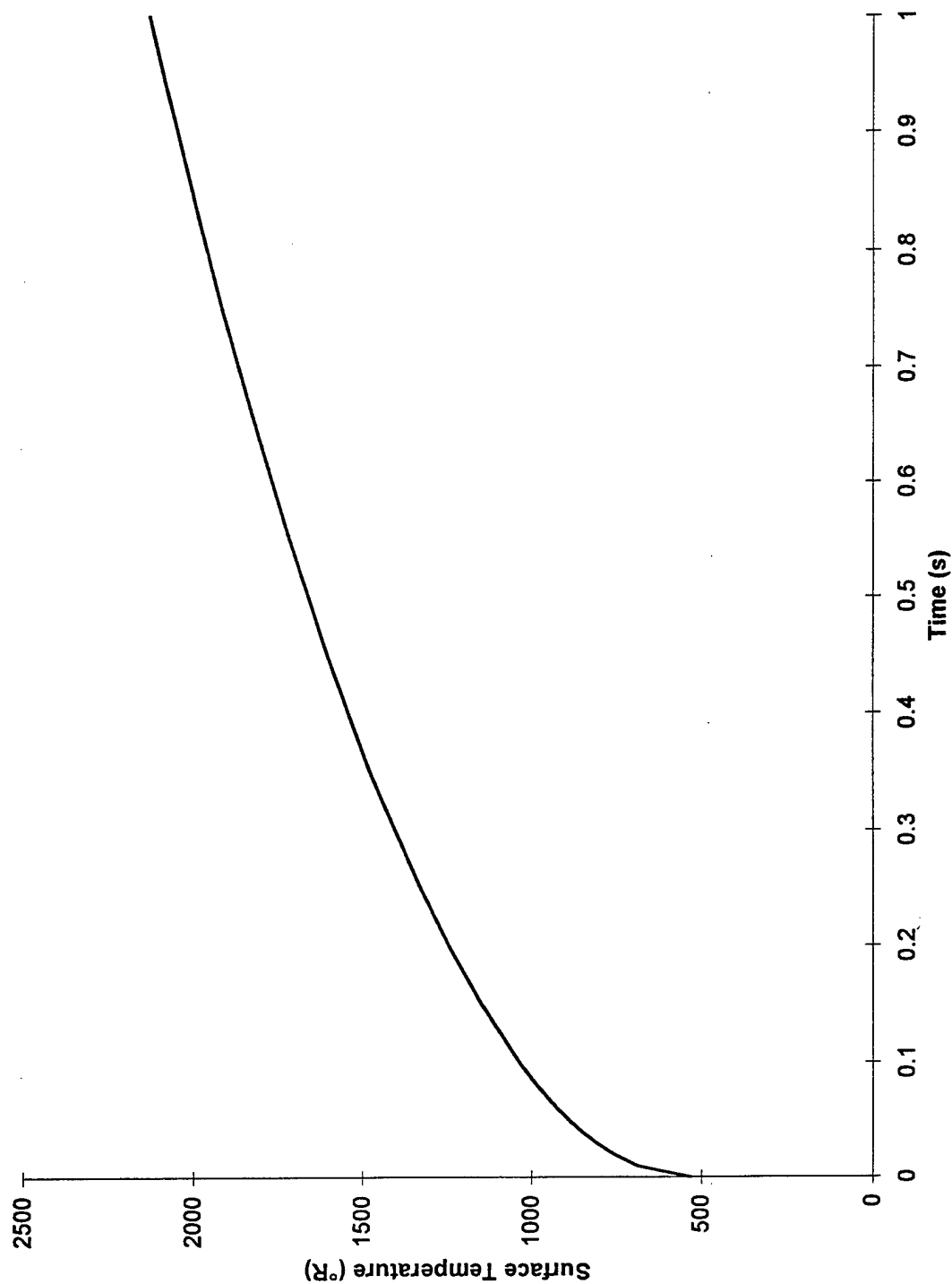


Figure 92. Semi-infinite Response of Dow-Corning Silicon Oil to a Constant Heat Flux of 10 BTU/ft²-s

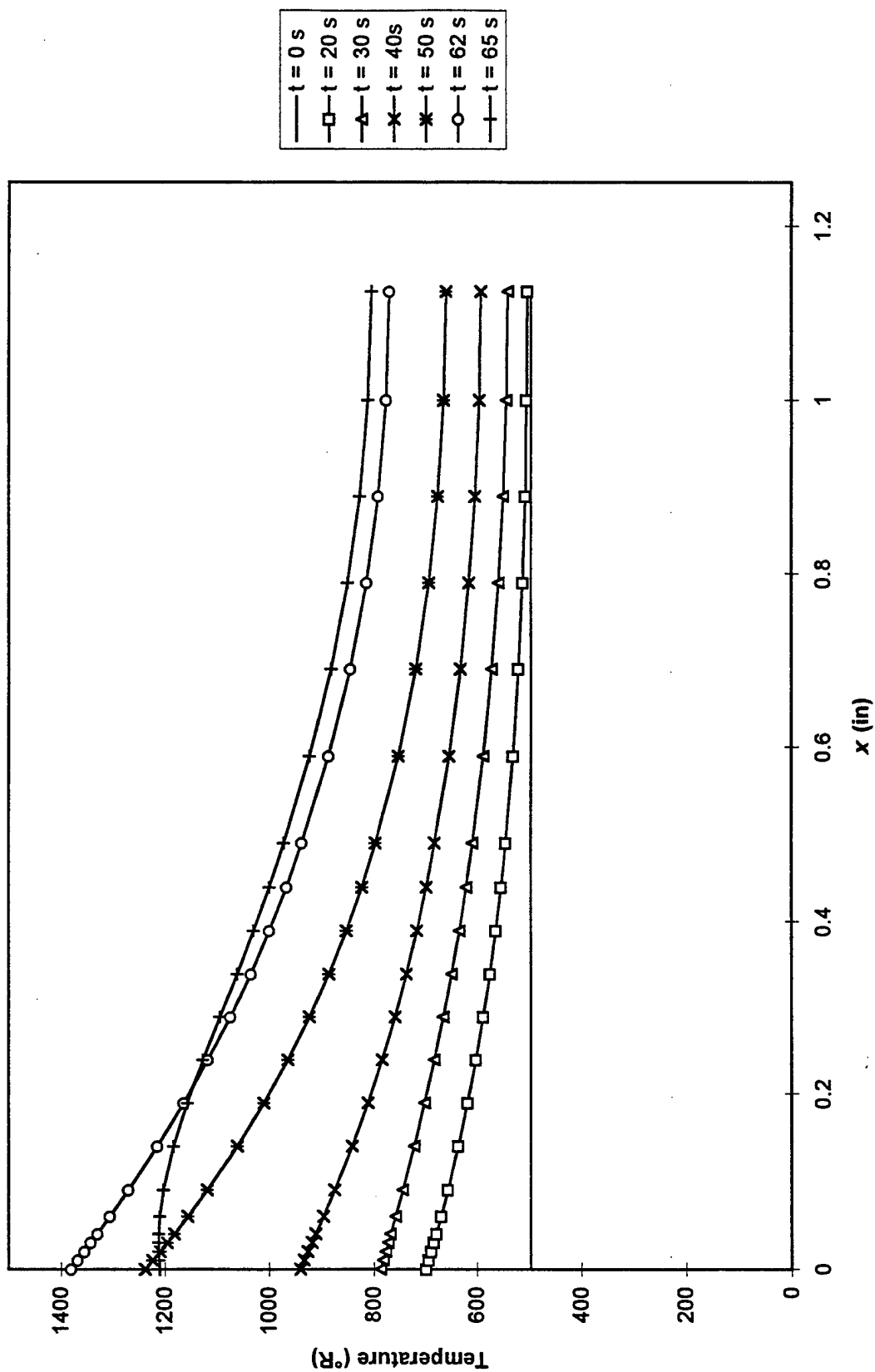


Figure 93. Temperature Distribution Through the Wall at $x = 23''$, $y = -1''$ During Run 886

data channel	33	26	119	...
gage #	73	66	1	...
type	1	1	1	...
gain	1	1	1	...
x	11.5	11.5	11.5	...
y	-1	1	2	...
time (sec)	x = 11.5, y = -1	x = 11.5, y = 1	x = 11.5, y = 2	...
0.025	0.14	-0.705	2.343	...
0.065	0.72	-1.34	0.402	...
0.105	-2.018	1.398	1.545	...
0.145	-0.223	0.375	0.672	...
0.185	0.21	0.042	-0.68	...
0.225	1.075	-2.01	1.058	...
.
.
.

Figure 94. A Section of File bt884fa.txt